THESIS

ANALYSIS OF MULTI-CHANNEL WIND LOADING USING PROPER ORTHOGONAL DECOMPOSITION

Submitted by

Rajendra Adhikari

Department of Civil and Environmental Engineering

In partial fulfillment of the requirements

For the Degree of Master of Science

Colorado State University

Fort Collins, Colorado

Summer 2014

Master's Committee:

Advisor: Bogusz Bienkiewicz

Suren Chen
Hiroshi Sakurai

ABSTRACT

ANALYSIS OF MULTI-CHANNEL WIND LOADING USING PROPER ORTHOGONAL DECOMPOSITION

Wind tunnel testing utilizing multi-channel pressure measurement system leads to large volume of the acquired wind pressure data. In the presented research, use of Proper Orthogonal Decomposition (POD), to analyze such data, is described. Wind pressure time series acquired for a generic low-rise building were used in the analysis. First, the pressure covariance matrices were calculated. They were subsequently used to determine the pressure eigenvalues and the eigenfunctions. These quantities were next employed to calculate the POD principal coordinates. Finally, the eigenvectors and the principal coordinates were used to reconstruct the pressure time series. This analysis was carried out for pressures exerted on the whole building and on its distinct surfaces – side walls and roof. The convergence of the pressure time series reconstruction was inspected. The mean, standard deviation and the peak values of the reconstructed pressure were evaluated. The effects of wind direction on the original and reconstructed pressures were investigated. The POD modal contributions and the convergence of the pressure reconstruction were quantified. Overall, the obtained results were found to be consistent with findings of related POD studies reported by other researchers. High spatial and temporal resolutions of the wind loading data used in the present research made possible refined quantification of the effects of the studied parameters.

ACKNOWLEDGEMENTS

I would like to gratefully and sincerely thank Dr. Bogusz Bienkiewicz for all his guidance, understanding and patience. His mentorship was paramount in providing a well rounded experience in my masters' thesis. I would like to thank Dr. Endo for the wind tunnel testing data that was used in this thesis. Without this data, my thesis would not have been successful. I would also like to thank my friend Abhishek Jain who helped me familiarize with matlab.

I would also like to thank my committee members for their support and advice on this project. Finally, I would like to express my gratitude to the Civil and Environmental Engineering Department of Colorado State University for the giving me this opportunity to pursue a masters program at this prestigious institution. I also thank my parents for their faith in me and allowing me to proceed however as I wanted

TABLE OF CONTENTS

Chapter 1

Introduction

To determine the static and dynamic response of structures, effects of wind on models of structures are analyzed for a safe and efficient design. Most of the experimental wind engineering investigations are done in wind tunnel laboratories. This is accomplished by measuring the pressure coefficients generated by wind. A lot of data is generated in this process and it requires a lot of computer memory and storage. Efforts have been made to address this issue in the past. Modal reduction procedures were used to reduce data sets that were generated during wind tunnel testing. As a result, the data was compressed and only the most pertinent information imbedded in the data was preserved. One of techniques employed to accomplish these goals is the Proper Orthogonal Decomposition (POD).

In this thesis, POD is applied to stationary pressure time series data generated during wind tunnel testing of a model of a low rise building furnished with 990 pressure taps, uniformly distributed over the building surface. Stationary time series implies that all the statistical parameters are time independent. POD procedure generates eigenfunctions and eigenvalues for the data set under consideration. The objective of POD is to find the structure which is best correlated with this data. POD extracts the identified structures by decomposing the data set into these characteristic modes. The eigenvalues associated with these modes represent the fraction of total energy of the signal captured in the considered mode. The idea is to store only those modes which contain the most energy of the particular data set or random field, in this case - the pressure coefficient time series. Effects of change in the wind approach angle and other

parameters are studied using this technique. The peak pressures are important in analysis of wind forces on the structure and they are typically studied in more detail. In the described research, the modal contributions and errors were analyzed for different areas on the building, with different number of pressure taps. POD is a useful technique in such analysis. It allows for the investigations of these and other parameters and their effects on the dominant POD modes of the extreme wind induced loading.

The thesis is organized as follows. Introduction and motivation for the research carried out in this thesis is described in Chapter 1. Chapter 2 contains the theoretical background of the research described in this thesis. The effects of wind on structures and formulation of POD analysis are described in the initial sections of this chapter. Next, the experimental setup and the data acquisition details are presented. Subsequently, the theory and formulations used for determining and comparing the effective modes retained for different wind approach angles are described.

Chapter 3 presents the results and discussion of the findings obtained from POD analysis, which was carried out for the different regions of the structure. First, a brief overview is given, in which the sequence of the data presentation is described. Next, the results are presented for the whole structure, for wind approach direction, $\alpha = 0, 45$ and 90 degrees. Subsequently, the results obtained from POD analysis carried out for wind pressures exerted on the roof, the longer wall and the shorter wall, considered as separate data sets, for wind approach directions, $\alpha = 0, 45$ and 90, are presented. These three wind approach directions - wind normal to shorter and longer walls and the mid angle wind direction, respectively $\alpha = 0, 45$ and 90 degrees, are chosen as two extreme cases ($\alpha = 0$ and $\alpha = 90$ degrees) and one intermediary ($\alpha = 45$ degrees) case. Similar sequence was implemented in analysis and presentation of the results for different regions of the

considered building. Data analyses was also carried out for other wind directions, and their results are listed in tables discussed in the fourth section of this chapter.

Chapter 4 presents the discussions of the POD results obtained earlier. The comparisons of the effects of various parameters, incorporated in POD analysis (e.g. change in the wind approach direction and other parameters) are included. Chapter 5 presents the conclusions drawn from the described research.

The structure used in the wind tunnel investigation is symmetric about the center line along the longer axis. Because of this symmetry, wind approach directions considered were $\alpha = 0$ through 180 degrees. The results are expected to be very similar to those anticipated for the remaining directions ($\alpha = 180$ through 360 degrees).

Figures and tables are collected at the end of each chapter. They are numbered according to their chapters. The table numbers and captions are placed above the respective tables, while the figure numbers and captions are below the respective figures.

Chapter 2

Theoretical Background

2.1 Wind Effects on Structures

Wind produces three different types of effects on structures: static, dynamic and aerodynamic (Adhikari, Sukanta, " Effect of Wind on Structures", unpublished manuscript, 2002). The response of the structure is dependent on the type of structure. If the deflection of the structure is large, then dynamic and aerodynamic forces are considered. Knowledge of both fluid mechanics and civil engineering is applied to analyze the complex interactions between the wind flow and the structural responses under consideration. The wind pressures on a structure are a function of the characteristics of the approaching wind, the geometry of the structure under consideration, and the geometry and proximity of the structures upwind and in near vicinity. The pressures are not steady, but highly fluctuating, partly due to the gustiness of the wind, but also because of local vortex shedding from the structures themselves and from neighboring structures.

The building experiences buffeting by the approach flow turbulence, primarily in the along wind direction. Buffeting can be described as repeated strikes by the wind gusts. In the across wind direction, vortex shedding causes static and dynamic responses of the structure. As wind blows past the sides of the building, the flow separates from the building and this leads to formation of vortices. These vortices are shed at periodic intervals. They are generated along two or more sides of the structure and cause alternating forces, predominantly in the direction normal to the wind direction. Downstream of the leeward side of the structure, a series of vortices line up parallel to each other, in an arrangement that is labeled as "von Kármán Street". For tall

structures, these vortices can significantly impact nearby structures. They can remain coherent for long distances in low-turbulence flows. Their effects on neighboring buildings can be substantial, especially when the frequency of vortex shedding is comparable to the fundamental frequency of vibration of such structures. For a better understanding of wind effects, wind tunnel testing is done on scaled structures, in many academic and commercial wind engineering laboratories all around the world.

2.2 POD Technique

Proper Orthogonal Decomposition (POD) method, as proposed by Lumley (1967) is a technique for decomposing a turbulent flow into "constituent" or characteristic modes. Using this technique, the velocity field of a turbulent flow, or the pressure distribution in the present case, is decomposed into a series of eigenvalues and the corresponding eigenfunctions. The eigenvalues indicate the signal energy associated with each mode (the modal energy), while the eigenfunctions exhibit the spatial distribution of the modal energy. The POD technique is used in this thesis to convert the data sets generated by the pressure tap readings into a set of the eigenmodes and the principal coordinates.

In POD technique, the data set is envisioned as a function p(x, t), which is a function of position (x) and time (t). The POD implementation employed in this thesis is similar to that described by Bienkiewicz et al (1993). A function Φ is sought which resembles p(x, t). To satisfy this condition, the following normalized integral requirement is enforced.

$$\frac{\int p(x,t)\Phi(x)dx}{\sqrt{(\int \Phi(x)dx)^2}} = maximum \qquad (2.1)$$

The maximization process implied by Equation 2.1 is implemented in a mean square sense. This leads to Equation 2.2.

$$\frac{<[\int p(x,t)\Phi(x)dx][\int p(x',t)\Phi'(x')dx']>}{\sqrt{(\int \Phi(x)dx)^2}} = \lambda \geq 0 \qquad (2.2)$$

where λ is the property to be maximized. Equation 2.2 can be rewritten as follows-

$$< [\int\int p(x,t)p(x',t)\Phi(x)\Phi'(x')dxdx'] > -\lambda \int(\Phi(x)dx)^2 = 0 \qquad (2.3)$$

Subsequently, factoring out Φ(x) leads to

$$\int \Phi(x)dx \{\int \langle p(x,t)p(x',t)\rangle \Phi'(x')dx' - \lambda\Phi(x)\}dx = 0 \qquad (2.4)$$

Since Φ(x) cannot be 0, the bracketed term in Equation 2.2 has to be equal to 0.

$$\{\int \langle p(x,t)p(x',t)\rangle \Phi'(x')dx' - \lambda\Phi(x)\} = 0 \qquad (2.5)$$

The averaged term on the left hand side of Equation 2.5 is the covariance matrix of the data set, Bienkiewicz et al. (1993). This equation can be written as

$$\int R_{pp'}(x,x')\Phi'(x')dx' = \lambda\Phi(x) \qquad (2.6)$$

where, $R_{pp'}(x, x')$ is the space covariance of the analyzed data set. Thus, the maximization condition is reduced to an eigenvalue problem, where Φ is the eigenfunction and λ is its corresponding eigenvalue. These two quantities provide the basis for the POD analysis.

Once the eigenfunctions and eigenvalues are known, principal coordinates are calculated as

$$a_n(t) = \frac{\int p(x,t)\Phi(x)dx}{\sqrt{(\int \Phi(x)dx)^2}} \quad (2.7)$$

It can be shown that the principal coordinates, $a_n(t)$ in Equation 2.7 satisfy the following condition.

$$\langle a_n(t)a_m(t)\rangle = \lambda_n\delta_{mn} \quad (2.8)$$

where, δ_{nm} is the Kronecker operator, defined as being equal to unity for m = n and equal to zero when m ≠ n. The eigenvectors and principal coordinates are used as base functions in a series expansion of the pressure coefficient.

$$p(x,t) = \sum_{n=1}^{N} a_n(t)\Phi_n(x) \quad (2.9)$$

Here, N represents the number of modal contributions being considered.

The eigenvalue, λ_n represents the energy of the system associated with the nth basis modal eigenvector $\Phi_n(x)$. The ratio of i^{th} mode cumulative energy to the total energy can be calculated as follows

$$E_i = \frac{\sum_{n=1}^{i} \lambda_n}{\sum_{n=1}^{N} \lambda_n} \quad (2.10)$$

where, N is the total number of POD modes.

The above section explains the general POD procedure employed in research deployed in this thesis. The involved calculations and data processing were performed using matlab. The processed data set comprised of the pressure coefficient readings obtained for different wind directions and for different regions of the considered building structure. This analysis was done

for the regions specified in Table 2.1. The considered wind directions are given in Table 2.2. The results of the POD analysis are presented in Chapter 3.

2.3 Experimental Setup

This chapter discusses the experimental setup, dimensions and other specifications for wind tunnel testing done to generate the data used for analysis described in this thesis. The fundamental concept is that the model of the structure and of the wind should be approximately at the same geometrical scale. A generic building with flat roof dimensions of 200ft x 100ft and a height of 40 ft. was selected. Figure 2.1 shows the building geometry, opened up building surfaces, and the labeled corners. This naming (labeling) pattern is used throughout this thesis.

In the figure, OO' represents the central reference line along the longer dimension of the building. Approach wind direction angle, α, is measured counterclockwise, as the angle between XX' and OO'. Line XX' (arrow shown) represents the wind direction.

For POD analysis of separate regions (roof, walls) wind direction, α, is measured in the same manner. The number of pressure taps for each region is given in Table 2.1.

The data sets used in this thesis p(x, t)), contain (non-dimensional) building pressure coefficients, C_p calculated as

$$C_p = \frac{P - P_{static}}{.5\rho\bar{U}(H)} \tag{2.11}$$

where, ρ is the air mass density and Ū(H) is the mean velocity at the roof height of the building model. Pressure was recorded using pressure taps located on the surface of the model tested in a boundary-layer wind tunnel. The pressure coefficients, C_p at the n^{th} pressure tap, each

comprising of m samples, were stored as an (m x n) matrix. The wind–induced pressures on the external surface of the building were obtained during wind tunnel testing of this building, carried out by Endo, M., (2005), in the Wind Engineering and Fluids Laboratory (WEFL) at Colorado State University. The building was furnished with a total of 990 pressure taps. The tap locations are shown in Figure 2.2 (numbering for the whole structure). For separate regions, Table 2.1 provides the number of the taps used, while the numbering of the taps is given in Figure 2.3, for each region. For all five areas, the numbering starts at 1 and the numbering proceeds from left to right and from top to bottom as shown.

The wind direction angles considered are given in the first column of Table 2.2. The pressure time series was nearly simultaneously measured at all the 990 taps using the Electronically Scanned 1024- channel Pressure Measurement system developed at WEFL. The sampling rate was 332 samples per second. Approximately 87-second long data records were acquired, each comprising of 30000 data points per record (channel/pressure tap). For the whole structure, a 30000 x 990 matrix of the pressure coefficient readings was considered as the data set employed in POD analysis. For other regions, the number of data channels (pressure taps) set is given in Table 2.1.

As can be seen in Figures 2.2 and 2.3, the pressure taps are uniformly distributed over the entire structure. Thereby, the tributary areas are the same for all the pressure taps. This tap layout simplifies the spatio-temporal analysis of the pressure time series.

As a part of the data analysis, locations (pressure taps) where the peak pressure occurs was found, over the considered wind directions. They are listed in Table 2.2. The largest in magnitude peak pressure coefficients occur on the roof for all angles. This is why columns 2 and

4 in Table 2.2 are same. Columns 5 and 6 give the location of peak pressures for shorter wall ABED and longer wall CDHG, respectively.

2.4 Procedure for Determining Most Significant Modes

Several models have been proposed over the years to determine the number of components that have the most significance in eigenvalue decomposition, i.e. those modes that account for the most variation in a principal component analysis of a covariance matrix. In this thesis, three models were used to compare the number of such modes.

a) Scree Test

Cattell (1966) proposed the Scree Test, which is a technique of visual inspection applied on the curve generated by the eigenvalues of the correlation matrix. It is used along with Kaiser's rule which is given as

$$\lambda_i \geq 1 \tag{2.12}$$

In this method, the eigenvalues above the scree are considered the most significant and are retained. In other words, only those modes are retained whose relative eigenvalue contributions follow a steep decrease in a linear representation of the eigenvalues ordered in a decreasing fashion. Over the years, several non-graphical methods have been proposed for this procedure. In this thesis, the method developed by Raiche, G. et al. (2012) has been used.

For finding the location of the scree non graphically, each eigenvalue has to be inspected one by one by tracing the line from the coordinate of the last eigenvalue through each of the preceding eigenvalue and verify if the observed eigenvalue is superior than or not equal to the

estimated projected eigenvalue. The number of principal components to retain is given by the last eigenvalue that is greater than or equal to the estimated predicted eigenvalue. This was done using a (p-2) two-point regression model and observing if the eigenvalue is, or is not, greater or equal to the one estimated by these models. These verifications, beginning at the second eigenvalue, and without interruption of the verification, are used to determine the number of principal components to retain. The eigenvalue also has to be greater than 1, according to Kaiser's rule (Eq. 2.12).

$$n_{oc} = \sum_i I[(\lambda_i \geq 1)\&(\lambda_i \geq \hat{\lambda})] \tag{2.13}$$

where, I is the indicator function, which is equal to 1, if both conditions are satisfied and 0 otherwise. Also, $\hat{\lambda}$ is the predicted eigenvalue and n_{oc} is the number of optimal coordinates. Figure 2.4a shows this process graphically. As we can see, the eigenvalue (circled) is above the eigenvalue estimated by this process, so all the eigenvalues till the circled one are retained.

The predicted eigenvalue λ_i, also referred to as the optimal coordinate, is obtained according to linear regression using only the last (p^{th}) eigenvalue and the $(i+1)^{th}$ eigenvalue given as-

$$\hat{\lambda} = a_{i+1} + b_{i+1} * (i) \tag{2.14}$$

where,

$$b_{i+1} = \frac{\lambda_p - \lambda_{i+1}}{(p-i-1)} \tag{2.15a}$$

$$a_{i+1} = \lambda_{i+1} - b_{i+1} * (i+1) \tag{2.15b}$$

Figure 2.4b presents an example of the optimal coordinates found using this procedure. Eigenvalues (λ_i) and optimal coordinates ($\hat{\lambda}$) obtained from Eq. 2.14 are plotted on the same plot for $\alpha = 0$. Eigenvalues from point O through point B are the most significant mode as calculated using this procedure.

These optimal coordinates were calculated for different regions with varying angles. These results are discussed in Chapter 3. For comparison of accuracy of this model, errors were calculated according to Equation 2.16

$$error = \left| \left\{ \frac{\{(actual\ value) - (observed\ value)\}}{(actual\ value)} \right\} \right| \tag{2.16}$$

Here, the observed value is obtained by adding the average to the fluctuation contributions generated by Equation 2.9, where, N is obtained from the non-graphical solution of scree test. Error was calculated at the location and time of the peak value (given in Table 4.7). These errors are also calculated for various angles and are discussed in the third section of Chapter 3.

b) Jolliffe's Rule

The main objective of POD in this analysis is the synthesis of a given data set in order to capture the desired degree of physical information. This criterion was reviewed by Jolliffe and it is used in this thesis. According to Jolliffe's rule, only those eigenvalues which exceed 70% of the average eigenvalue are retained. Here, $\Delta = N^{-1} \Sigma_i \lambda_i$ is the average eigenvalue.

c) 90 % Cumulative Eigenvalues

As stated earlier, the eigenvalues represent the fraction of total energy of the system contained by that particular mode. The method used here for determining the number of

significant eigenvalues is to retain only those values for which the cumulative energy, as given by Equation 2.10 is lower than or equal to 0.9, as illustrated in Figure 2.5.

In this figure, only eigenvalues ranging from A to B are retained and used in the data reconstruction. This method is widely used in wind engineering analysis of POD results

Tables- (Chapter 2)

Table 2.1 : Number of pressure taps

Region	Number of pressure taps
Whole structure	990
Roof (DEIH)	450
Shorter wall (ABED)	90
Longer wall (EFJI)	180
Shorter wall (HILK)	90

Table 2.2 : Locations of peak pressure coefficients for different wind directions

Angle	Location	Value	Roof/Whol	Wall ABED	Wall CDHG
	Whole str		Location	Location	Location
0	2	-6.328862	2	72	1
5	1	-4.927854	1	65	1
10	2	-5.782674	2	72	1
15	1	-5.9687	1	63	13
20	1	-6.402023	1	66	12
25	2	-6.928991	2	61	6
30	2	-7.460607	2	61	6
35	2	-6.400677	2	76	6
40	1	-7.118787	1	61	5
45	16	-5.773015	16	46	5
50	16	-9.733546	16	76	4
55	16	-6.908501	16	77	5
60	16	-6.978912	16	76	5
65	16	-6.593843	16	16	5
70	16	-6.087906	16	46	22
75	16	-6.114973	16	31	11
80	16	-5.604716	16	1	180
85	1	-5.73267	1	64	101
90	361	-4.632933	361	79	167
95	436	-5.392052	436	87	113
100	181	-7.119191	181	2	64
105	436	-7.100508	436	87	173
110	421	-7.26608	421	90	173
115	421	-7.170783	421	89	125
120	421	-7.51476	421	90	179
125	421	-7.052786	421	86	179
130	421	-7.084449	421	89	179
135	437	-6.785236	437	88	180
140	421	-7.873215	421	89	178
145	421	-7.041929	421	90	180
150	437	-6.147479	437	89	174
155	436	-5.859611	436	90	180
160	436	-6.153564	436	74	180
165	437	-6.492349	437	75	174
170	437	-5.867481	437	26	176
175	437	-5.990945	437	42	170
180	445	-5.029848	445	45	176

Figures- (Chapter2)

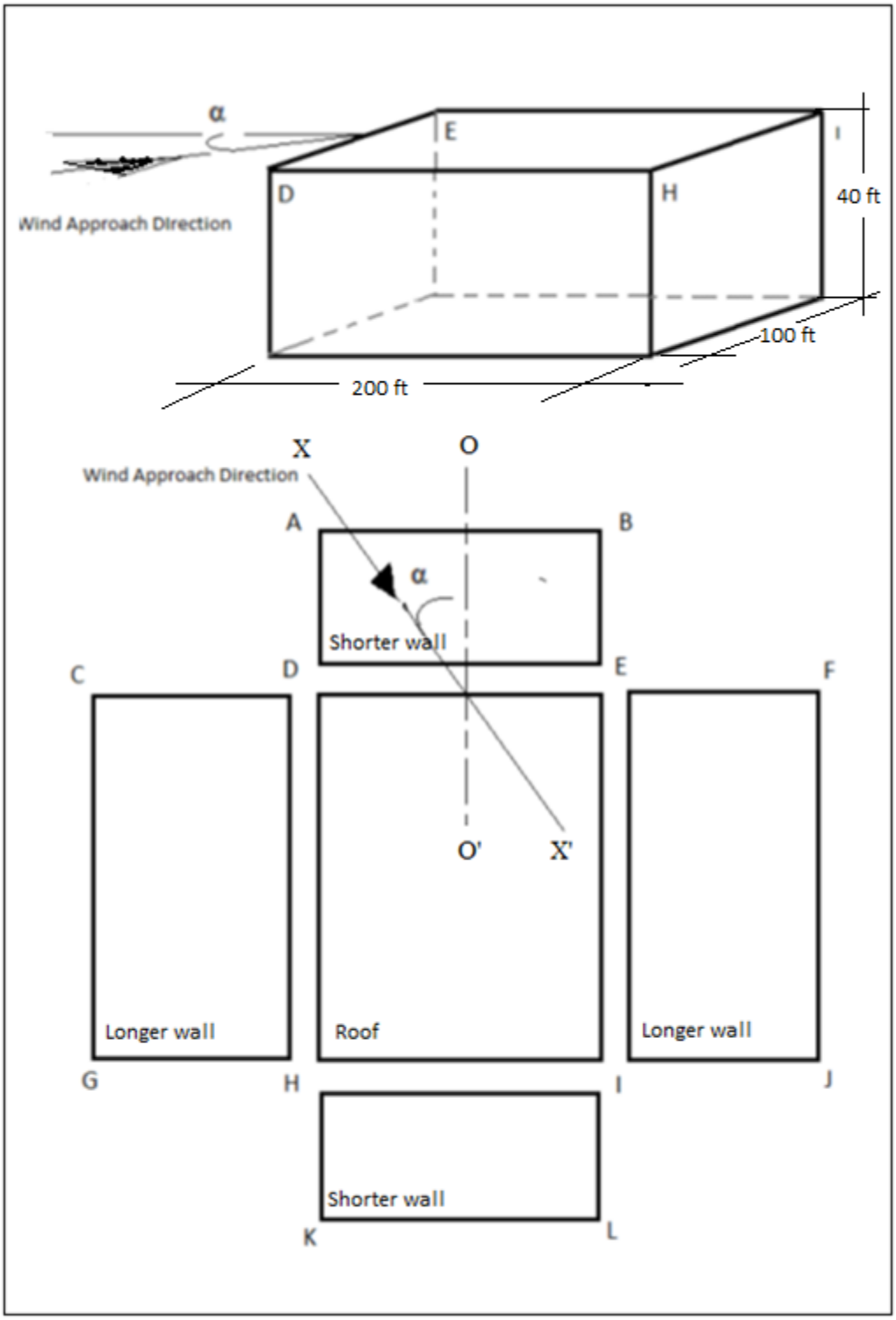

Figure 2.1 : Naming used , Wind direction

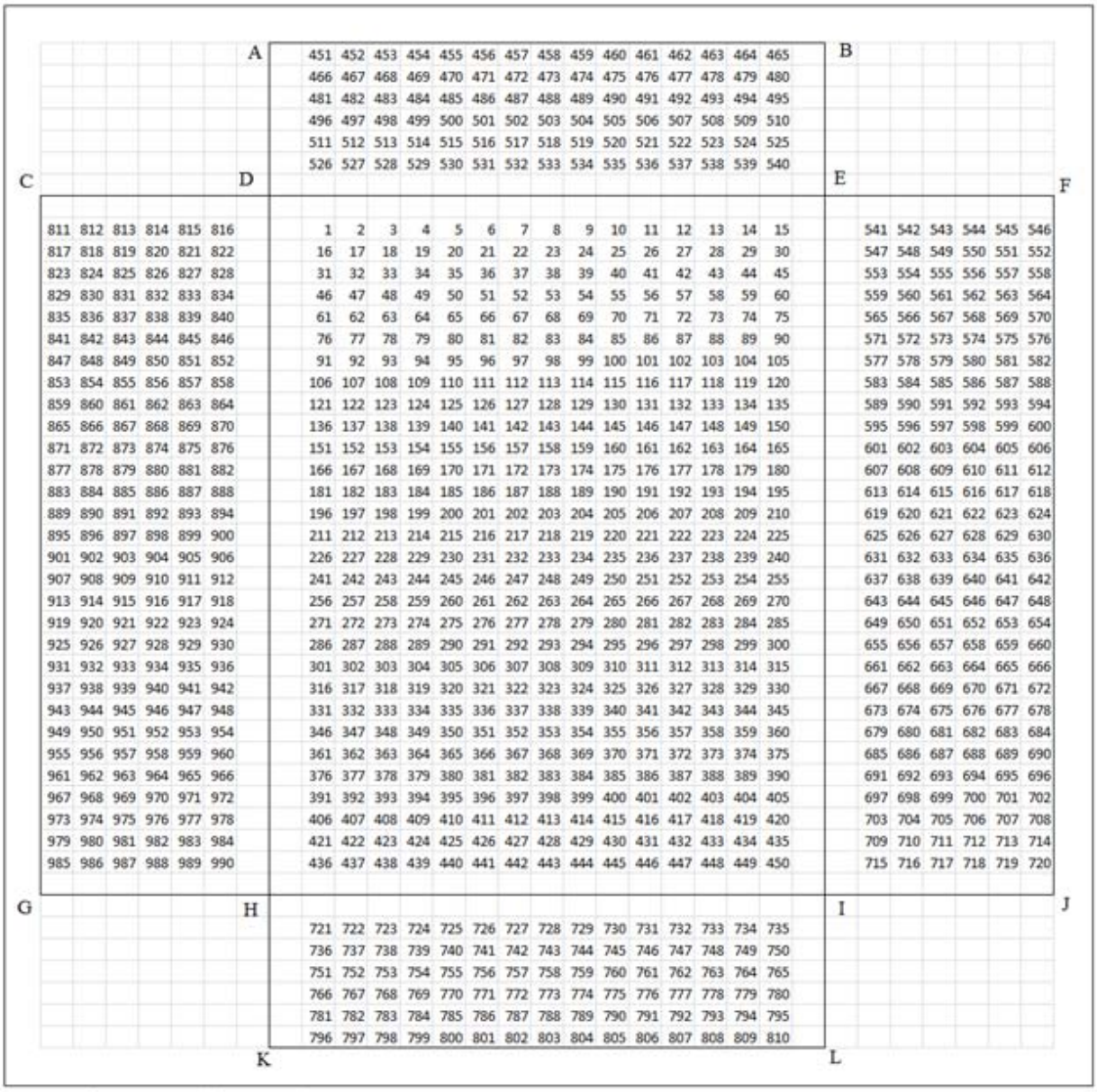

Figure 2.2 : Pressure tap numbering over entire structure

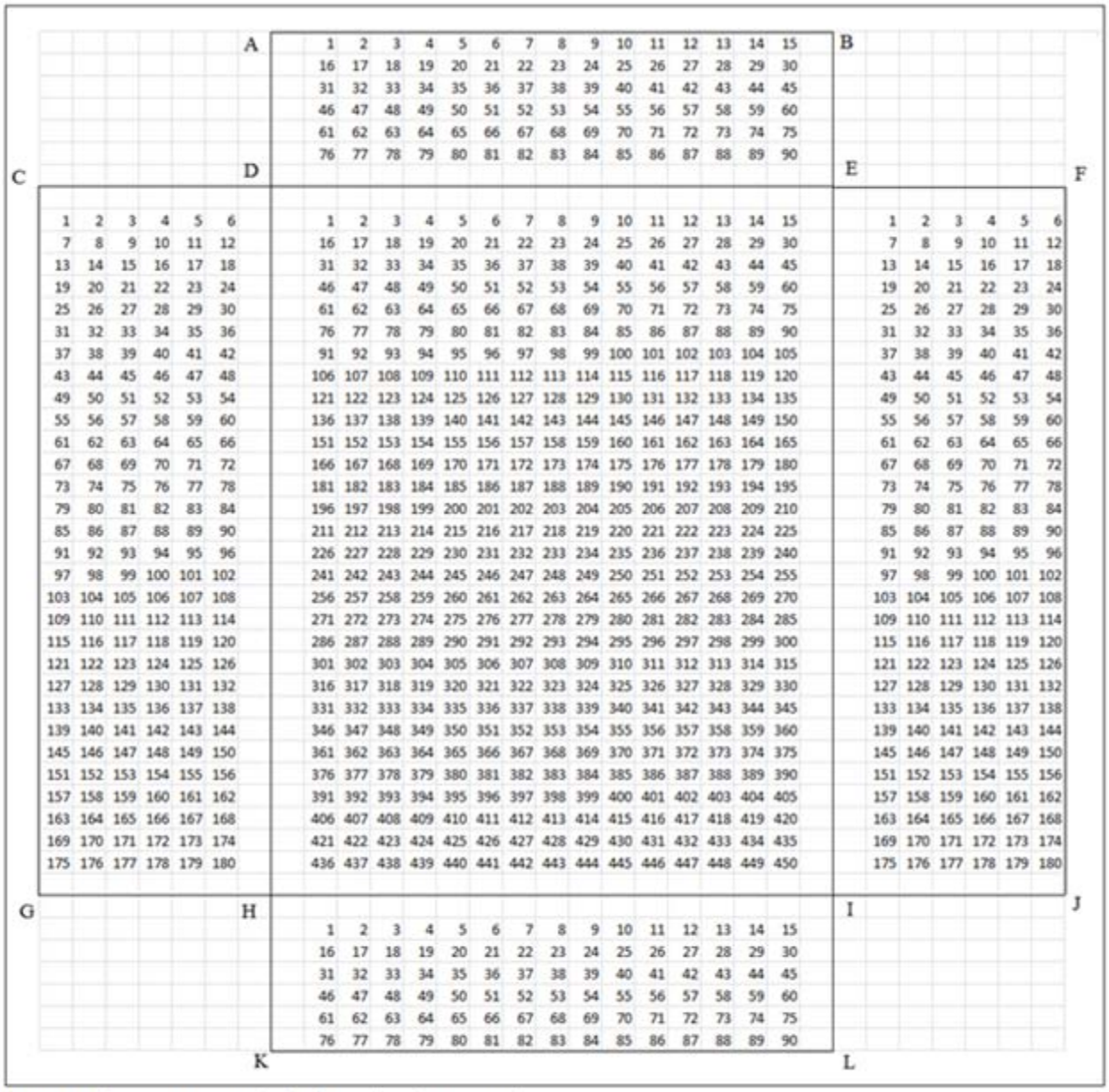

Figure 2.3 : Pressure tap numbering for each region separately.

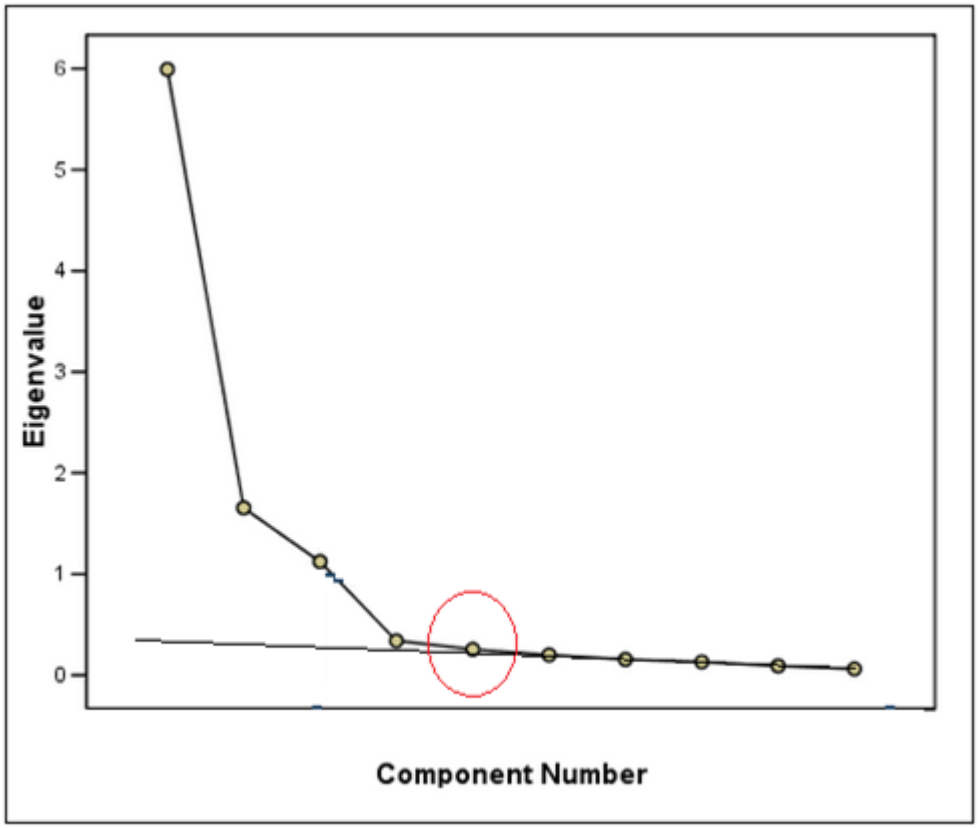

Figure 2.4 a : Non graphical solution of scree test

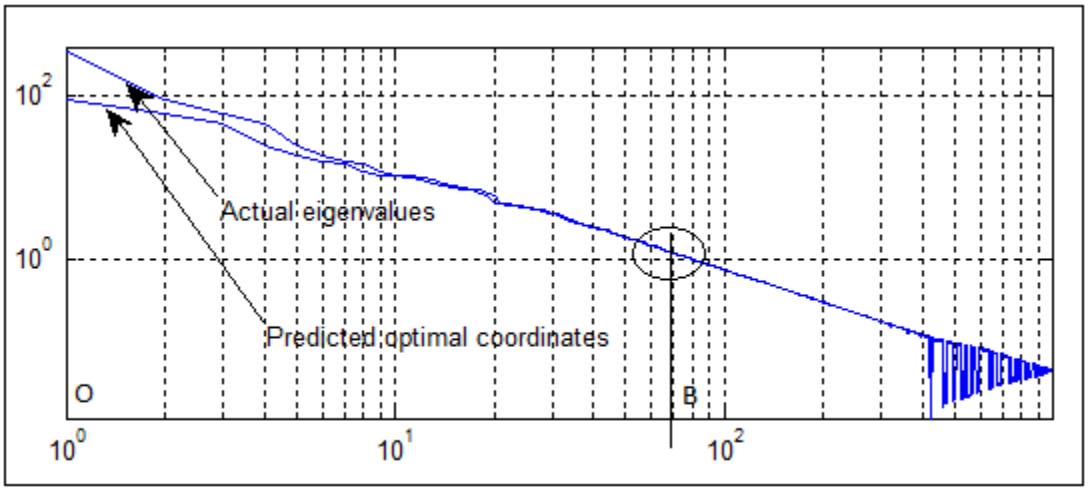

Figure 2.4b : Actual vs Predicted Eigenvalue

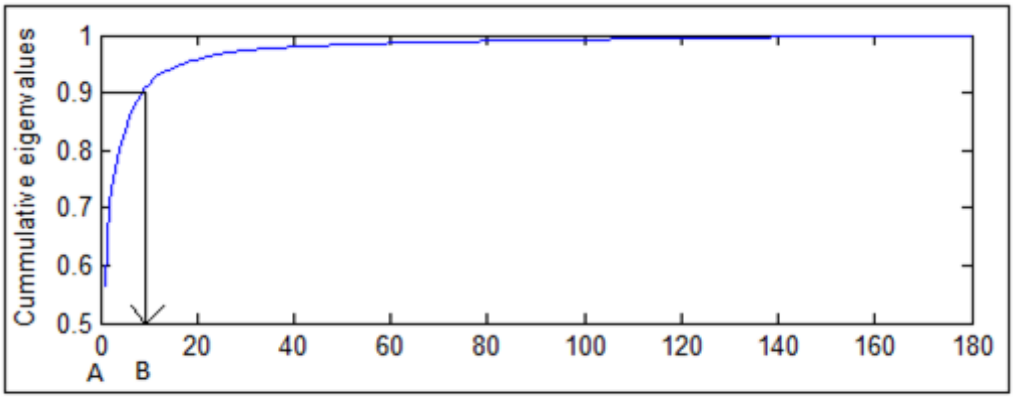

Figure 2.5 : 90% of cumulative eigenvalues

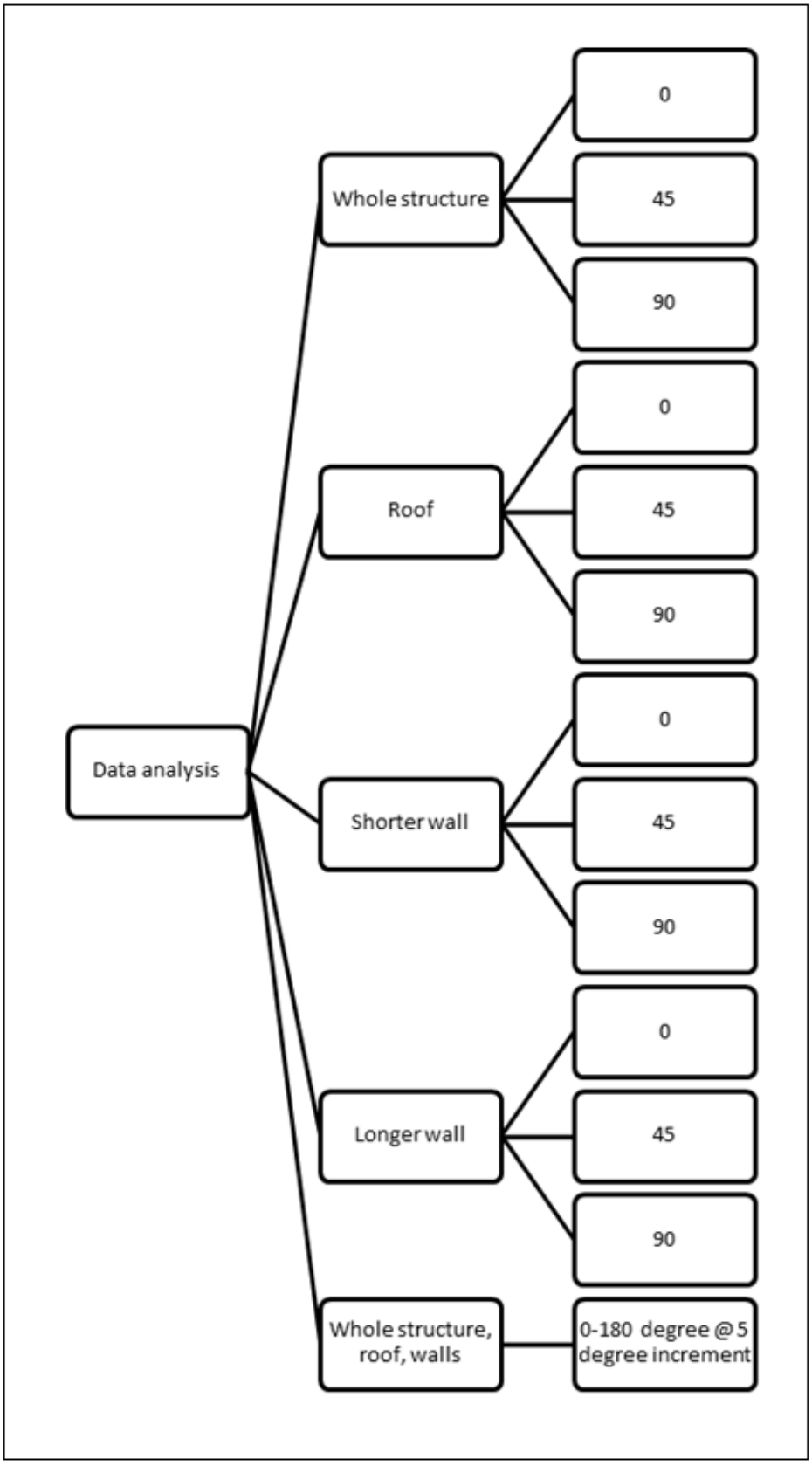

Figure 2.6 : Flowchart showing the data representation

Chapter 3

Results and Discussion

3.1 Overview

This chapter describes the results obtained from POD analysis. The results are displayed using contour plots. The naming of the corners of the structure is defined in Figure 2.1. Four intersecting corners are named separately after opening up the structure (shown in Figure 2.1). Table 3.1 shows the order in which the data is presented. As discussed earlier, the entire structure was furnished with 990 uniformly distributed pressure taps. Data from all the taps was used in the POD analysis of the whole structure. For the POD analysis of other regions, the number of pressure taps used is listed in Table 2.1. For each case, the results are presented in the following order

- 1st figure displays the average values which are calculated as follows

$$p(x)_{avg} = \frac{\sum_{t=0}^{k} p(x,t_i)}{k} \tag{3.1}$$

where, k is the total number of the samples.

- 2nd figure displays the standard deviation.

$$p(x)_{std} = \frac{\sum_{t=0}^{k} (p(x,t_i) - p(x)_{avg})^2}{k} \tag{3.2}$$

- 3rd figure displays the absolute value of the peaks.
- 4th figure displays the eigenvalues.

- 5th figure displays the cumulative eigenvalues, which represent the fractional total energy, Eq. 2.10.
- 6th figure displays the eigenvectors. They are normalized using as follows

$$\sqrt{\sum_{i=1}^{N}(\Phi n(i))^2} = 1. \quad (3.4)$$

where, n is the mode and N is the total number of pressure taps.

- 7th figure displays the standard deviation of contributions, calculated (using Eq. 3.2) for the reconstructed pressure obtained using first mode, first 10 modes and first 30 modes. Since the standard deviation is the square root of the variance, this figure represents the convergence of the variance with an increase in the number of the employed modes.
- 8th figure shows the convergence of reconstruction of peak pressures. The curve with the maximum value of peak (negative or positive) is the original pressure time series. The remaining lines are the reconstructed time series, in vicinity of the peak value. The pressure reconstruction is carried out in accordance with Eq. 2.9.
- 9th figure shows the error of reconstruction of the peak pressure pertaining to the value at the time and position of the peak coefficient, calculated using Eq. 2.16.

These nine figures are presented for 0, 45 and 90 degree wind directions. A schematic layout of the presented data is shown in Figure 2.6.

3.2 POD Results for Whole Structure

- **Results for $\alpha = 0^0$**

Figures 3.1 through 3.9 present the results obtained for the whole structure for $\alpha = 0$ degrees. The presentation order is consistent with Figure 2.6. Figure 3.1 displays the average of Cp values for all the pressure taps. As expected, the roof and both longer walls have negative pressure coefficients on the windward portions of these surfaces. As can be seen, the pressure coefficient is small over the leeward portion of the roof and both the longer walls, walls CDHG and EFJI. This implies that these regions have pressure coefficients close to the static pressure coefficient. Figure 3.2 displays the standard deviation calculated using Eq. 3.2 for all pressure taps. Figure 3.3 shows the peak coefficients (absolute values), for all the pressure taps. As can be seen, the peak contour lines are very rugged and non-uniform, as expected. Figure 3.4 presents the POD eigenvalues, while Figure 3.5 shows the cumulative contributions of these values. Figure 3.6 presents the 1^{st}, 2^{nd} and 3^{rd} eigenvectors found from POD analysis carried out for the whole structure. Figure 3.7 presents the convergence of the standard deviation reconstructions. In these plots, the first mode, first 10 modes and first 30 modes were used to reconstruct the pressure time series, before calculating their standard deviation, using Eq.3.4. Figure 3.8 presents the peak pressure reconstruction obtained using 1, 5, 15 and 50 modes. The original time series is also included in the figure. Figure 3.9 displays the error associated with the peak pressure reconstructions displayed in Fig. 3.8. These errors were calculated using Eq. 2.16.

- **Results for $\alpha = 45^0$**

Figure 3.10 presents the average values of Cp calculated for the entire structure, for $\alpha = 45$ degrees. Standard deviation values for all the pressure taps are given in Figure 3.11. Peak pressure coefficient plot is presented in Figure 3.12. Figure 3.13 presents the eigenvalues while

Figure 3.14 presents the cumulative contributions of these values. Figure 3.15 presents the 1st, 2nd and 3rd POD eigenvectors. Figure 3.16 presents the convergence of the standard deviation reconstruction. In these plots, the first mode, the first 10 modes and first 30 modes were used to reconstruct the pressure series, before calculating their standard deviation, using Equation 3.4. Figure 3.17 shows the reconstruction of the peak pressure using different number of modal contributions. Figure 3.18 shows the error associated with the peak pressure reconstructions displayed in Fig 3.17.

- **Results for $\alpha = 90^0$**

Figure 3.19 displays the contour plot for the average values of the pressure coefficients for α=90 degrees. It can be seen that the pressure coefficients are positive on longer wall CDHG and negative for the remaining walls and the roof. Figure 3.20 presents the standard deviation. Peak pressure coefficients plot is presented in Figure 3.21. As can be seen, it has a rugged contour pattern, similar to that of the peak contours obtained for the remaining analyzed wind directions. Figure 3.22 presents the eigenvalues, while Figure 3.23 presents the cumulative contributions of these values. Figure 3.24 presents the 1st, 2nd and 3rd eigenvectors found from POD analysis. Figures 3.25 and 3.26 respectively show the reconstruction of the pressure standard deviation and peak, obtained using different number of modes. Figure 3.27 displays the convergence of the peak pressure reconstruction.

3.3 POD Results Obtained Using Roof and Wall Data

POD analysis was also carried out for the roof and walls, considered separately. Wall analysis was limited to walls ABDE (shorter wall) and CDGH (longer wall). The pressure taps

in each region are specified in Figure 2.2. In the present analysis, they were re-numbered, as is indicated in Figure 2.3.

- **Roof**

POD results for the roof (DEHI) only, for approach wind direction $\alpha = 0^0$, are shown in Figures 3.28 through 3.36. The data presentation sequence is consistent with Table 3.1. Next, in Figures 3.37 through 3.45, the results are presented for $\alpha = 45^0$, in the same order. Since the pressure coefficient in this region is predominantly negative, the 3-D plots are displayed using inverted positive direction of the pressure (upward direction of z-axis indicated negative values). The wind direction is indicated using line arrow in the figures and in the icons (upper right corner). Finally, Figures 3.46 through 3.54 present the results for $\alpha = 90^0$, in the same data presentation sequence.

- **Walls**
    - **Shorter Wall**

POD results for the shorter wall (ABED) only are shown in Figures 3.55 through 3.63, for approach wind direction $\alpha = 0^0$. The data presentation sequence is consistent with Table 3.1. Next, in Figures 3.64 through 3.72, the results are presented for $\alpha = 45^0$, in the same sequence. Since the pressure coefficient in this region is predominantly negative, the 3-D plots are displayed using inverted positive direction of the pressure (upward direction of z-axis indicates negative values). The wind direction is indicated using line arrow in the figures and in the icons (upper right corner). Finally, Figures 3.73 through 3.81 present the results for $\alpha = 90^0$, in the same sequence.

- **Longer Wall**

POD results for the longer wall (CDHG) only are shown in Figures 3.82 through Figure 3.90, for approach wind direction $\alpha = 0^0$. Their presentation order is consistent with Table 3.1. Next, in Figures 3.91through 3.99, the results are presented for $\alpha = 45^0$, in the same sequence. Since the pressure coefficient in this region is predominantly negative, the 3-D plots are displayed using inverted positive direction of the pressure (upward direction of z-axis indicates negative values). The wind direction is indicated using line arrow in the figures and in the icons (upper right corner). Finally, Figures 3.100 through 3.108 present the results for $\alpha = 90^0$. The same sequence of data presentation is employed.

3.4 . Wind Direction Effect on POD Results for The Whole Structure

In the previous section, POD results for wind directions $\alpha = 0^0$, 45^0 and 90^0 were presented. Similar analysis was carried out for other wind directions. To investigate the effects of wind direction on the POD results, 37 cases – wind directions ranging from 0^0 through 180^0, with 5^0 increments – were selected. POD eigenvectors, eigenvalues, principal coordinates and other quantities were calculated for these data. These results enabled the comparison of different parameters, such as eigenvalues, eigenvectors, fractional modal energy and others. To identify significant modes associated with the above cases, methodology discussed in Chapter 2, Section4, was employed. The reconstruction error was obtained for different wind directions. The significant eigenmodes calculated for different wind directions were established using the Scree test , the Jolliffe's rule and the 90% cumulative eigenvalues criterion. The results of this analysis are summarized in Table 4.7. The data displayed in this table was obtained for the whole structure. The results of similar investigation carried out for isolated regions of this structure,

namely Roof (DEHI), Shorter Wall (ABDE) and Longer Wall (CDGH) are presented in the next chapter.

Tables- (Chapter3)

Table 3.1 : Repetitive diagrams

	Title	Figure shown
1	Avg	Average values of Cp values over entire time domain
2	Stdev	Standard deviation of Cp values over entire time domain
3	Peak	Maximum (absolute values) value of Cp at that location over entire time domain
4	Eigenvalues	Eigenvalues plotted on log scale
5	Cumulative eigenvalues	Cumulative eigenvalues
6	Eigenvectors	1^{st}, 2^{nd} and 3^{rd} eigenvectors
7	Stdev of contributions	Standard deviation of 1^{st}, first 10 and first 30 contributions
8	Convergence of time series	Convergence of time series at peak value with increasing contributions
9	Error	Error in the convergence at peak location and time

Figures-(Chapter 3)

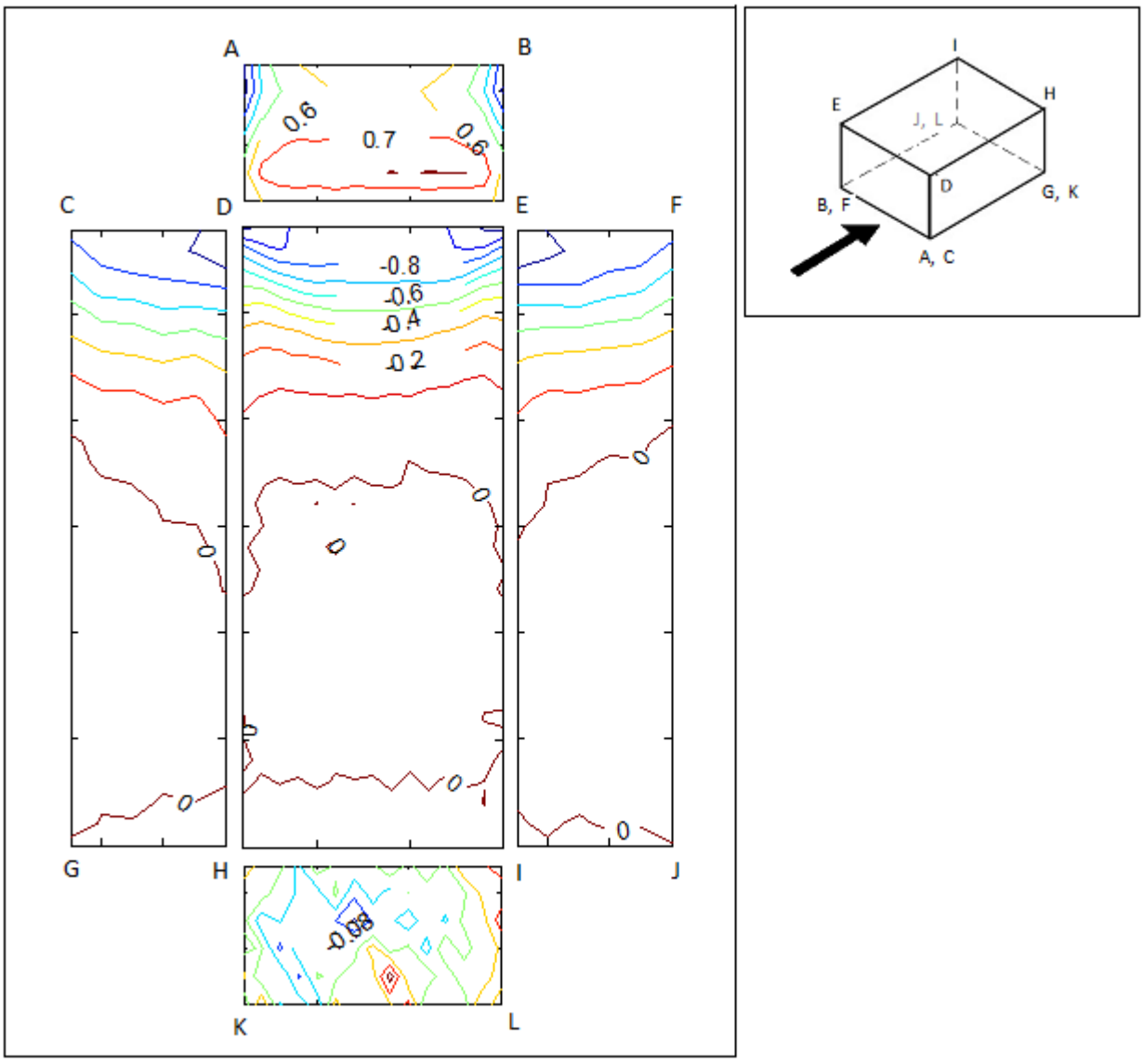

Figure 3.1 : Avg values for whole structure for $\alpha = 0$

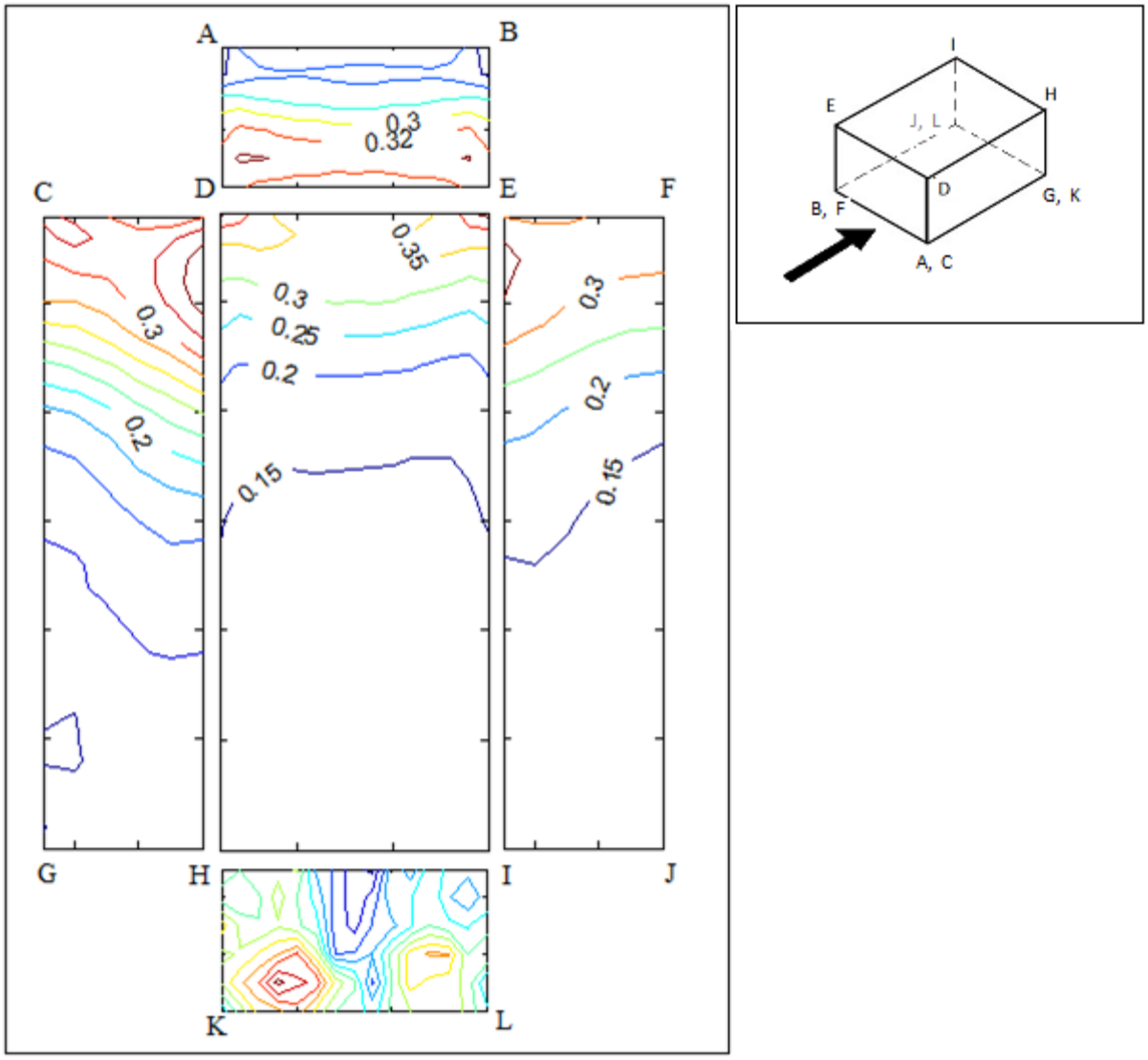

Figure 3.2 : Stdev values for whole structure for $\alpha = 0$

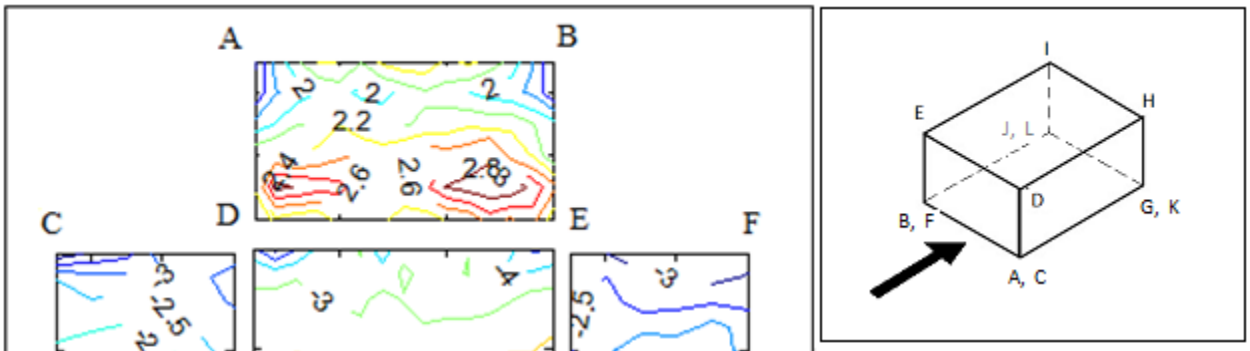

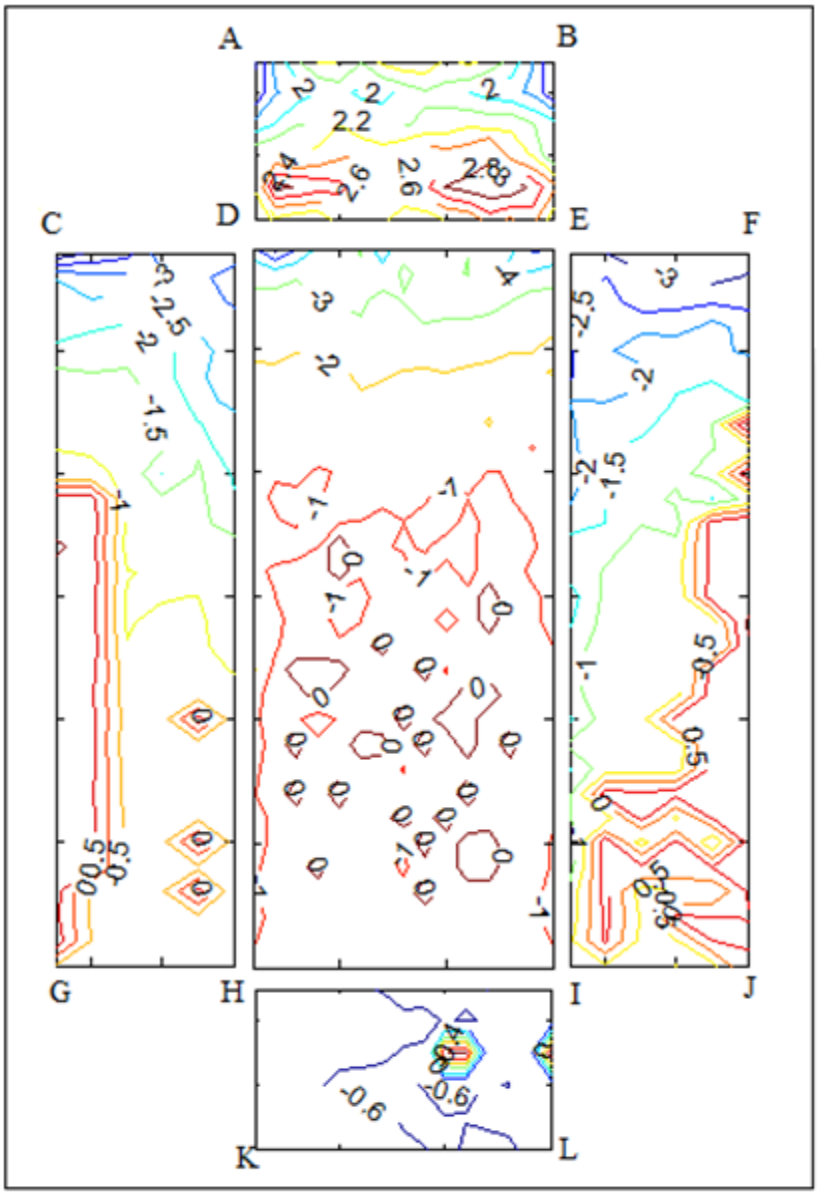

Figure 3.3 : Peak values for whole structure for $\alpha = 0$

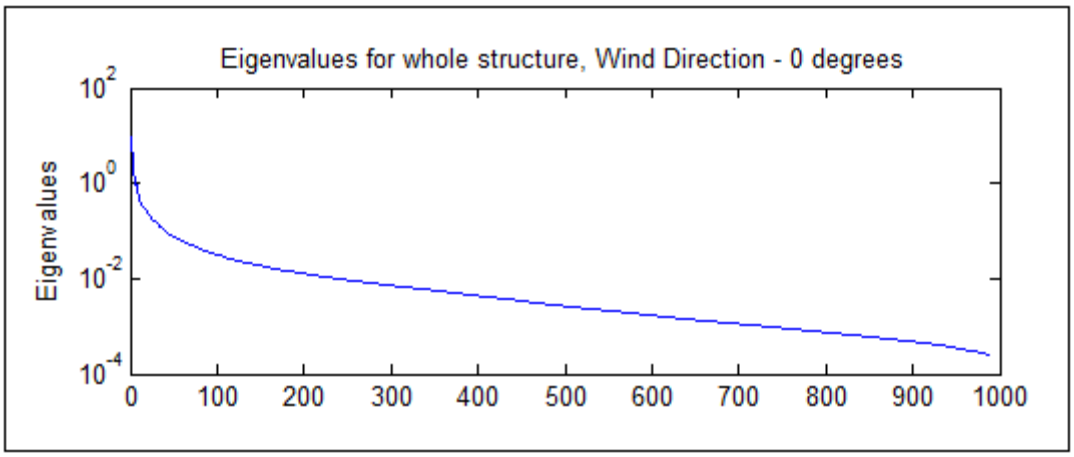

Figure 3.4 : Eigenvalues for whole structure for $\alpha = 0$

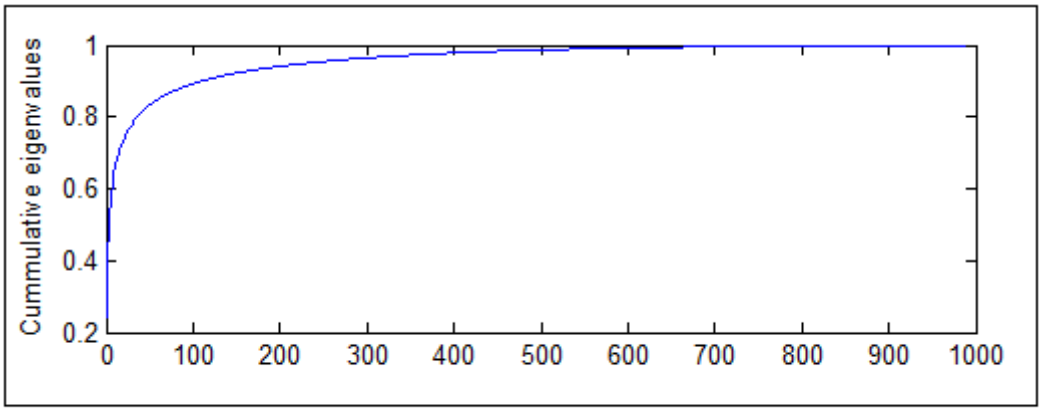

Figure 3.5 : Cumulative Eigenvalues for whole structure for $\alpha = 0$

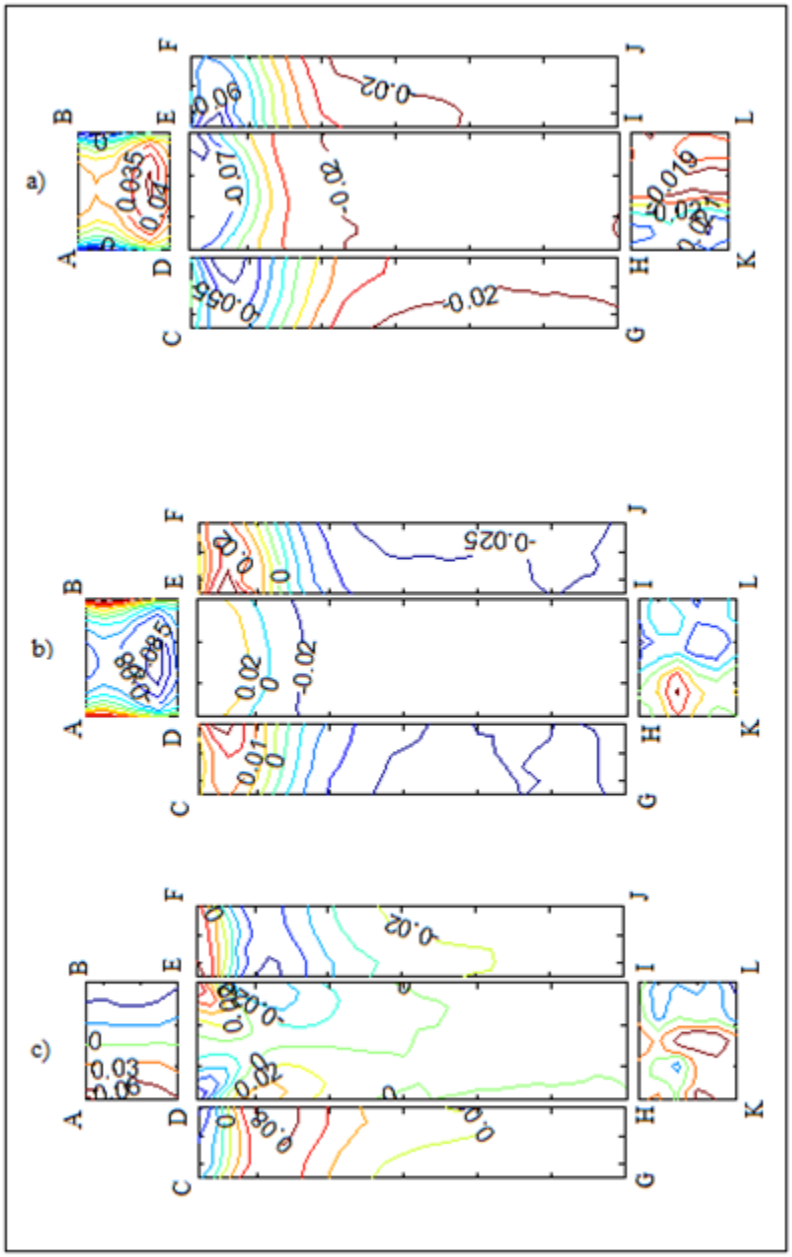

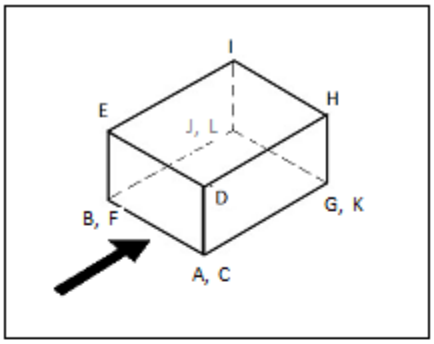

Figure 3.6 : 1st, 2nd and 3rd eigenvectors for whole structure for $\alpha = 0$
a) 1st; b) 2nd; c) 3rd

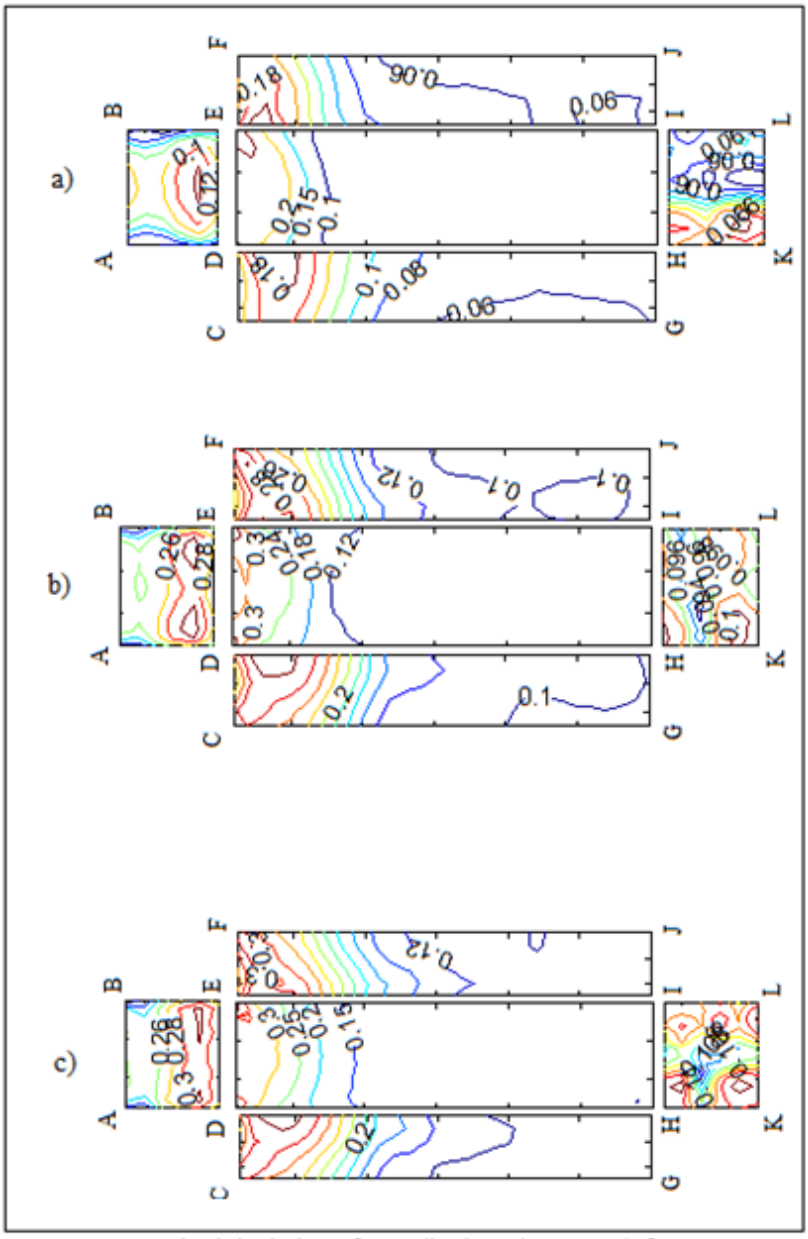

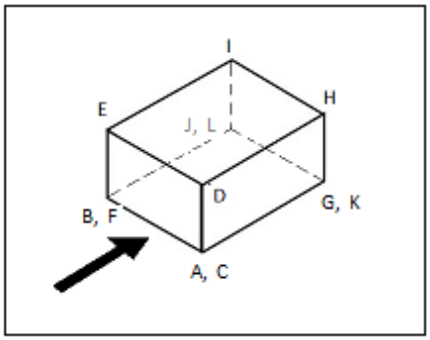

1

Figure 3.7 : Standard deviation of contributions (1, 10, 30) for $\alpha = 0$
a) 1st; b) First 10; c) First 30

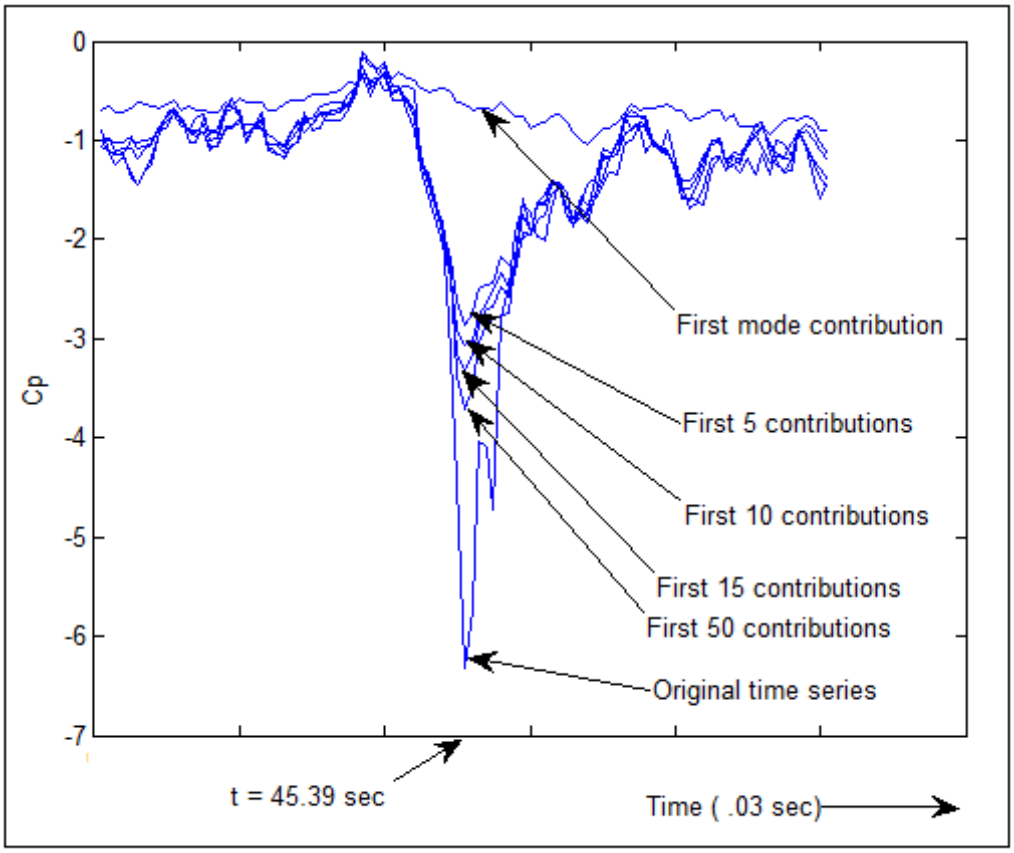

Figure 3.8 : Convergence of time series at maximum pressure position for $\alpha = 0$

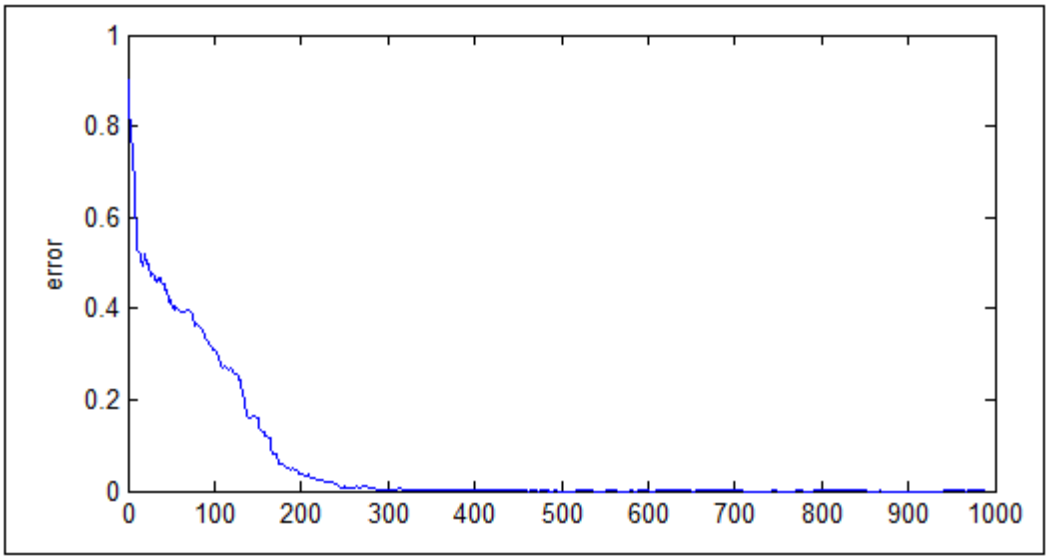

Figure 3.9 : Error at the maximum position with contribution for $\alpha = 0$

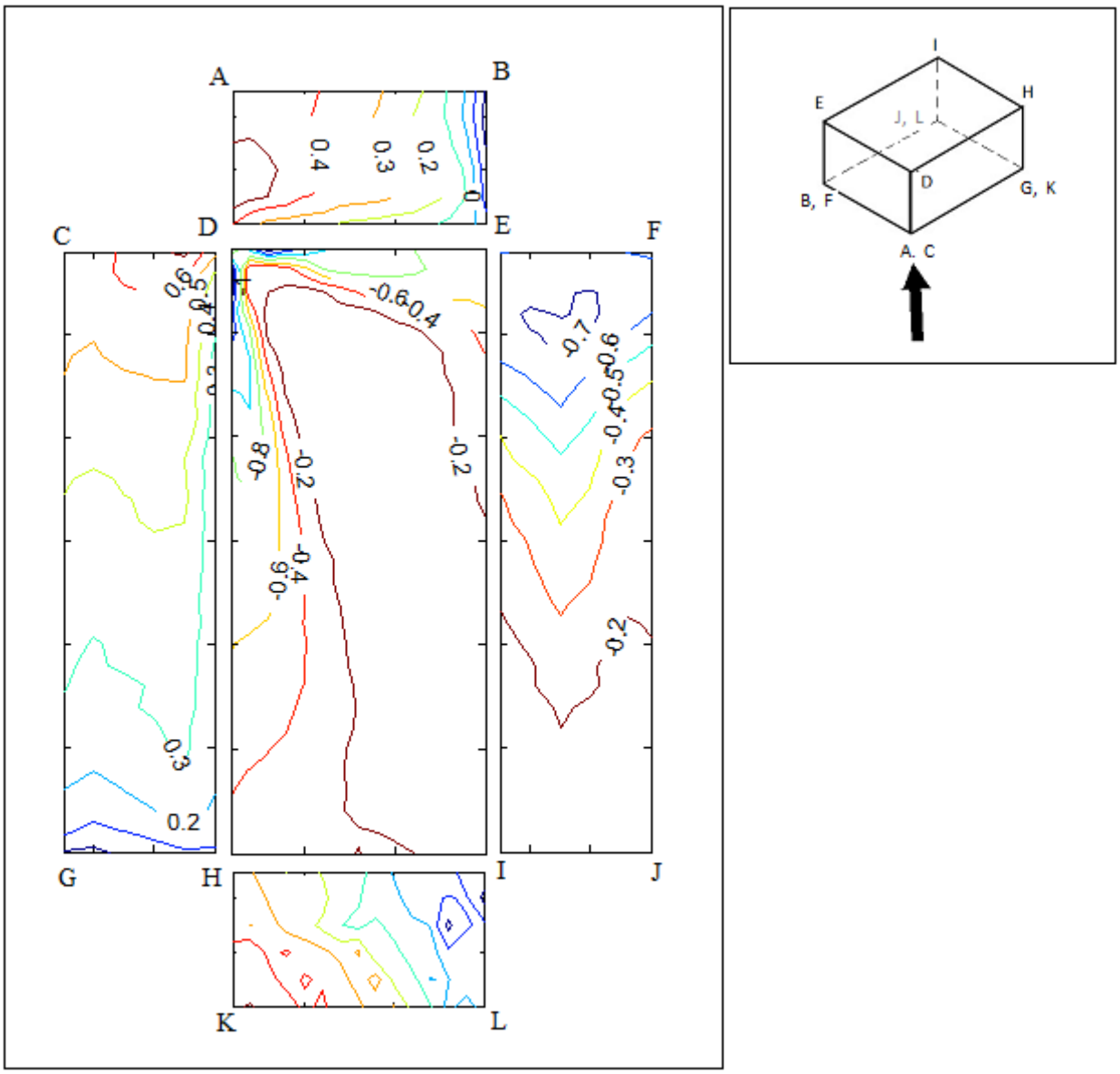

Figure 3.10 : Avg values for whole structure for α = 45

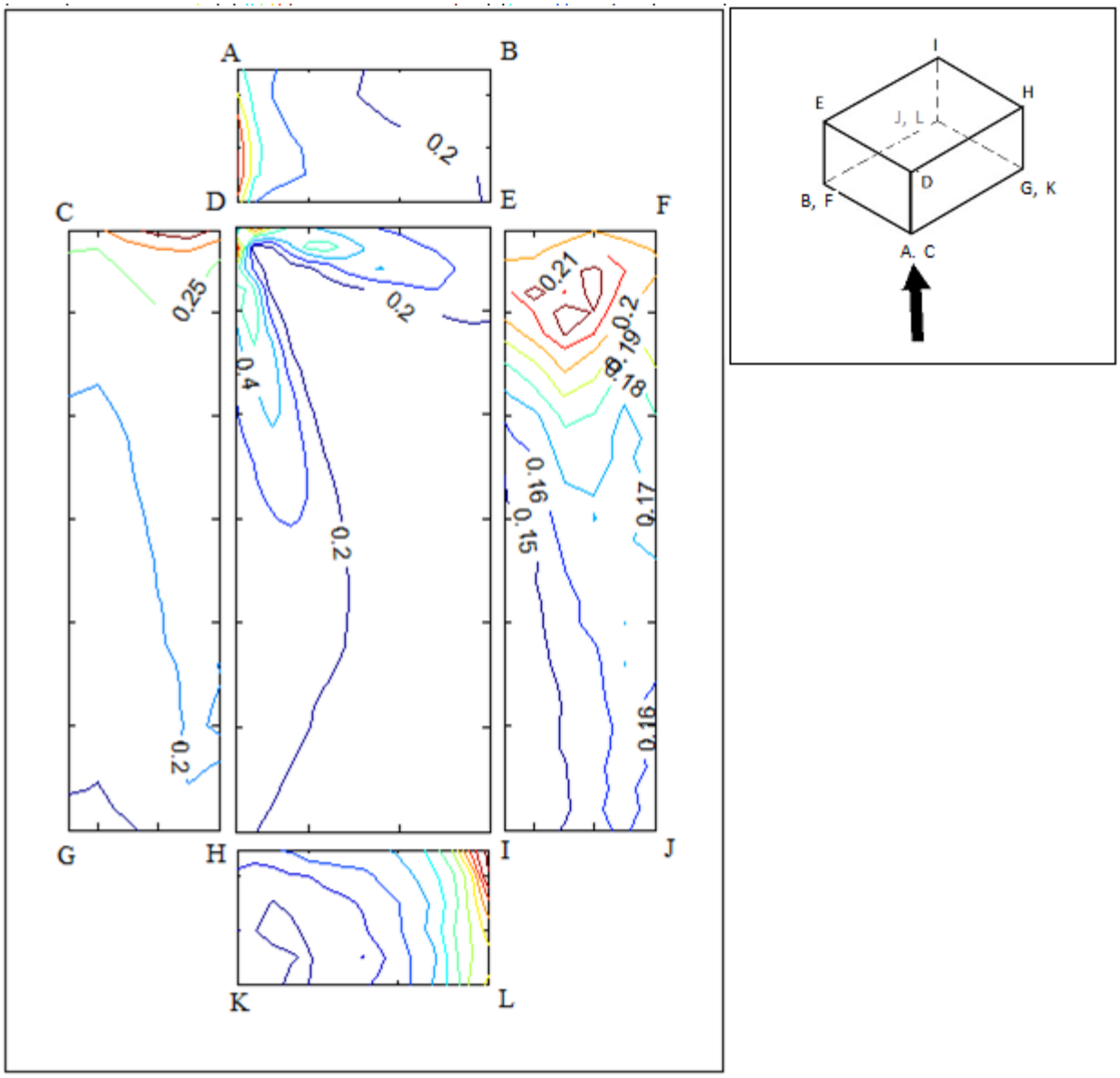

Figure 3.11 : Stdev values for whole structure for α = 45

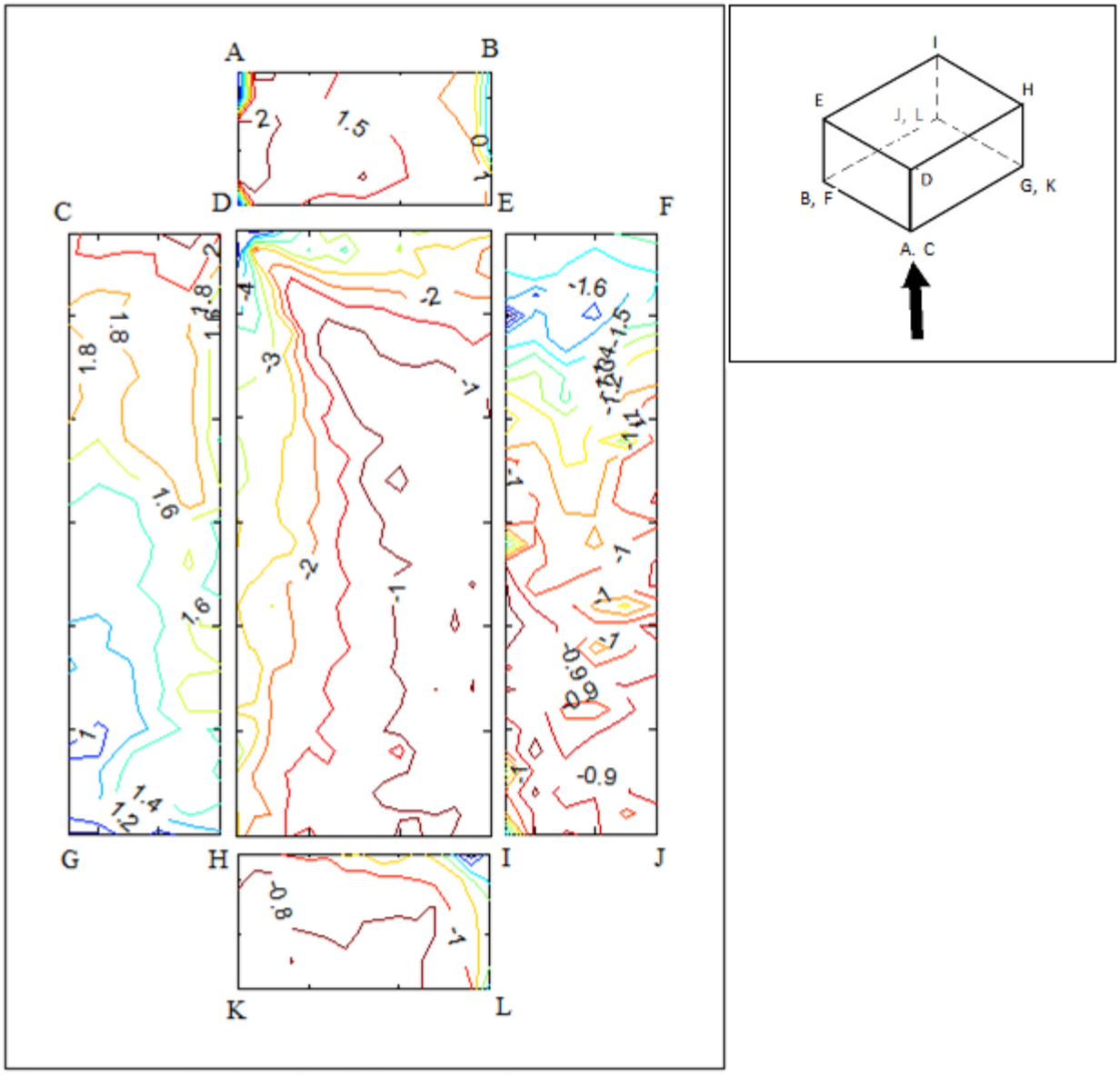

Figure 3.12 : Peak values for whole structure for $\alpha = 45$

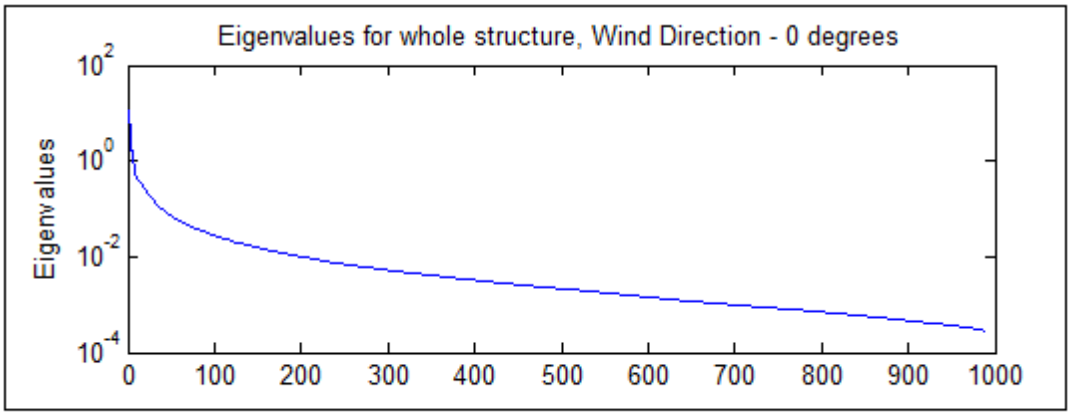

Figure 3.13 : Eigenvalues for whole structure for α = 45

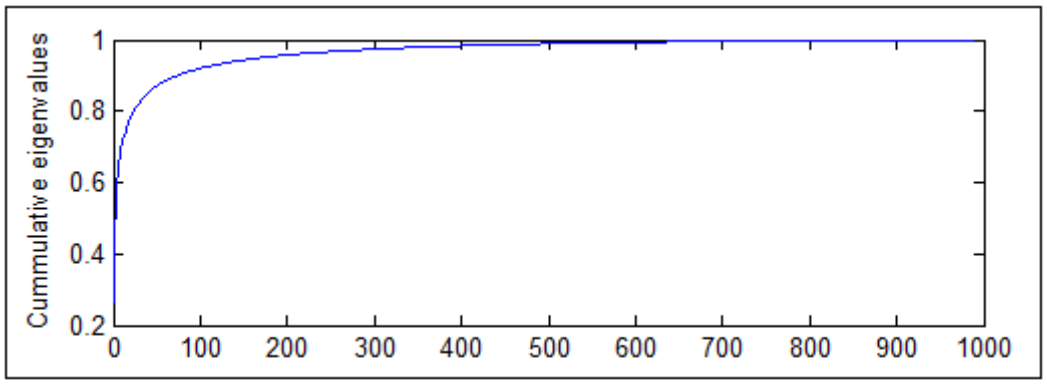

Figure 3.14 : Cumulative Eigenvalues for whole structure for α = 45

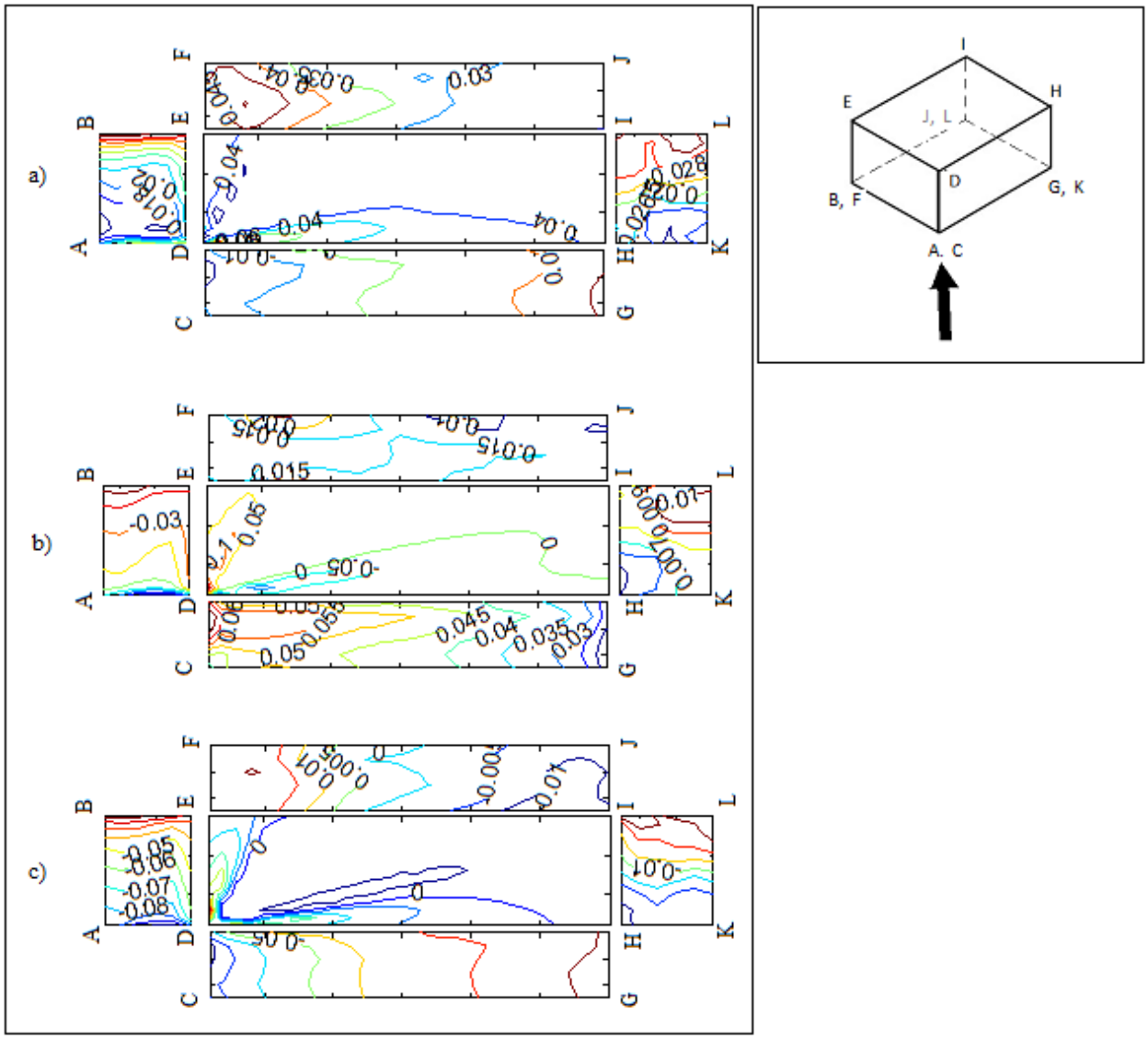

Figure 3.15 : 1st, 2nd and 3rd eigenvectors for whole structure for α = 45
a) 1st; b) 2nd; c) 3rd

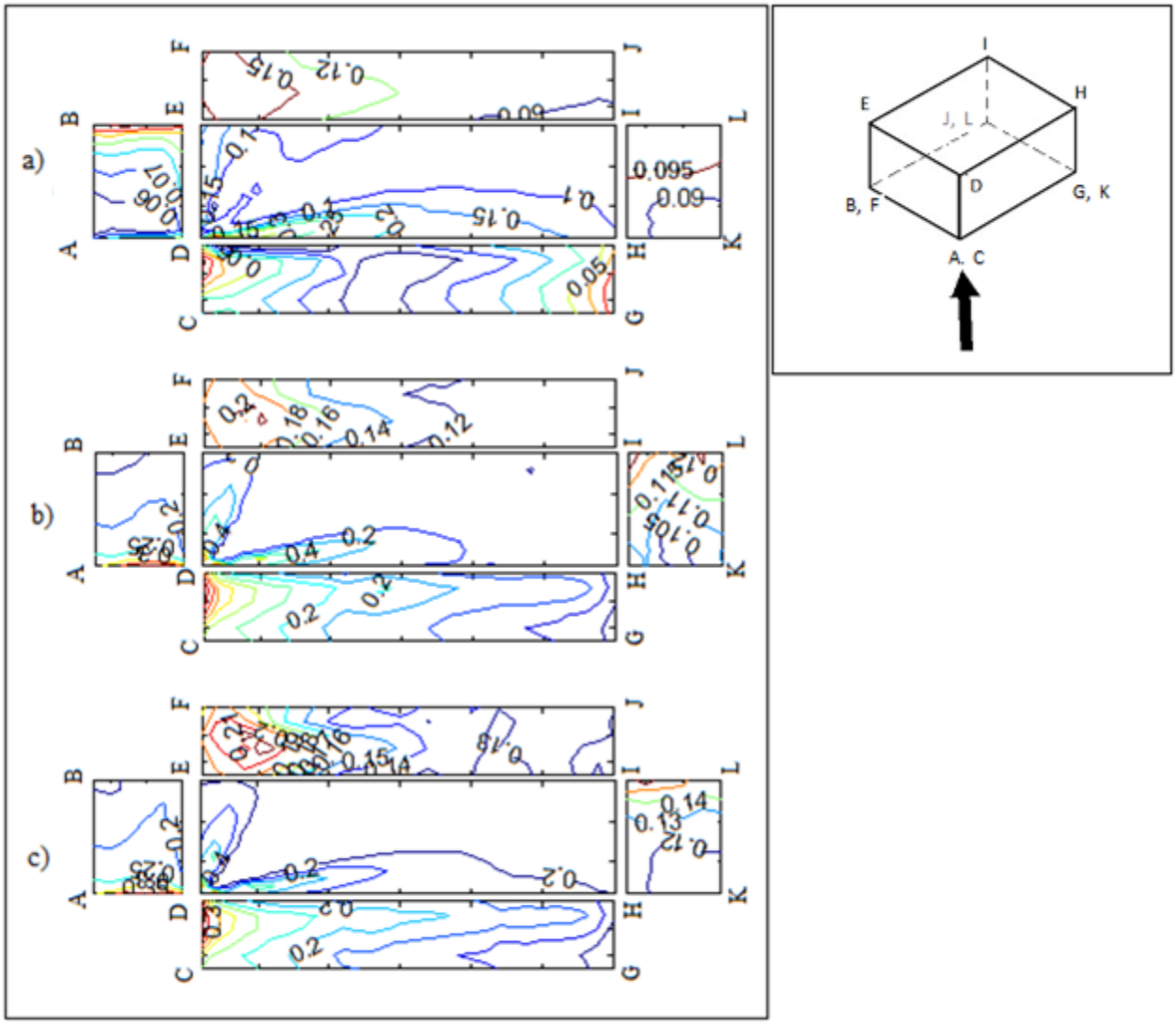

Figure 3.16 : Standard deviation of contributions (1, 10, 30) for α = 45
a) 1st; b) First 10; c) First 30

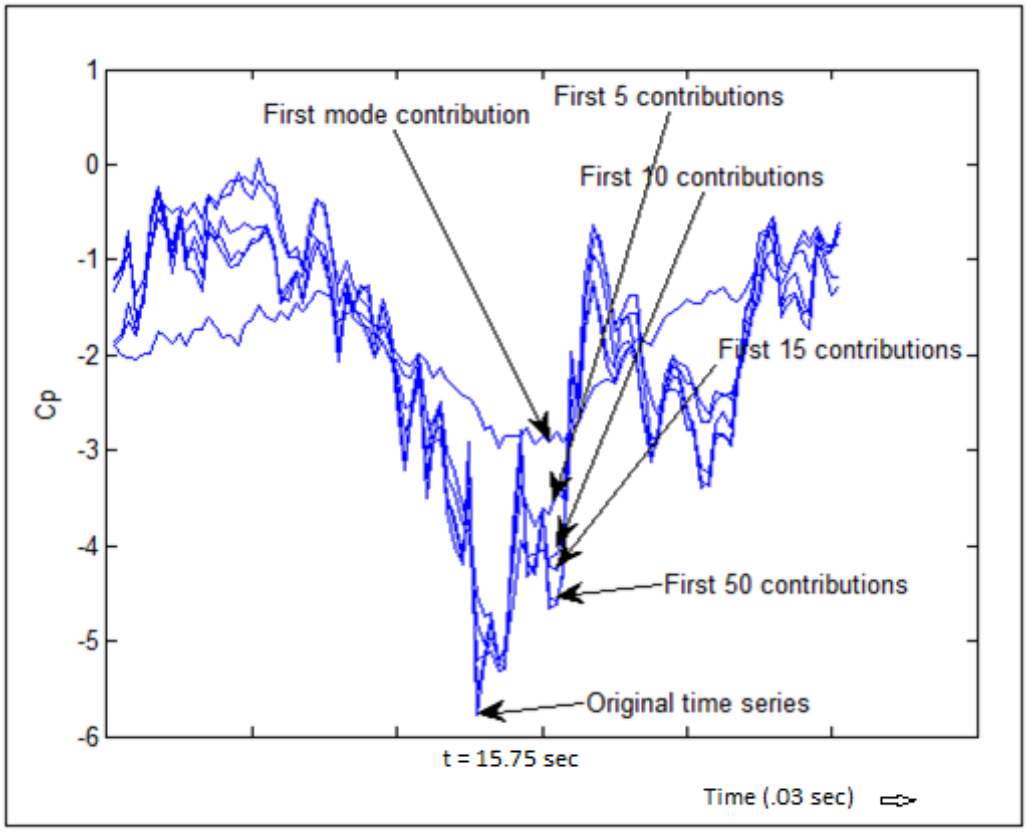

Figure 3.17 : Convergence of time series at maximum pressure position for α = 45

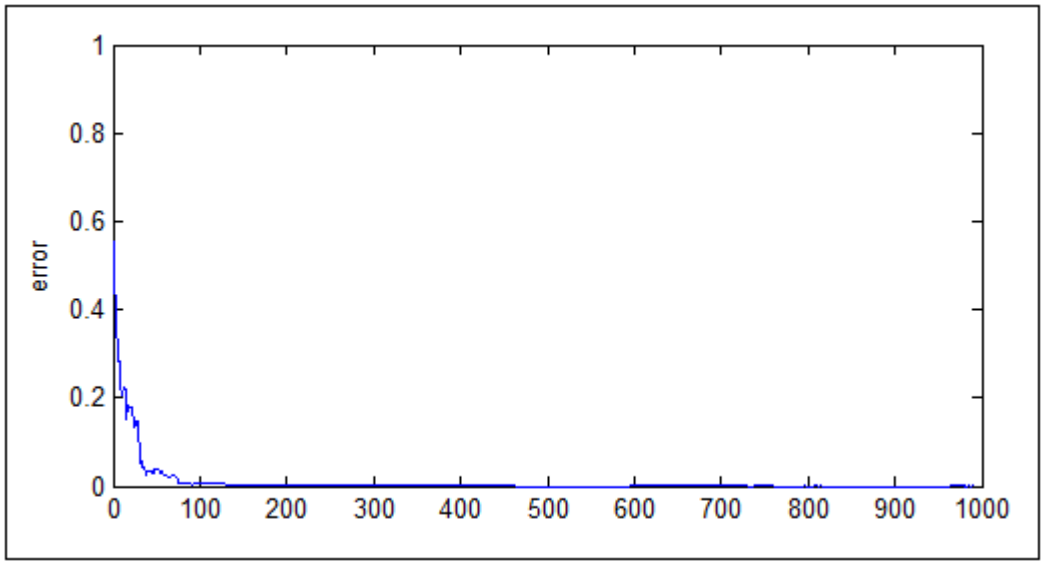

Figure 3.18 : Error at the maximum position with contribution for α = 45

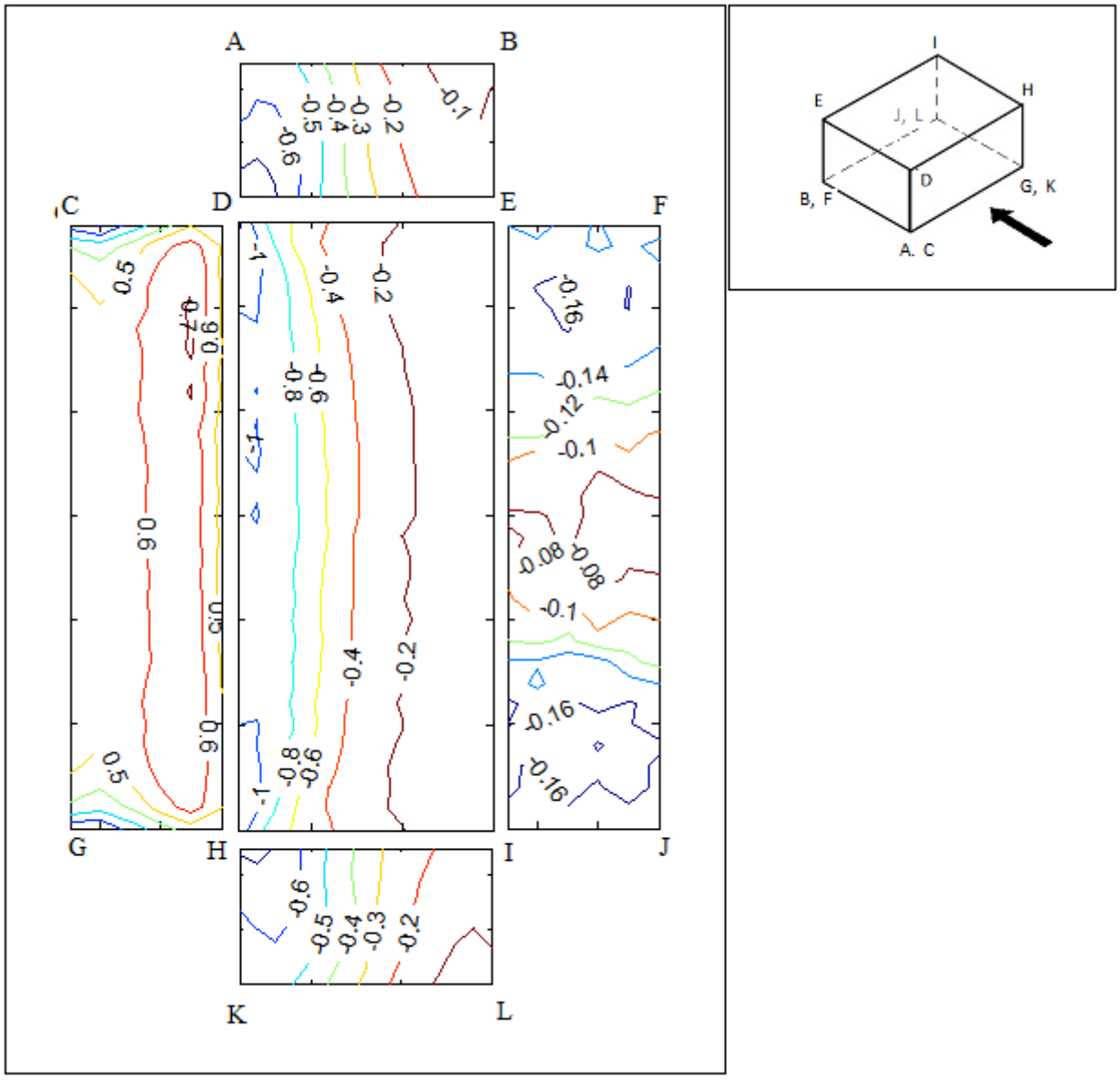

Figure 3.19 : Avg values for whole structure for $\alpha = 90$

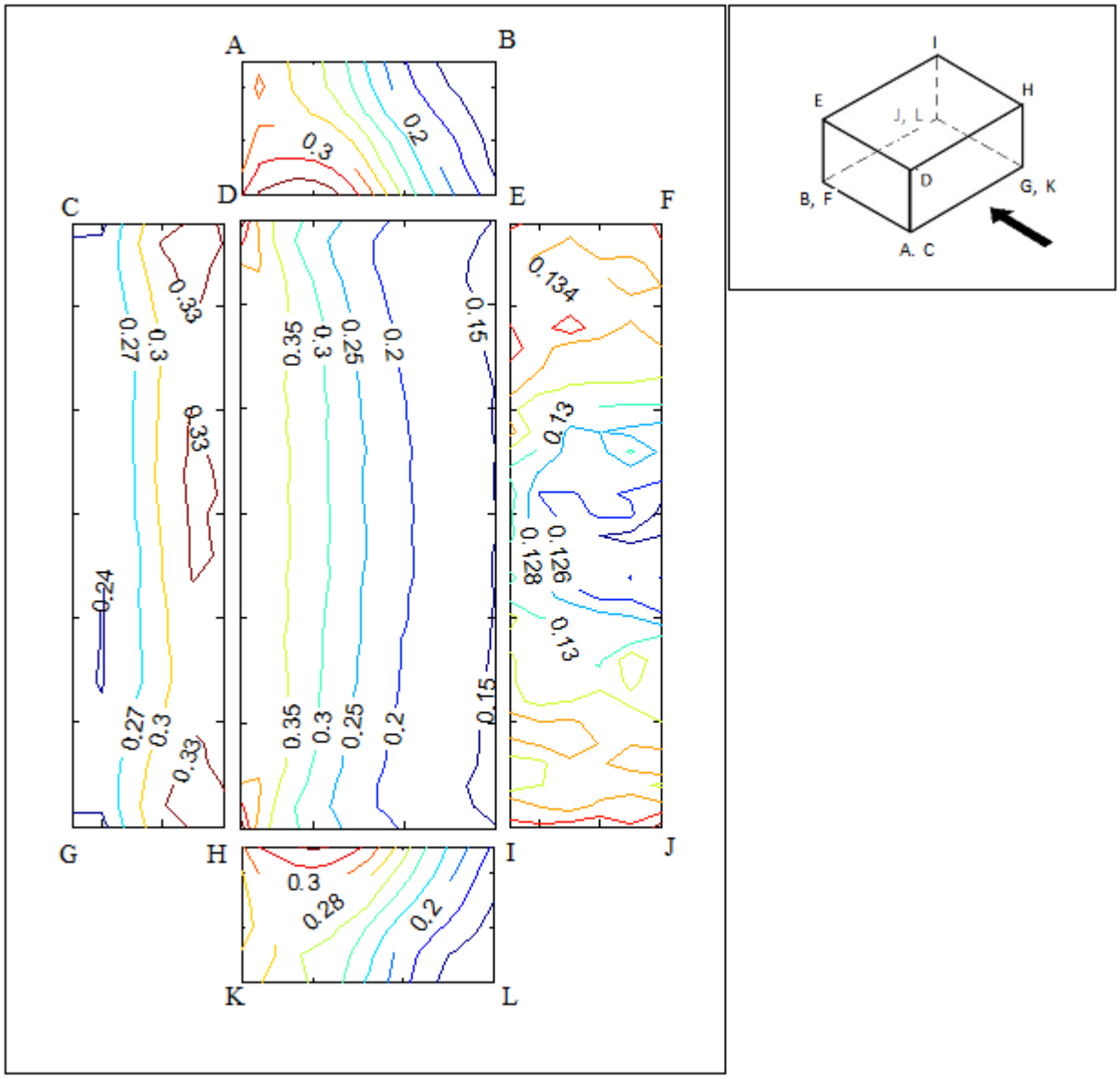

Figure 3.20 : Stdev values for whole structure for α = 90

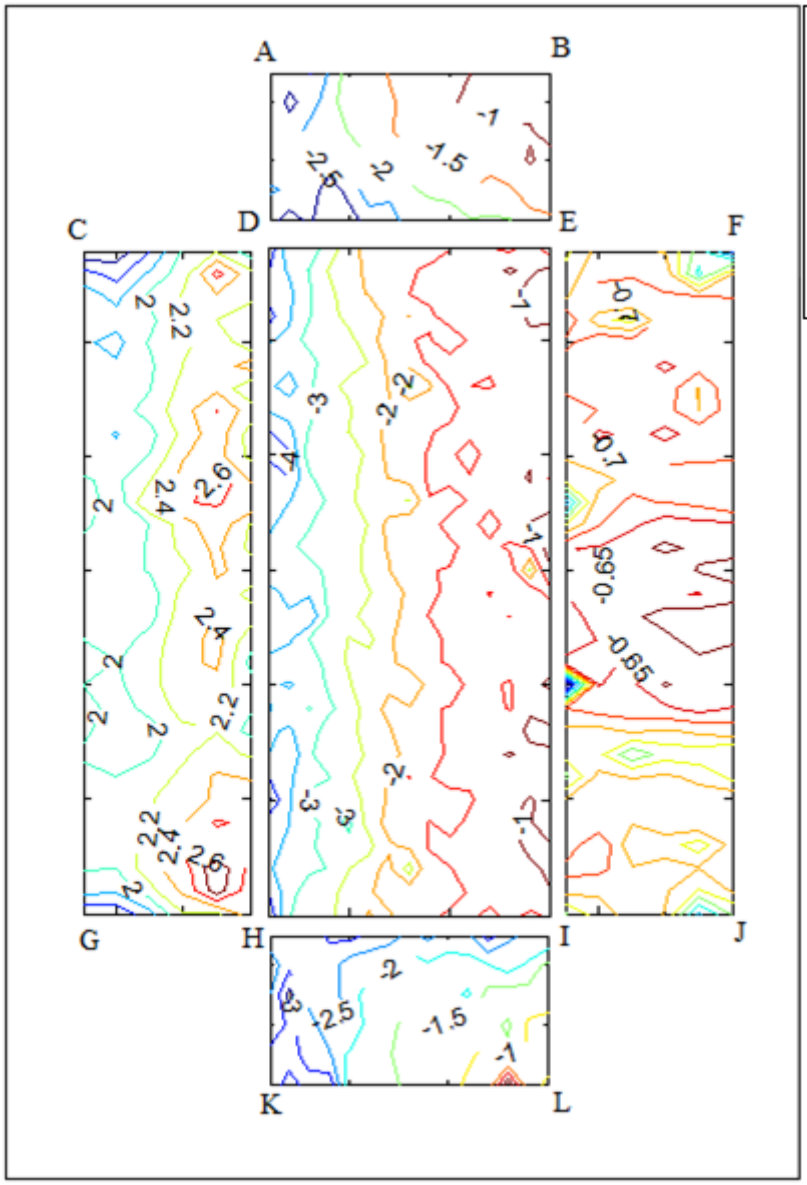

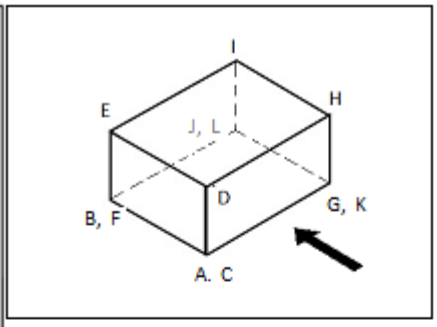

Figure 3.21 : Peak values for whole structure for α = 90

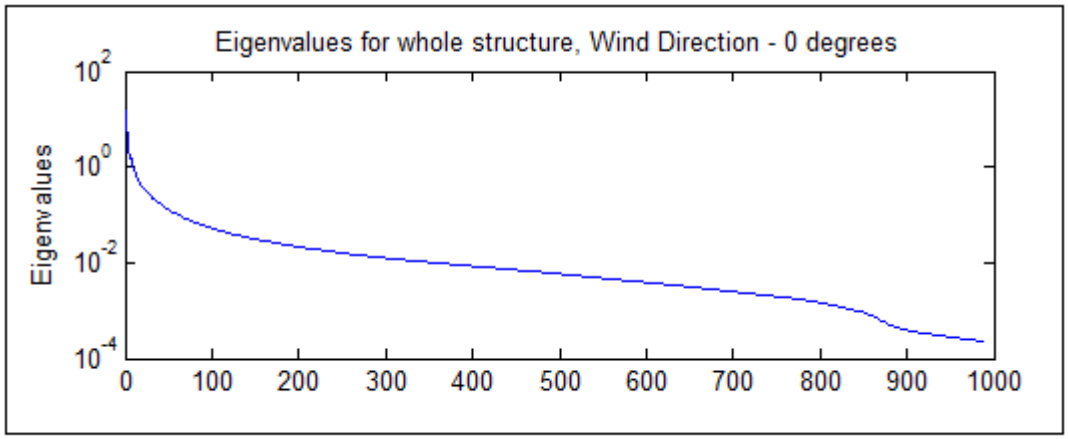

Figure 3.22 : Eigenvalues for whole structure for α = 90

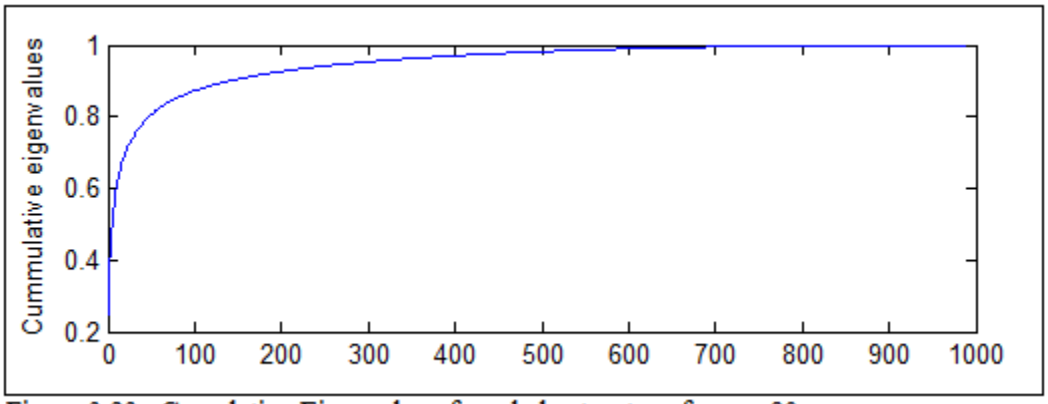

Figure 3.23 : Cumulative Eigenvalues for whole structure for α = 90

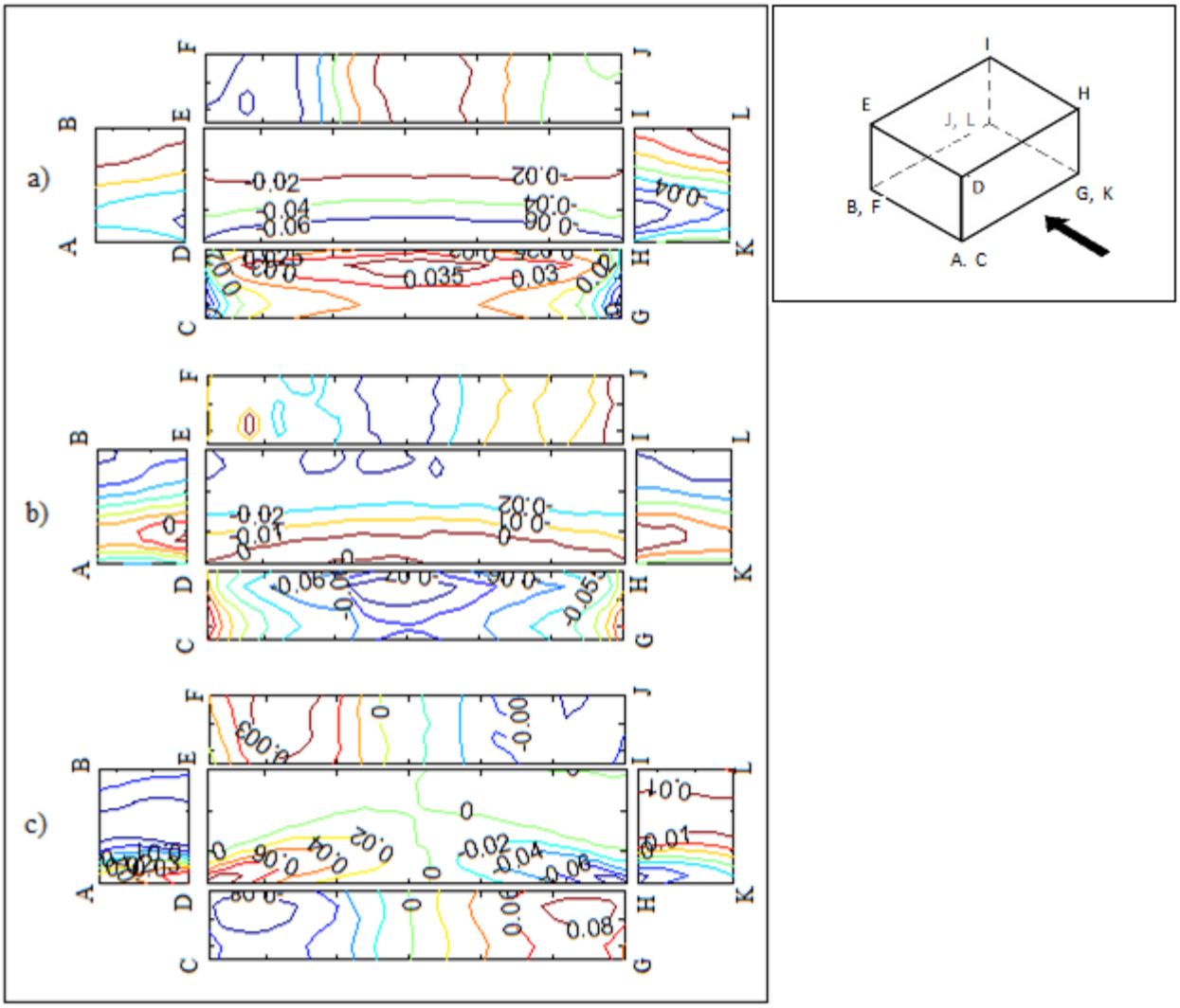

Figure 3.24 : 1st, 2nd and 3rd eigenvectors for whole structure for α = 90
a) 1st; b) 2nd; c) 3rd

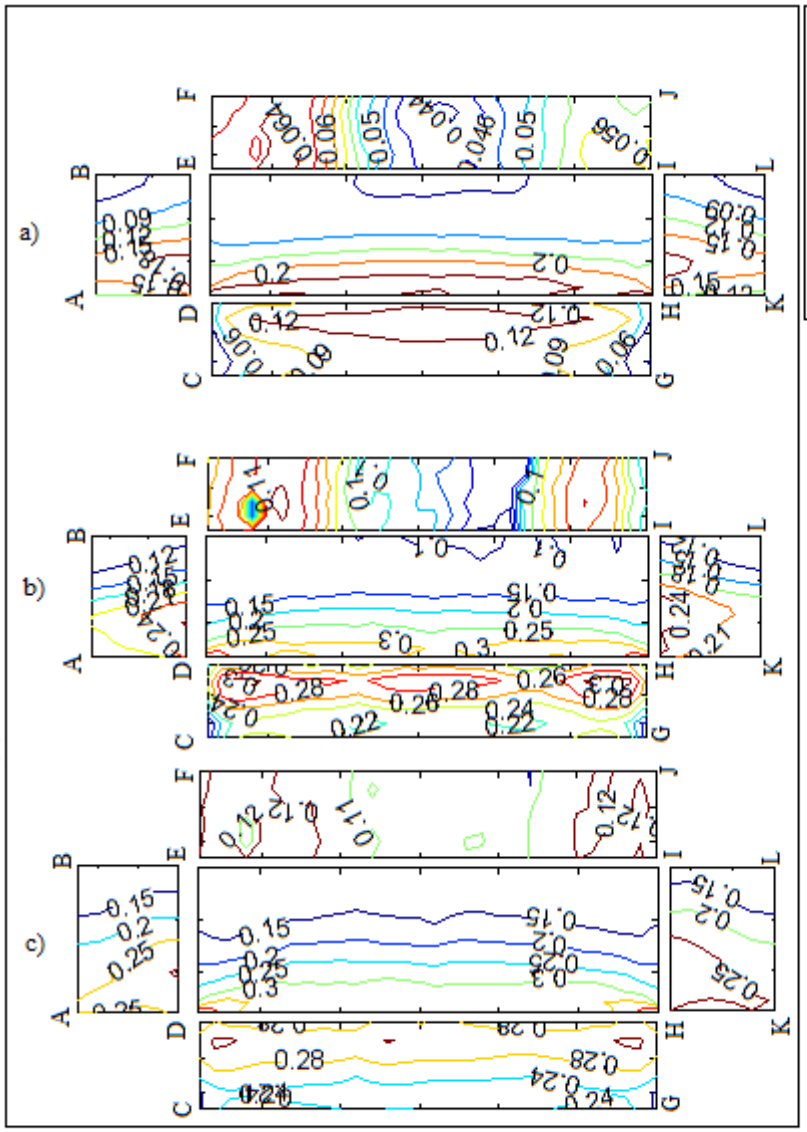

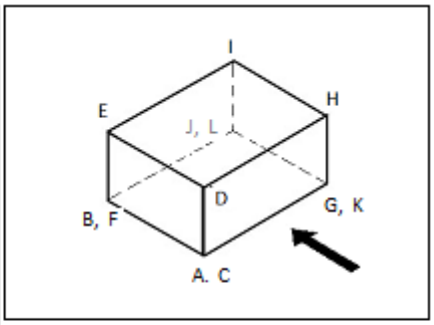

Figure 3.25 : Standard deviation of contributions (1, 10, 30) for α = 90
a) 1st; b) First 10; c) First 30

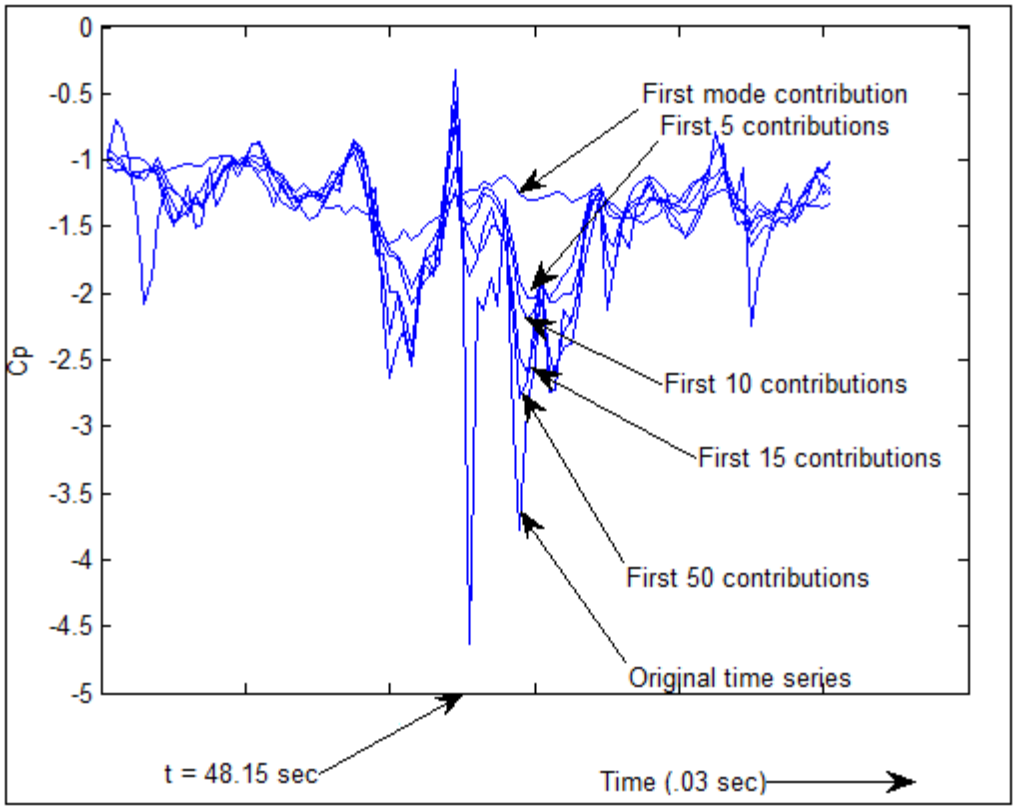

Figure 3.26 : Convergence of time series at maximum pressure position for α = 90

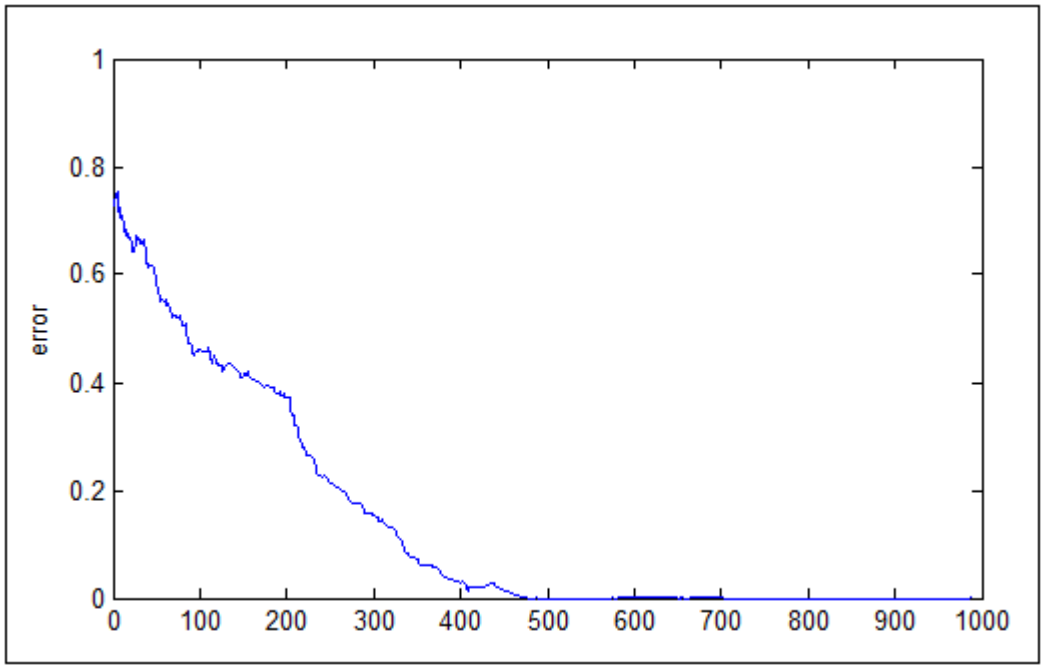

Figure 3.27 : Error at the maximum position with contribution for α = 90

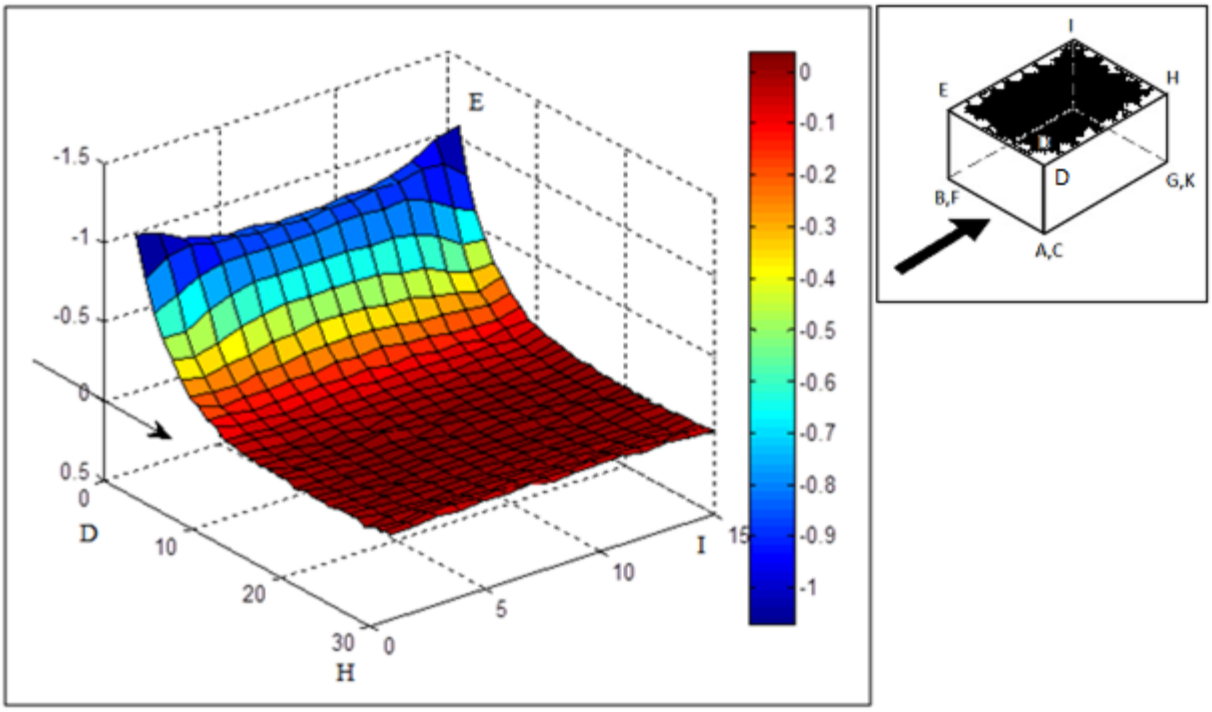

Figure 3.28 : Avg values for Roof for $\alpha = 0$

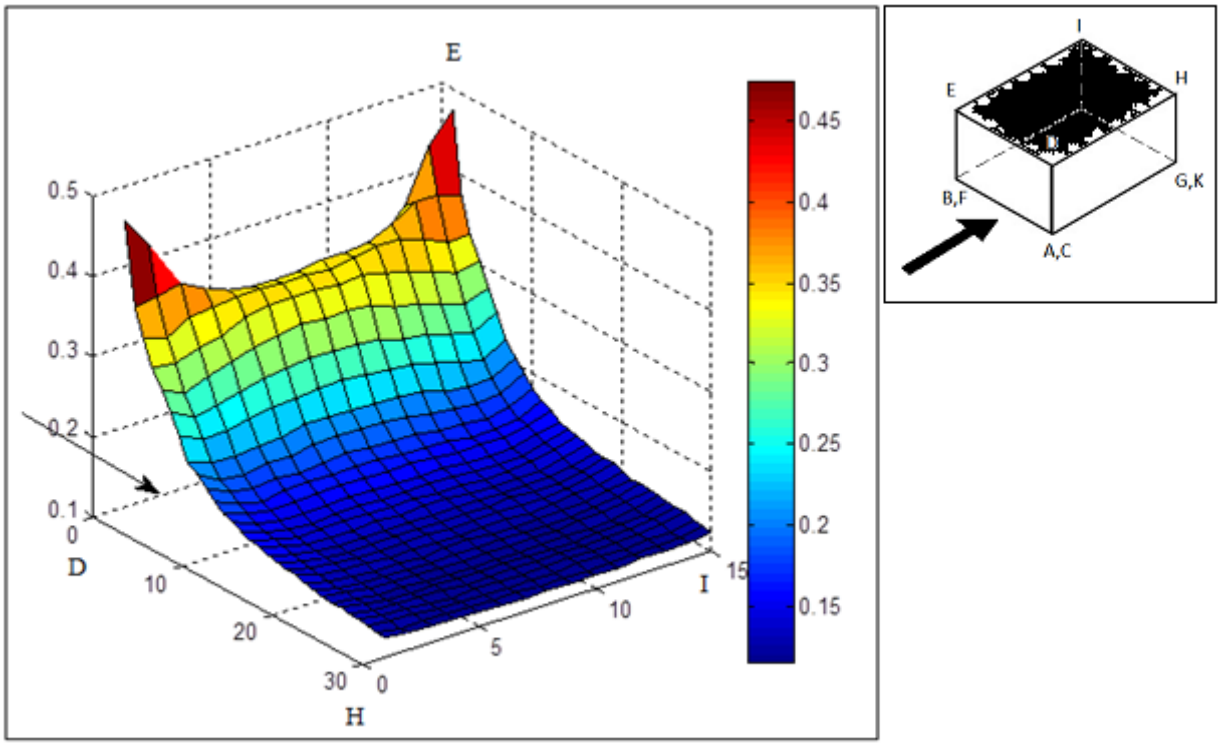

Figure 3.29 : Stdev values for Roof for $\alpha = 0$

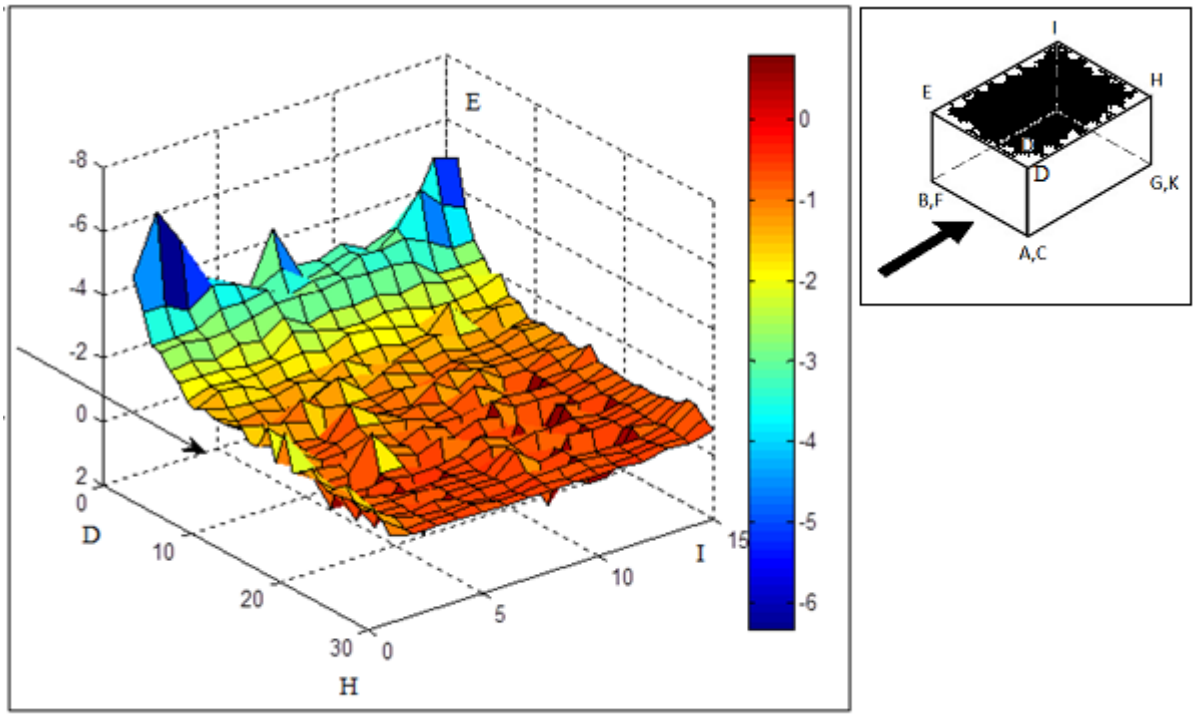

Figure 3.30 : Peak values for Roof for $\alpha = 0$

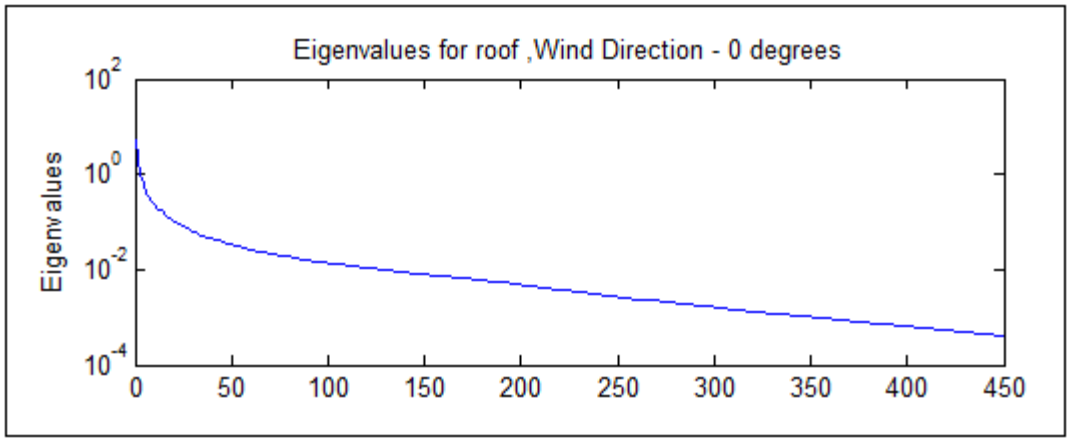

Figure 3.31 : Eigenvalues for Roof for α = 0

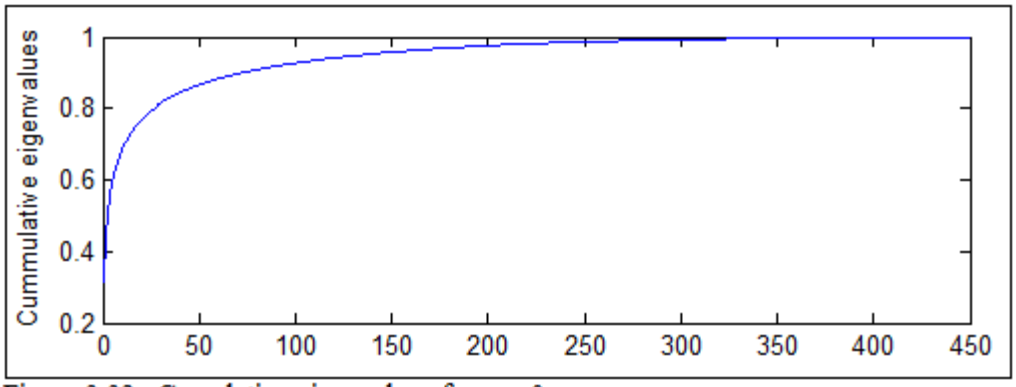

Figure 3.32 : Cumulative eigenvalues for α = 0

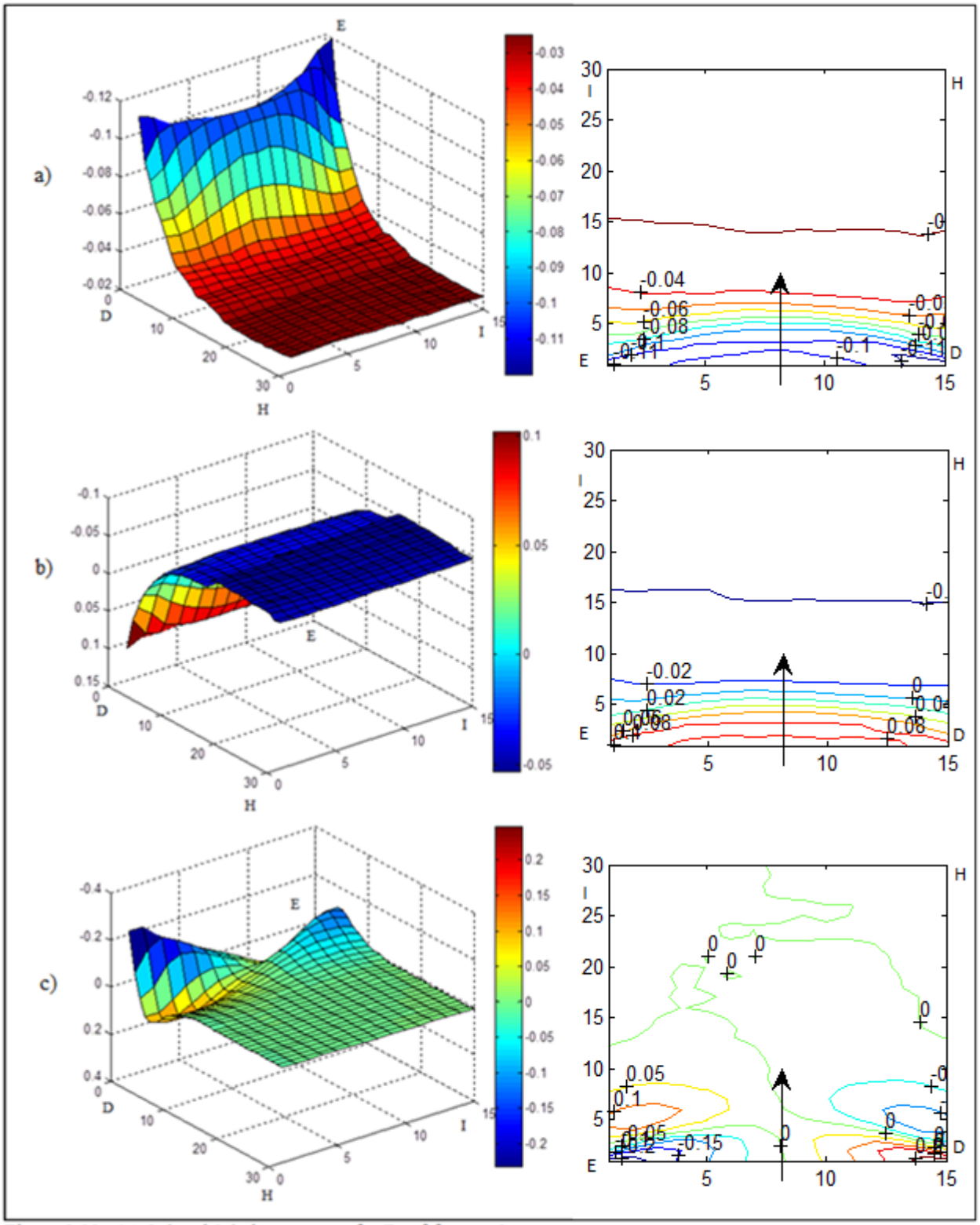

Figure 3.33 : 1st, 2nd and 3rd eigenvectors for Roof for α = 0
a) 1st; b) 2nd; c) 3rd

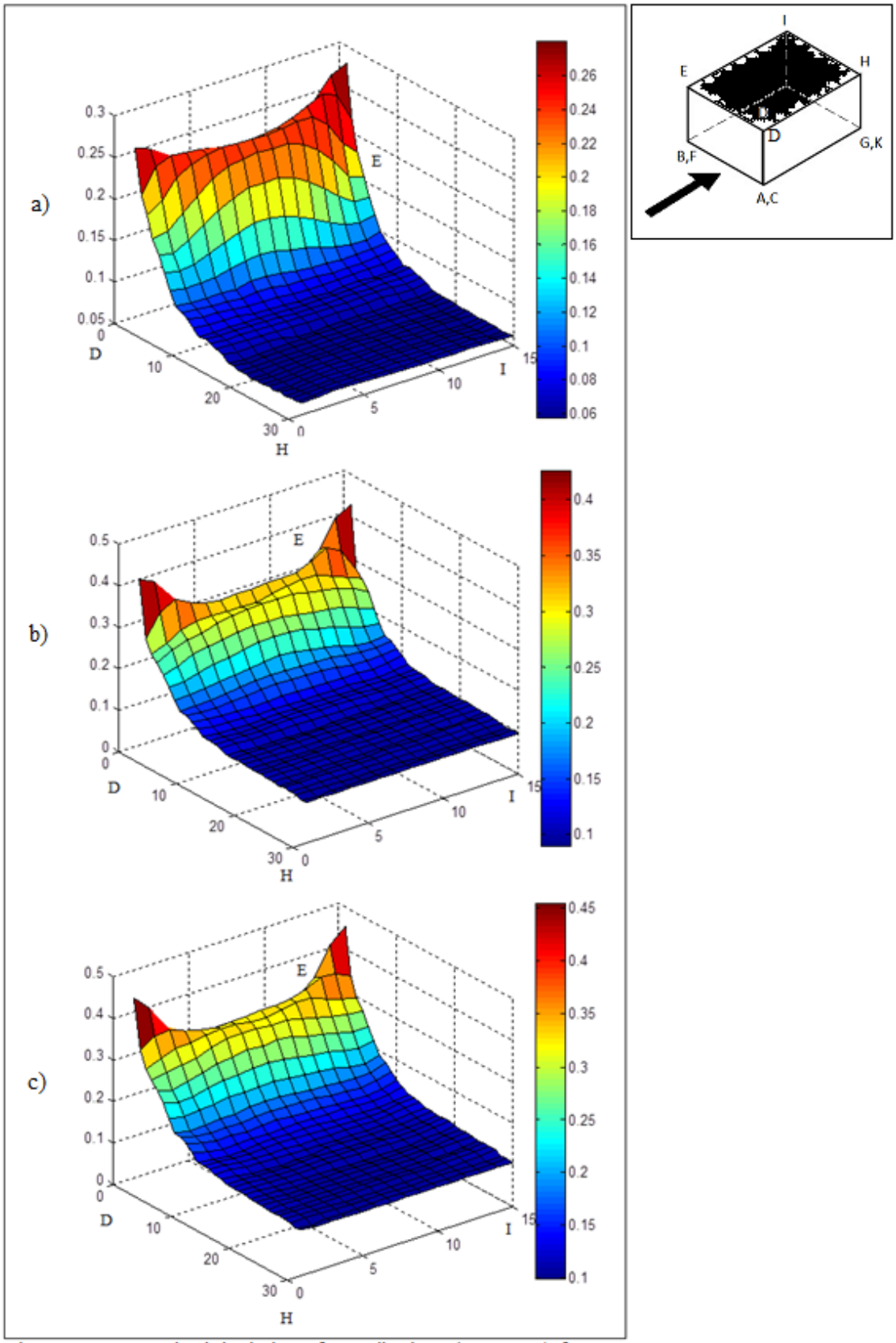

Figure 3.34 : Standard deviation of contributions (1, 10, 30) for $\alpha = 0$
a) 1st; b) First 10; c) First 30

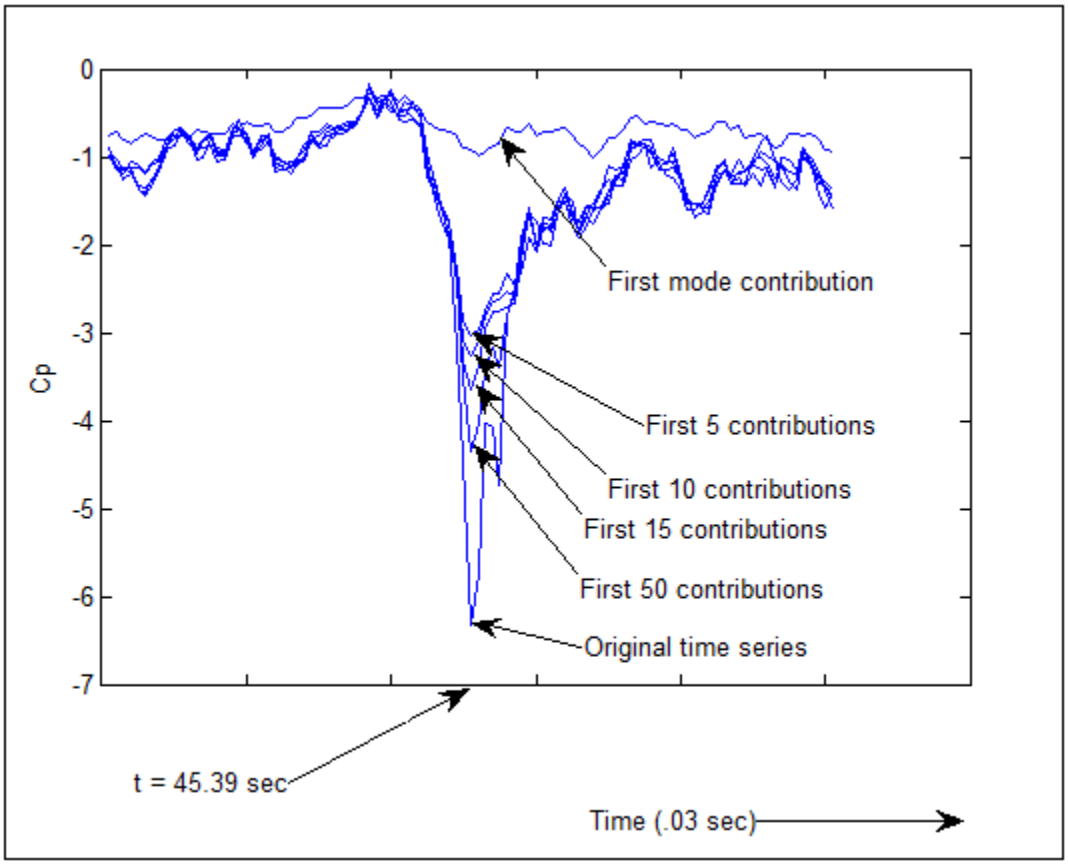

Figure 3.35 : Convergence of time series at position of maximum value for $\alpha = 0$

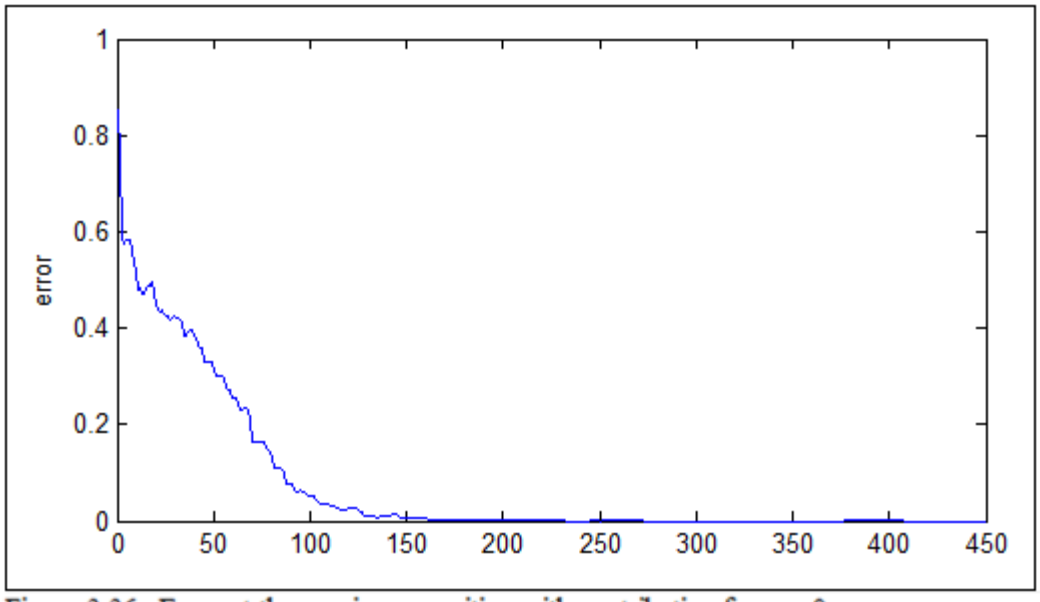

Figure 3.36 : Error at the maximum position with contribution for $\alpha = 0$

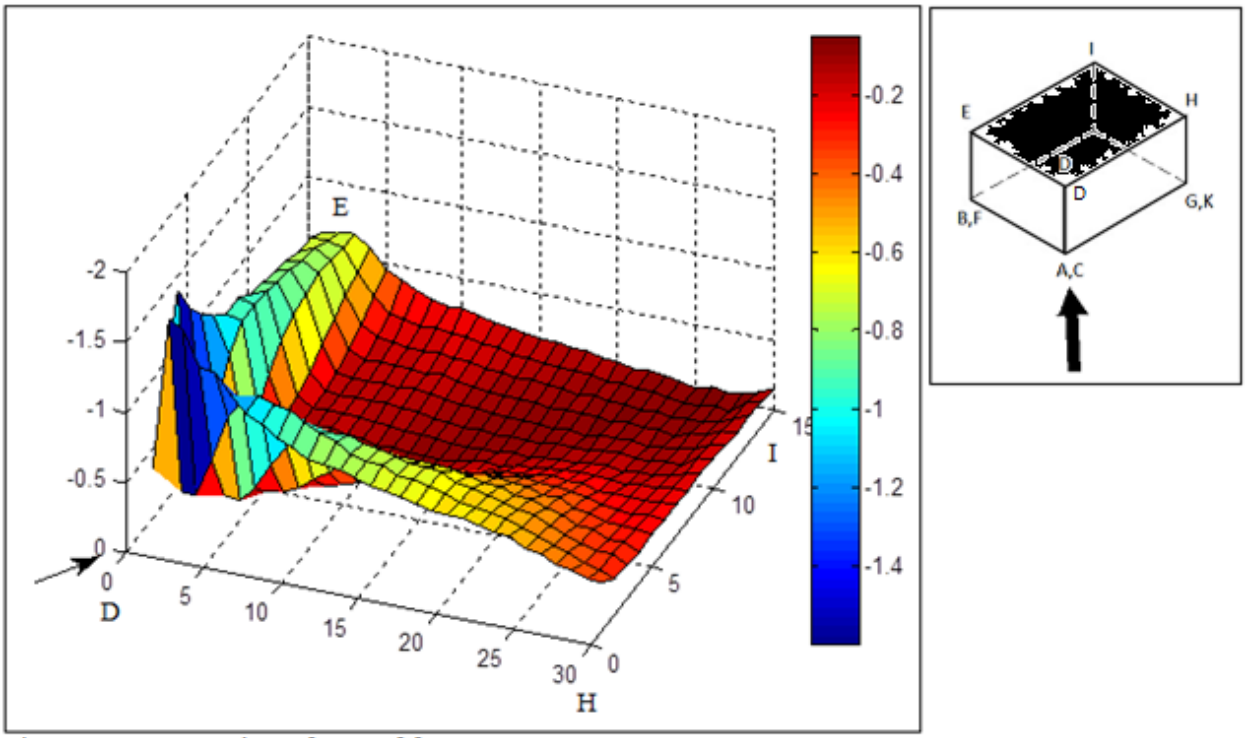

Figure 3.37 : Avg values for Roof for α = 45

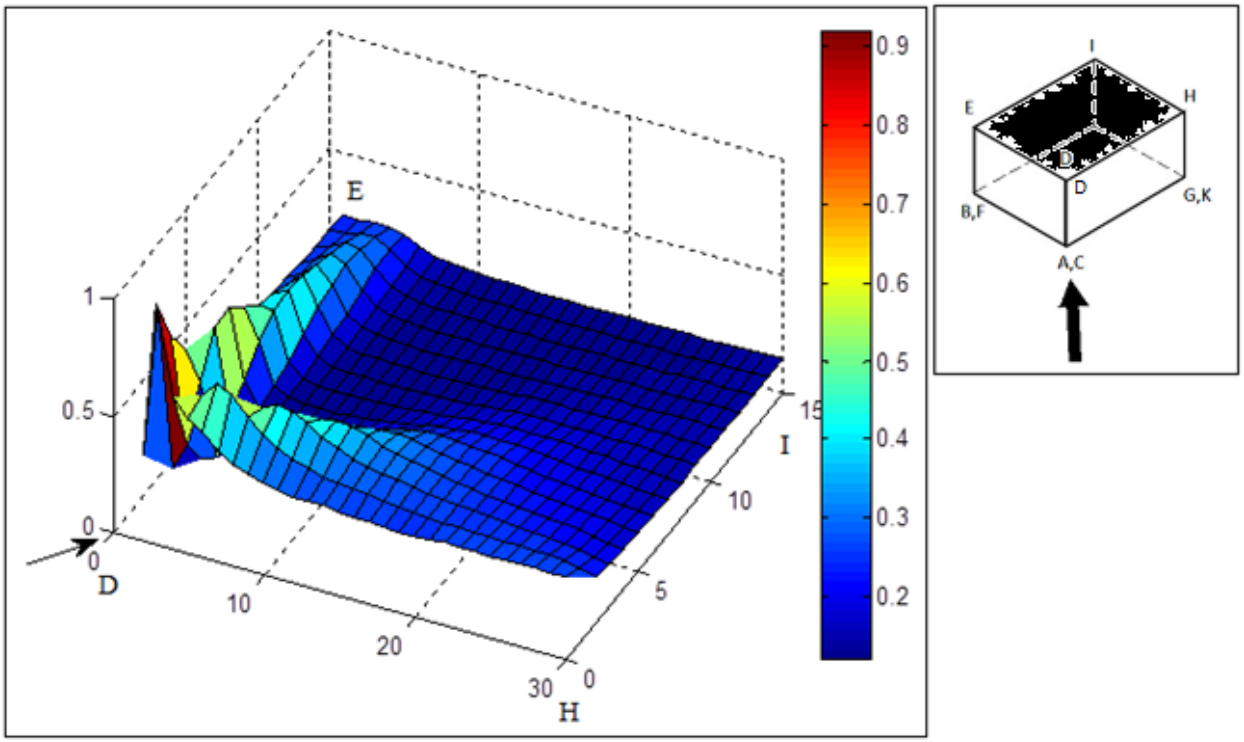

Figure 3.38 : Stdev values for Roof for α = 45

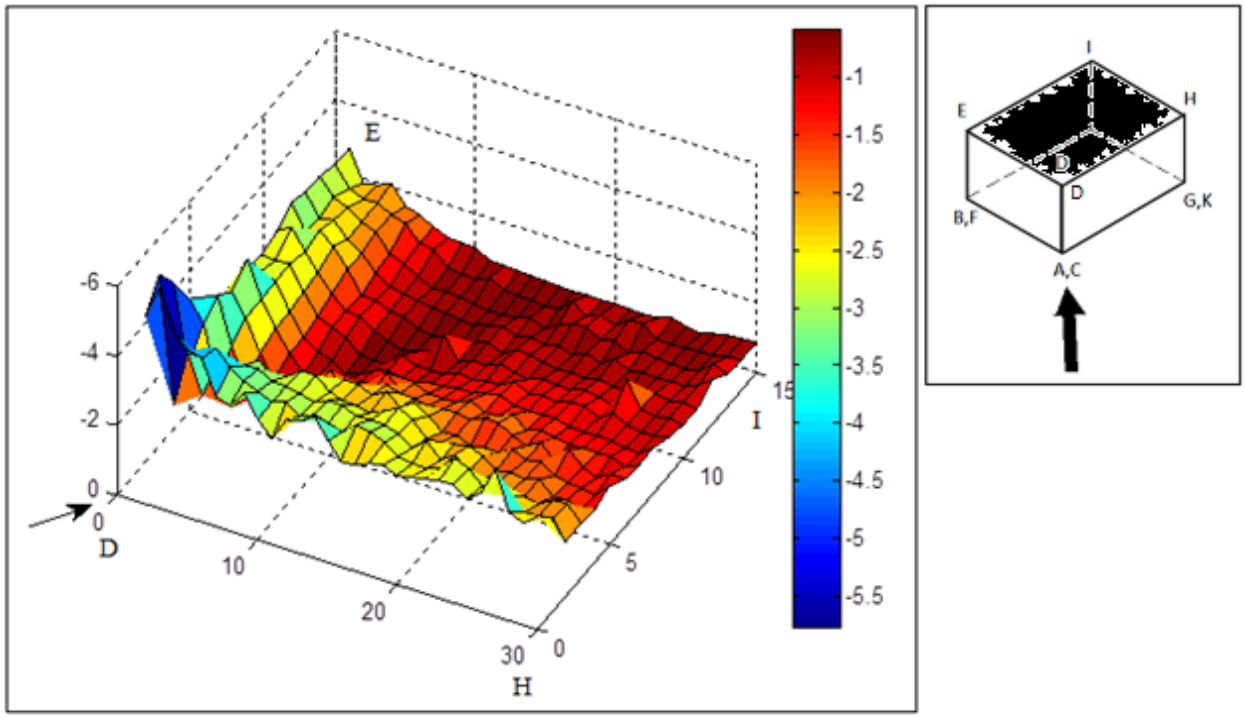

Figure 3.39 : Peak values for Roof for $\alpha = 45$

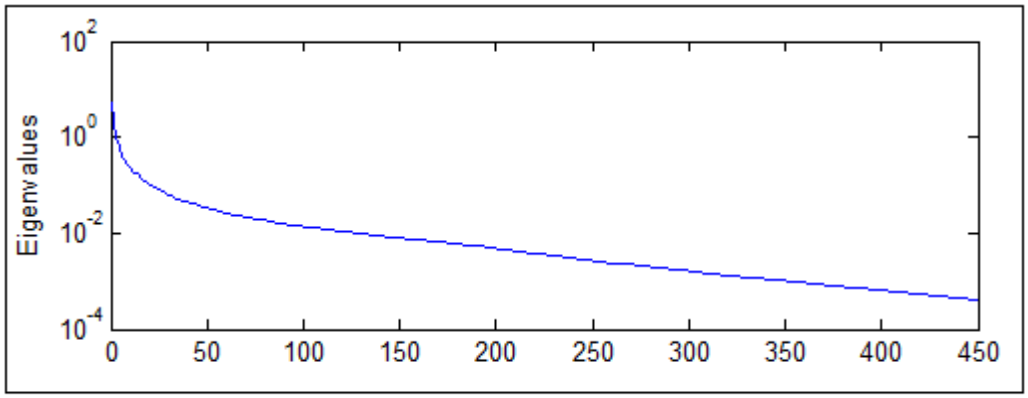

Figure 3.40 : Eigenvalues for Roof for α = 45

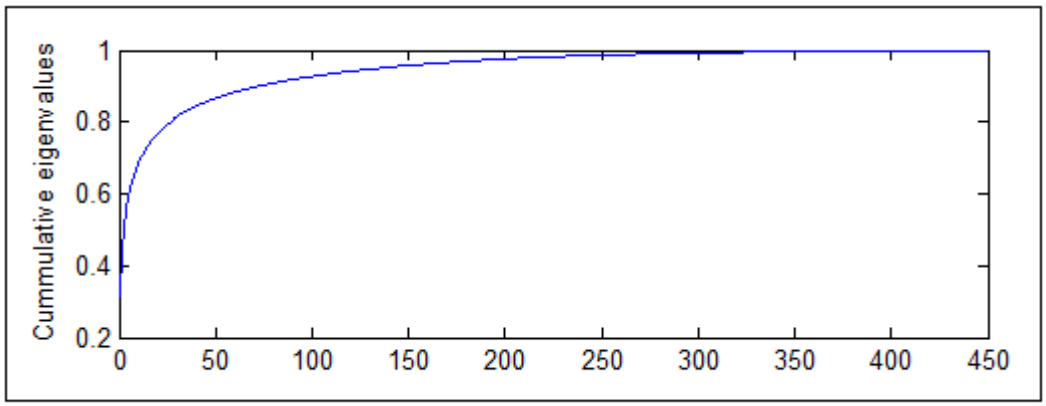

Figure 3.41 : Cumulative eigenvalues for α = 45

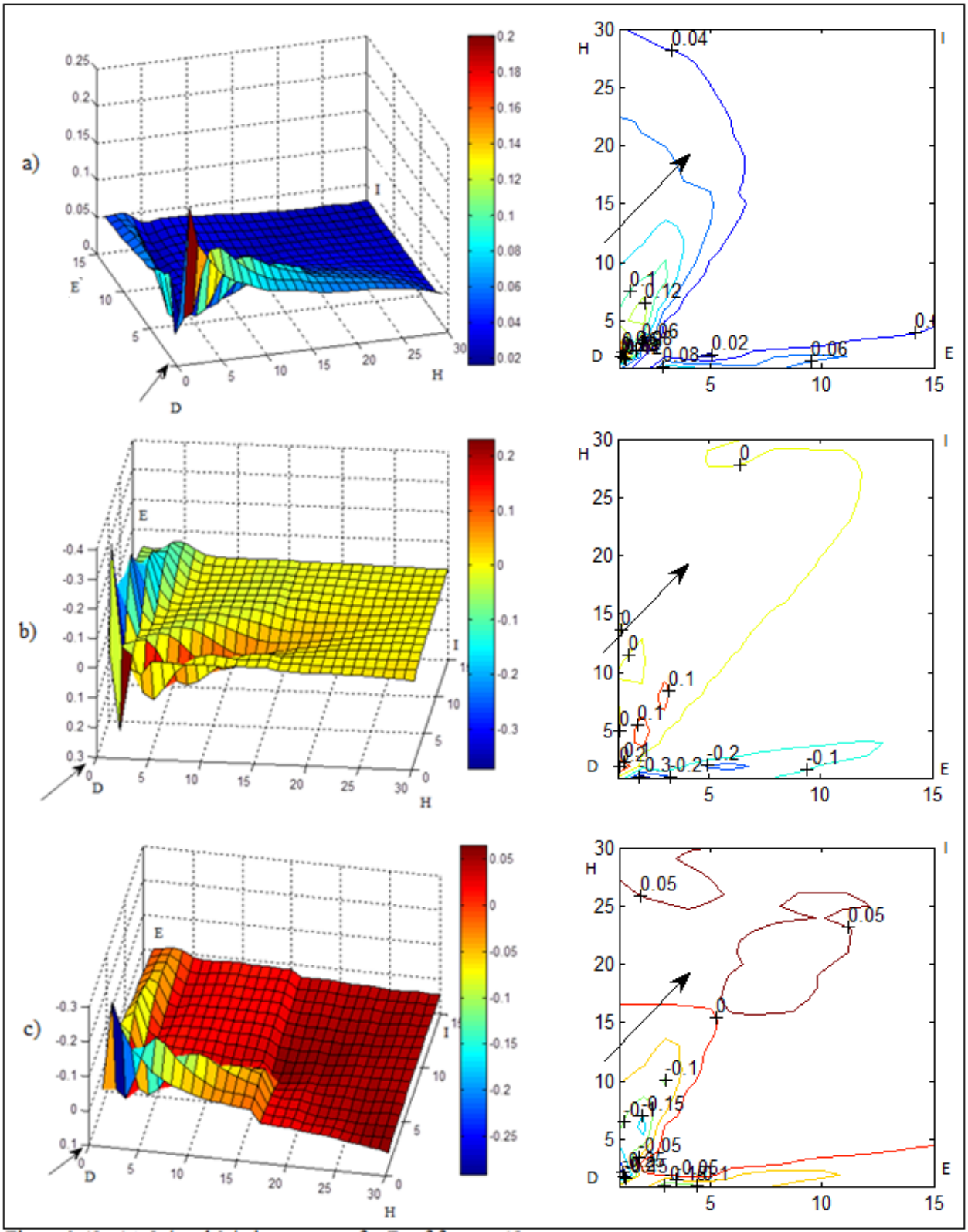

Figure 3.42 : 1st, 2nd and 3rd eigenvectors for Roof for α = 45
a) 1st; b) 2nd; c) 3rd

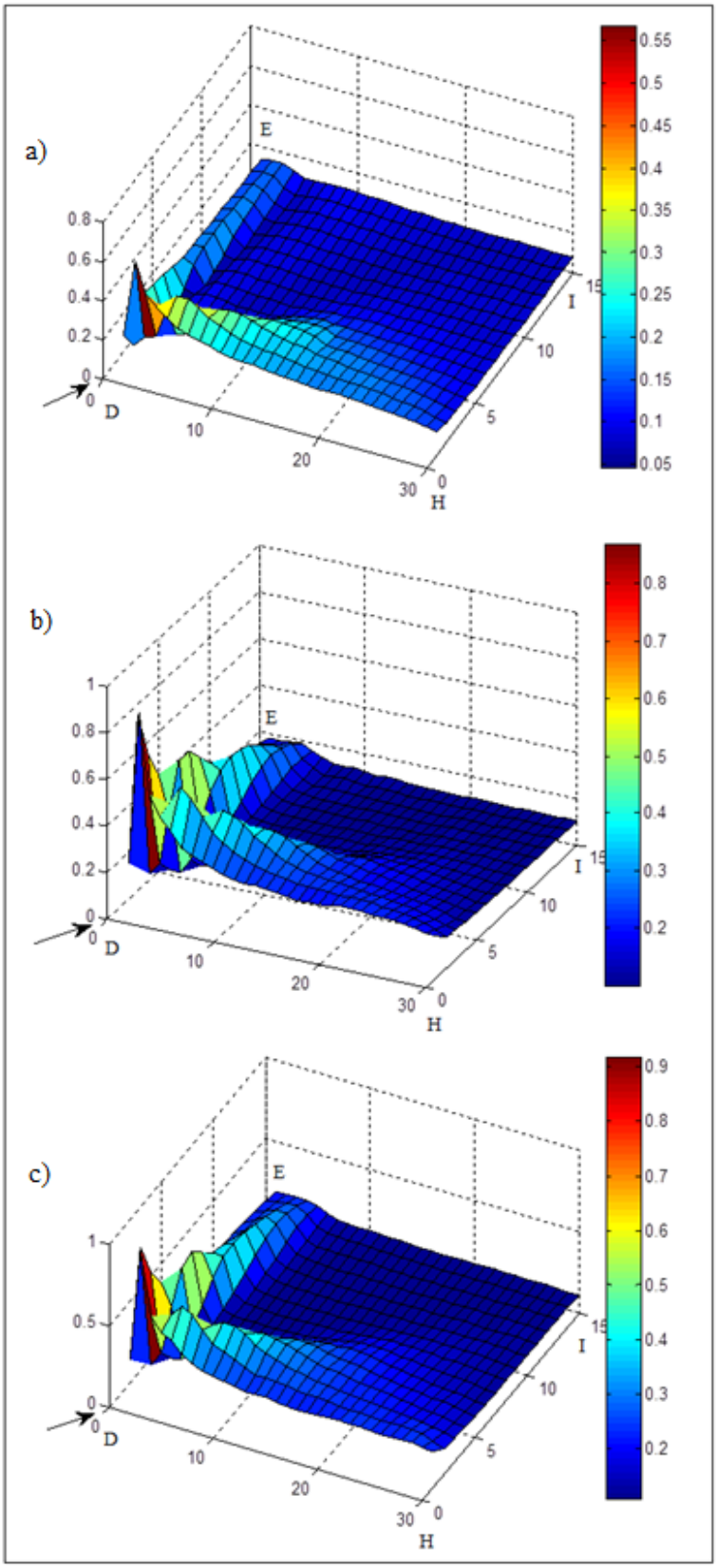

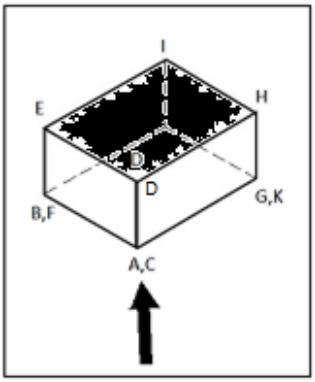

Figure 3.43 : Standard deviation of contributions (1, 10, 30) for α = 45
a) 1st; b) First 10; c) First 30

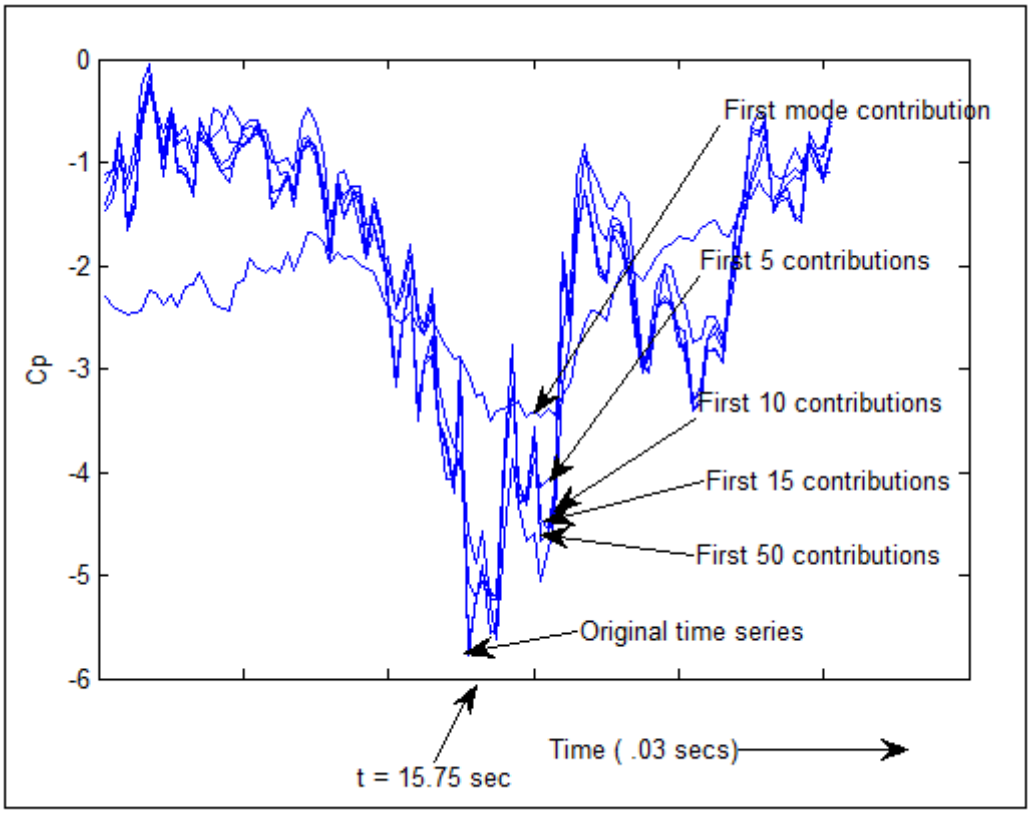

Figure 3.44 : Convergence of time series at position of maximum value for α = 45

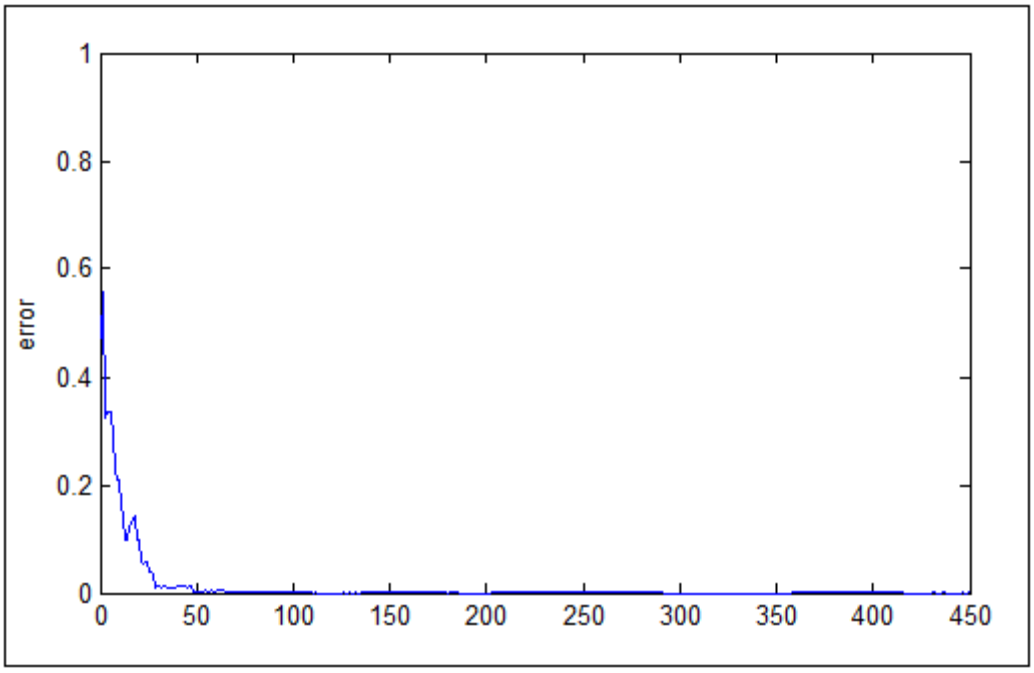

Figure 3.45 : Error at the maximum position with contribution for α = 45

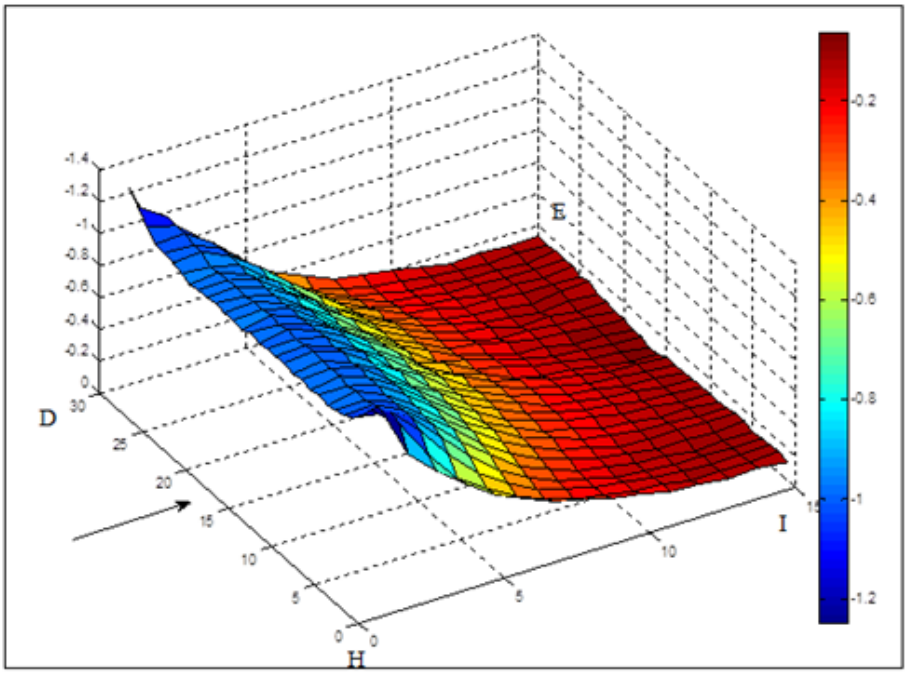

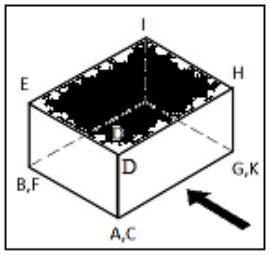

Figure 3.46 : Avg values for Roof for α = 90

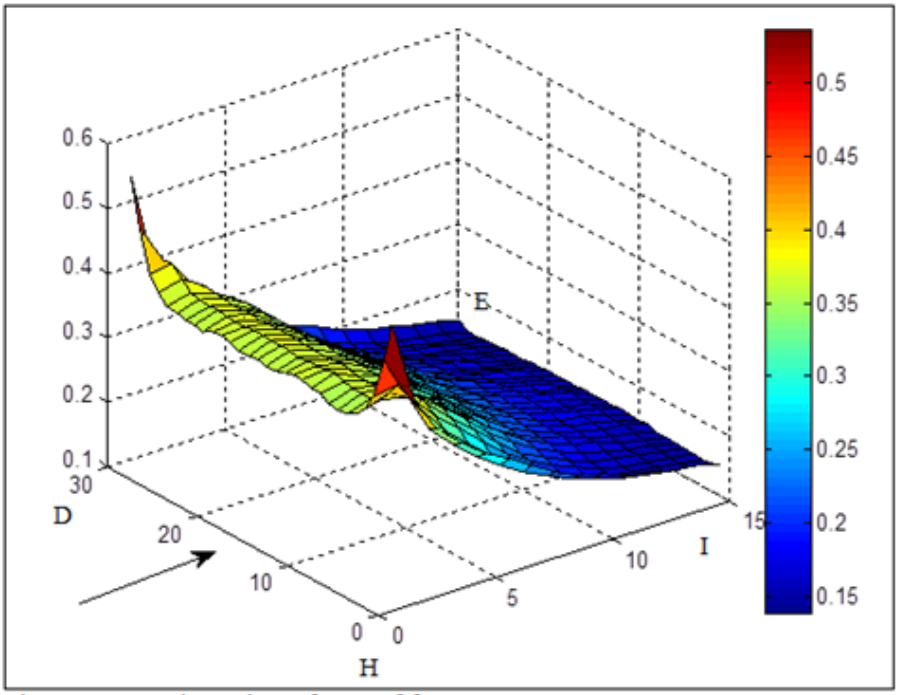

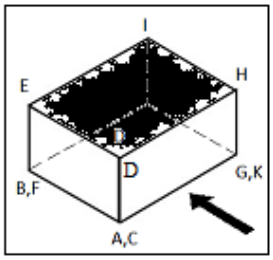

Figure 3.47 : Stdev values for Roof for α = 90

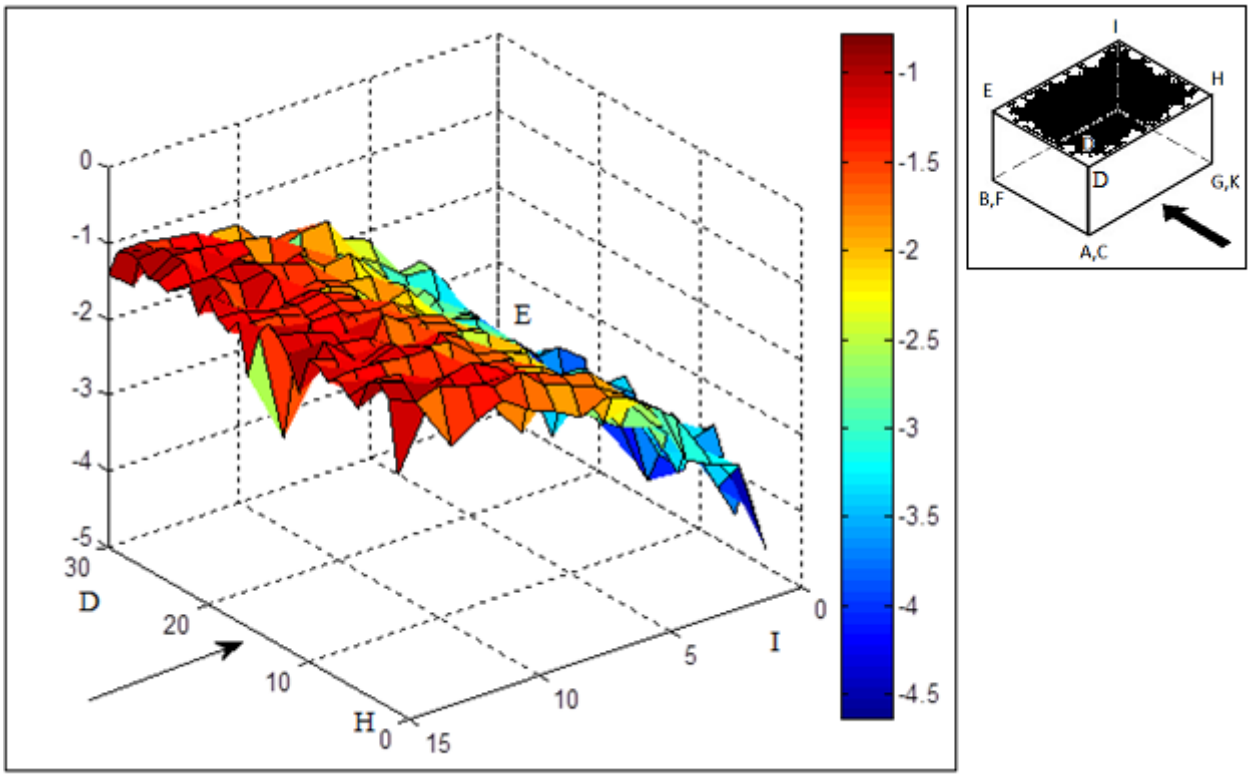

Figure 3.48 : Peak values for Roof for $\alpha = 90$

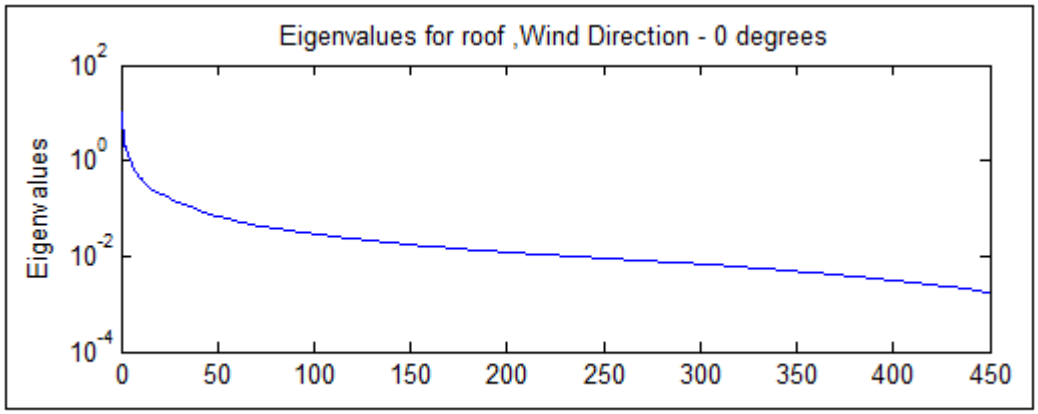

Figure 3.49 : Eigenvalues for Roof for α = 90

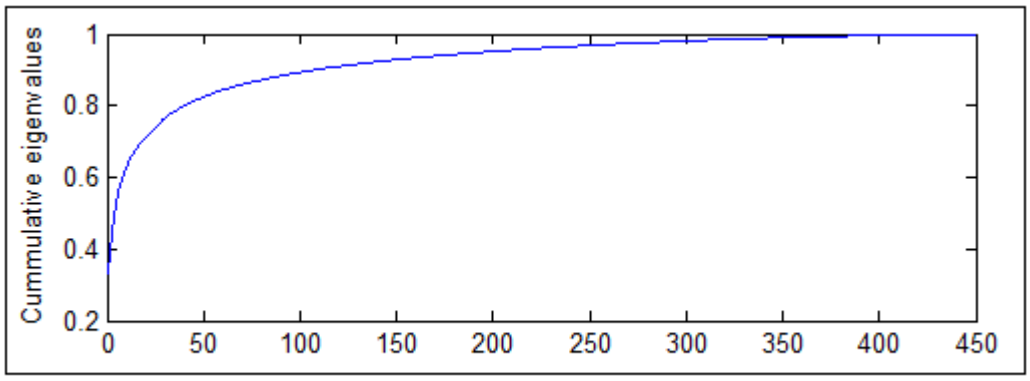

Figure 3.50 : Cumulative eigenvalues for α = 90

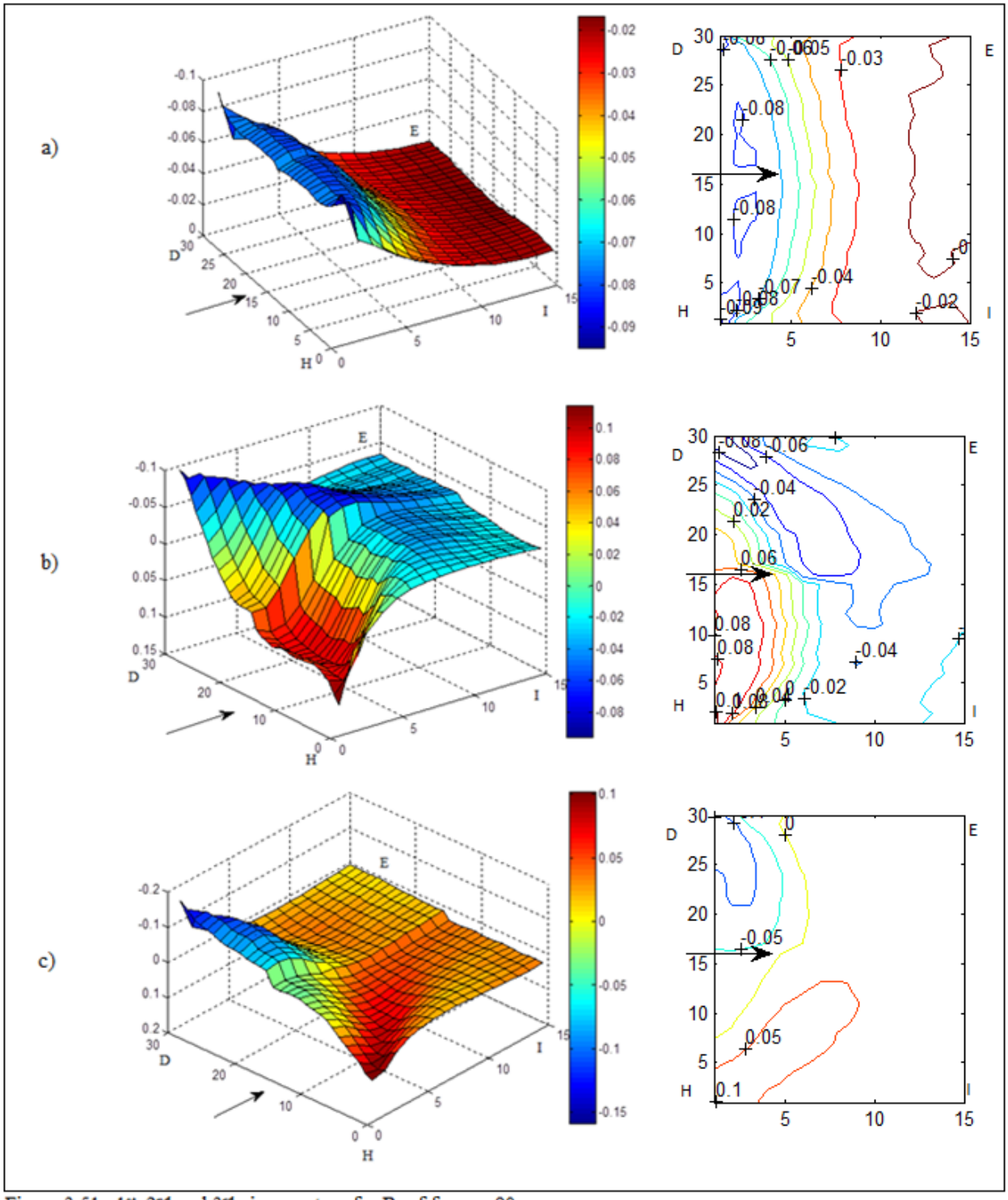

Figure 3.51 : 1st, 2nd and 3rd eigenvectors for Roof for α = 90
a) 1st; b) 2nd; c) 3rd

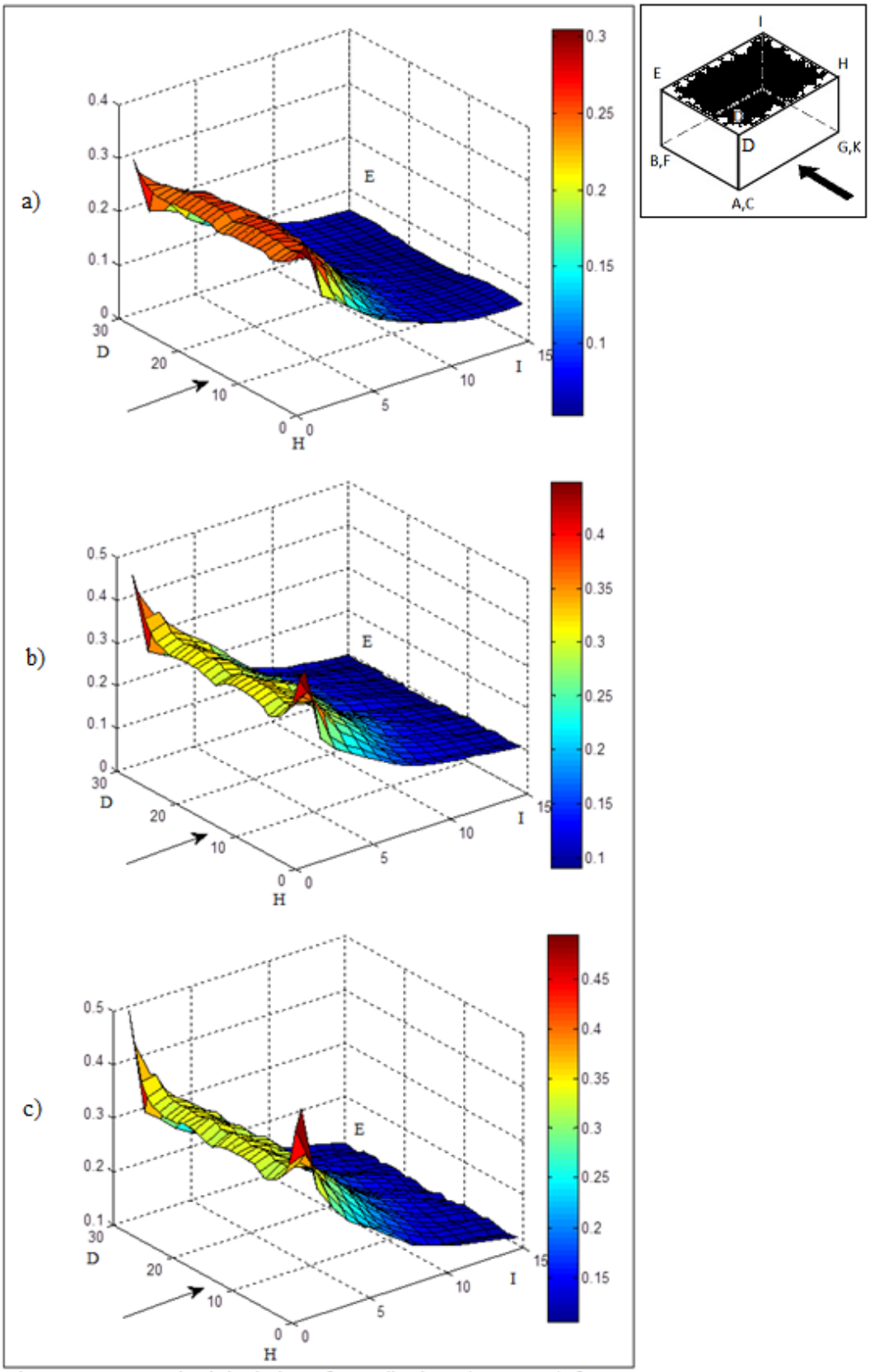

Figure 3.52 : Standard deviation of contributions (1, 10, 30) for α = 90
a) 1st; b) First 10; c) First 30

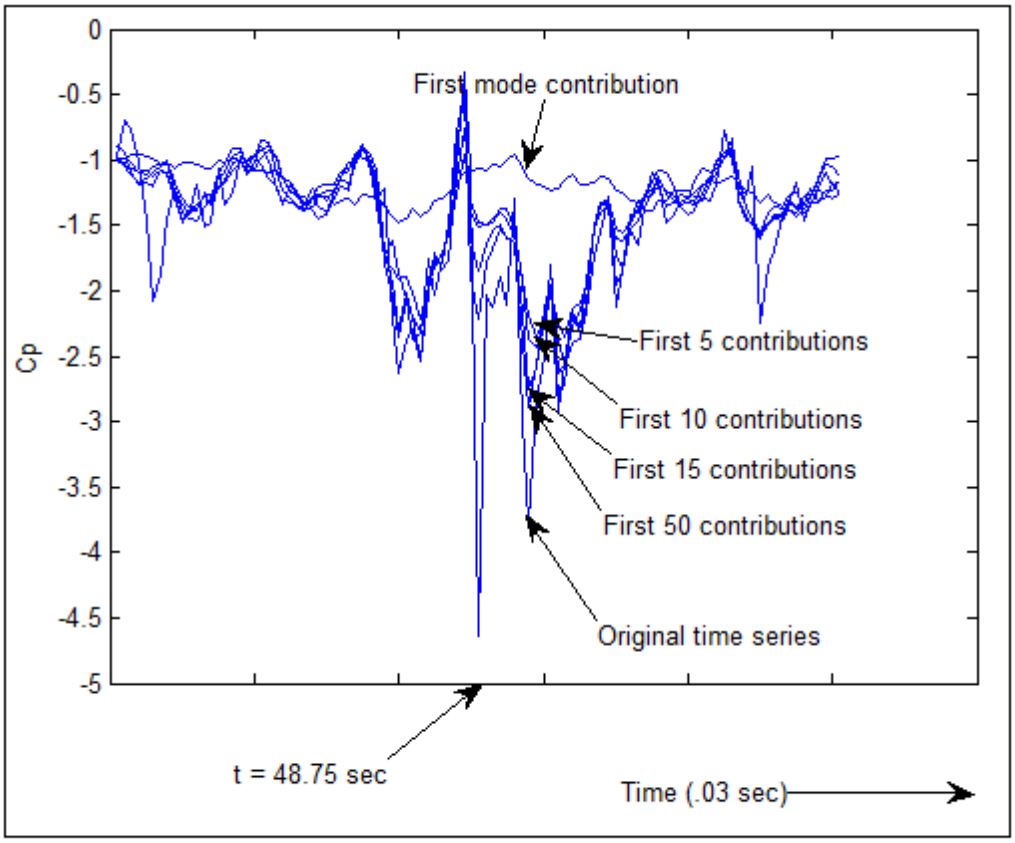

Figure 3.53 : Convergence of time series at position of maximum value for α = 90

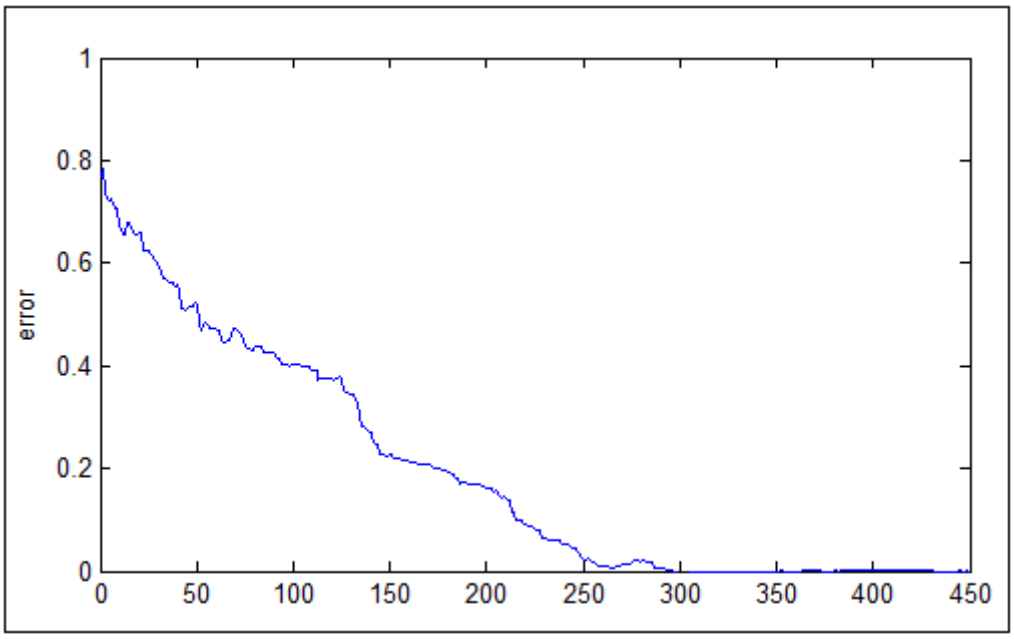

Figure 3.54 : Error at the maximum position with contribution for α = 90

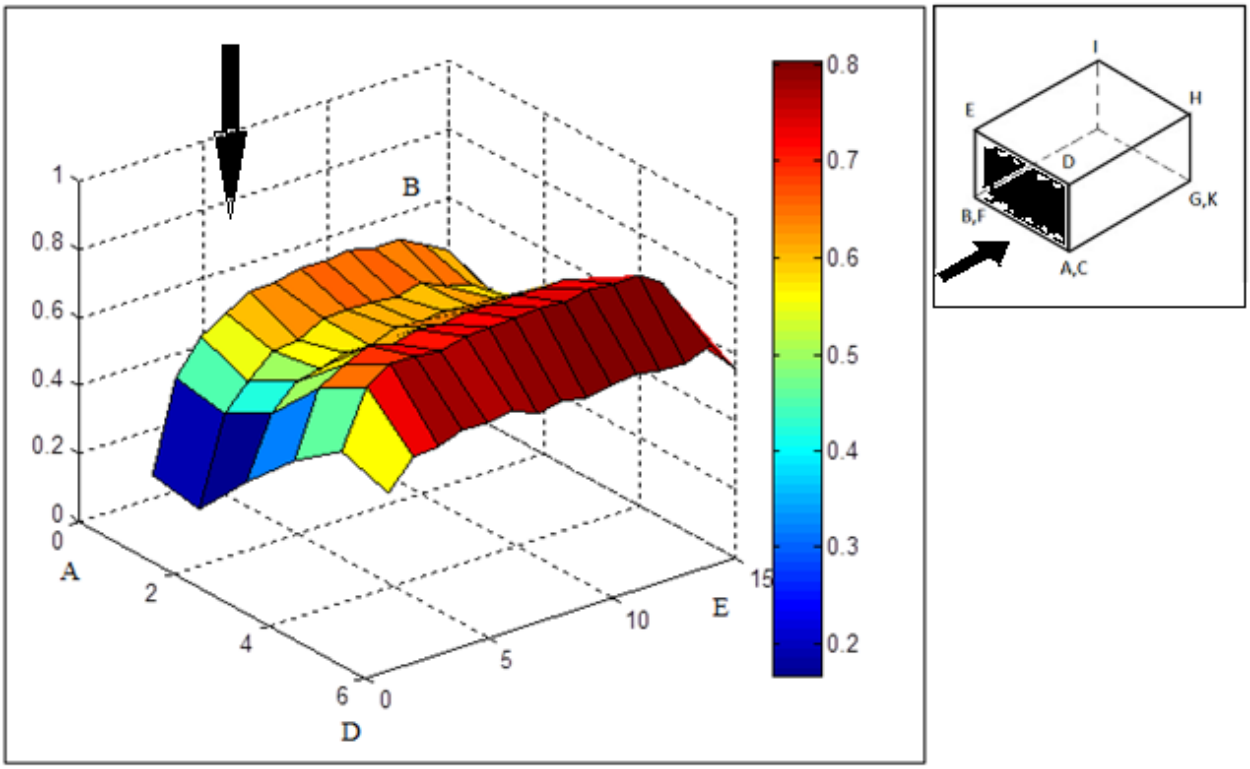

Figure 3.55 : Avg values for Shorter wall for $\alpha = 0$

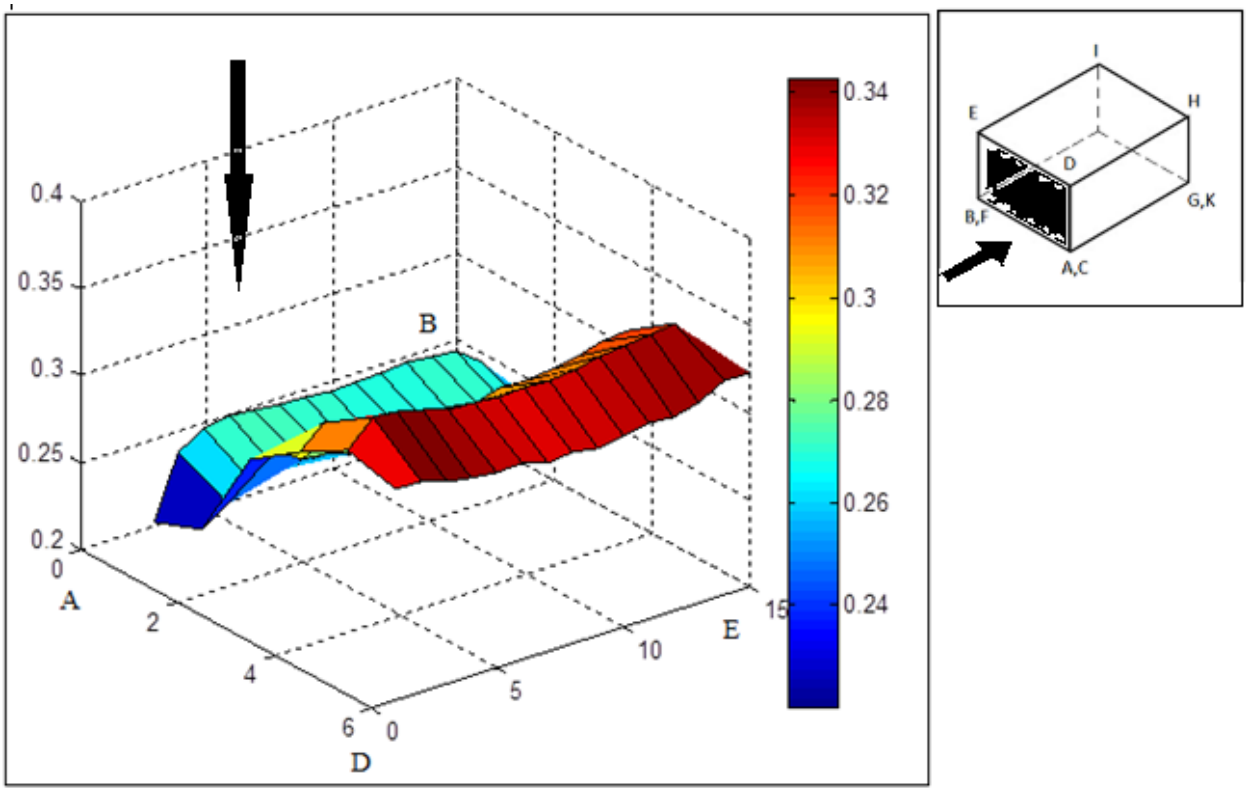

Figure 3.56 : Stdev values for Shorter wall for α = 0

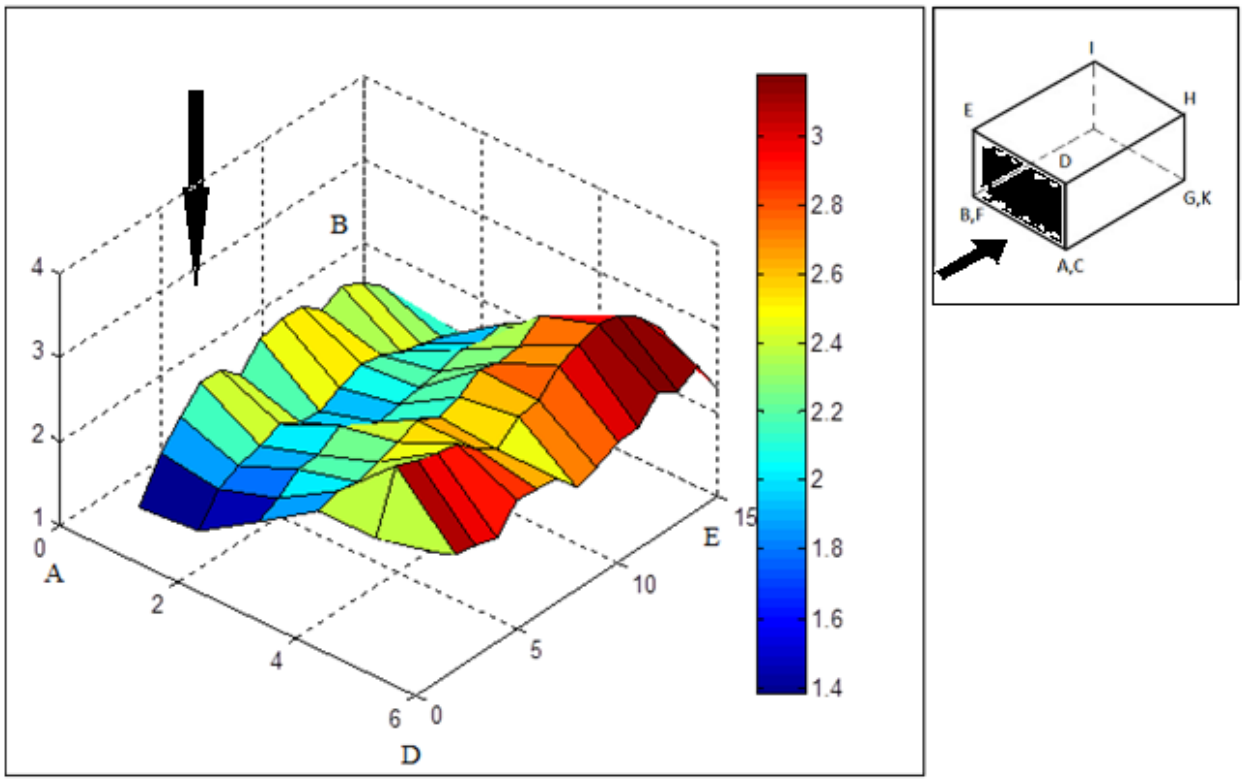

Figure 3.57 : Peak values for Shorter wall for α = 0

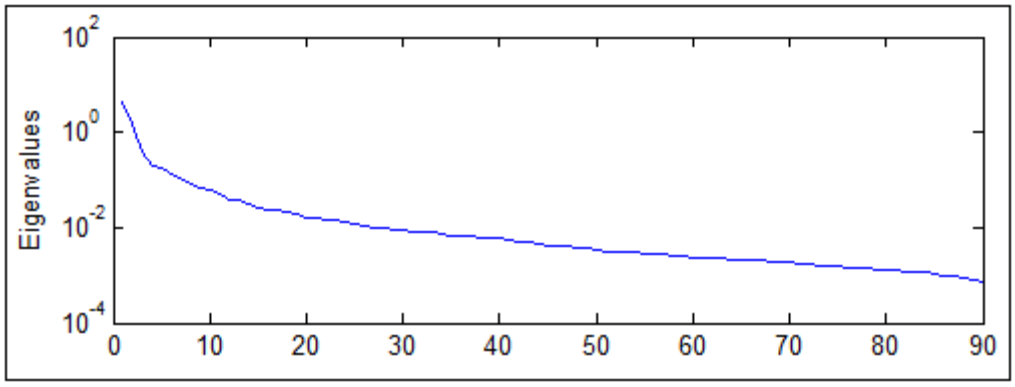

Figure 3.58 : Eigenvalues for Shorter wall for $\alpha = 0$

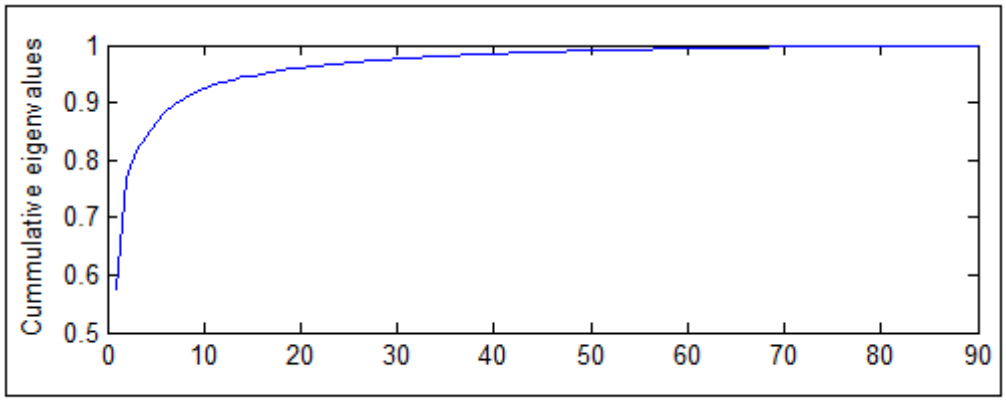

Figure 3.59 : Cumulative Eigenvalues for Shorter wall for $\alpha = 0$

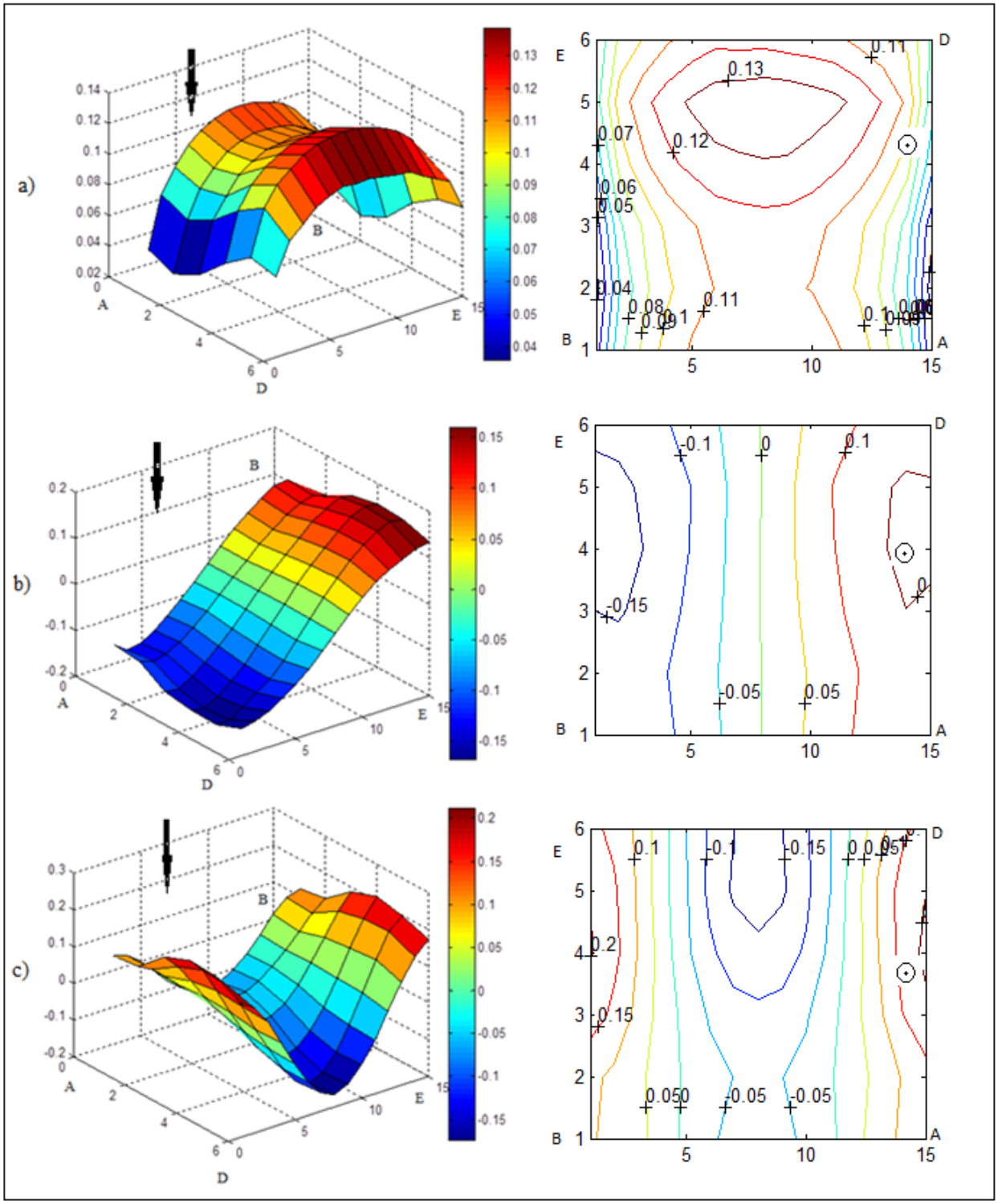

Figure 3.60 : 1st, 2nd and 3rd eigenvectors for Shorter wall for $\alpha = 0$

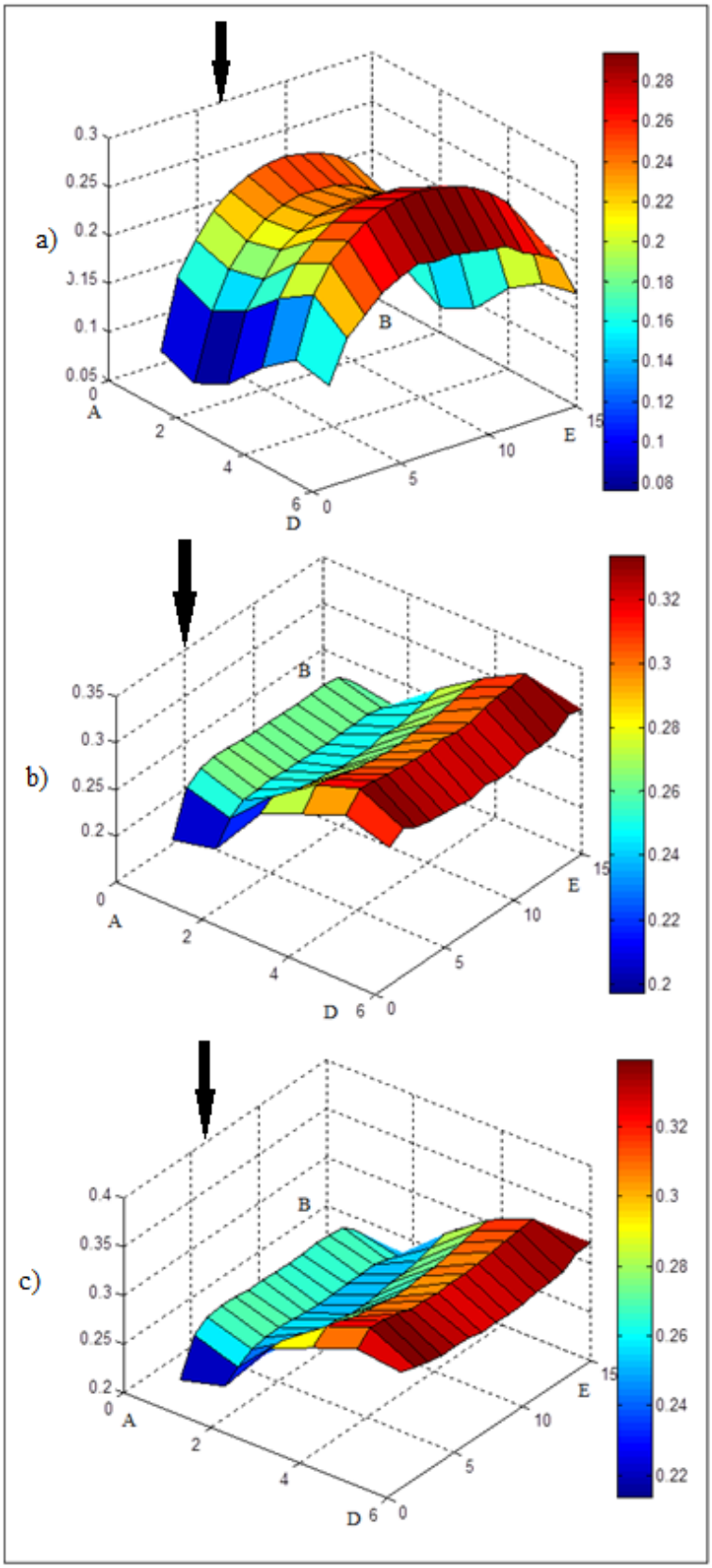

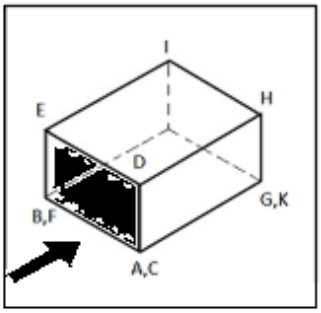

Figure 3.61 : Standard deviation of contributions (1, 10, 30) for $\alpha = 0$
a) 1st; b) First 10; c) First 30

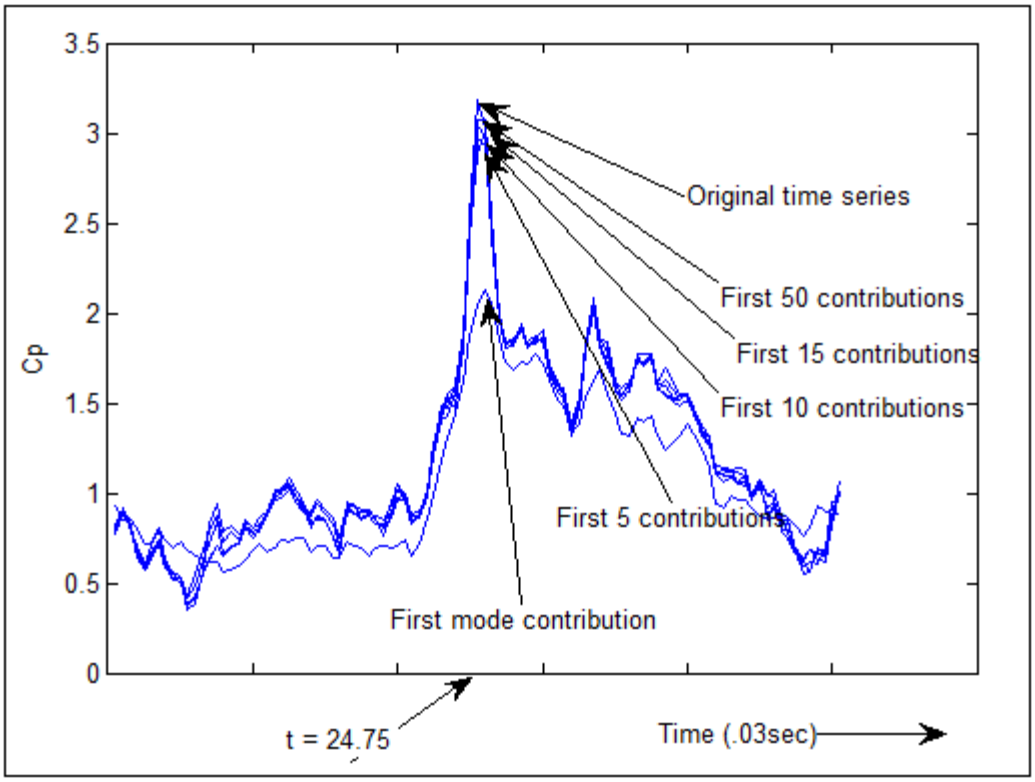

Figure 3.62 : Convergence of time series at position of maximum pressure for $\alpha = 0$

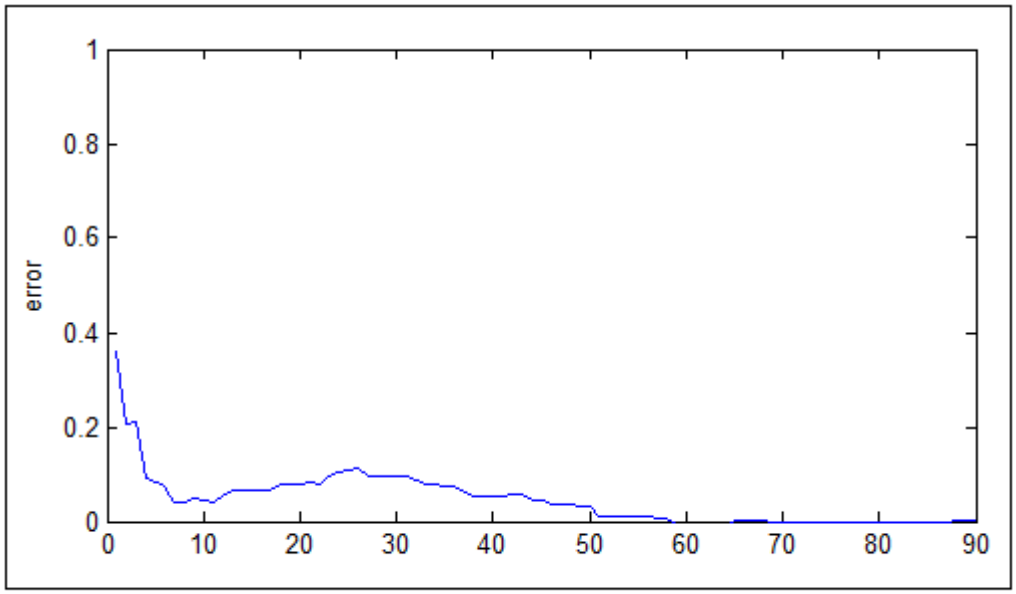

Figure 3.63 : Error at position of maximum pressure changing with contribution for $\alpha = 0$

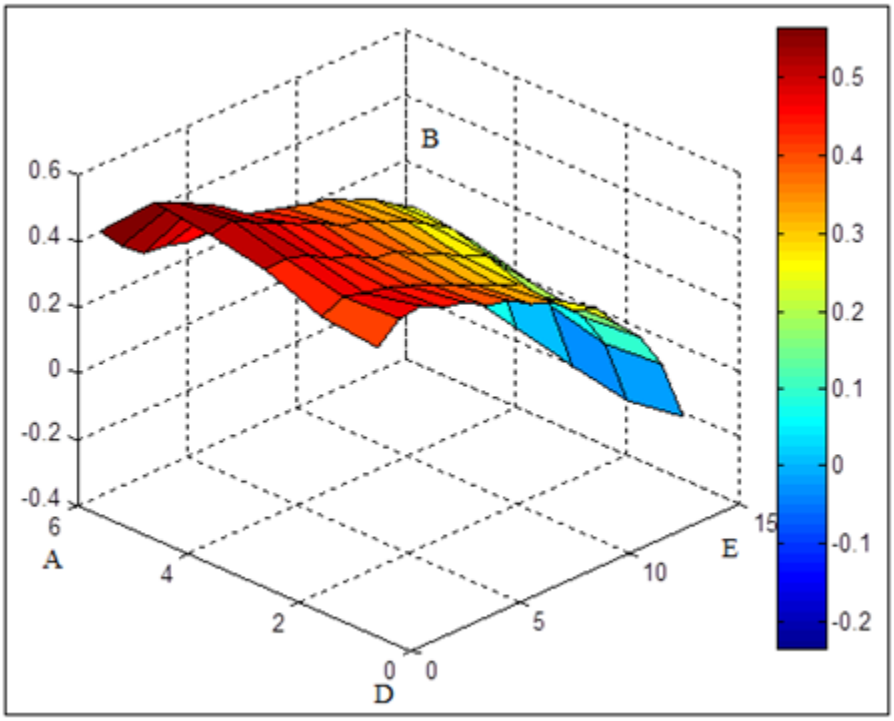

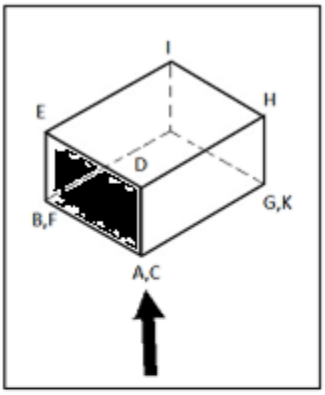

Figure 3.64 : Avg values for Shorter wall for $\alpha = 45$

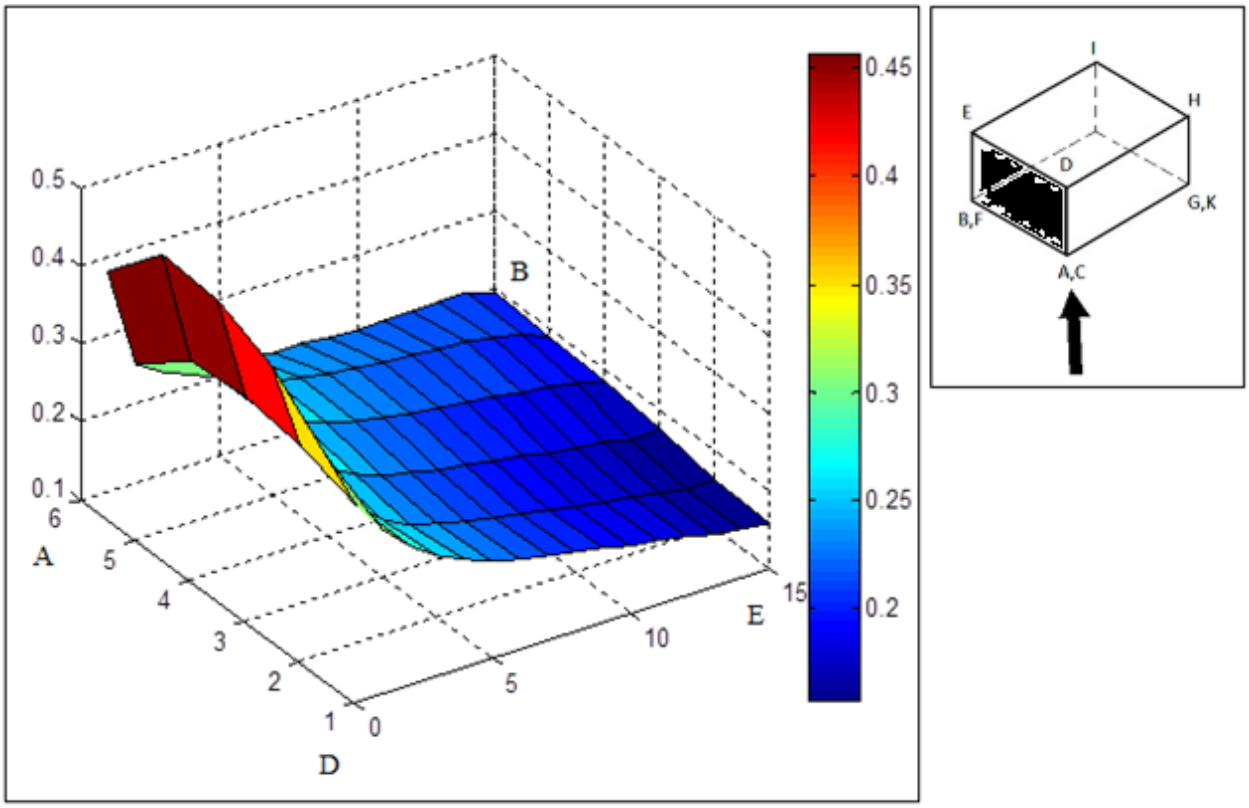

Figure 3.65 : Stdev values for Shorter wall for α = 45

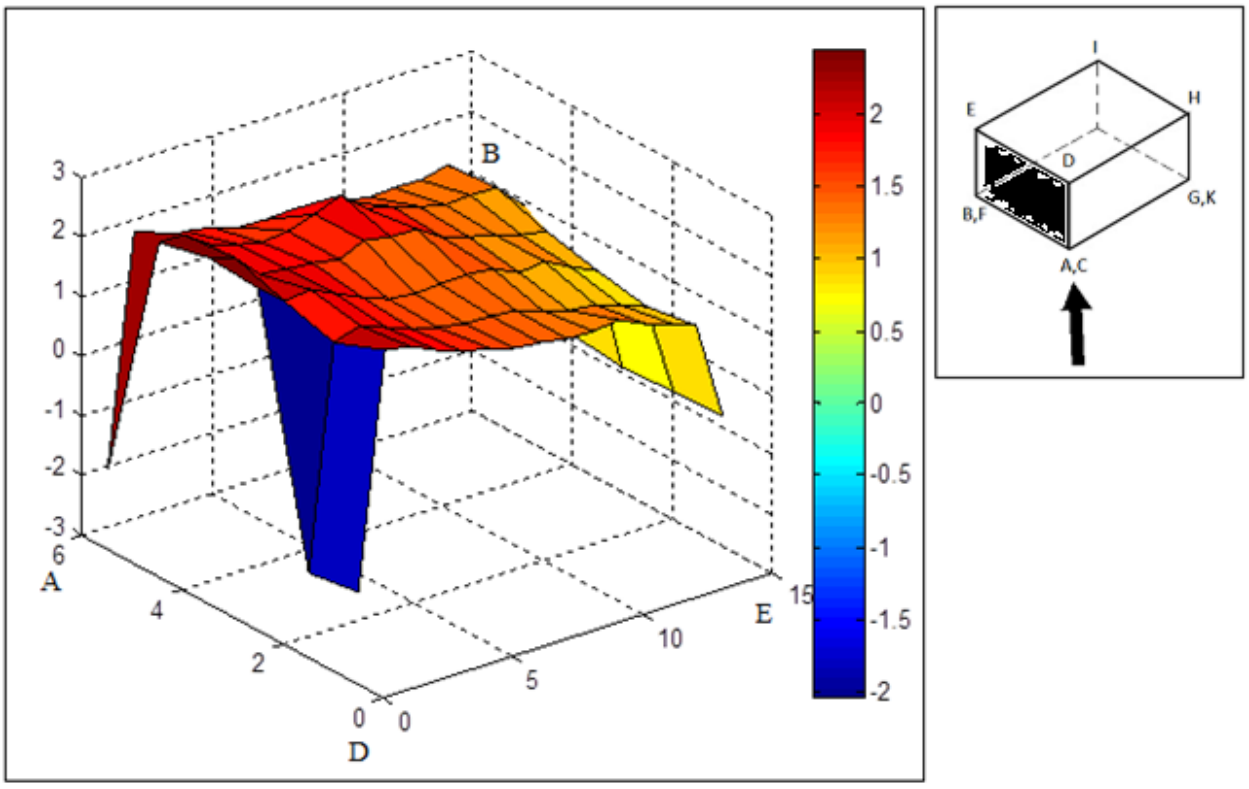

Figure 3.66 : Peak values for Shorter wall for α = 45

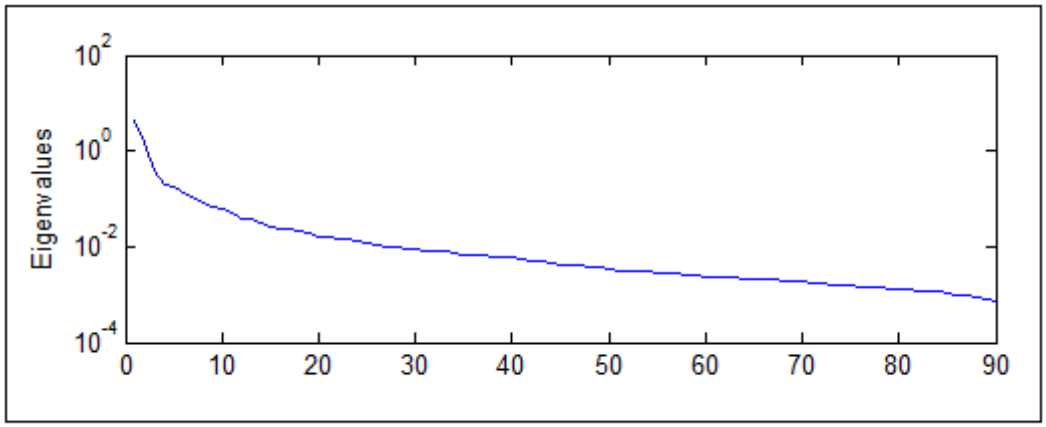

Figure 3.67 : Eigenvalues for Shorter wall for $\alpha = 45$

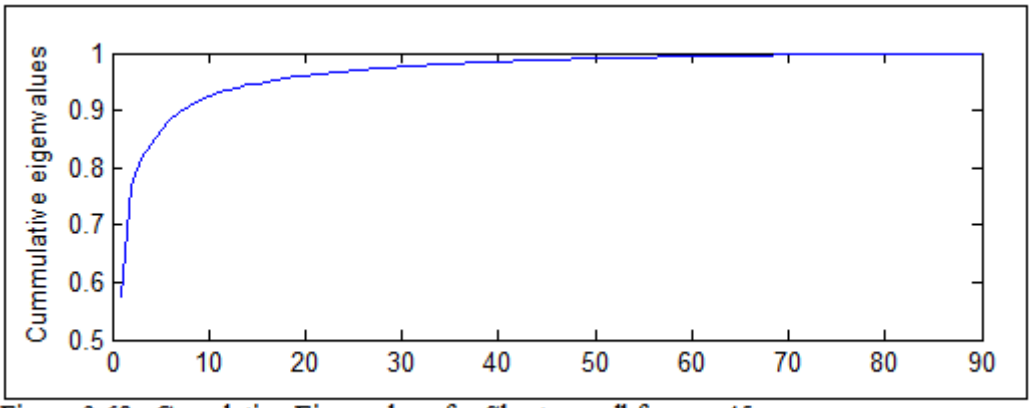

Figure 3.68 : Cumulative Eigenvalues for Shorter wall for $\alpha = 45$

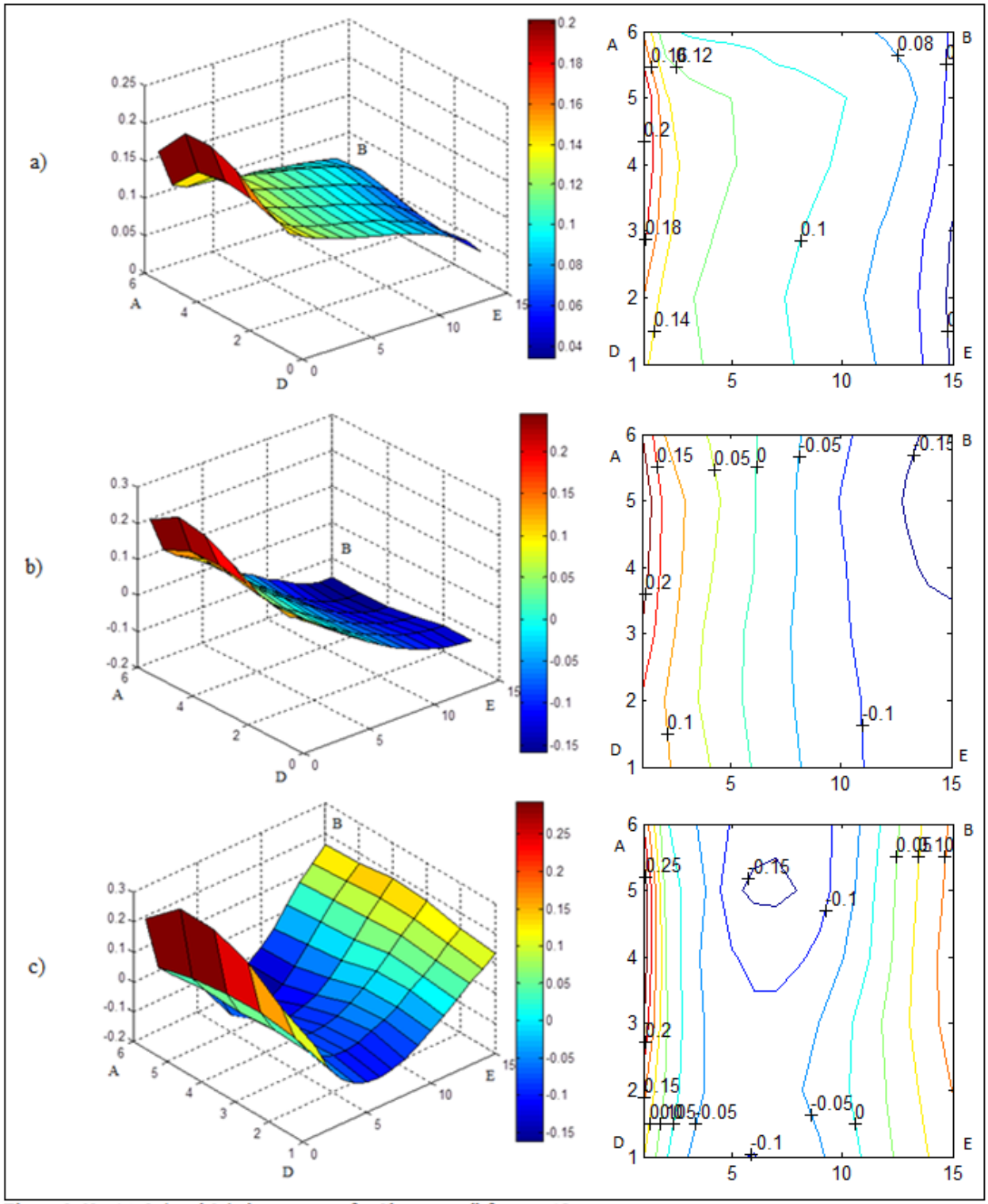

Figure 3.69 : 1st, 2nd and 3rd eigenvectors for Shorter wall for α = 45
a) 1st; b) 2nd; c) 3rd

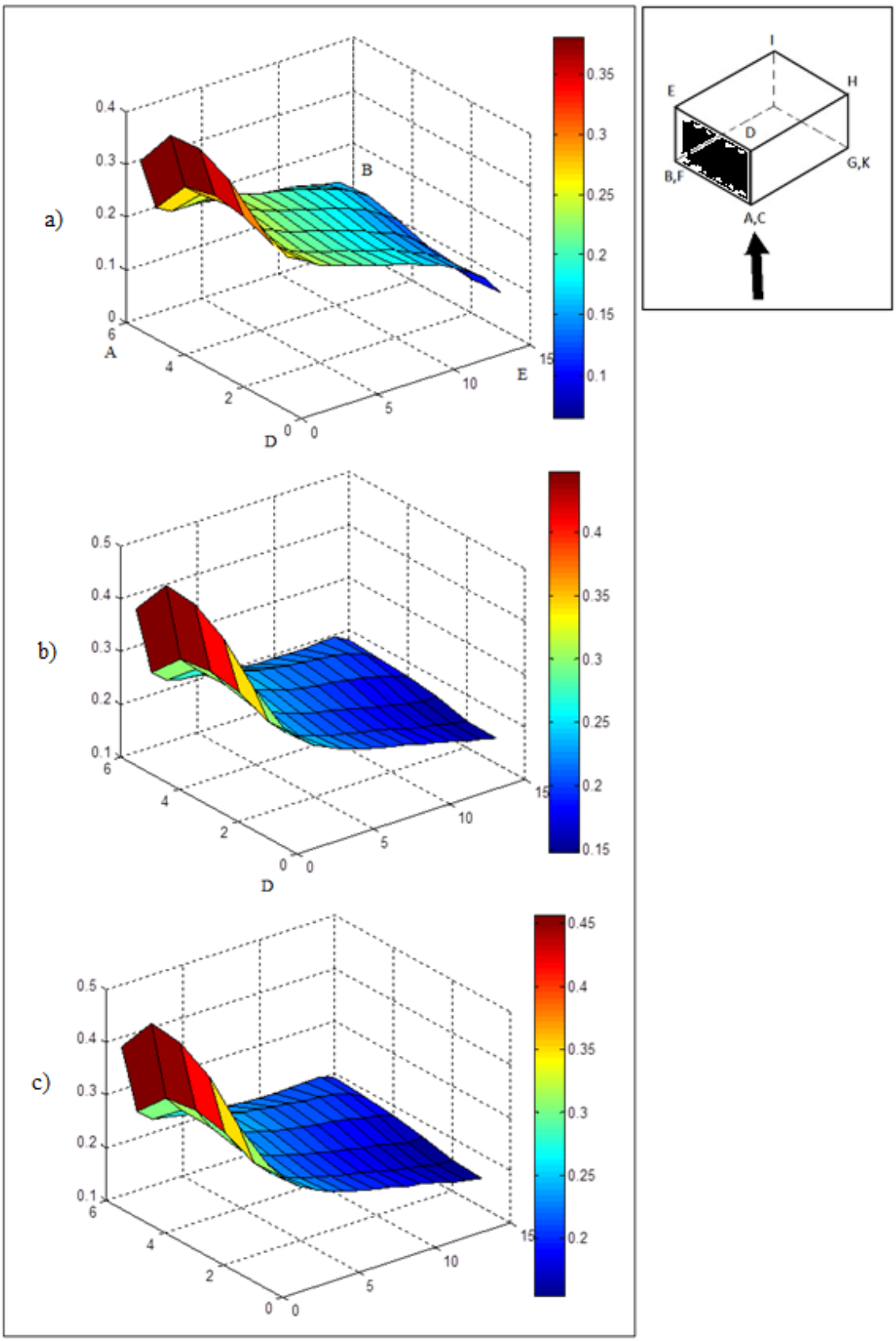

Figure 3.70 : Standard deviation of contributions (1, 10, 30) for α = 45
a) 1st; b) First 10; c) First 30

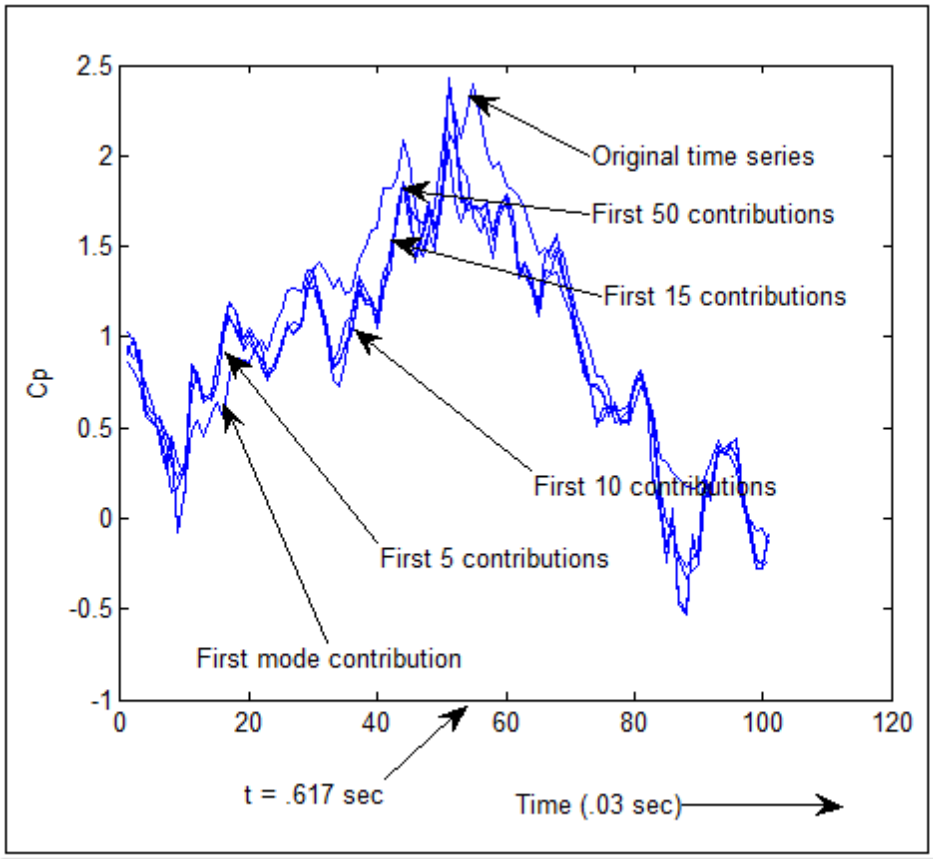

Figure 3.71 : Convergence of time series at position of maximum pressure for $\alpha = 45$

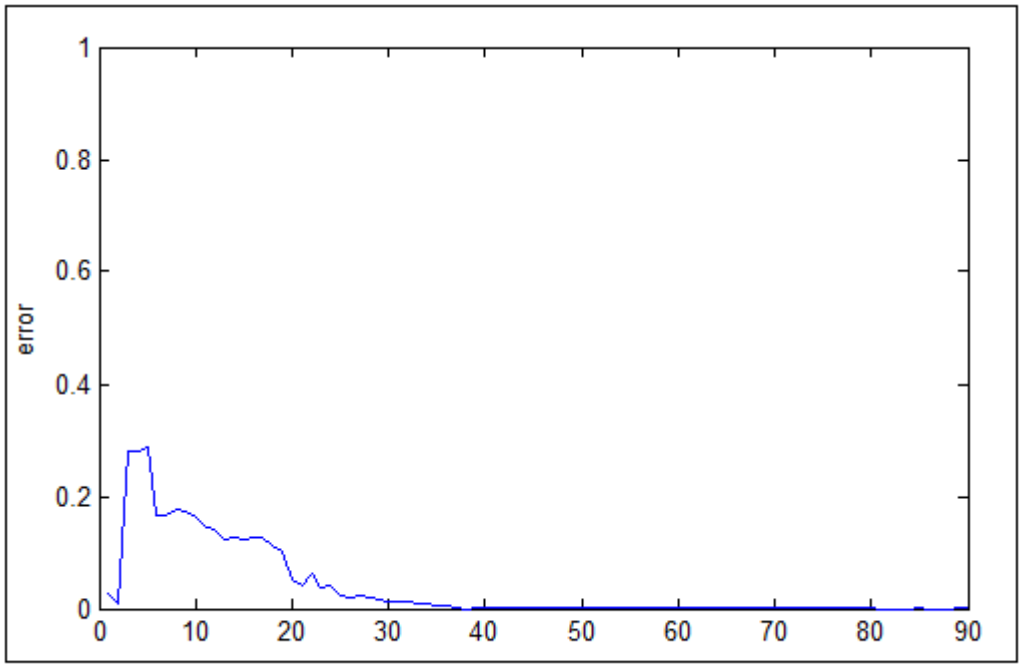

Figure 3.72 : Error at position of maximum pressure changing with contribution for $\alpha = 45$

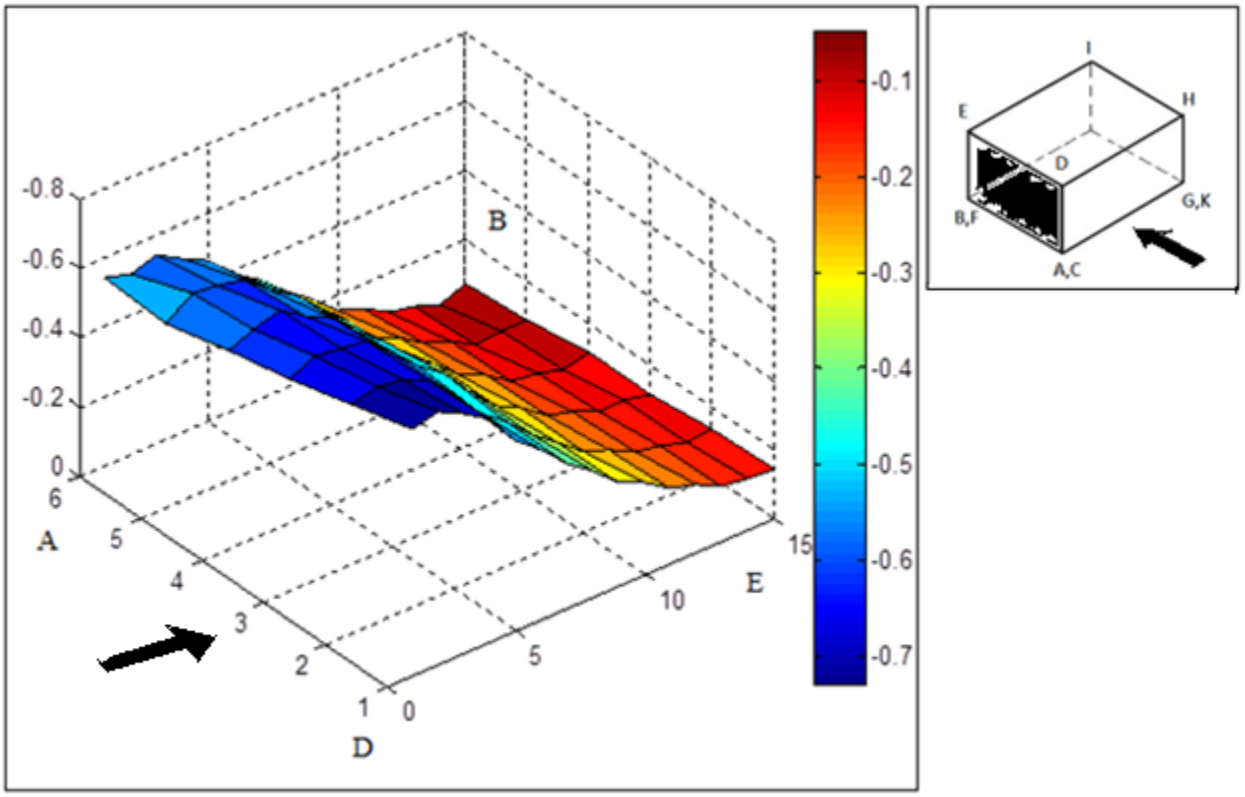

Figure 3.73 : Avg values for Shorter wall for α = 90

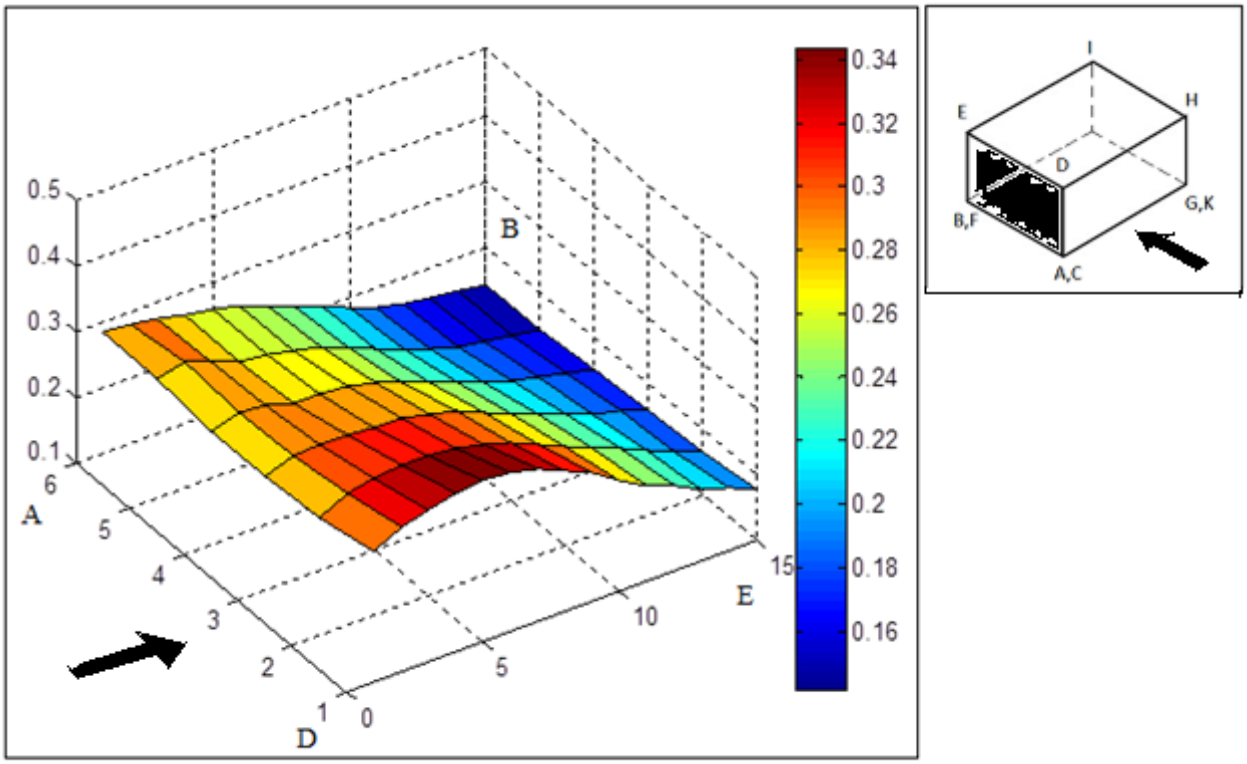

Figure 3.74 : Stdev values for Shorter wall for α = 90

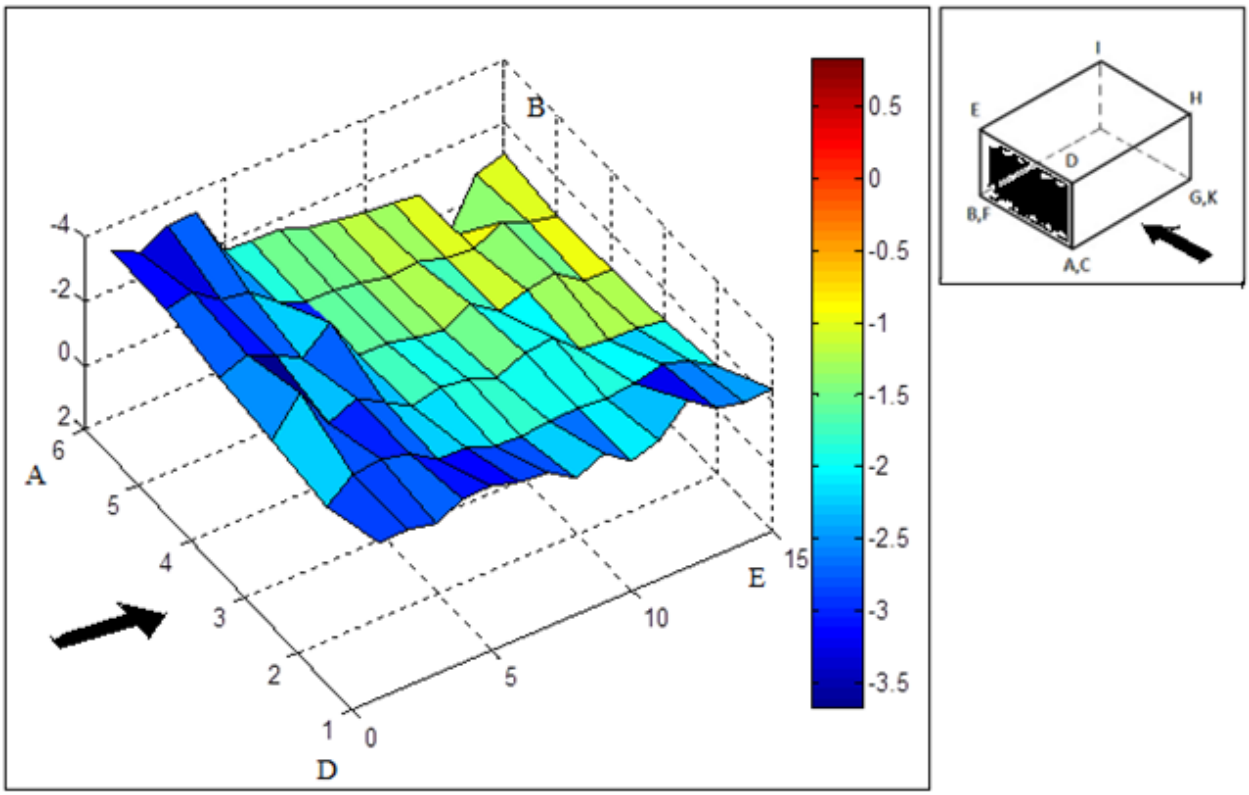

Figure 3.75 : Peak values for Shorter wall for α = 90

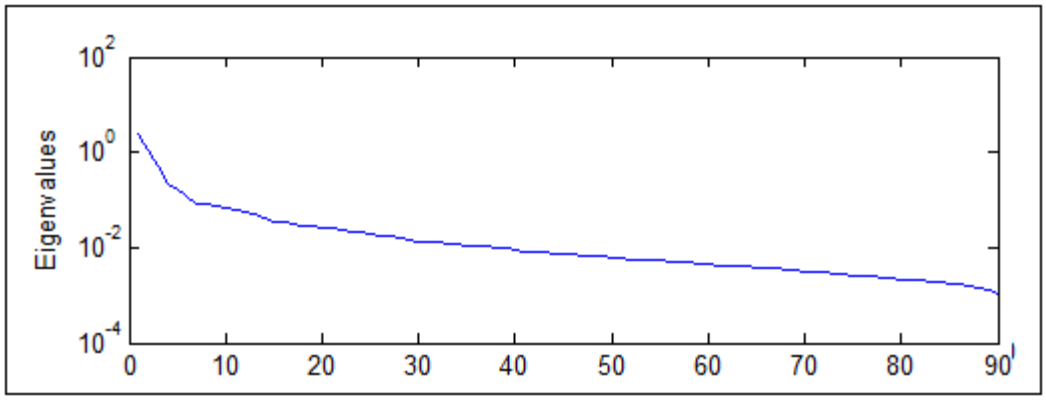

Figure 3.76 : Eigenvalues for Shorter wall for $\alpha = 90$

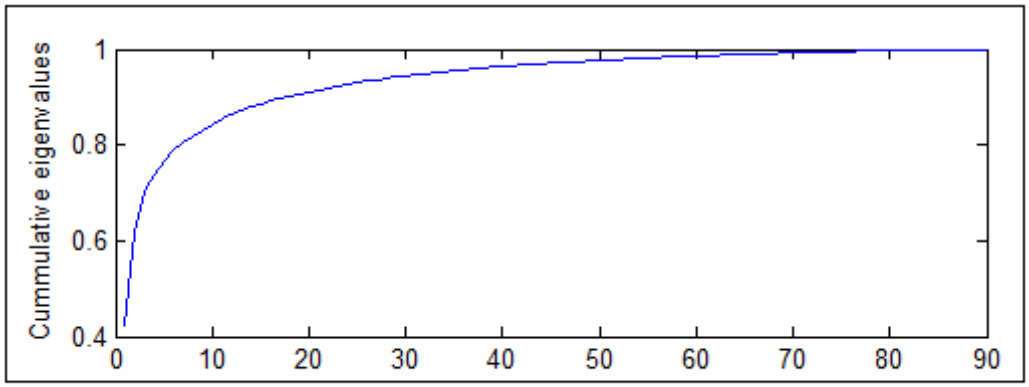

Figure 3.77 : Cumulative Eigenvalues for Shorter wall for $\alpha = 90$

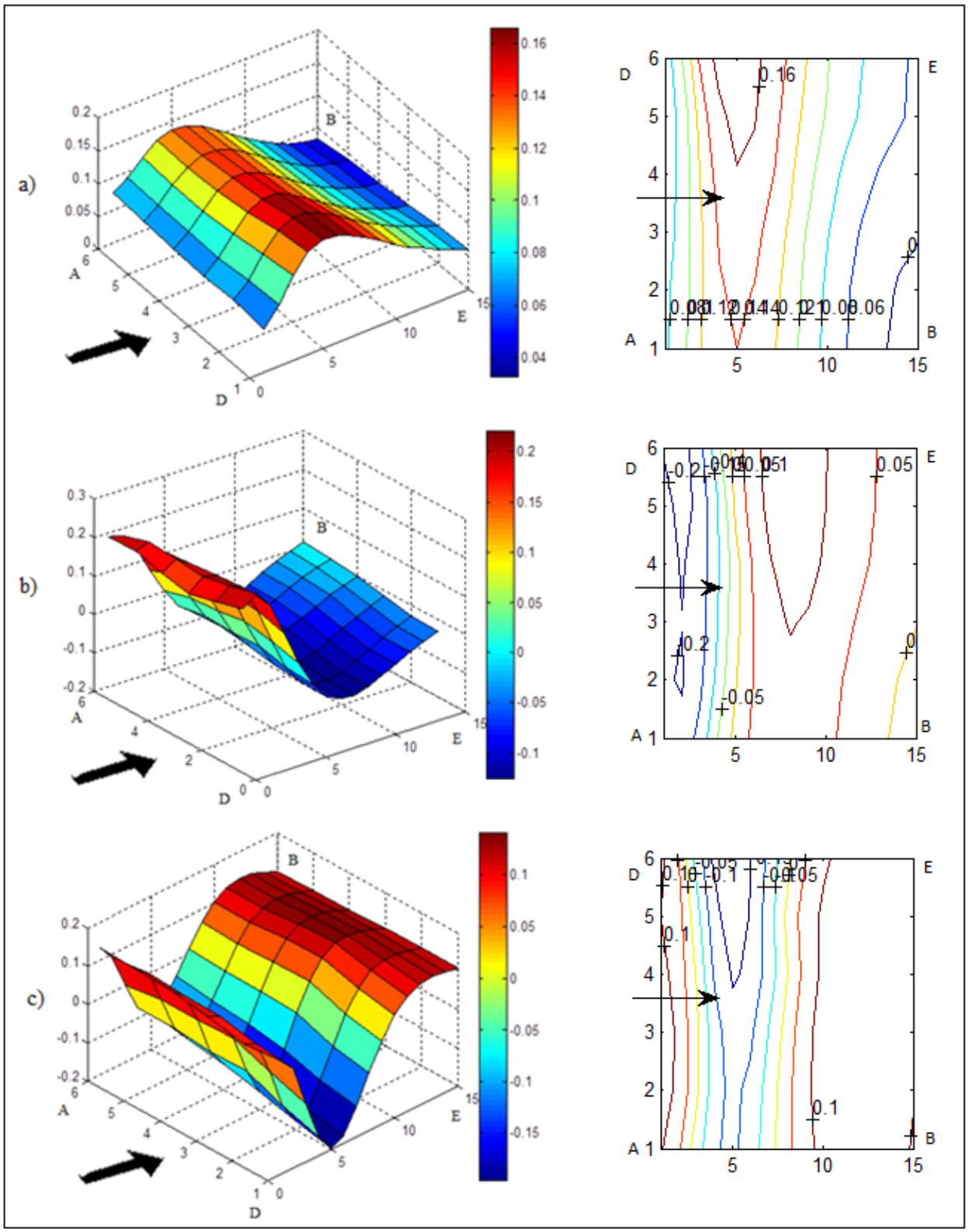

Figure 3.78 : 1st, 2nd and 3rd eigenvectors for Shorter wall for α = 90
a) 1st; b) 2nd; c) 3rd

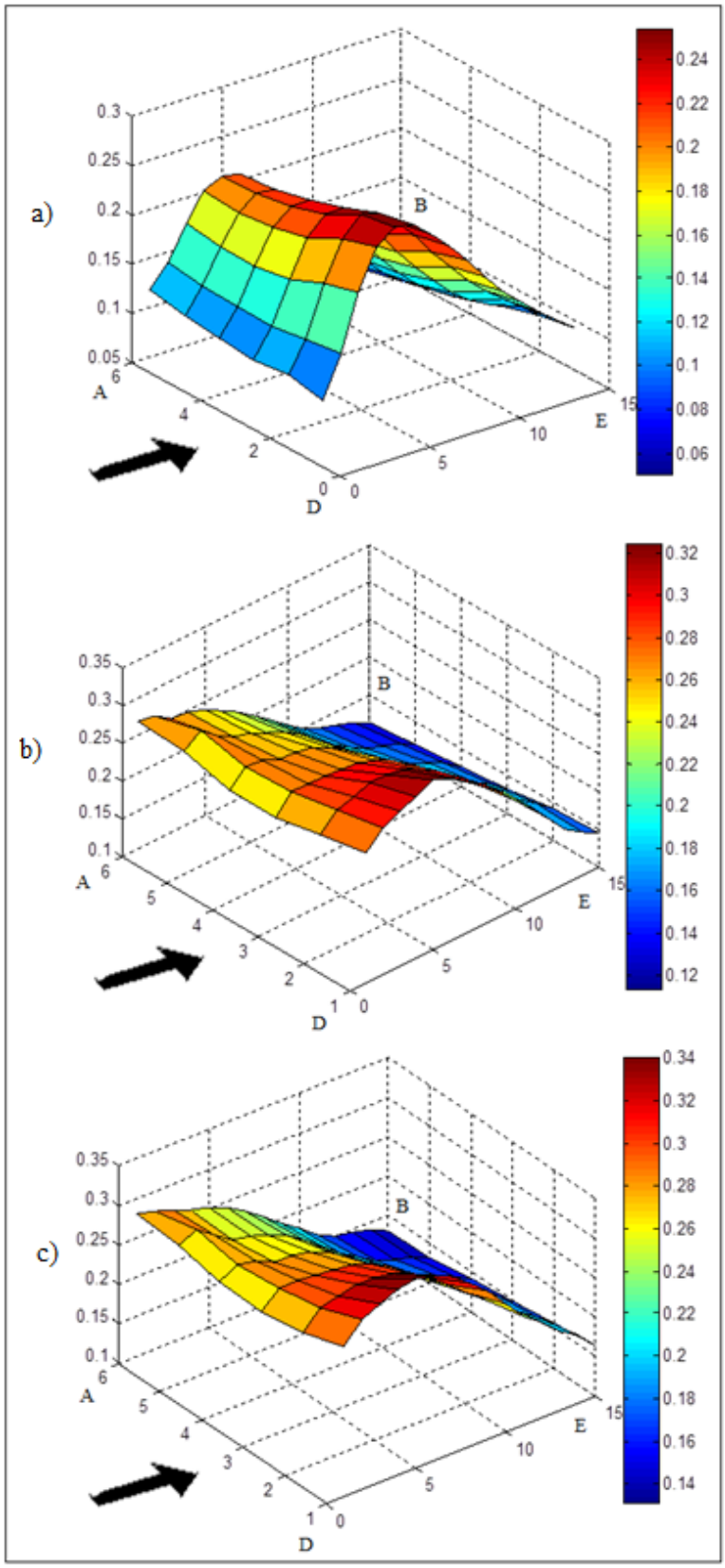

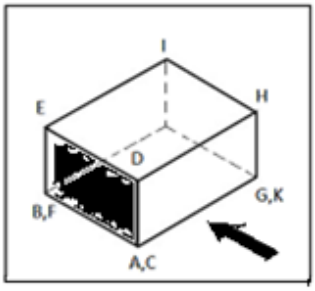

Figure 3.79 : Standard deviation of contributions (1, 10, 30) for α = 90
a) 1st; b) First 10; c) First 30

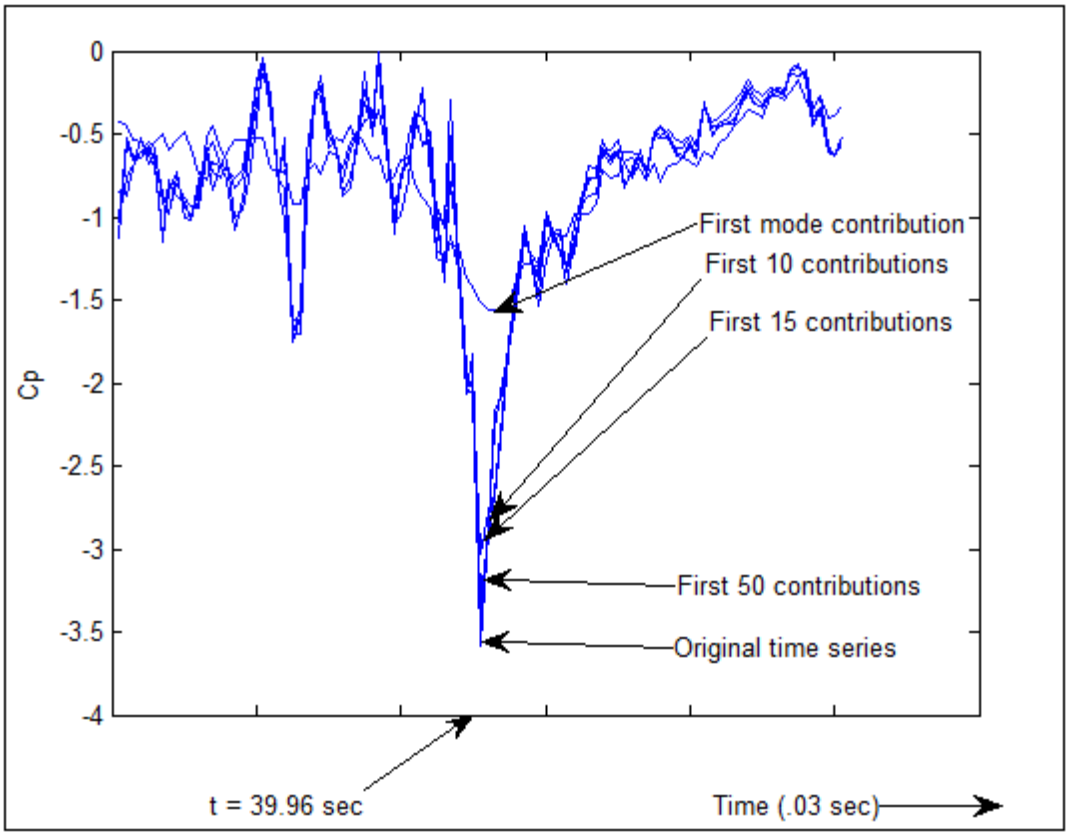

Figure 3.80 : Convergence of time series at position of maximum pressure for $\alpha = 90$

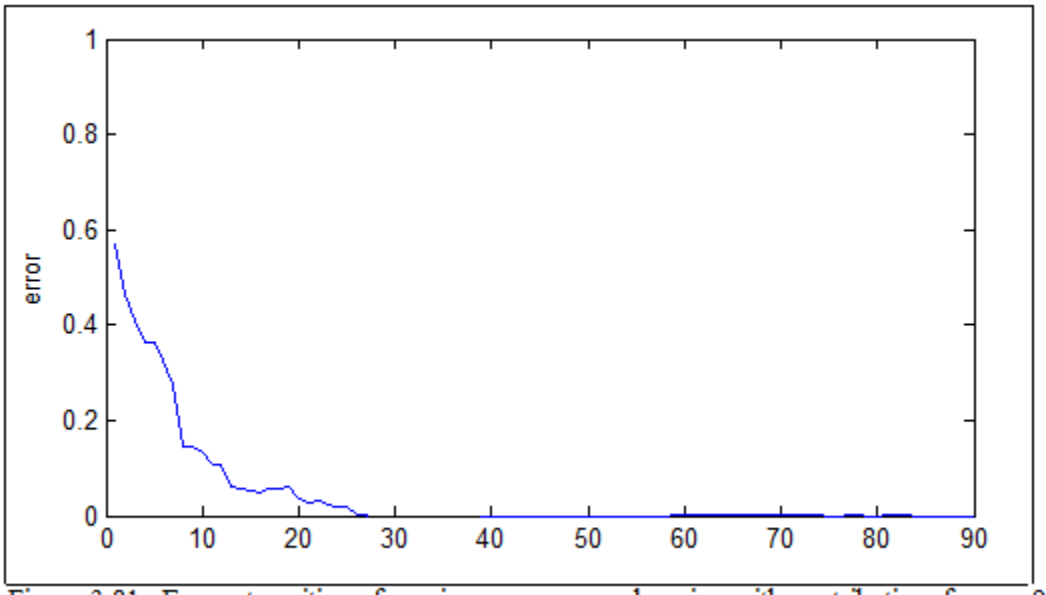

Figure 3.81 : Error at position of maximum pressure changing with contribution for $\alpha = 90$

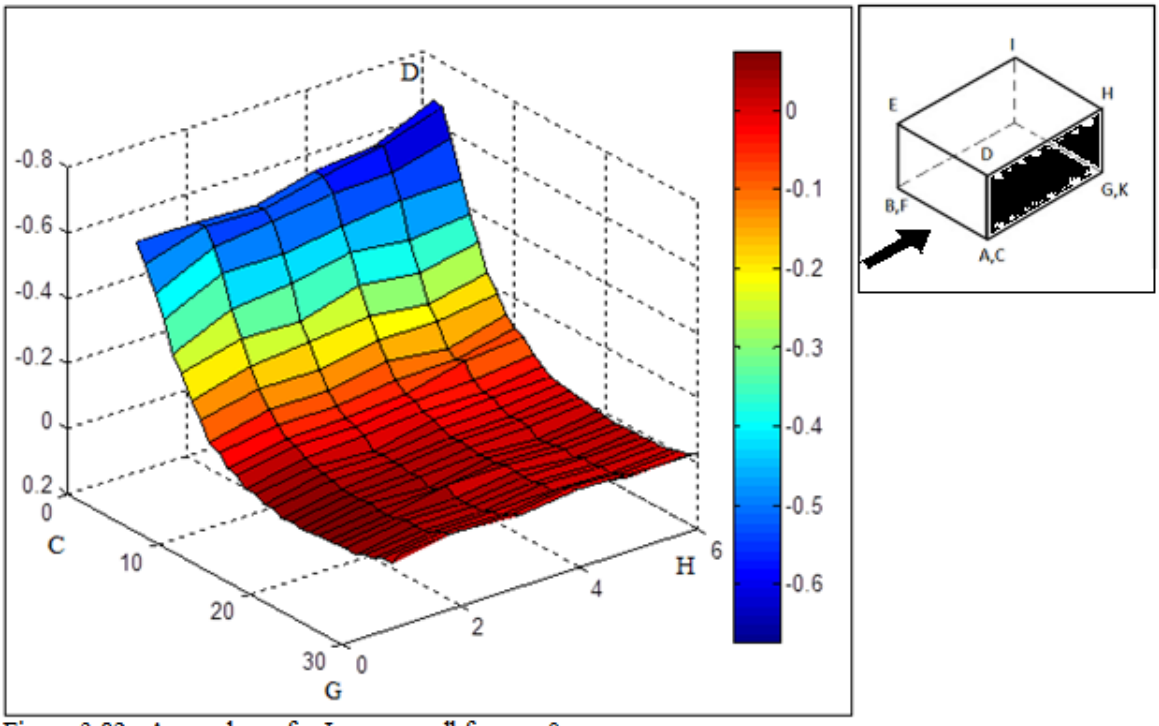

Figure 3.82 : Avg values for Longer wall for $\alpha = 0$

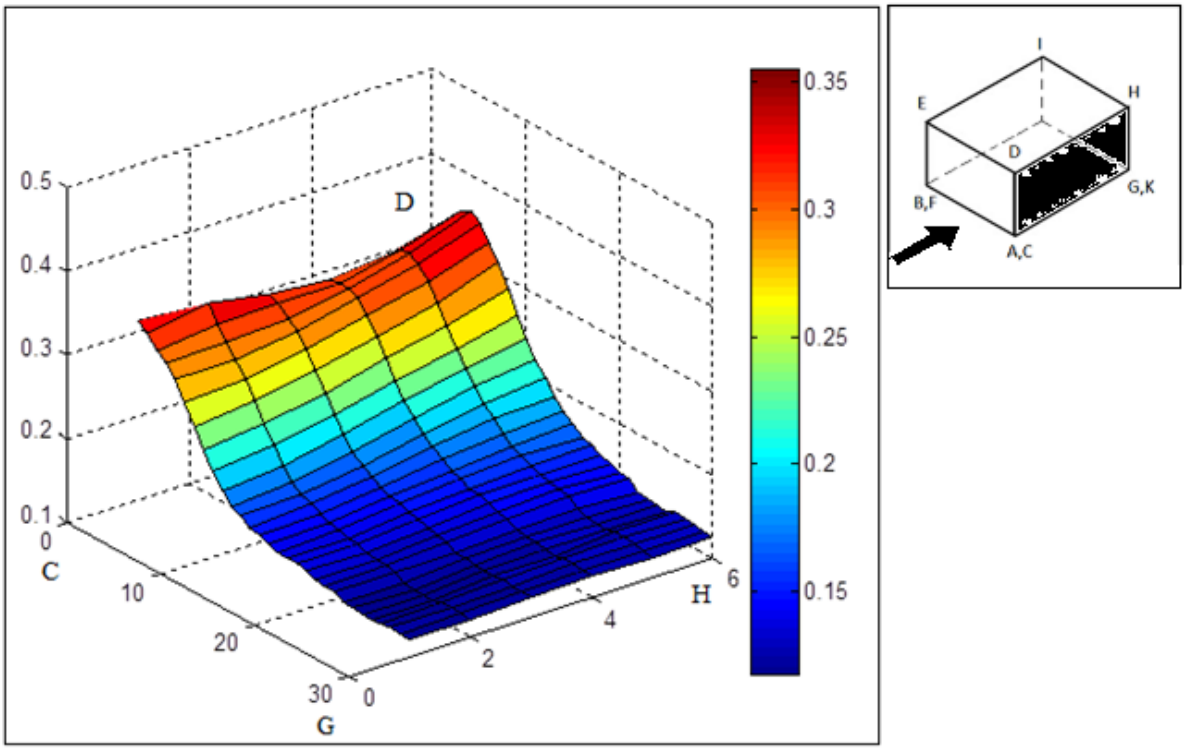

Figure 3.83 : Stdev values for Longer wall for α = 0

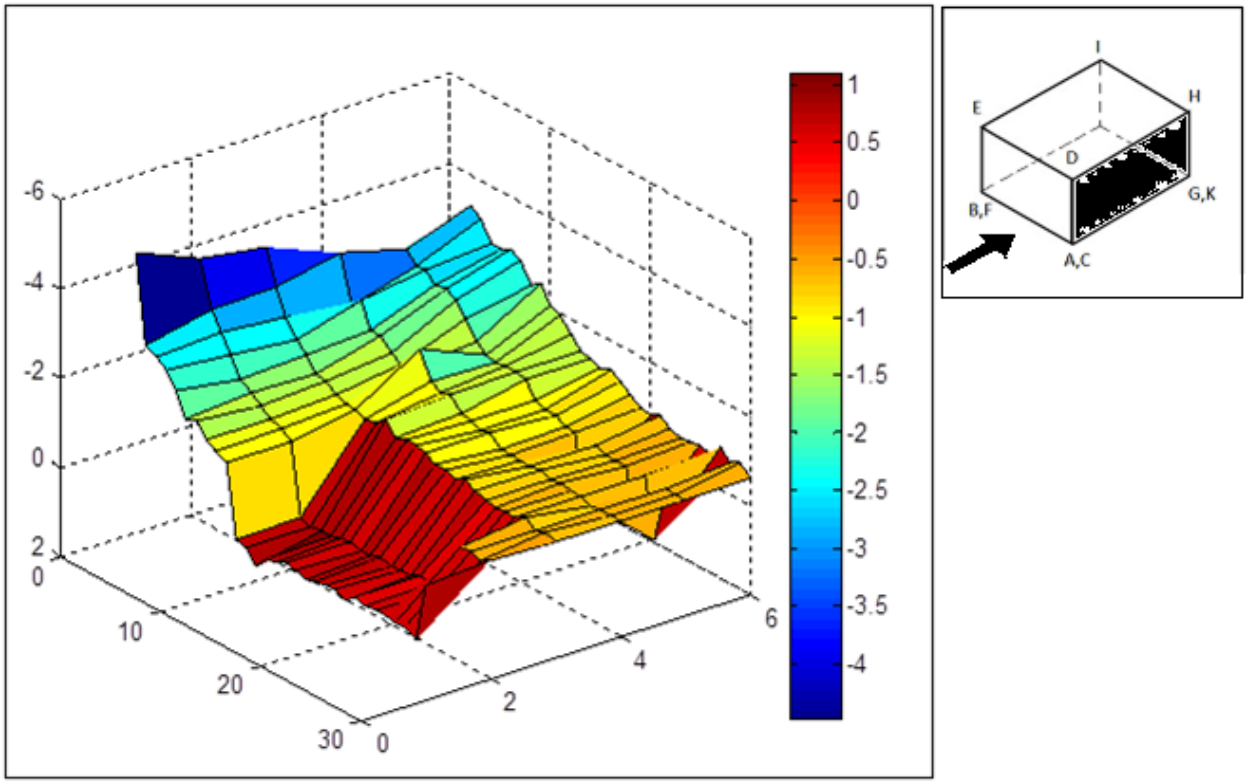

Figure 3.84 : Peak values for Longer wall for α = 0

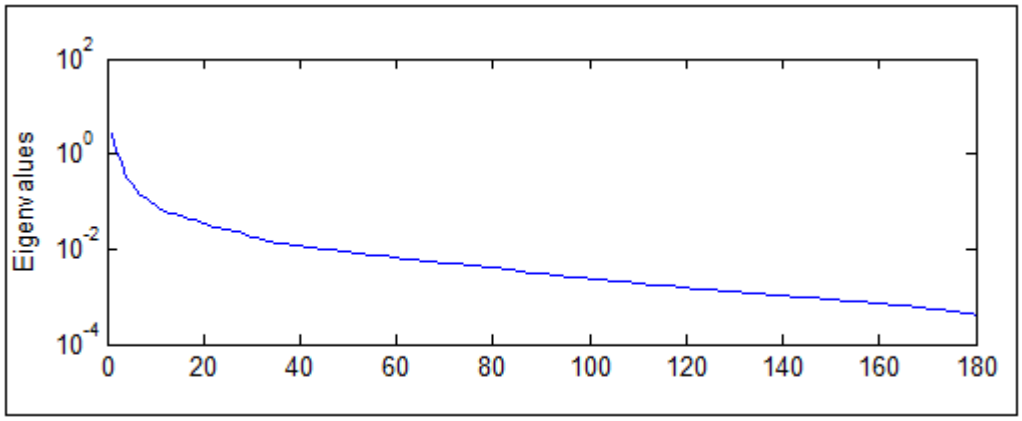

Figure 3.85 : Eigenvalues for Longer wall for $\alpha = 0$

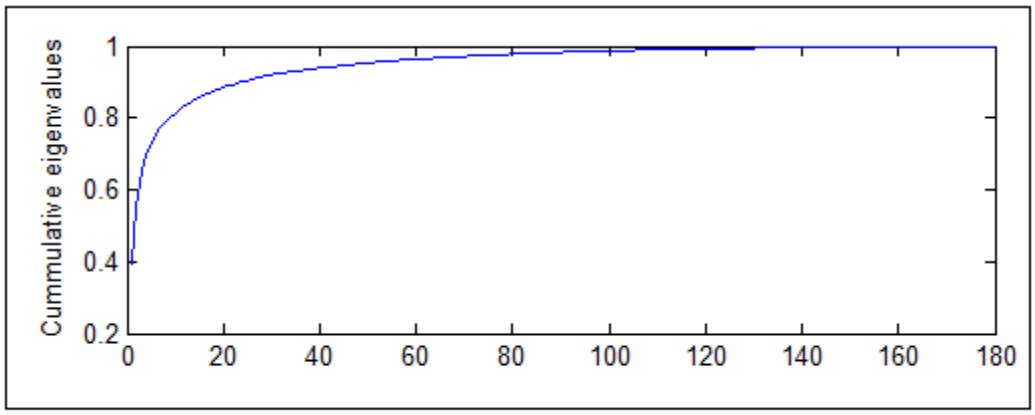

Figure 3.86 : Cumulative eigenvalues for Longer wall for $\alpha = 0$

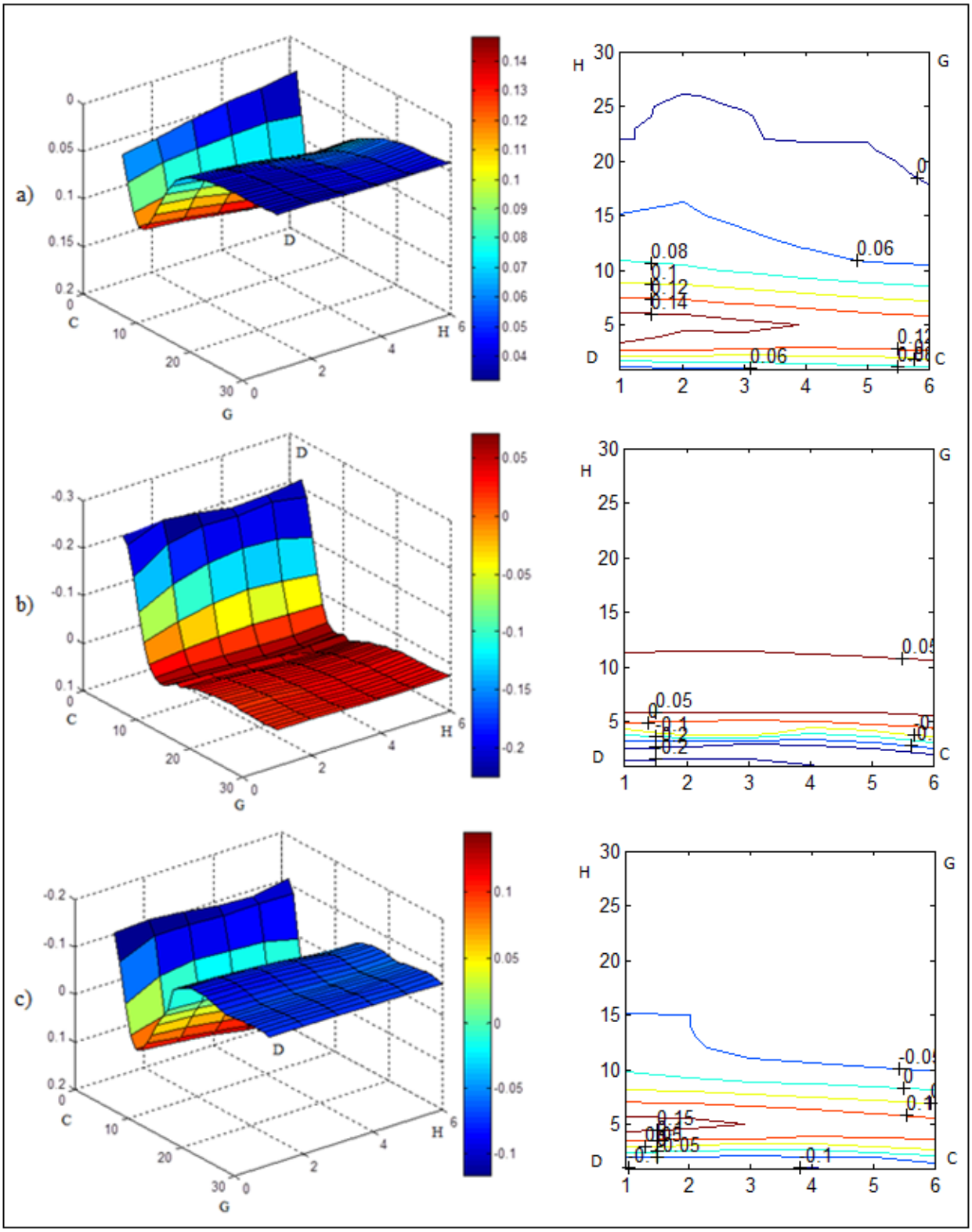

Figure 3.87 : 1st, 2nd and 3rd eigenvectors for Longer wall for $\alpha = 0$
a) 1st; b) 2nd; c) 3rd

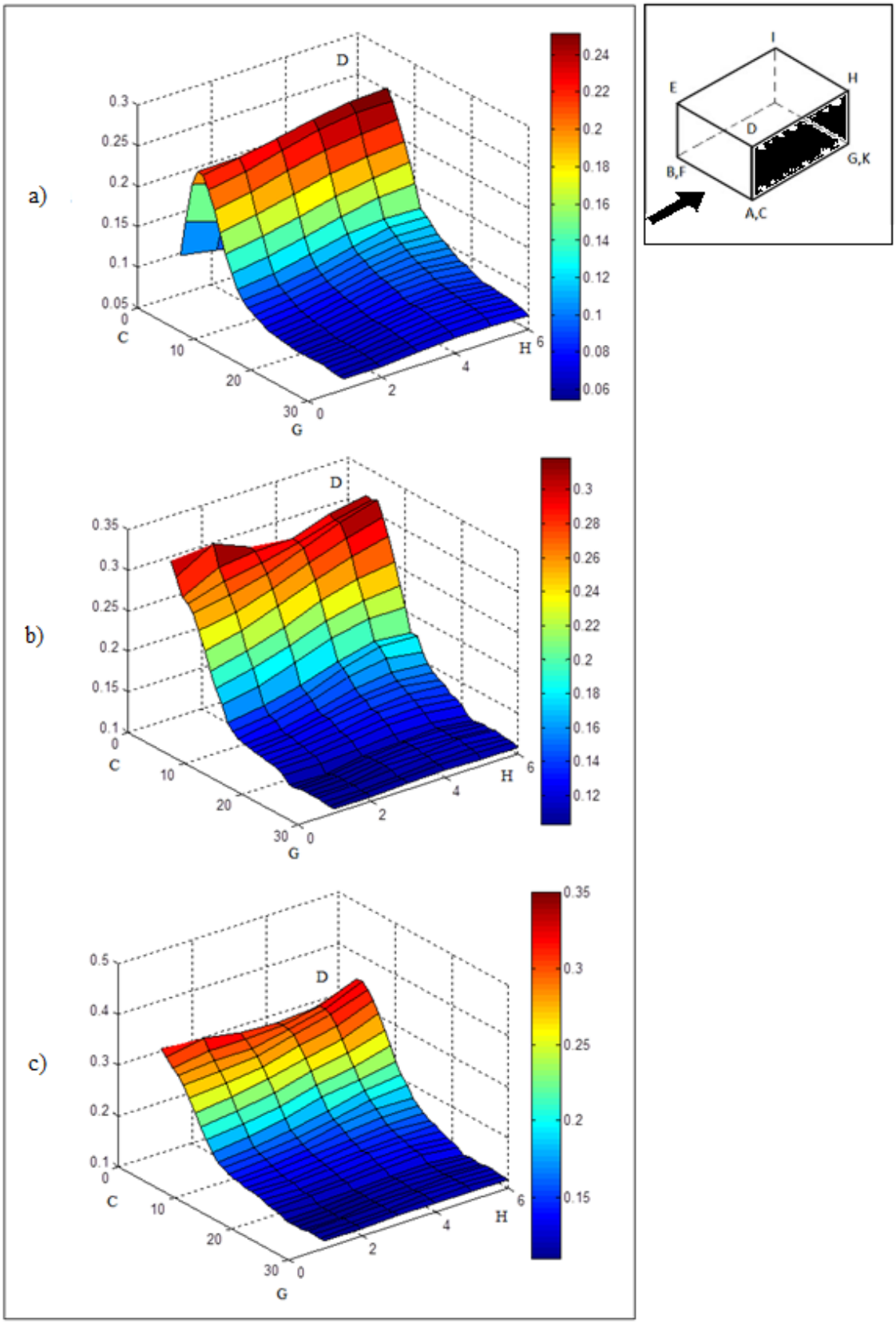

Figure 3.88 : Standard deviation of contributions (1, 10, 30) for $\alpha = 0$
a) 1st; b) 2nd; c) 3rd

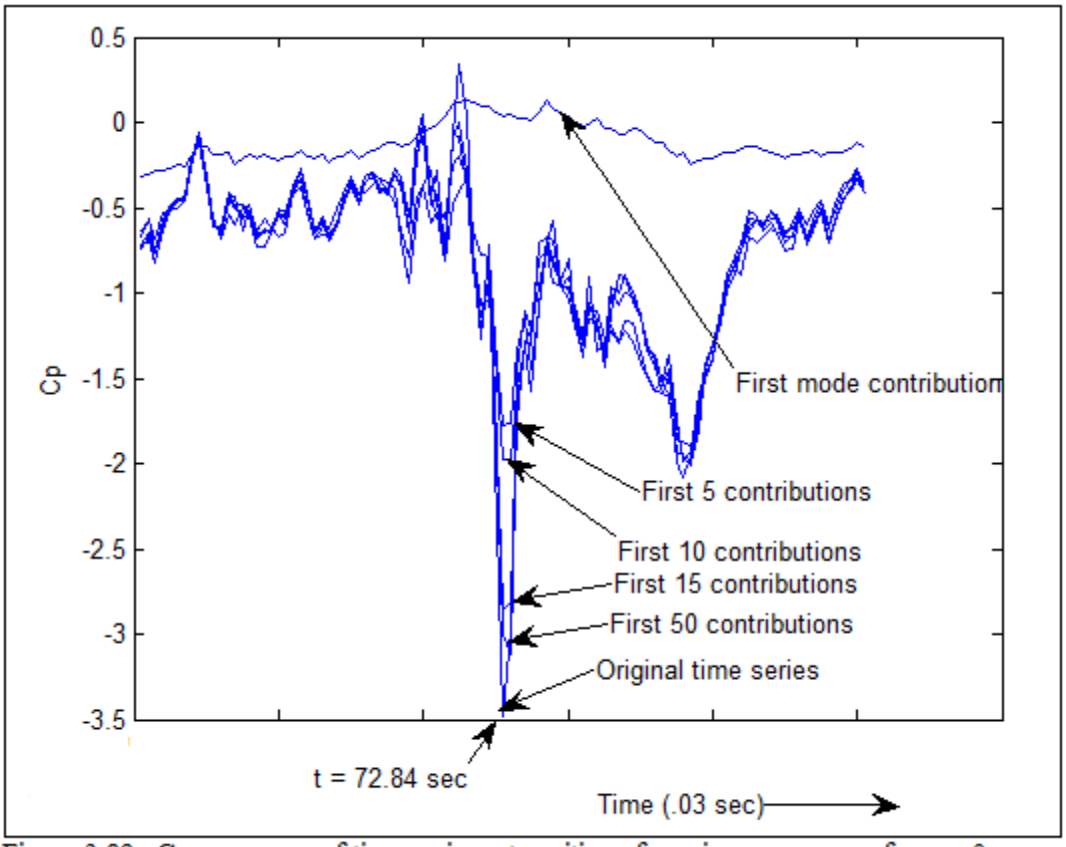

Figure 3.89 : Convergence of time series at position of maximum pressure for $\alpha = 0$

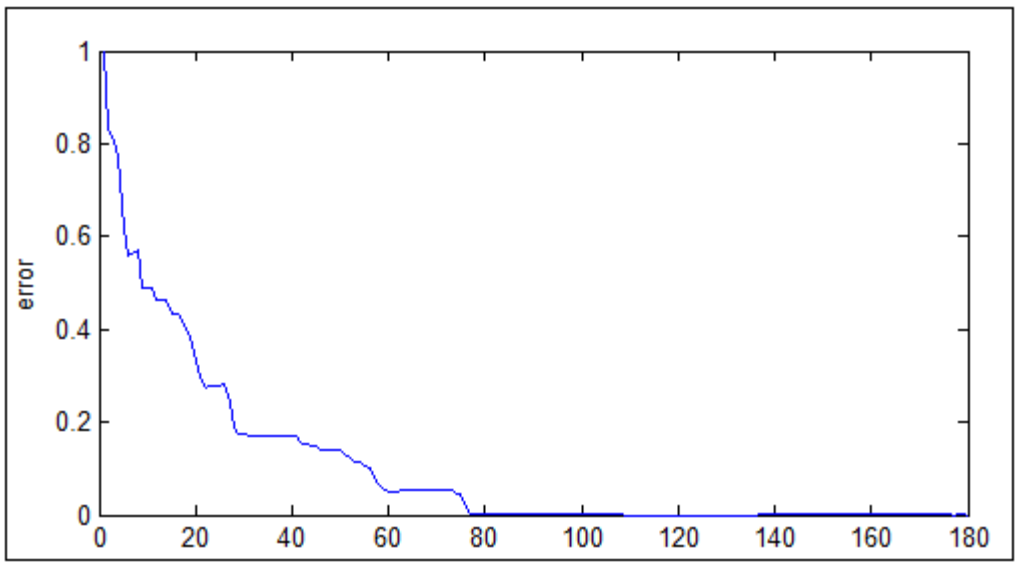

Figure 3.90 : Error at position of maximum pressure changing with contribution for $\alpha = 0$

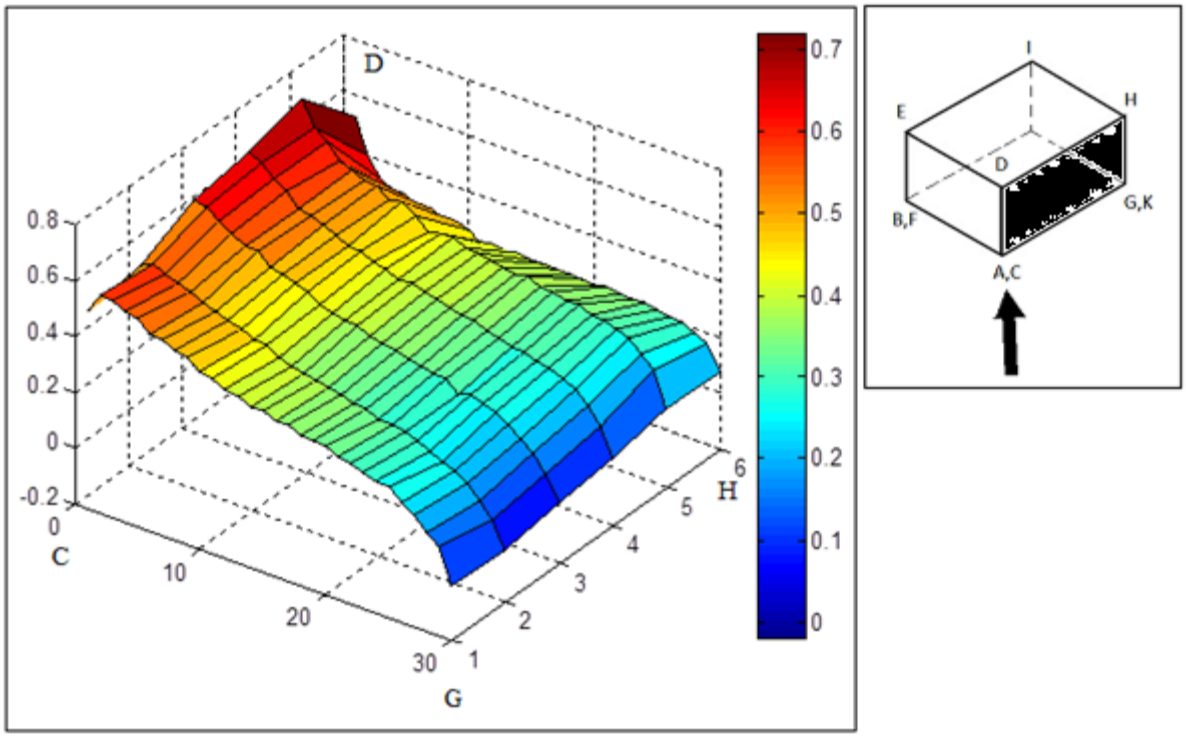

Figure 3.91 : Avg values for Longer wall for $\alpha = 45$

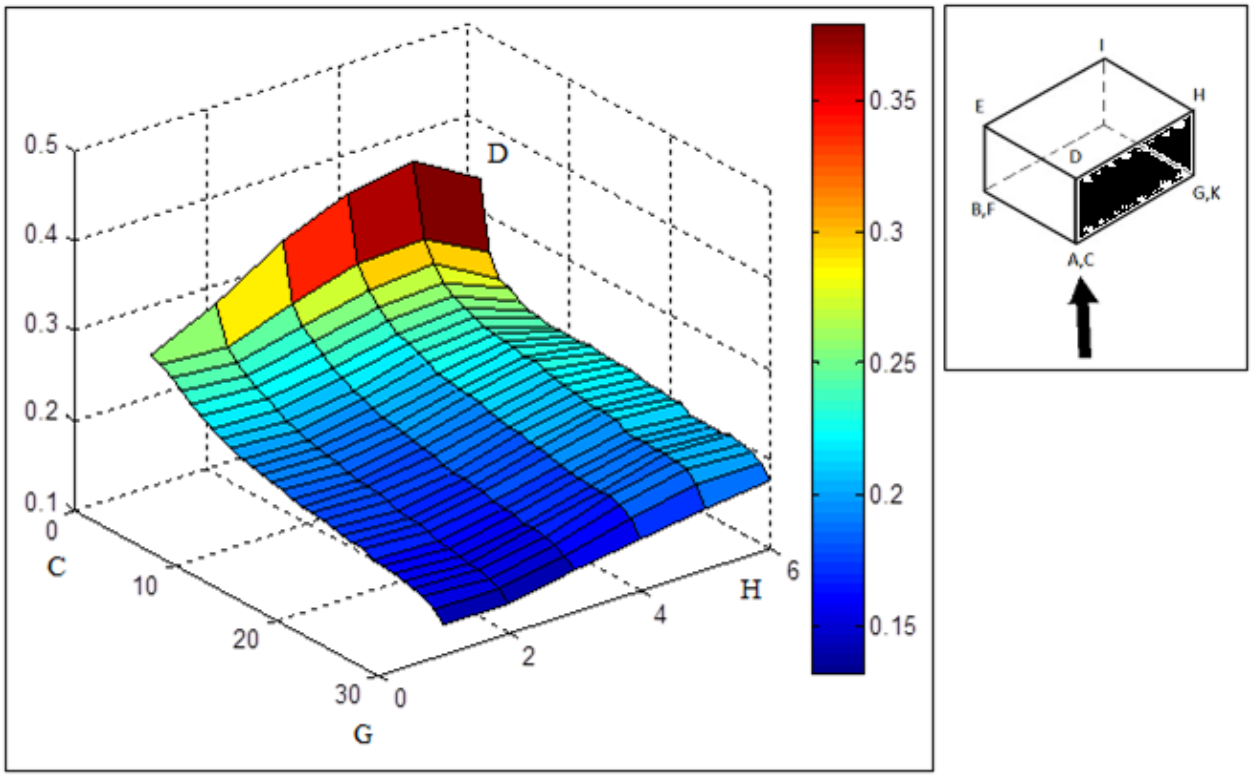

Figure 3.92 : Stdev values for Longer wall for $\alpha = 45$

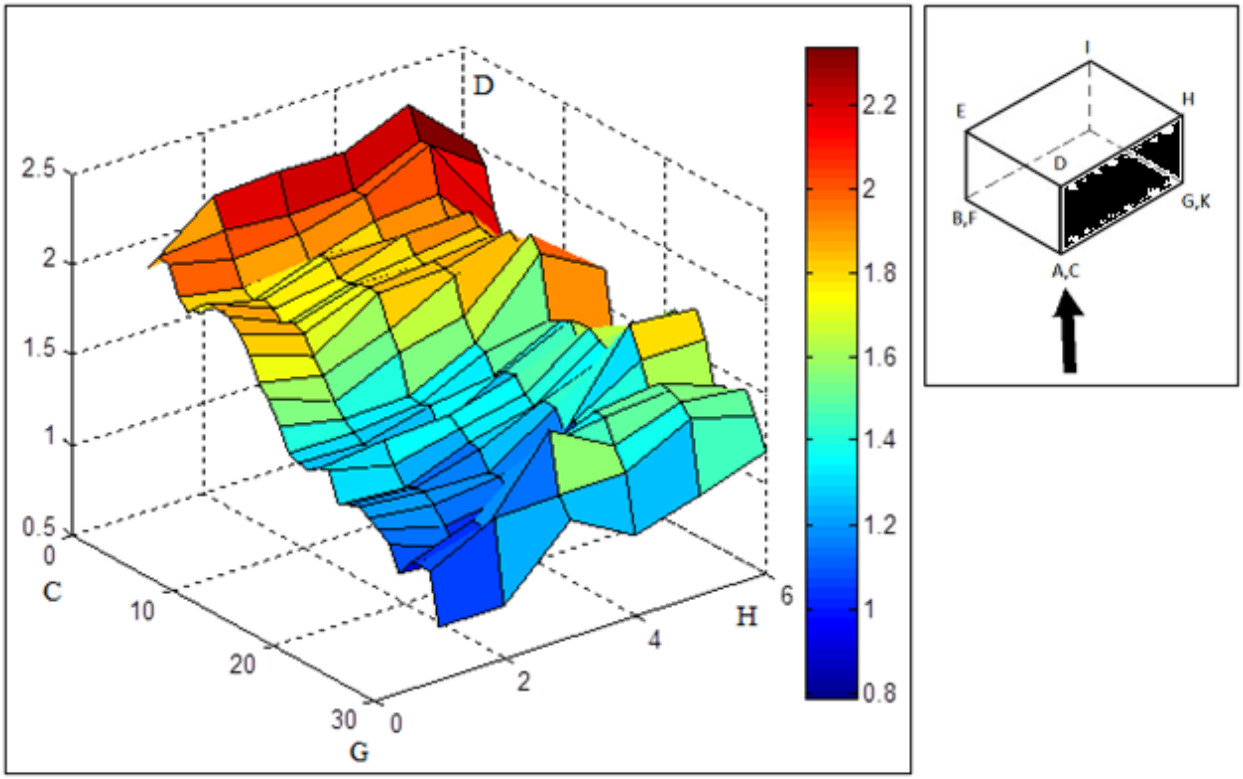

Figure 3.93 : Peak values for Longer wall for $\alpha = 45$

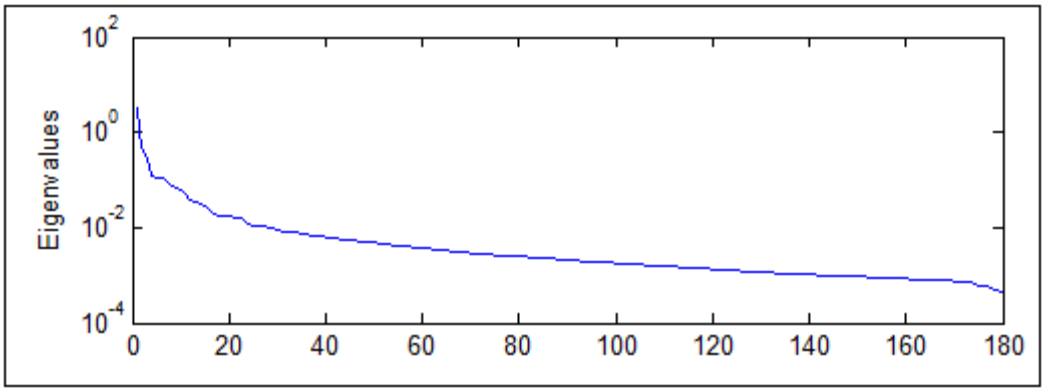

Figure 3.94 : Eigenvalues for Longer wall for $\alpha = 45$

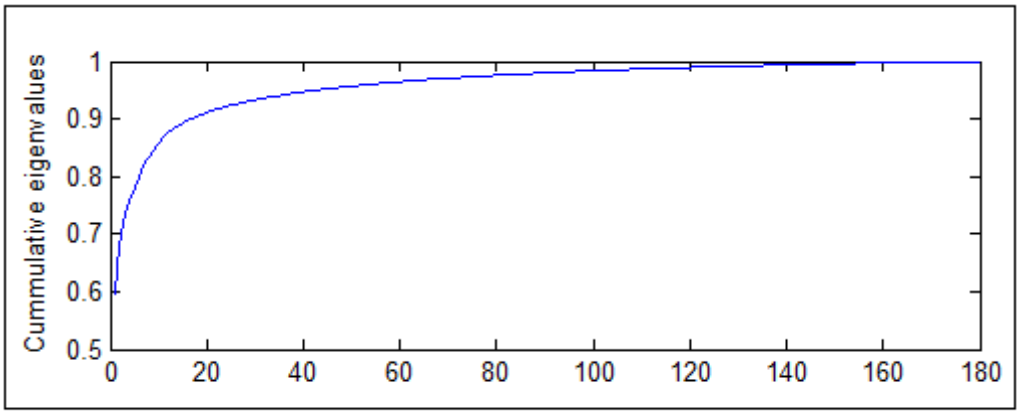

Figure 3.95 : Cumulative eigenvalues for Longer wall for $\alpha = 45$

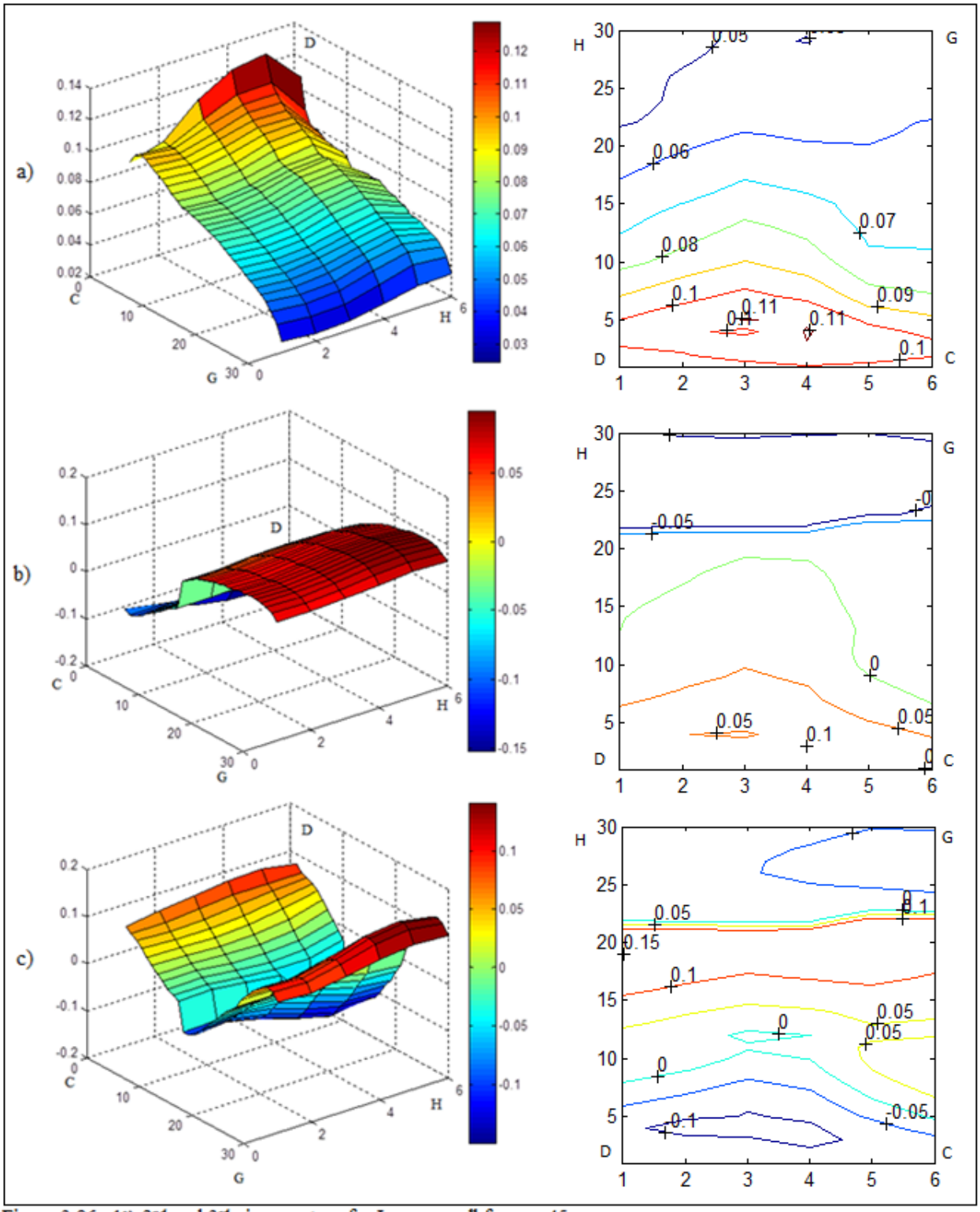

Figure 3.96 : 1st, 2nd and 3rd eigenvectors for Longer wall for $\alpha = 45$
a) 1st; b) 2nd; c) 3rd

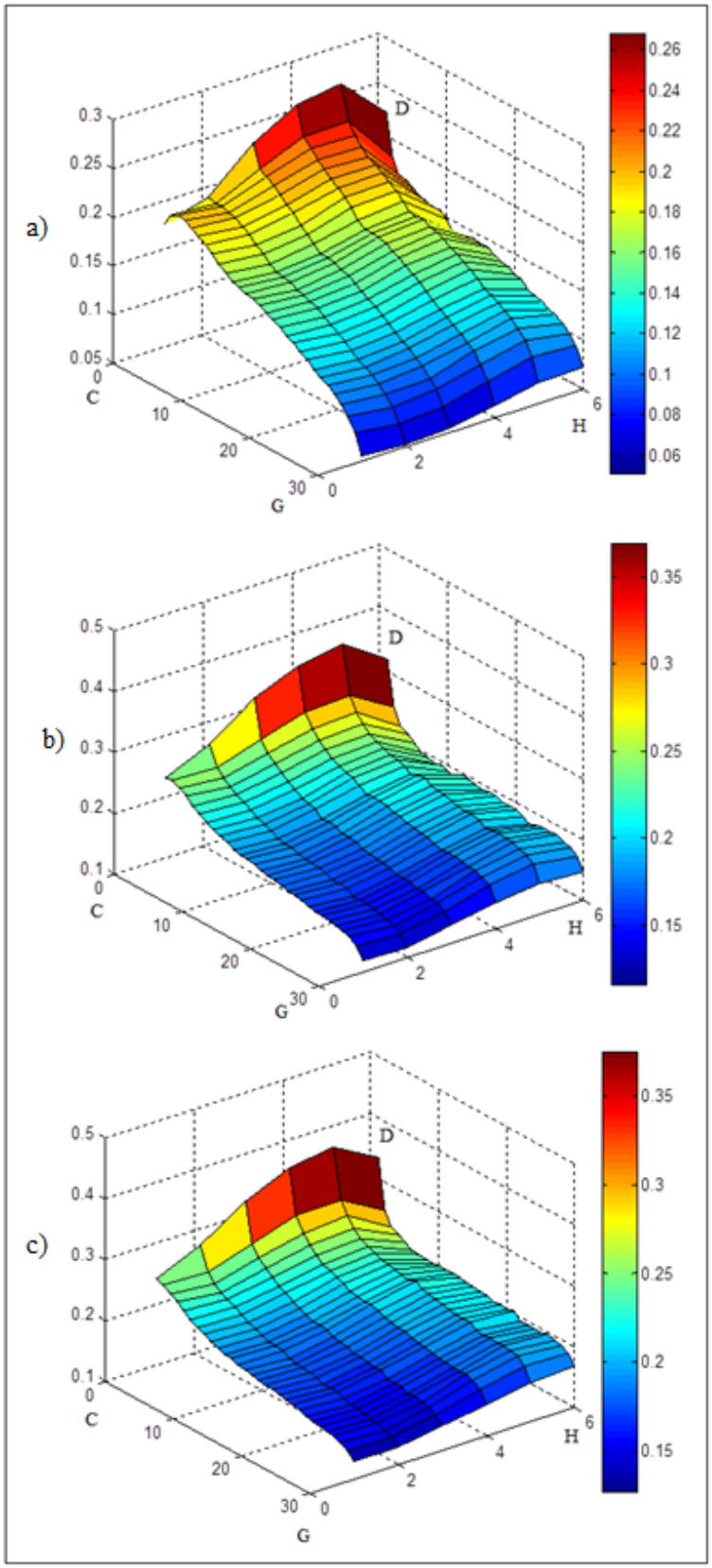

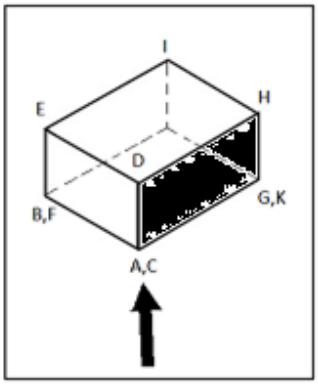

Figure 3.97 : Standard deviation of contributions (1, 10, 30) for α = 45
a) 1st; b) First 10; c) First 30

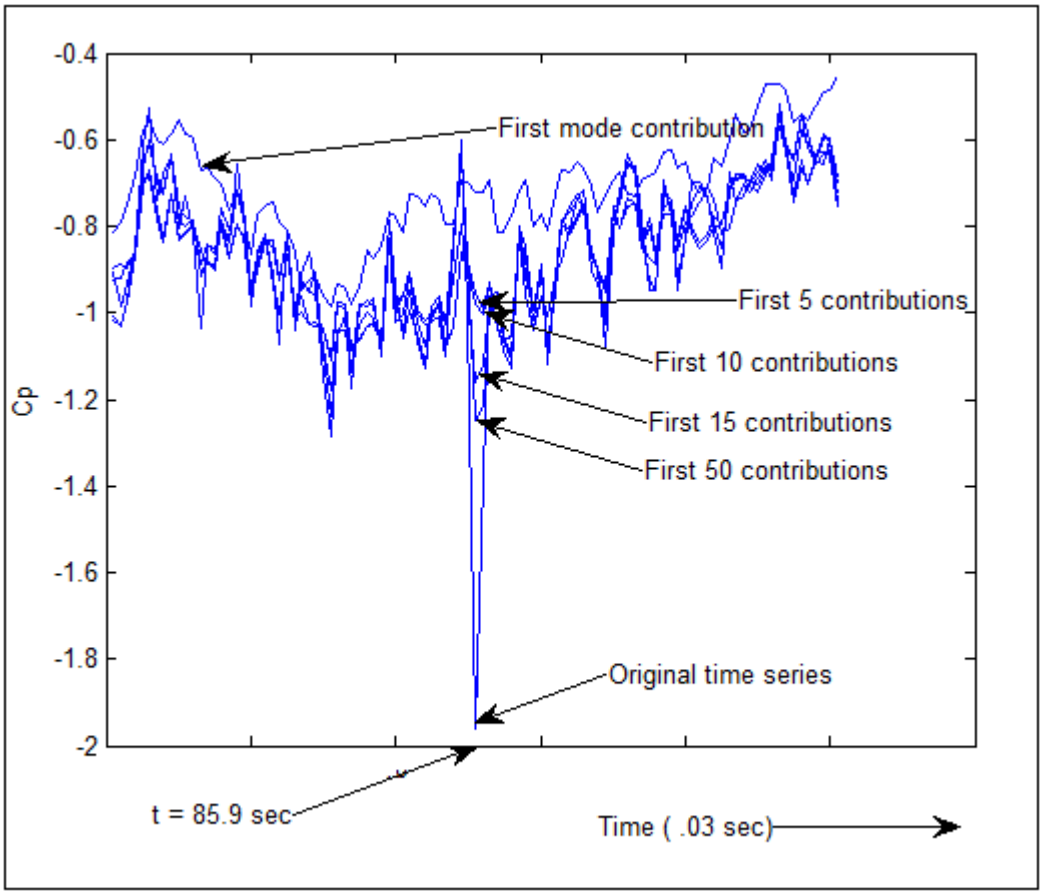

Figure 3.98 : Convergence of time series at position of maximum pressure for $\alpha = 45^{\circ}$

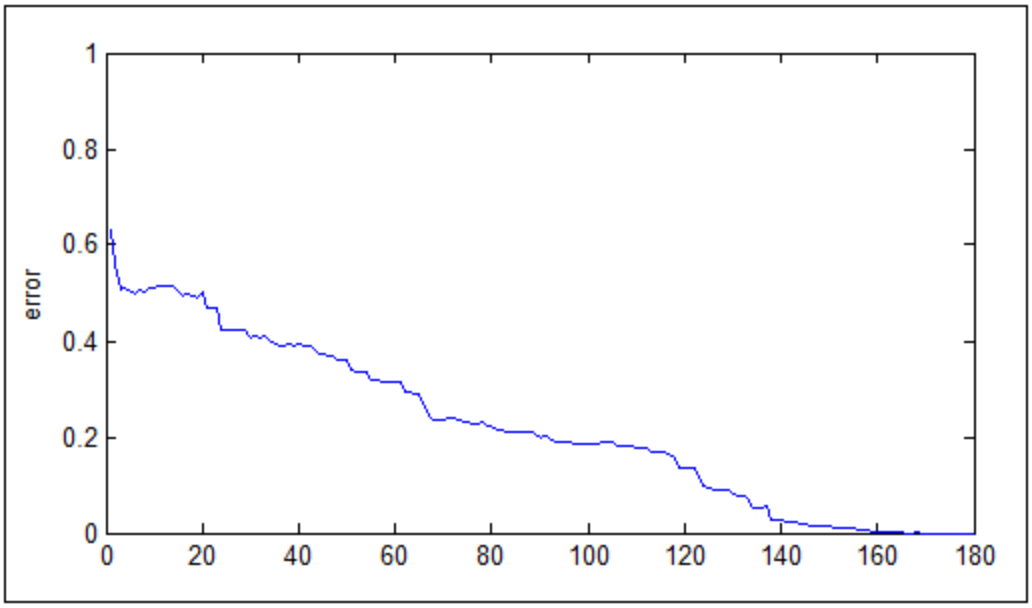

Figure 3.99 : Error at position of maximum pressure changing with contribution for $\alpha = 45$

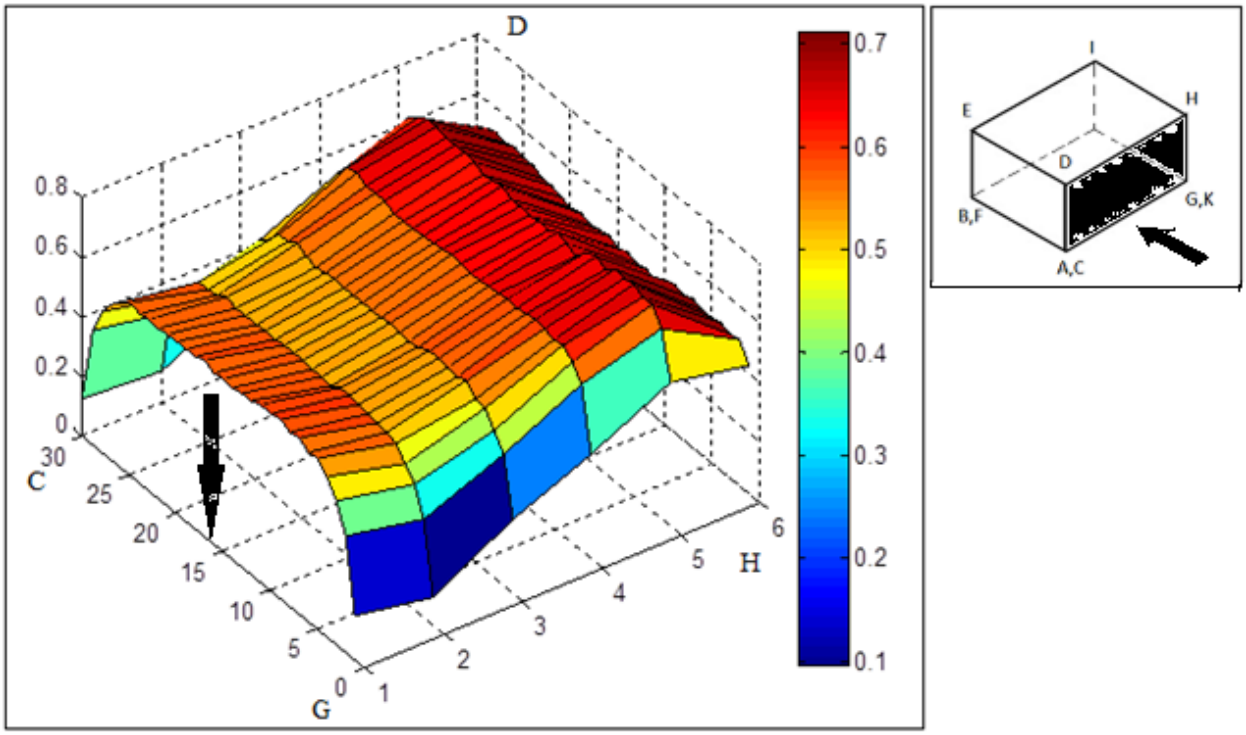

Figure 3.100 : Avg values for Longer wall for α = 90

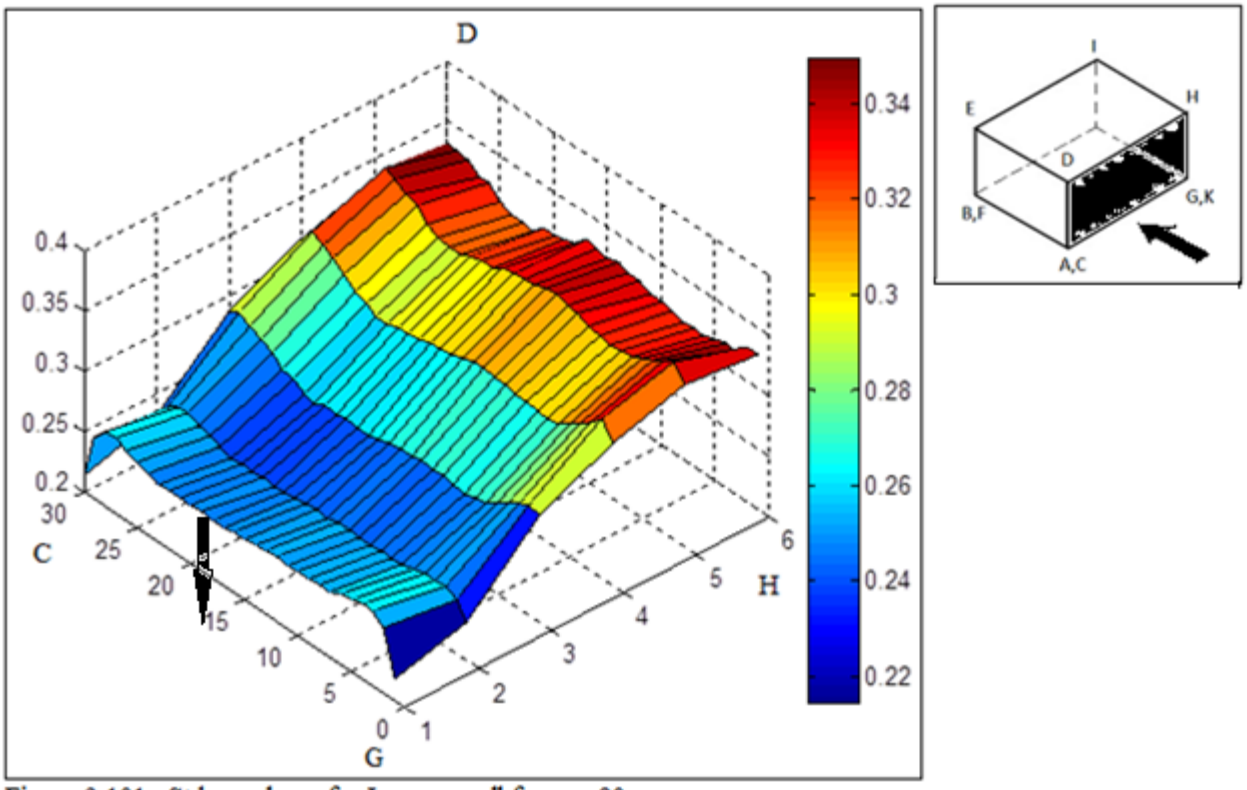

Figure 3.101 : Stdev values for Longer wall for α = 90

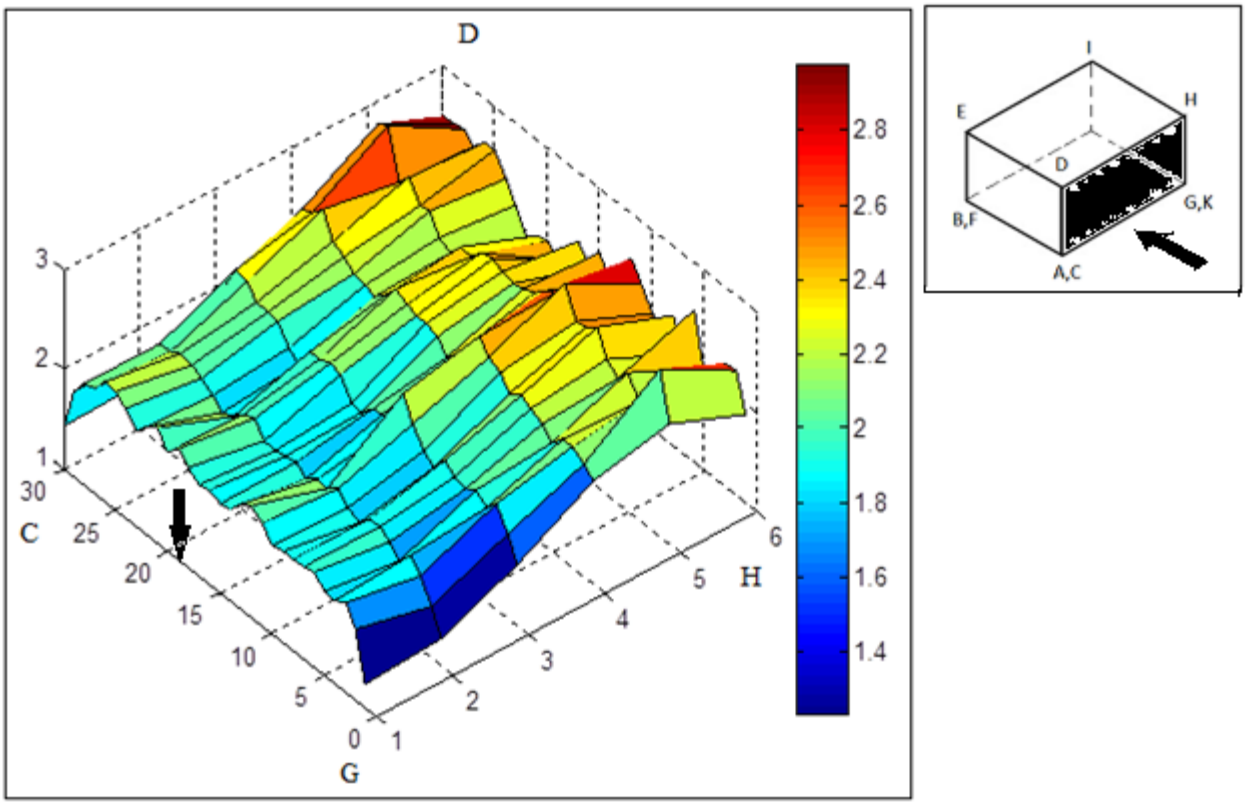

Figure 3.102 : Peak values for Longer wall for $\alpha = 90$

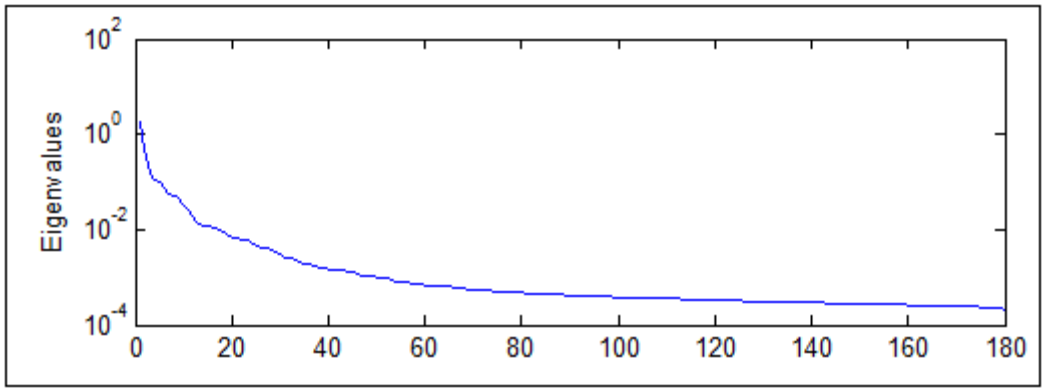

Figure 3.103 : Eigenvalues for Longer wall for $\alpha = 90$

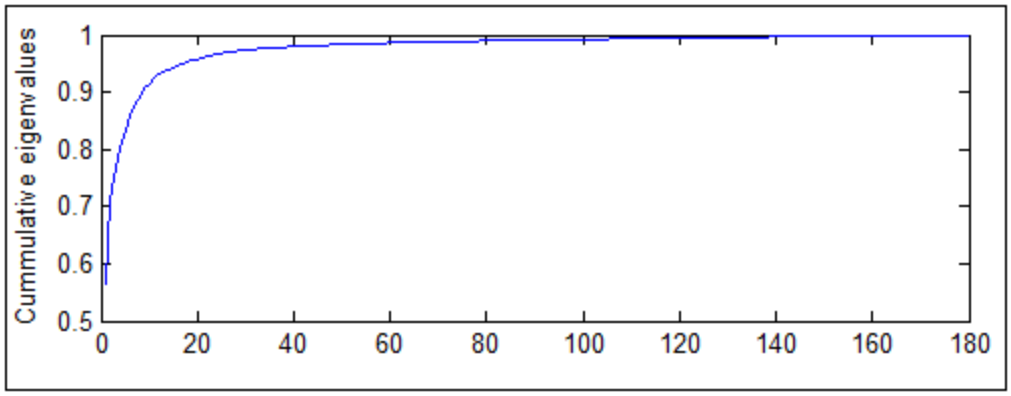

Figure 3.104 : Cumulative eigenvalues for Longer wall for $\alpha = 90$

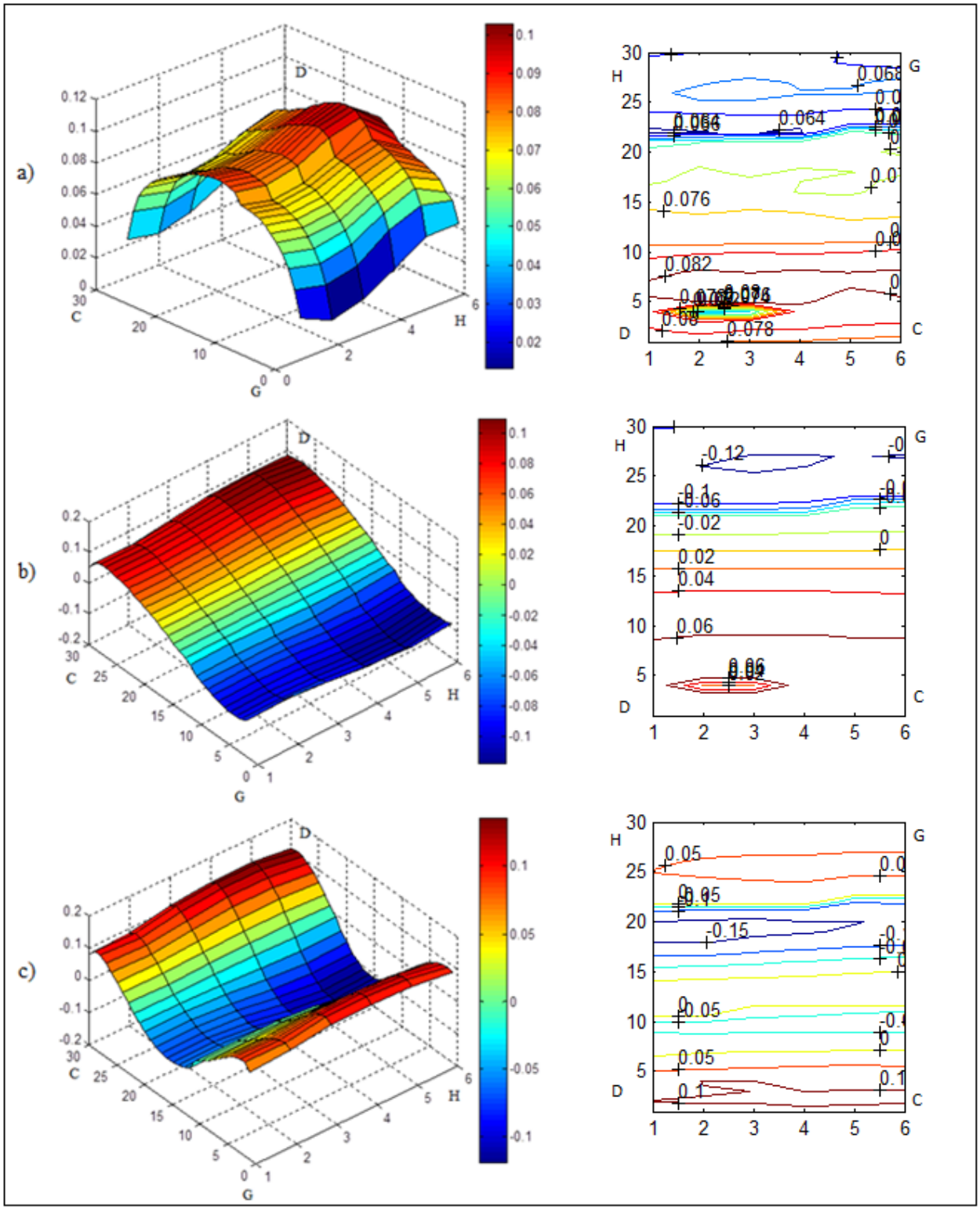

Figure 3.105 : 1st, 2nd and 3rd eigenvectors for Longer wall for α = 90
a) 1st; b) 2nd; c) 3rd

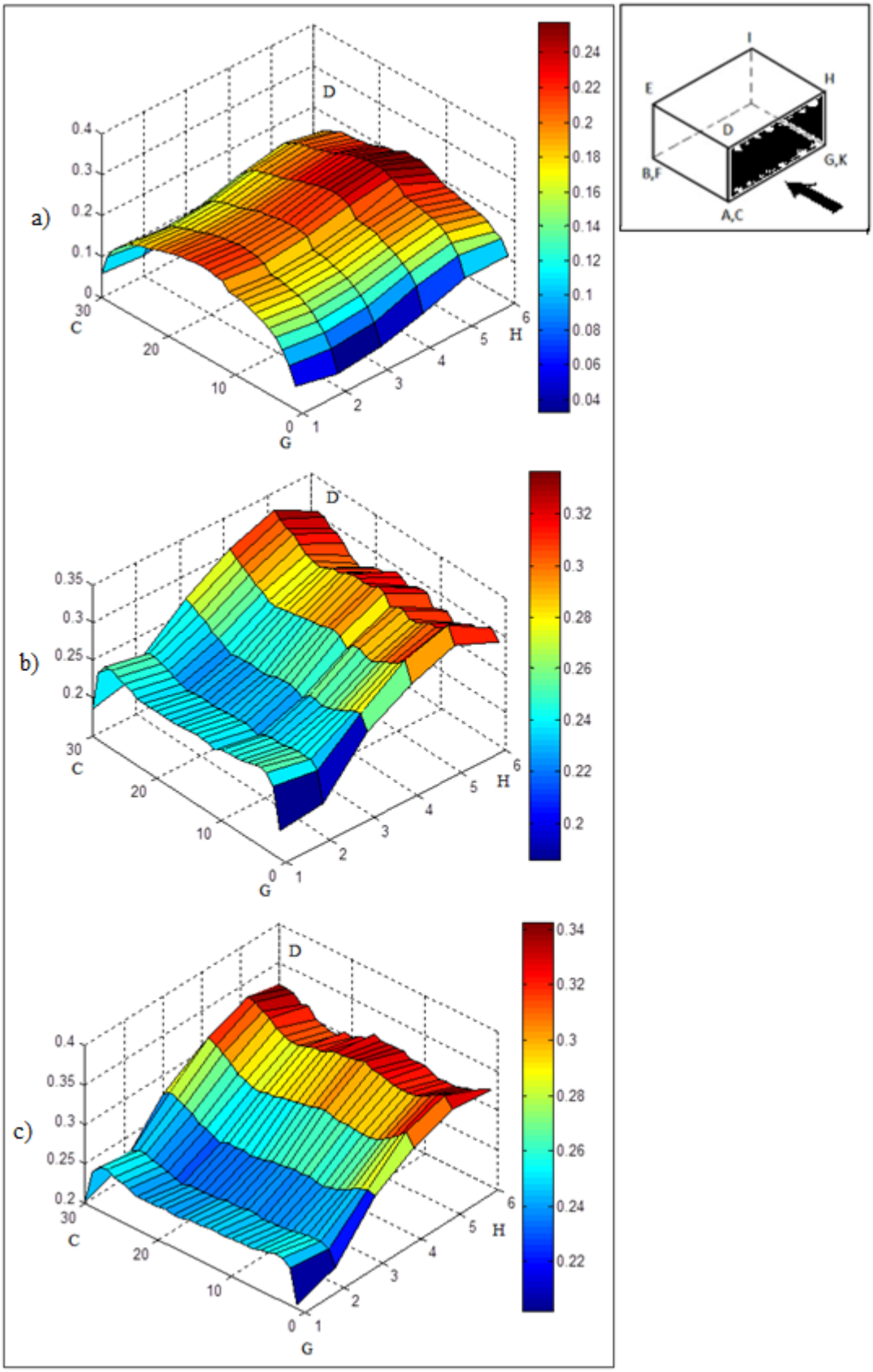

Figure 3.106 : Standard deviation of contributions (1, 10, 30) for α = 90

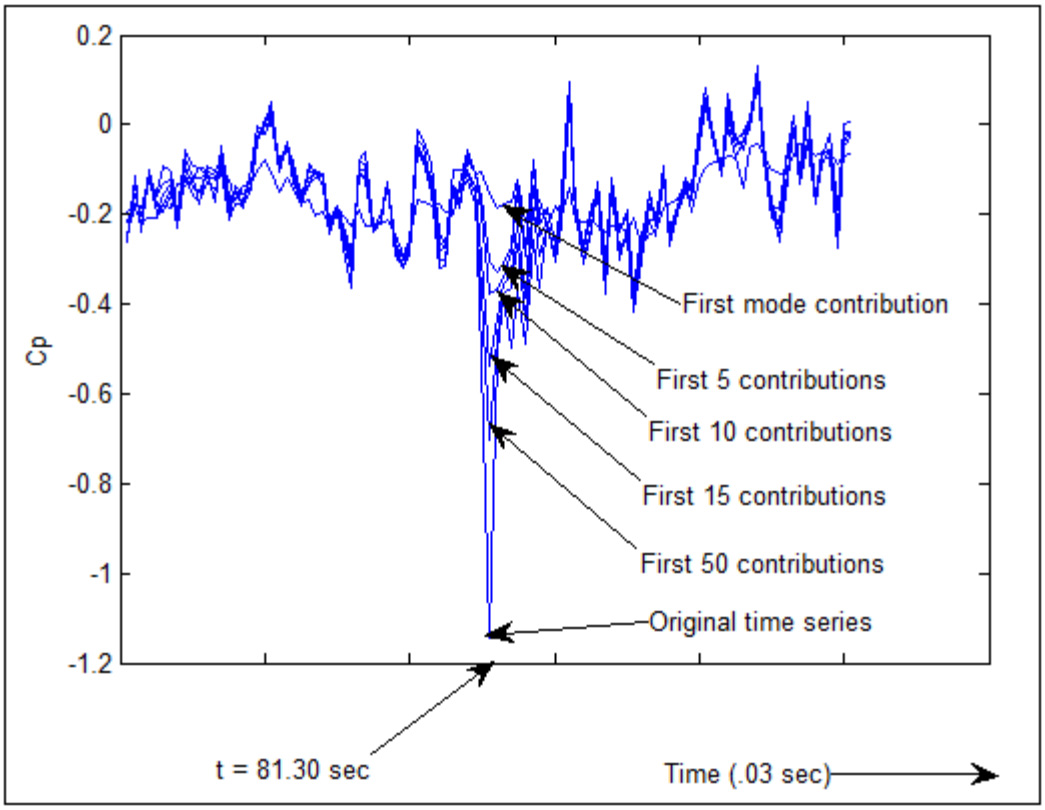

Figure 3.107 : Convergence of time series at position of maximum pressure for α = 90

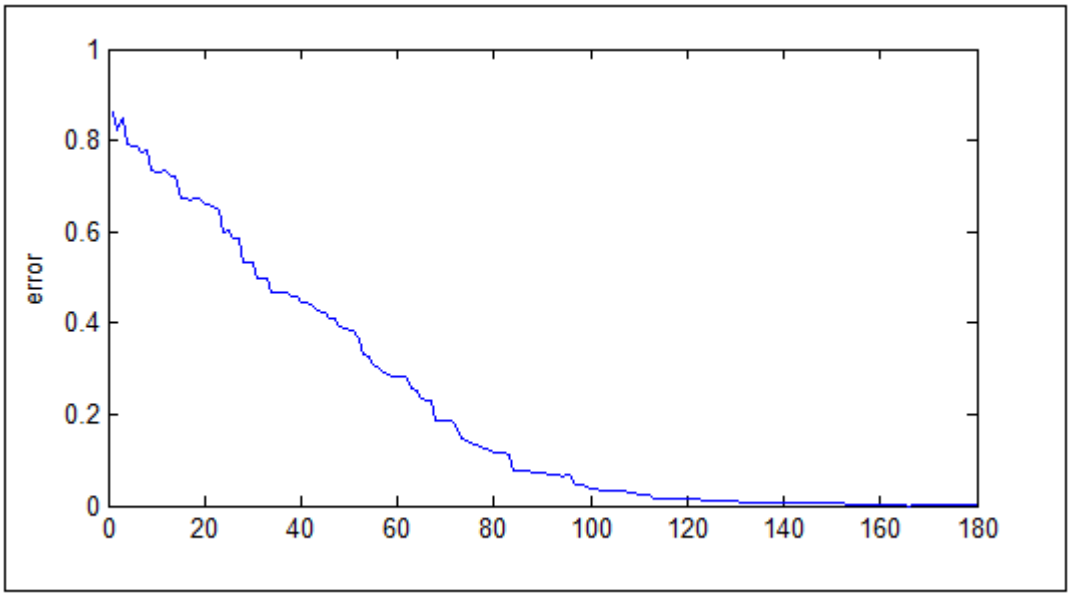

Figure 3.108 : Error at position of maximum pressure changing with contribution for α = 90

Chapter 4

Discussion of Findings

4.1 . Overall Data Analysis

- **Average Pressure**

For $\alpha = 0^0$, the average pressure is approximately equal to static pressure, for half the roof. On the leeward shorter wall, the pressure coefficients are low negative numbers. Peak pressure reaches its maximum for $\alpha = 45^0$ and 90^0. For $\alpha = 45^0$, walls ABED and CDHG exhibit positive pressure coefficients, while the remaining walls and roof show predominantly negative pressure coefficients. The pressure coefficients are low on the shorter wall HILK and on the leeward side, when compared with those on the adjoining longer wall (CDHG). The same trend is also observed for longer wall EFJI, on the leeward side.

- **Standard Deviation of Pressure**

The standard deviation is higher over the taps that have higher fluctuations, which are the taps on the windward side for any structure. As can be observed, the standard deviation is more than two times higher on the windward side than on the middle and negligible on the leeward side of the roof, and the leeward wall, for $\alpha = 0^0$. This pattern is also observed for $\alpha = 90^0$. However, it is different for $\alpha = 45^0$. Standard deviation for $\alpha = 45^0$ is presented in Figure 3.11. It can be observed that the variance is high over the walls on the windward side and is low over wall HILK. For both $\alpha = 0^0$ and $\alpha = 45^0$, it can be observed that the windward side experiences higher fluctuations than the leeward side. However, for $\alpha = 90^0$, Figure 3.20, it can be observed

that the values are more uniformly distributed. These comparisons confirm observations drawn results of reported investigations of wind-induced pressures on low-rise buildings.

- **Comparisons of Results Obtained from Data Sets for Portions of the Structure**

The locations of peak pressures were determined to be on the first two rows of pressure taps, for windward direction, compare Table 2.2.

Figure 3.9 presents the dependence of the error of the peak pressure reconstruction, as a function of the number of modal contributions, for the whole structure ($\alpha = 0^0$). By comparing this dependence with the corresponding reconstruction errors obtained for wind directions $\alpha = 45^0$ (Figure 3.18) and 90^0 (Figure 3.27), it can be observed that for $\alpha = 45^0$ the error decreases faster (with the increasing number of the modes used) than for the remaining wind directions. Similar trend was found when the data from roof only was employed in the peak pressure reconstruction, compare Figures 3.36, 3.45 and 3.54. Examination of the peak pressure reconstruction errors obtained using the data from the shorter and longer walls, treated separately, led to the same conclusion.

Since the largest peak pressures were found for roof locations, the eigenfunctions and eigenmodes (described in Chapter 4, Section 2) were compared separately for the roof Figures 3.33 ($\alpha = 0^0$), 3.42 ($\alpha = 45^0$) and 3.51 ($\alpha = 90^0$) display the eigenvectors obtained for the roof separately. The first eigenvector is symmetric for the three angles. The third eigenvector is anti-symmetric for $\alpha = 0^0$, whereas both the 2^{nd} and 3^{rd} eigenvectors are anti-symmetric with respect to the wind direction, for $\alpha = 45^0$ and $\alpha = 90^0$. In case of the shorter wall, for $\alpha = 0^0$, the

eigenvectors were as expected: 1st - symmetric, 2nd - anti-symmetric and 3rd - symmetric. They can be envisioned as the different fundamental modes on the wall. The same pattern can be observed for the longer wall, for $\alpha = 90^0$ (Figure 3.105). The fundamental modes can also be identified from the number of crossings through zero-level (number of up-crossings and down-crossings) of and eigenvector. It can be observed that the numbers of up crossings and down crossings are same for both the walls for the three considered wind directions, compare Figures 3.69 (shorter wall $\alpha = 45^0$), 3.78 (shorter wall $\alpha = 90^0$), 3.87 (longer wall $\alpha = 0^0$), 3.96(longer wall $\alpha = 45^0$).

4.2 Analysis of POD Results

- **Peak Pressure Coefficients for Different Angles**

Figure 4.1 presents the peak pressure coefficients for different approach wind directions. These peak values and their locations are listed in Table 2.2. Since the roof experienced maximum pressure, all the points of maximum pressure coefficients are on the roof of the structure. It is observed that the values are the largest in magnitude for wind directions of $\alpha = 45^0$ and 135^0.

- **Comparison of Eigenvalues for Different Wind Directions**
  - **90 % of Peak Pressure Coefficient Value**

The number of eigenmodes required to capture 90% of the peak value ($.9*Cp_{max}$), calculated for α= 0, 45 and 90 degrees for different regions of the structure, is presented in Table4.1. As expected in this figure, the roof

The above analysis was also carried out for a broader range of wind directions and the results for the whole structure and the roof are compared in Figure 4.2. It can be observed that the wind direction effects on the number of the modes are similar, for both the cases. The number of the required modes is different for the compared cases. However it should be noted that the roof data set comprised of time series from only 450 pressure taps, while the set used in POD analysis of the whole structure included the time series from 990 taps. It should also be noted that although the roof and whole structure have similar curves for 90% peak pressure eigenvalues, the walls don't follow this pattern observed from Table 4.1.

- **Rules for Determining Significant Modes**

As discussed in Chapter 2, three methods were used to determine the number of the most significant POD modes. Figure 4.4, upper plot presents the result of this analysis obtained using the Scree test. The lower plot in the figure is the corresponding error at the peak position, Eq.2.16. It can be observed from this figure that the number of significant modes is the largest for $\alpha = 90^0$, and the smallest for $\alpha = 45^0$ and $\alpha = 135^0$. For $\alpha = 90^0$, the error is also the largest.

The second method used was the Jolliffe's rule. In Figure 4.5, the upper plot gives the number of the significant modes established using this rule. The lower plot is the corresponding error. It can be seen that the wind direction effects on the number of the significant modes resulting from use of the Scree test and Jolliffe's rule are similar.

In the third method (see Figure 4.6), the number of the significant modes was determined based on the cumulative eigenvalue reaching 0.9, as discussed in Chapter 2, see Figure 2.2. The

results of this analysis are presented in Figure 4.6, upper plot. The corresponding error is displayed in the lower plot.

Overall, the results obtained using the three methods are similar. A comparison of the obtained values is presented in Table 4.4. It can be observed that the Scree test led to smaller values, while the Jolliffe's rule resulted in acceptable results for most of the considered wind directions. However, 90% cumulative eigenvalue rule gives more accurate reconstruction if required. All three tests give maximum error (approximately 40%) at $\alpha = 90°$. They also give high errors for $\alpha = 45°$ but not for $\alpha = 135°$. This can be investigated further.

A similar analysis was carried out to determine the number of significant modes for the roof and walls data, treated separately. The results of this effort are summarized in Tables 4.4 ($\alpha= 0^0$), 4.3 ($\alpha= 45^0$) and 4.4 ($\alpha= 90^0$). These tables show the effect of change in wind direction on the different eigenmodes tests. It is noted that Jolliffe's test is more conservative than Scree test for our structure, but they both give higher errors than 90% cumulative rule, which gives an error of < 10% for all cases irrespective of wind direction and number of pressure taps.

- **Effects of Number of Taps on POD Eigenvalues**

Figures 4.7 through 4.9 present the normalized eigenvalues on the upper graph and cumulative normalized eigenvalues on the lower graph plotted against the normalized mode index.

$$\Lambda_i = \frac{\lambda_i}{\sum_{j=1}^{N} \lambda_j} \tag{4.1}$$

where, Λ_i is the normalized eigenvalue and the cumulative normalized eigenvalues

$$\Lambda_{ci} = \sum_{j=1}^{i} \Lambda_j \tag{4.2}$$

where, Λ_{ci} is the normalized cumulative eigenvalue, plotted as functions of the normalized mode index given as-

$$I = \frac{i}{N} \tag{4.3}$$

where

$\lambda_i =$ POD eigenvalue associated with mode i, $(i = 1, ..., N)$

$N =$ total number of POD modes (= total number of pressure time series/pressure taps)

The results are presented (in the figures) for three wind directions, $\alpha = 0^0, 45^0$ and 90^0. It can be seen that the eigenvalue curve is the lowest for the whole structure. For $\alpha = 0^0$, the normalized eigenvalues are the largest for the shorter wall ABED. They are also the largest for $\alpha = 45^0$. However, for $\alpha = 90^0$, they are the largest for the longer wall CDHG. It is observed that the normalized eigenvalues are the largest for the region that is on the windward side.

The lower plots in the above figures show the cumulative eigenvalues for $\alpha = 0^0, 45^0$ and 90^0. For $\alpha = 0^0$, the shorter wall requires the smallest number of modes needed to capture 90 % of the total energy of the pressure. For $\alpha = 45^0$, similar requirement is observed for both the longer and shorter walls. For $\alpha = 90^0$, the longer wall requires the smallest number of modes, to capture 90% of the pressure energy. In addition, it can be observed that the windward surface requires the smallest number of the modes to capture most of the energy of the system. Figure 4.10 shows that, for the three wind directions studied ($\alpha = 0^0, 45^0$ and 90^0), $\alpha = 45^0$ requires the smallest number of the modes to capture 90% of the total energy of the pressure time series.

- **Most Significant Eigenvalue**

Figure 4.3 presents the numerical value of the largest eigenvalue (1^{st} eigenvalue) obtained from POD analysis, carried out for the whole structure, and plotted as a function of wind direction. It can be seen that it is the biggest when wind direction $\alpha = 90^0$. Figure 4.11 presents plots, obtained for different regions, analyzed separately. It is observed from this figure that for the whole structure, the 1^{st} eigenvector is the largest for $\alpha = 90^0$. Fort wall EFJI, which is the leeward wall for most of the angles considered, the value of this (most significant eigenvalue) is the smallest, for this ($\alpha = 90^0$) wind direction. For wall HILK and wall ABED, it is observed that the eigenvalue is maximum when the projected area (perpendicular to the wind) is the largest, and it decreases as the projected area gets smaller.

- **Eigenvectors**

Figures 4.12 through 4.20 show the 1^{st}, 2^{nd} and 3^{rd} eigenvectors for the roof, obtained from analysis of the POD analysis of the datasets for the whole structure and for the roof analyzed separately.

For all the displayed cases, the first eigenvector is found to be similar to the distribution of the roof mean (time-averaged) pressure. The second eigenvector is antisymmetric (in shape) with respect to the wind direction, for $\alpha = 0^0$ and $\alpha = 45^0$. For wind direction of $\alpha = 90^0$, the third eigenvector is found to be antisymmetric with respect to the wind direction. In this case, the eigenvector values over the windward longer wall are also found to be antisymmetric with respect to the wind direction. The eigenvectors for the roof are larger in magnitude than the eigenvectors calculated for the whole structure. Figures 4.15 through 4.17 show that the 1^{st}

eigenvector is similar in shape for α = 45 but the 2nd and 3rd eigenvectors are almost opposite in shape. The eigenvector for the roof is still greater in magnitude than the one for the whole structure. The same pattern is also seen for $\alpha=90^0$ (Figures 4.18 through 4.20), but only for the 1st and 3rd eigenvector. The 2nd eigenvector is found to be different for the roof and the whole structure.

- **Memory requirements**

Table 4.6 accounts the space used to store the POD matrices. The space required to store the eigenvectors are negligible as compared to other matrices so, it can be assumed that the space required to store the significant modes is directly proportional to the number of modes retained. Also, each principle component requires .228 MB to store, which is roughly equal to the total data divided by the number of taps. The roof requires half the data as the whole structure, since it has half the pressure taps. Figure 4.24 shows the relative memory space (calculated by Equation 4.4) required by different rules.

$$\text{Relative } \textit{memory} \text{ used} = \frac{\text{Memory } \textit{space} \text{ used by that mode/region}}{\text{Memory space used to store entire data set}} \qquad (4.4)$$

Both Scree test and Jolliffe's rule require 10 to 15% of the total space. The 90% cumulative rule requires 30% data space for α = 75 to α = 110 but requires 5 to 10% of total space with the exception of α = 45, which requires near about 15 % relative data space. Since the data required for the roof will be half of that required for the whole structure due to half the number of taps, it is more advisable to use 90% rule on the roof separately to save most memory space.

Tables- (Chapter4)

Table 4.1 : Number of contributions to attain 90% of peak value for different regions for α = 0, 45 & 90

	0	45	90
Whole Structure	165	30	335
Roof (DEIH)	88	19	217
Shorter wall (ABED)	27	20	13
Longer wall (EFJI)	57	124	84
Shorter wall (HILK)	12	20	53
Longer wall (CDHG)	42	38	66

Table 4.2 : Significant modes as given by the rules used and the corresponding errors for α = 0

	Scree test		Jolliffe's rule		90% cumulative eig	
	Significant modes	Error	Significant modes	Error	Significant modes	Error
Whole Structure	79	0.364668	107	0.277246	165	0.097171
Roof (DEIH)	42	0.366425	59	0.271681	88	0.078757
Shorter wall (ABED)	7	0.039011	10	0.04595	27	0.096559
Longer wall (EFJI)	17	0.428052	23	0.280108	57	0.079127
Shorter wall (HILK)	7	0.114154	8	0.11916	12	0.071763
Longer wall (CDHG)	16	0.413928	22	0.324288	42	0.092095

Table 4.3 : Significant modes as given by the rules used and the corresponding errors for α = 45

	Scree test		Jolliffe's rule		90% cumulative eig	
	Significant modes	Error	Significant modes	Error	Significant modes	Error
Whole Structure	71	0.023825	92	0.003646	30	0.097217
Roof (DEIH)	44	0.014456	53	0.003681	19	0.099292
Shorter wall (ABED)	6	0.16973	8	0.175828	20	0.052205
Longer wall (EFJI)	14	0.471097	16	0.494966	124	0.098529
Shorter wall (HILK)	7	0.045883	10	0.358765	20	0.070961
Longer wall (CDHG)	12	0.422687	15	0.074215	38	0.02853

Table 4.4 : Significant modes as given by the rules used and the corresponding errors for α = 90

	Scree test		Jolliffe's rule		90% cumulative eig	
	Significant modes	Error	Significant modes	Error	Significant modes	Error
Whole Structure	89	0.471137	116	0.449146	335	0.093078
Roof (DEIH)	52	0.05571	65	0.445617	217	0.097951
Shorter wall (ABED)	11	0.050266	13	0.060174	13	0.060174
Longer wall (EFJI)	12	0.535373	14	0.719715	84	0.078369
Shorter wall (HILK)	10	0.123005	13	0.360061	53	0.097744
Longer wall (CDHG)	13	0.287166	17	0.179229	66	0.099486

Table 4.5 : Most significant Eigen modes as given by different rules

Angle	Scree test	Jolliffe's rule	90% cumulative eig
0	79	104	110
45	71	91	65
90	89	117	140
135	68	92	82
180	65	102	104

Table 4.6 : Memory space required by different POD data matrices

Size of data set		**Memory required**
Whole structure (30000x990)		226.59 MB
Principle components (30000x990))		226.59 MB
Eigenvectors(990x990)		.006866MB
1 principle component (30000x1)		.228MB
Roof (30000x450))		113.3MB
Principle components (30000x450))		113.3MB
Eigenvectors(450x450)		0.003433 MB
1 principle component (30000x1)		.228MB

Table 4.7 : Significant modes as given by different rules

Angle (α)	Scree test	Scree test error	Jolliffe's rule	Jolliffe's rule error	90% cumulative	90%cumulative error
0	79	0.36466795	107	0.277246126	165	0.097171012
5	76	0.02796202	103	0.030835959	57	0.099477873
10	72	0.072483048	101	0.050976434	54	0.099417227
15	69	-0.007613888	96	0.002097543	28	0.046715853
20	66	0.004685432	92	0.002091021	23	0.093308903
25	65	0.03174783	89	0.011373243	39	0.061607394
30	67	-0.002367198	89	0.000515206	7	0.087637426
35	68	-0.006990712	89	0.006441527	31	0.035178544
40	70	0.462169388	91	0.345388163	148	0.093248636
45	71	0.02382502	92	0.003646305	30	0.097217405
50	72	-0.026668343	95	-0.01212616	24	0.071628092
55	72	0.003389687	98	-0.0032311	6	0.066226069
60	75	0.021296136	103	0.000370775	11	0.061386642
65	75	0.055210732	103	0.01698356	33	0.097478503
70	80	0.040704535	105	0.019002357	53	0.099917876
75	83	-0.016011689	110	0.015962348	47	0.08940521
80	85	0.108179162	113	0.08454176	105	0.089243933
85	88	0.053483753	115	0.052417114	68	0.090186159
90	89	0.471136702	116	0.449145795	335	0.093078297
95	86	0.07882054	114	0.046651778	80	0.09708259
100	84	0.443164407	113	0.349992832	272	0.099786872
105	83	0.022201844	113	0.008066141	42	0.093932131
110	77	0.011581141	105	0.019212853	39	0.093329421
115	75	0.011860891	104	0.006079063	14	0.069241325
120	73	0.007684648	102	0.000106213	10	0.087489771
125	71	0.005615726	97	0.009146233	30	0.077992986
130	69	0.005477557	93	-0.003298093	2	0.054146089
135	68	0.001161718	91	0.004583642	27	0.09391096
140	68	0.013249856	92	0.010709968	13	0.076303218
145	65	0.017152207	89	0.011623857	25	0.091854065
150	62	0.010643425	86	0.007736962	19	0.098344675
155	62	0.010935311	87	0.018306215	36	0.050569922
160	62	0.0197428	91	0.014609869	31	0.086421059
165	65	0.076694995	95	0.033853999	33	0.086750335
170	68	0.130850014	99	0.074581568	87	0.098959403
175	68	0.020154828	98	-0.00748897	36	0.086799947
180	70	0.042178316	99	-0.035499767	68	0.049701816

Figures- (Chapter4)

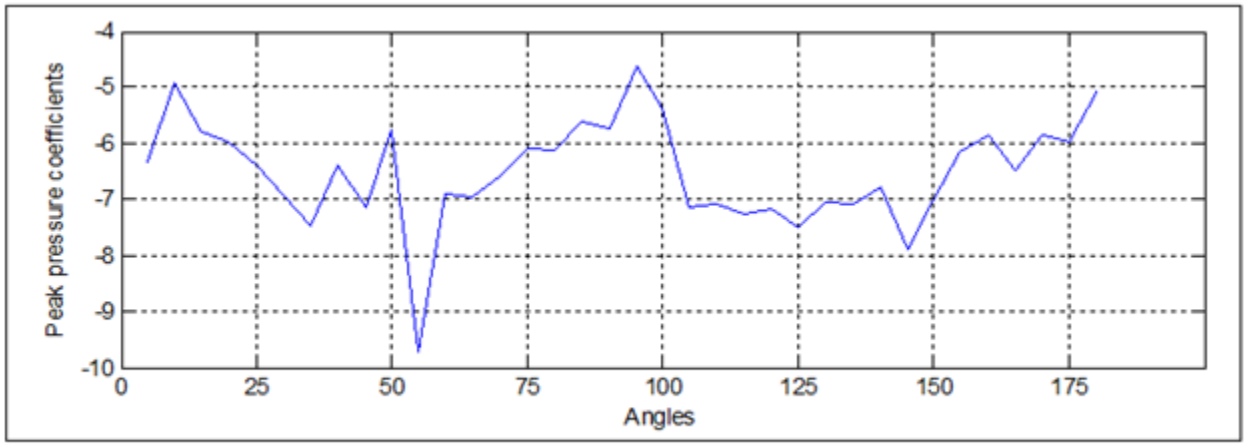

Figure 4.1 : Peak pressure coefficients varying with angle

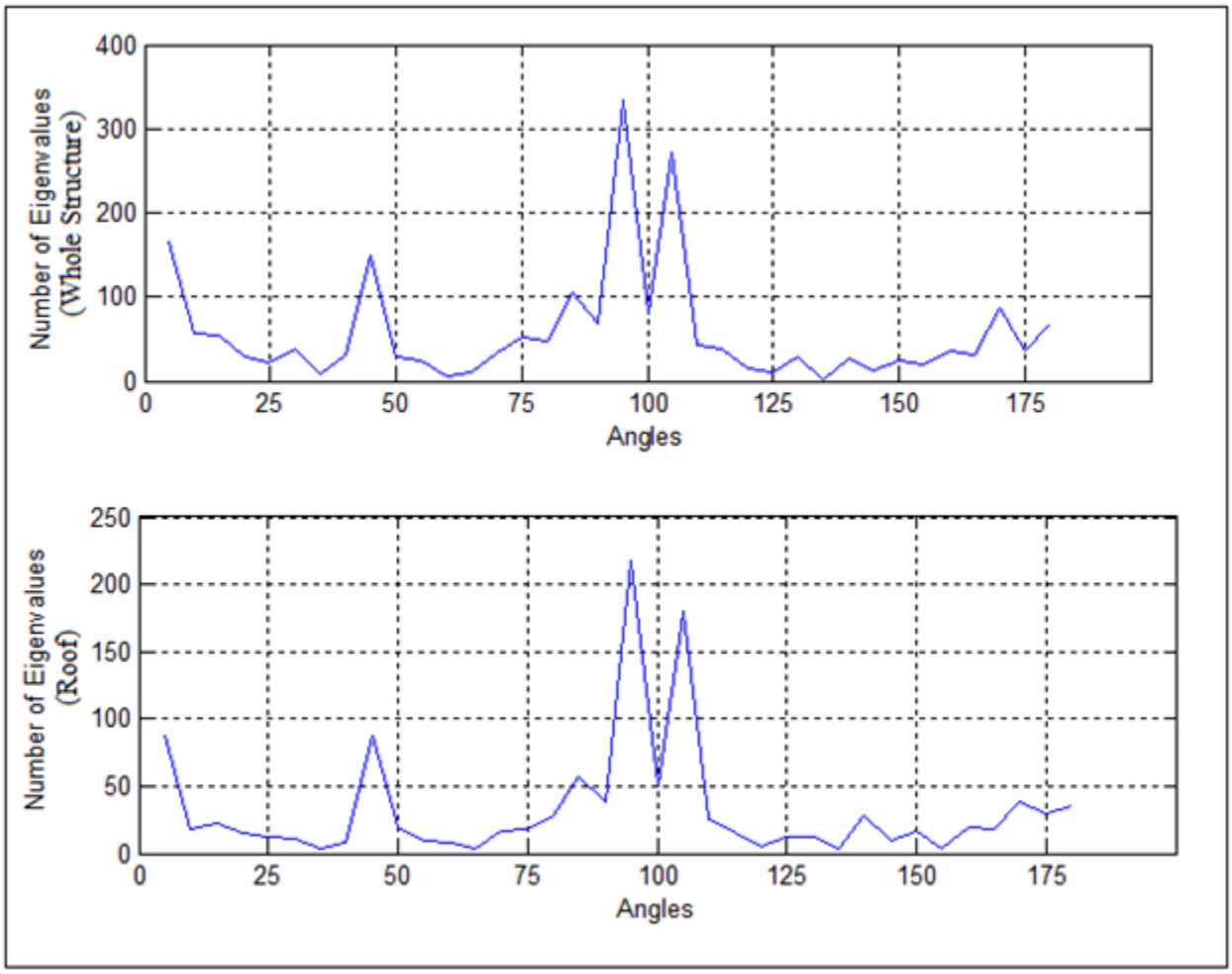

Figure 4.2 : Eigenvalues required for 90% contribution to peak pressure coefficient

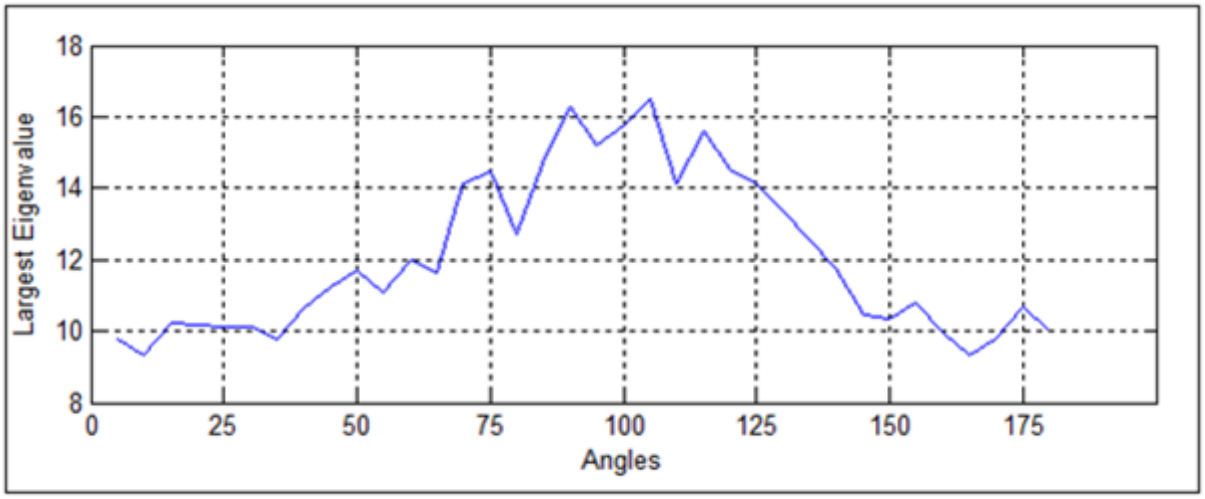

Figure 4.3 : Numerical value of the eigenvalue of the most significant mode varying with angle

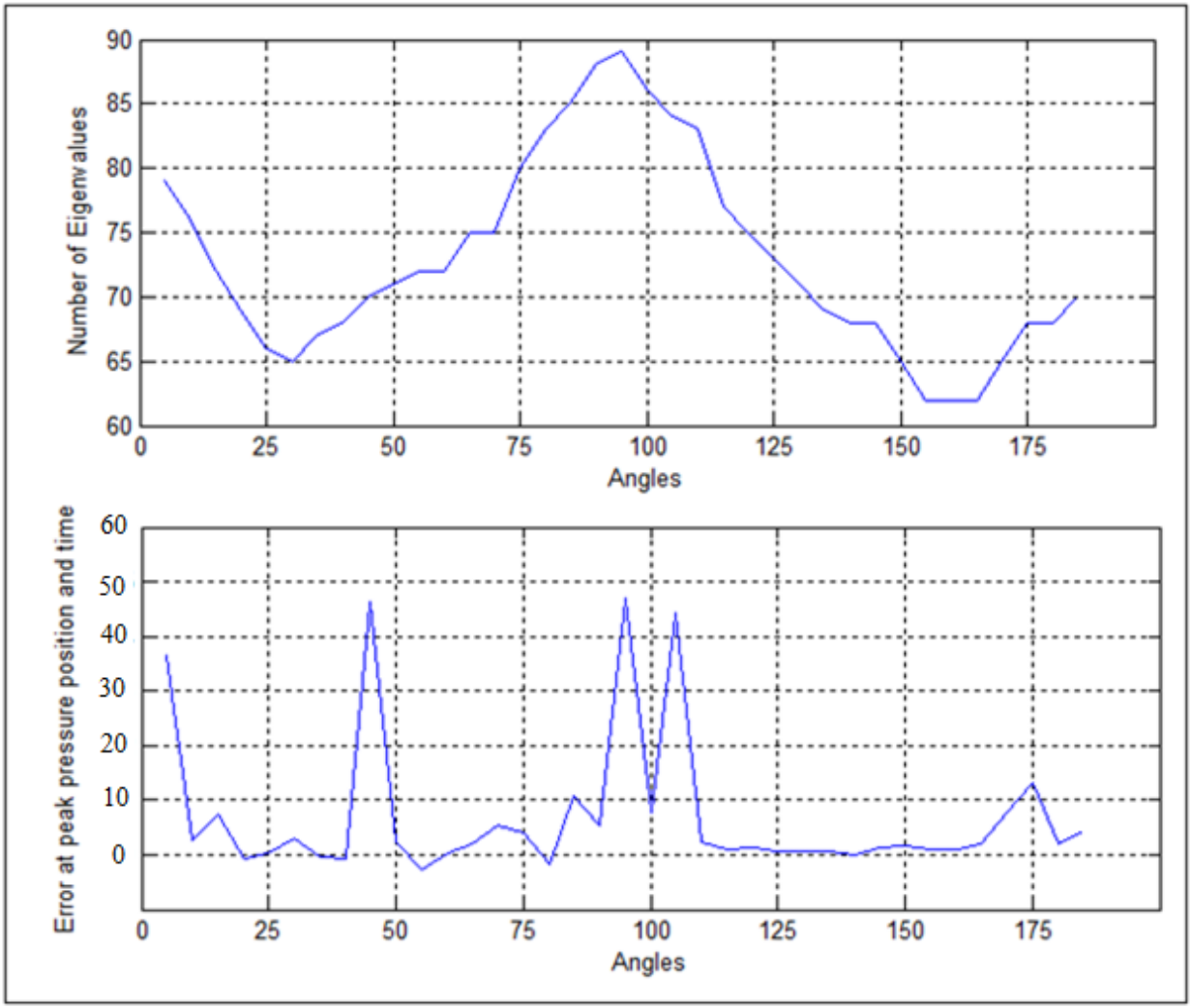

Figure 4.4 : Number of Eigenvalues retained as given by Scree test and error varying with angles

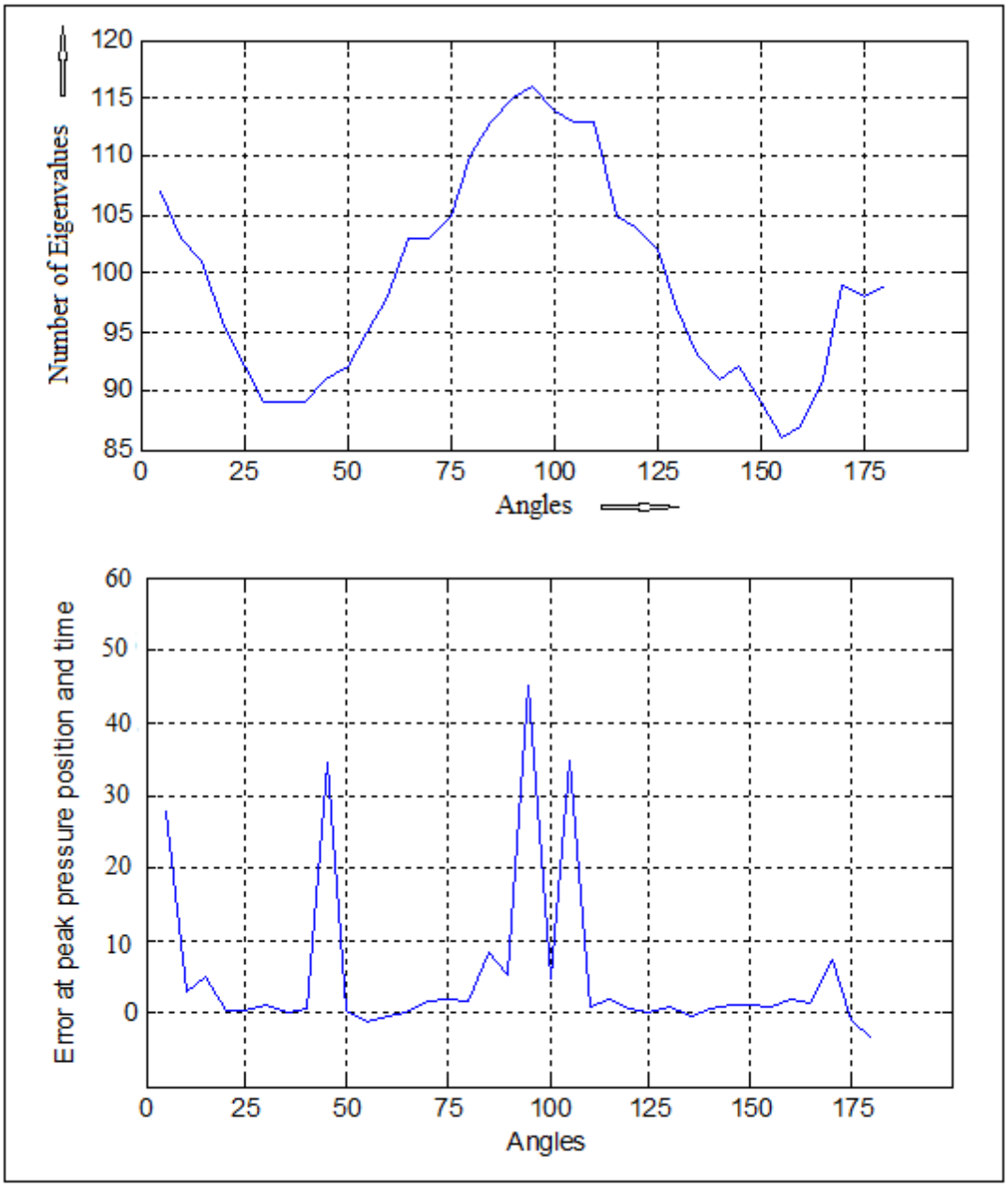

Figure 4.5 : Number of Eigenvalues retained as given by jolliffe's rule and error varying with angles

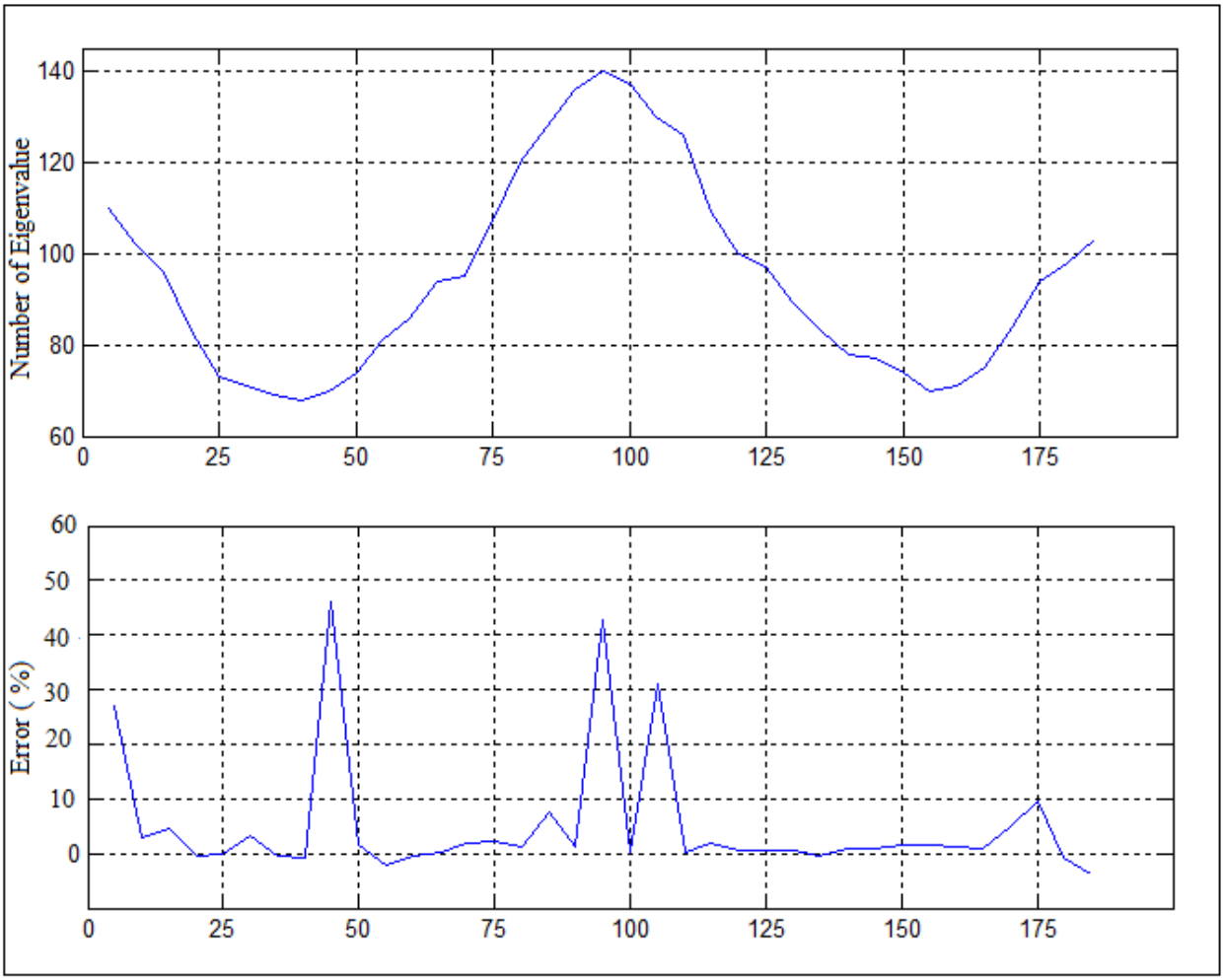

Figure 4.6 : Number of Eigenvalues retained as given by 90% cumulative eigenvalue and error varying with angles

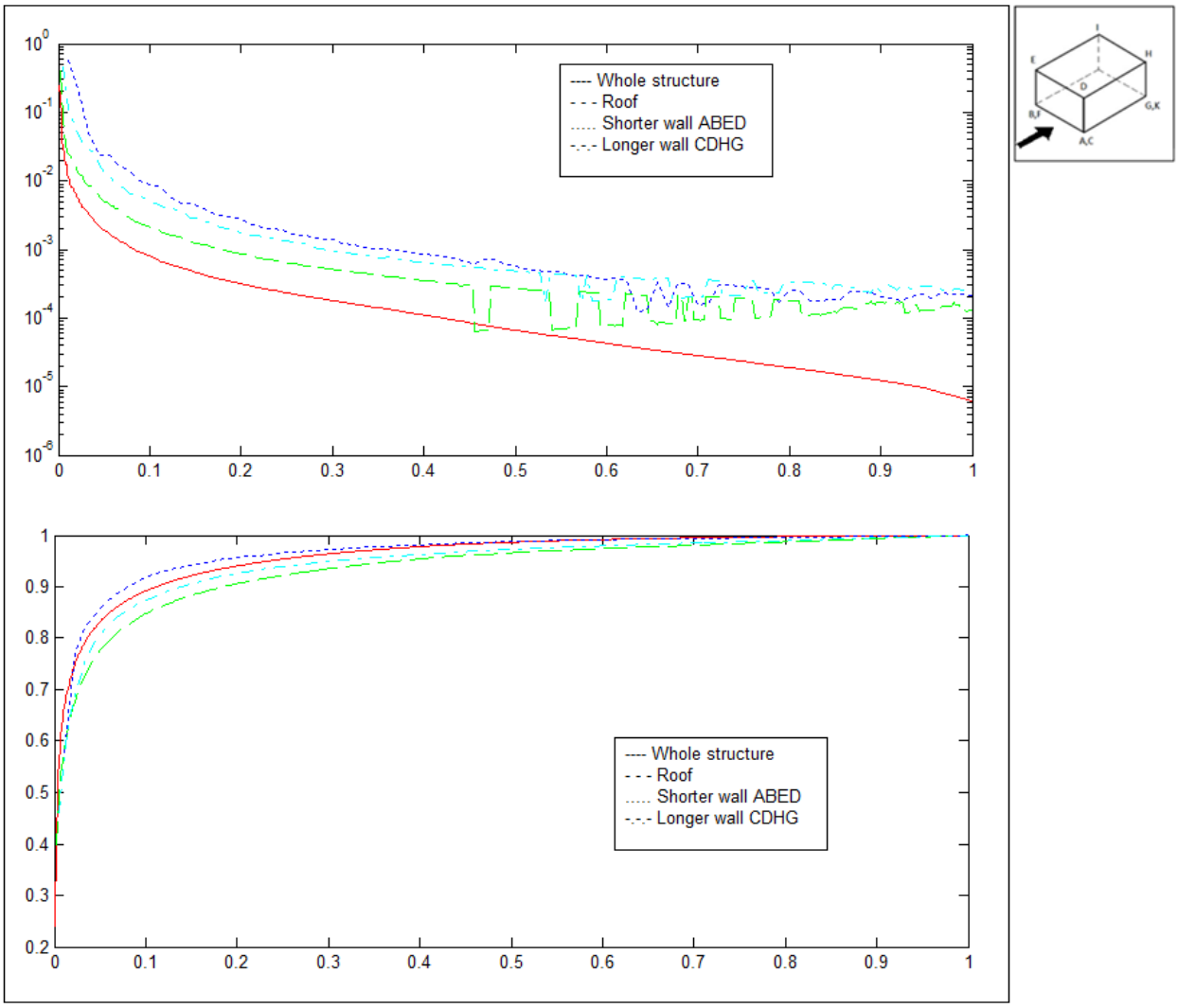

Figure 4.7 : Comparison of Eigenvalues on normalized scale for $\alpha = 0$

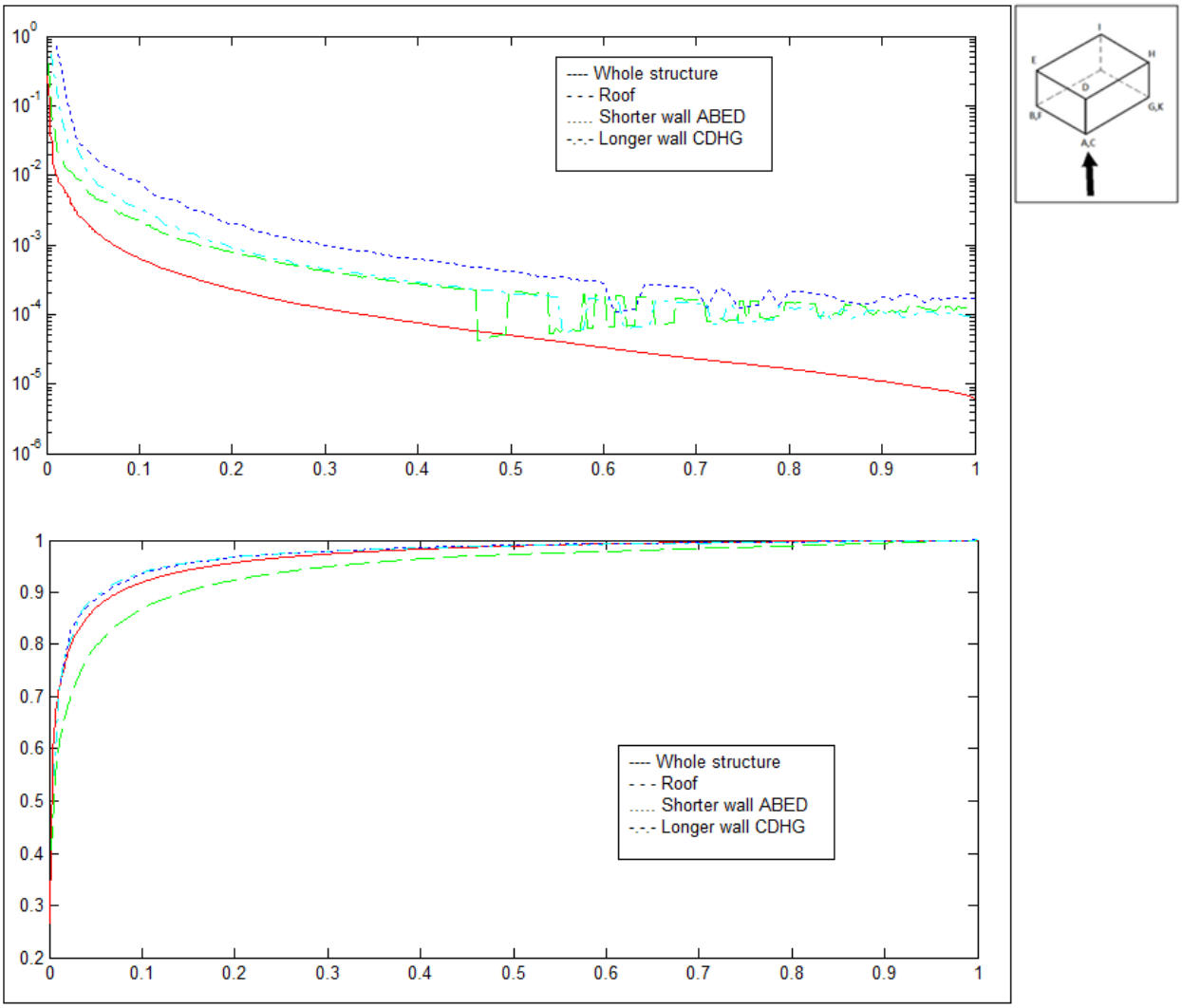

Figure 4.8 : Comparison of Eigenvalues on normalized scale for $\alpha = 45$

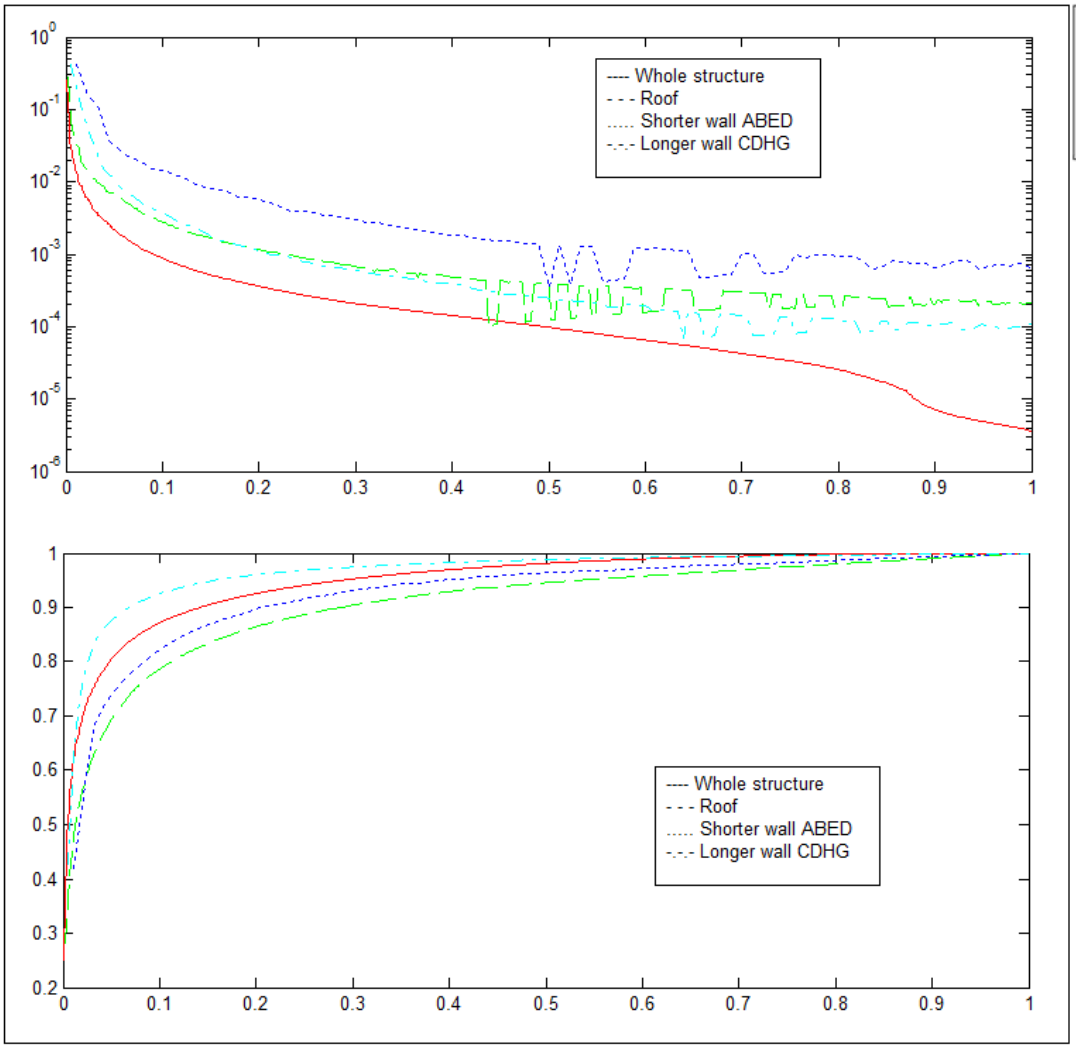

Figure 4.9 : Comparison of Eigenvalues on normalized scale for $\alpha = 90$

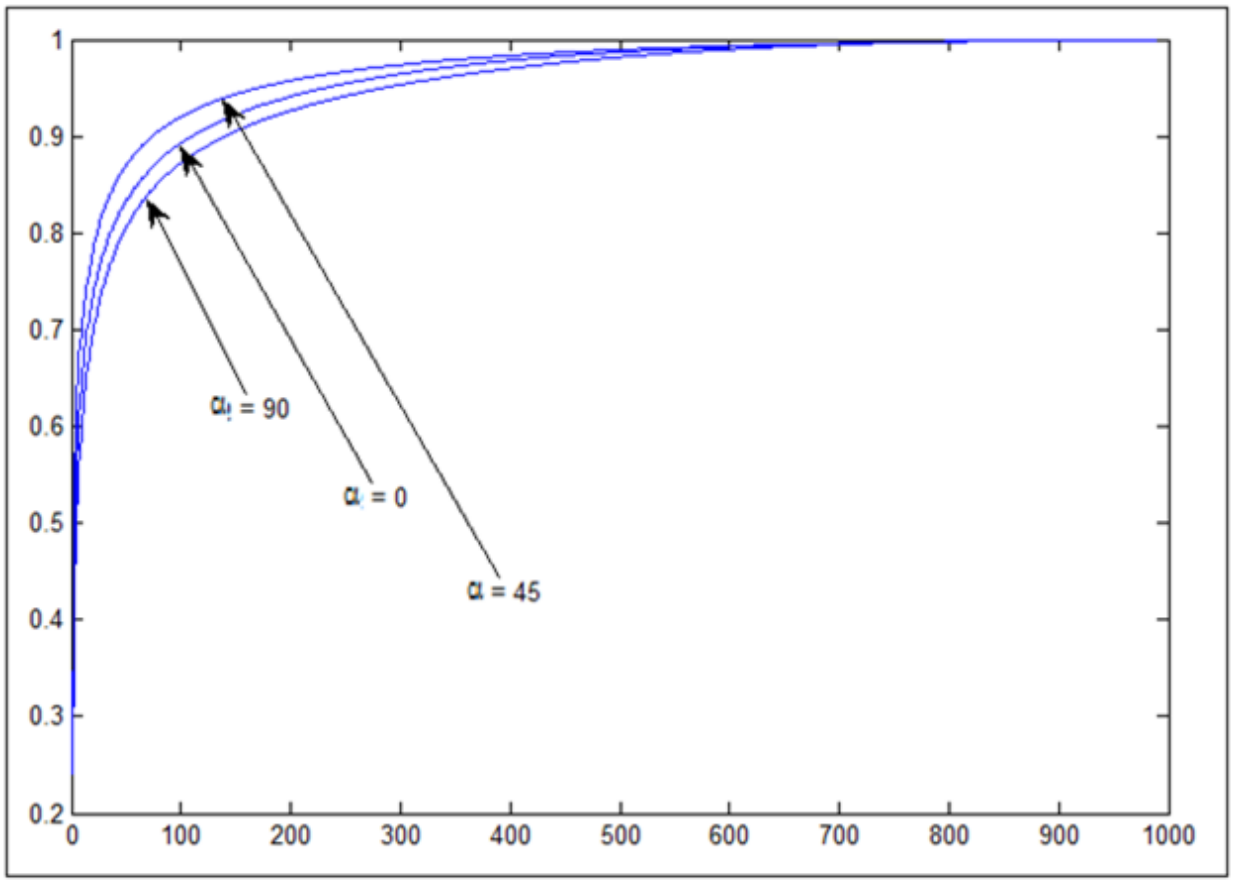

Figure 4.10 : Cumulative eigenvalues for whole structure

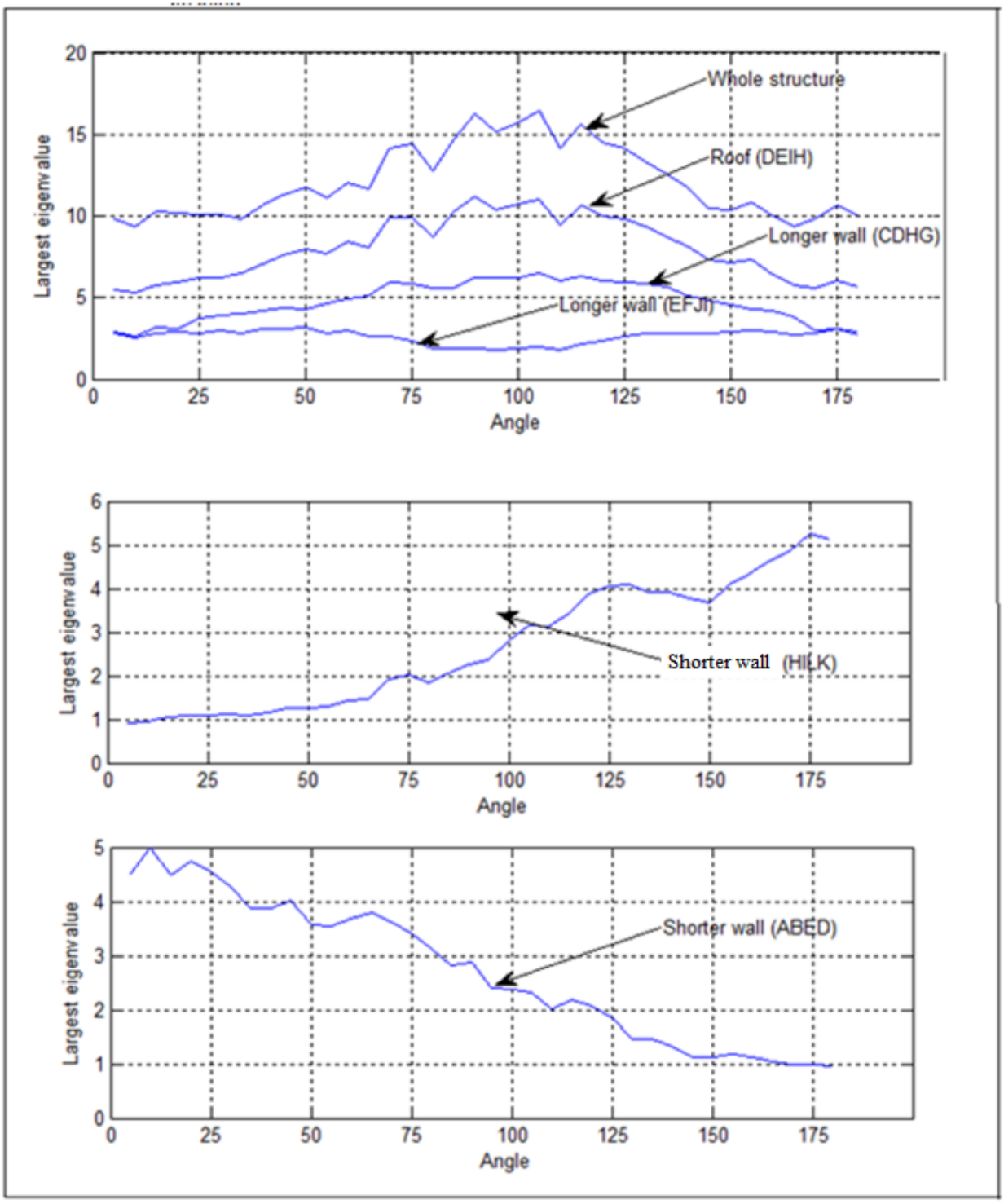

Figure 4.11 : Comparison of largest eigenvalues for different areas varying with angles

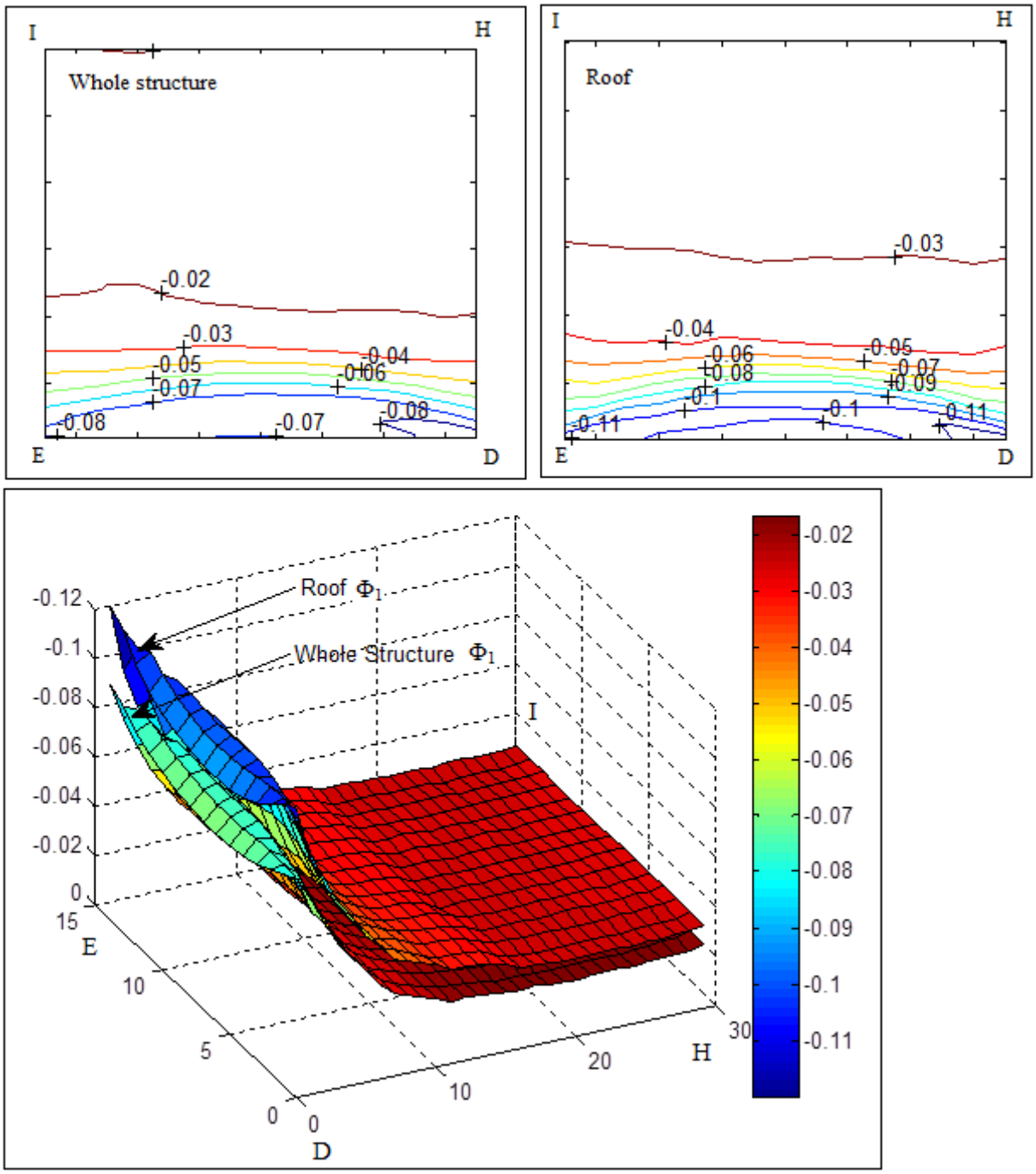

Figure 4.12 : 1st Eigenvector calculated for roof and whole structure separately for $\alpha = 0$

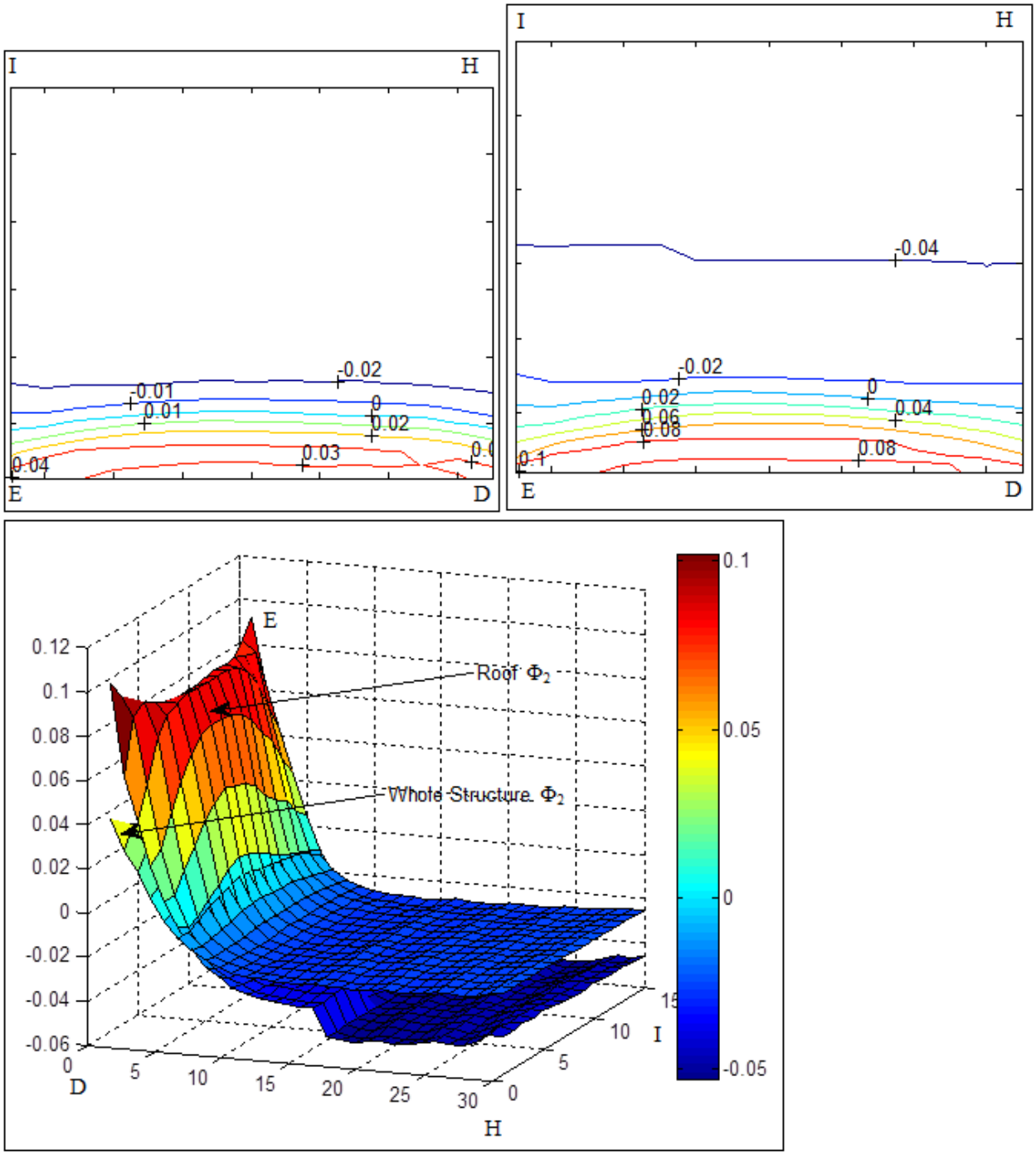

Figure 4.13 : 2nd Eigenvector calculated for roof and whole structure separately for $\alpha = 0$

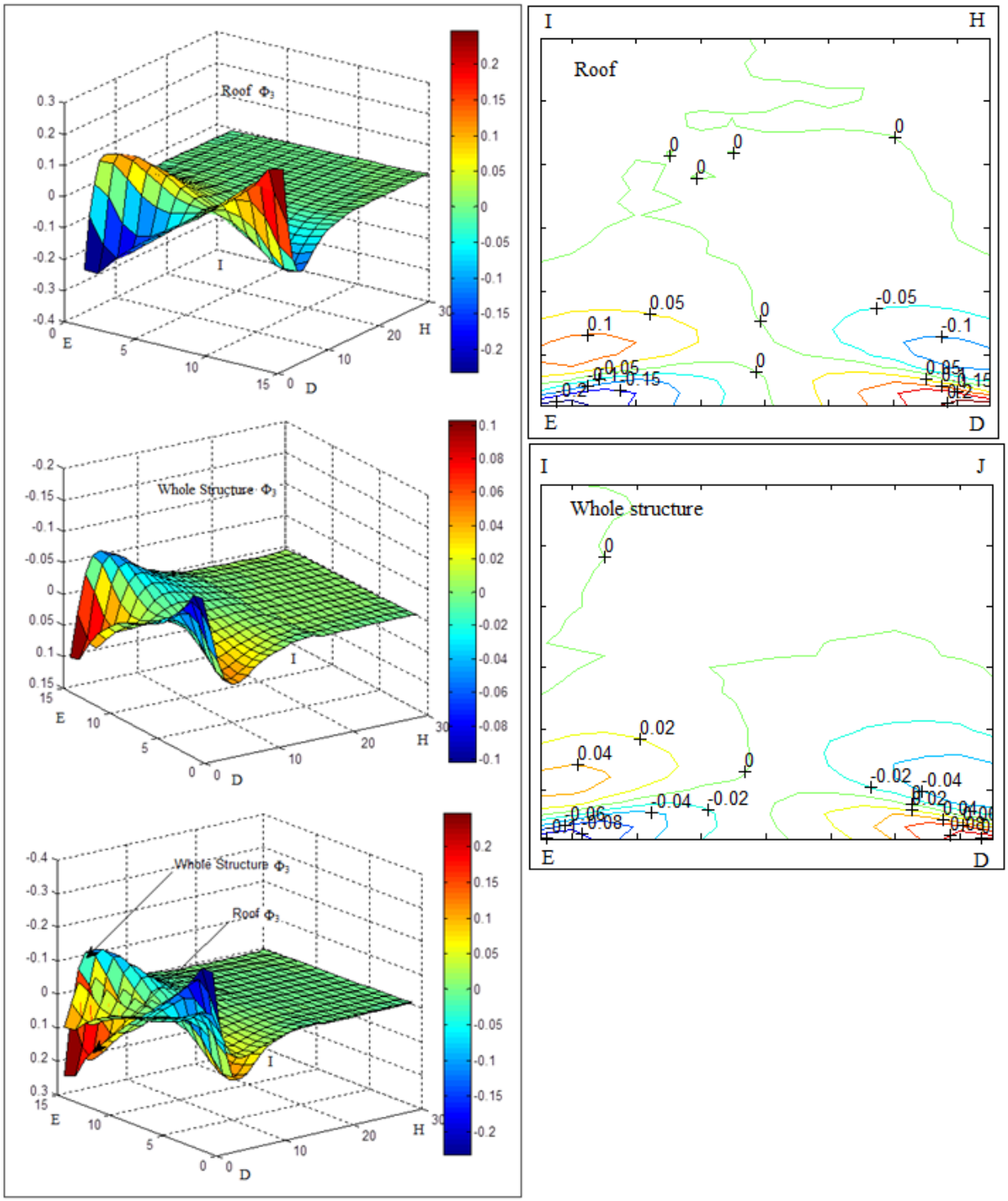

Figure 4.14 : 3rd Eigenvector calculated for roof and whole structure separately for $\alpha = 0$

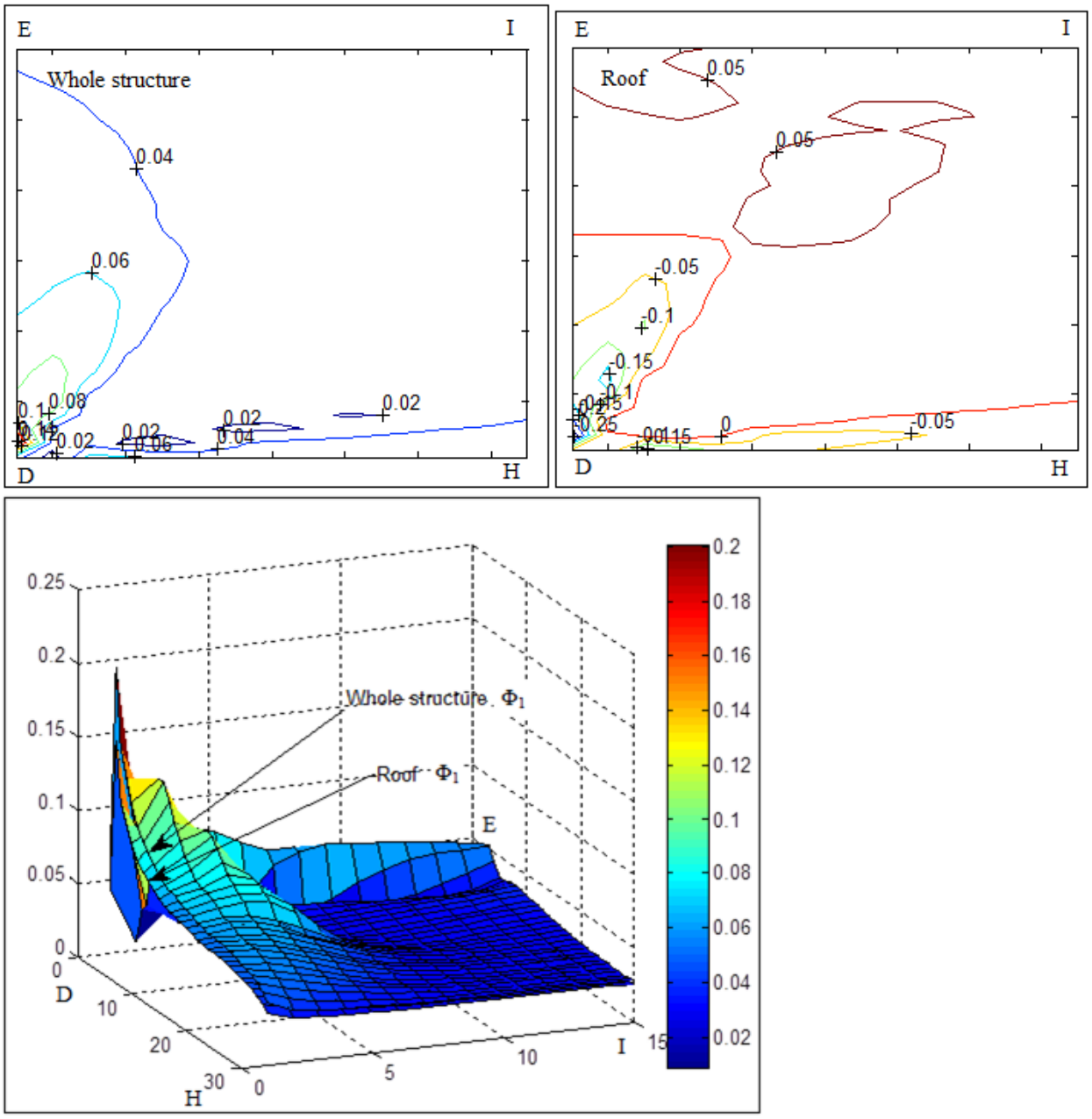

Figure 4.15 : 1st Eigenvector calculated for roof and whole structure separately for $\alpha = 45$

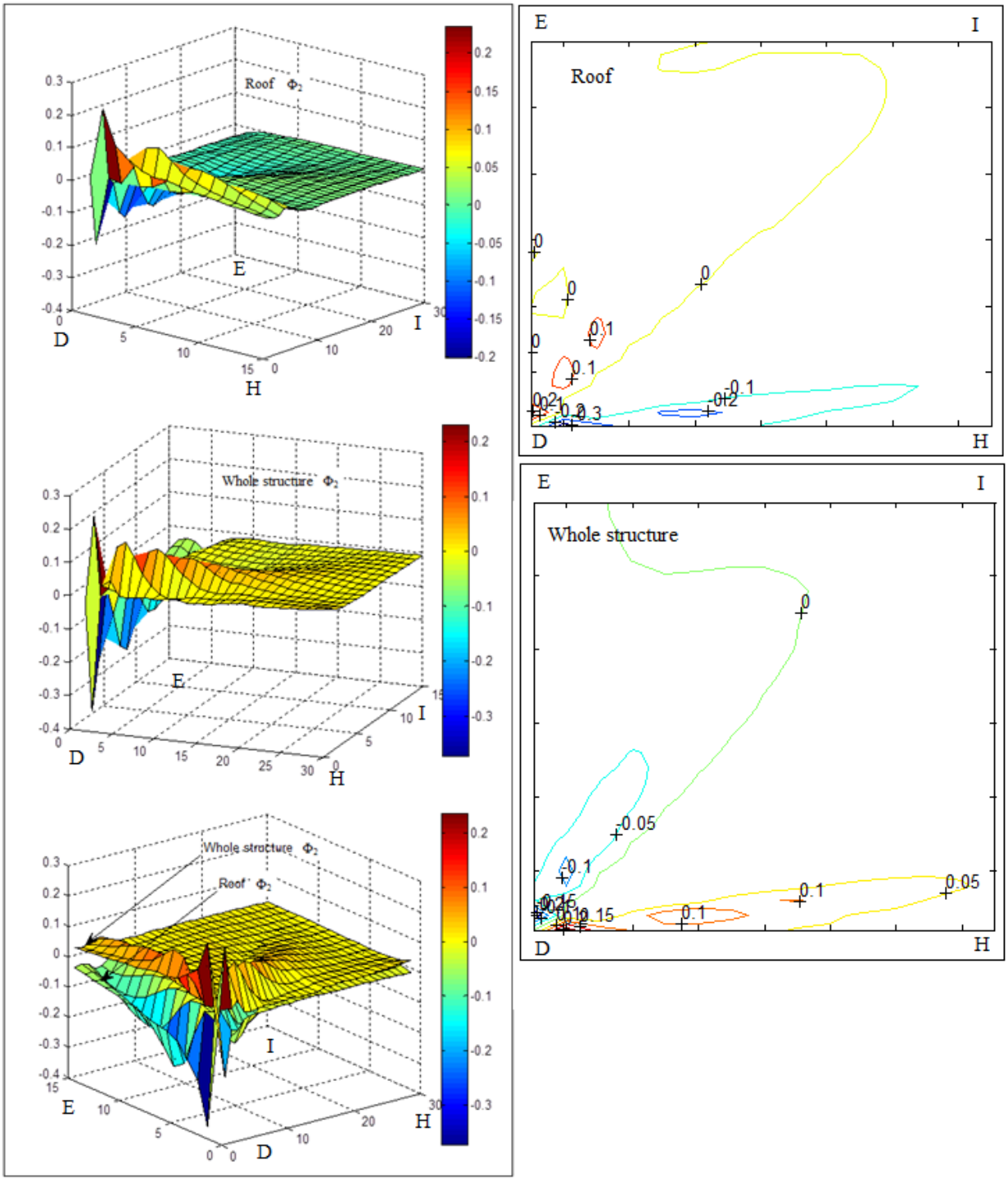

Figure 4.16 : 2nd Eigenvector calculated for roof and whole structure separately for α = 45

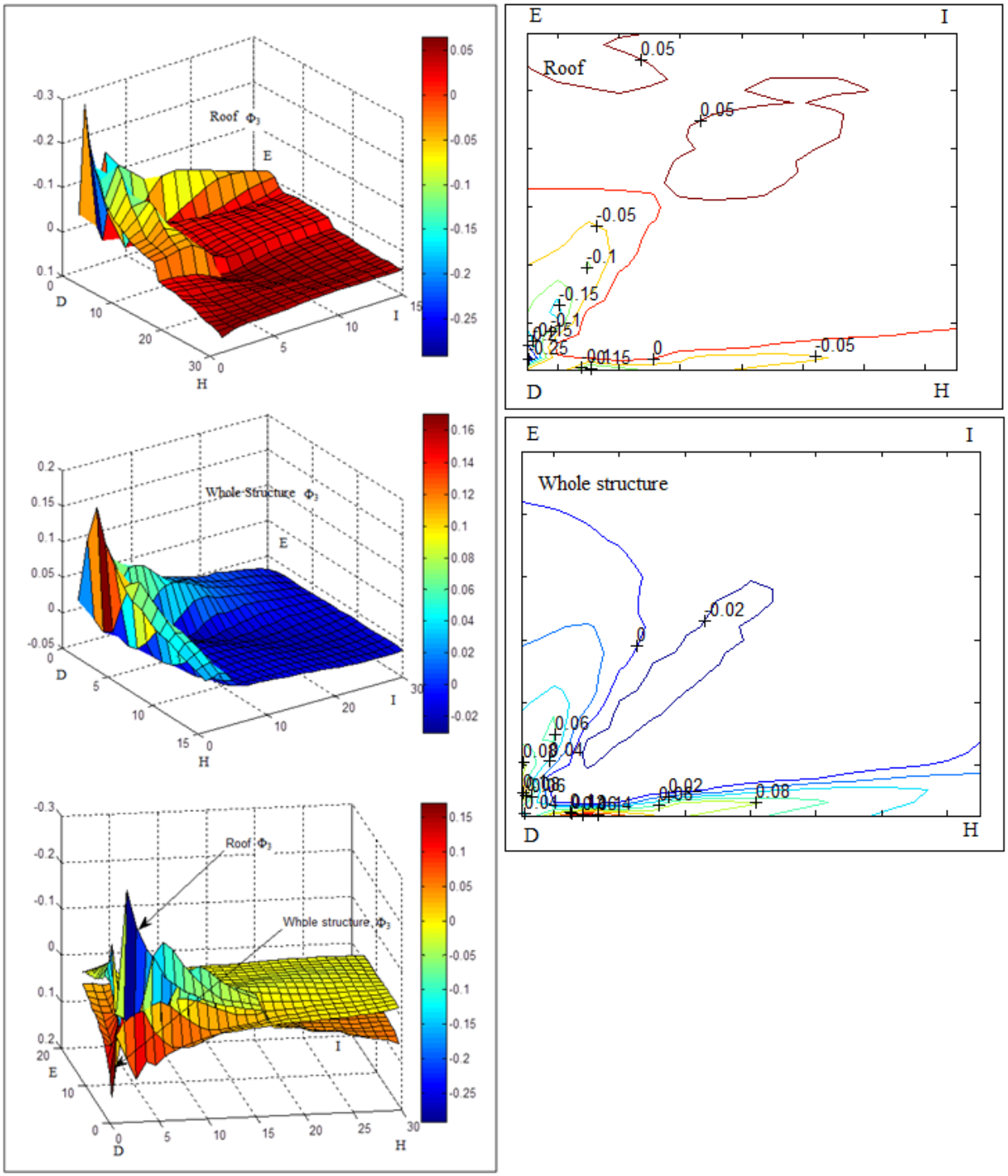

Figure 4.17 : 3rd Eigenvector calculated for roof and whole structure separately for α = 45

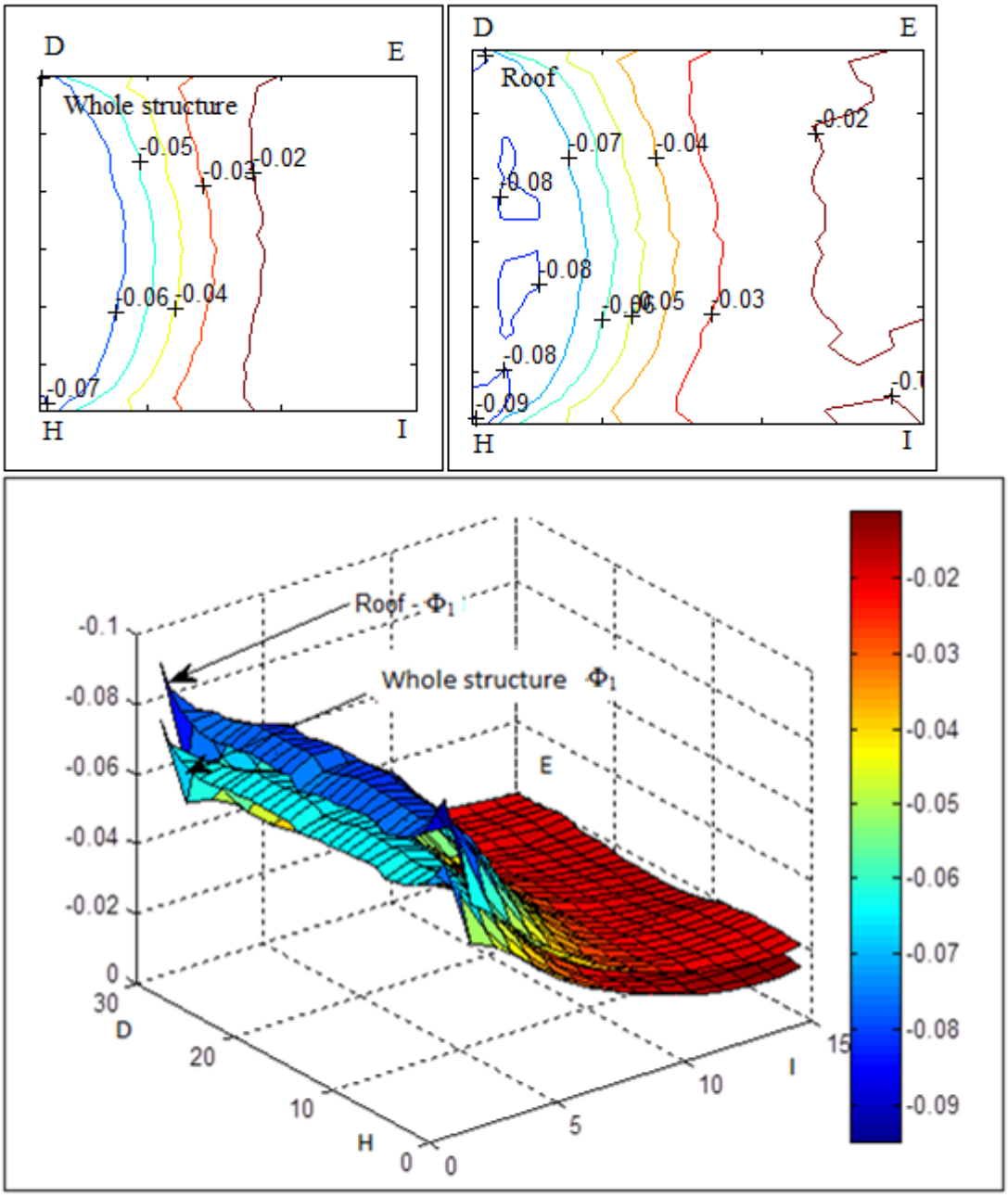

Figure 4.18 : 1st Eigenvector calculated for roof and whole structure separately for α = 90

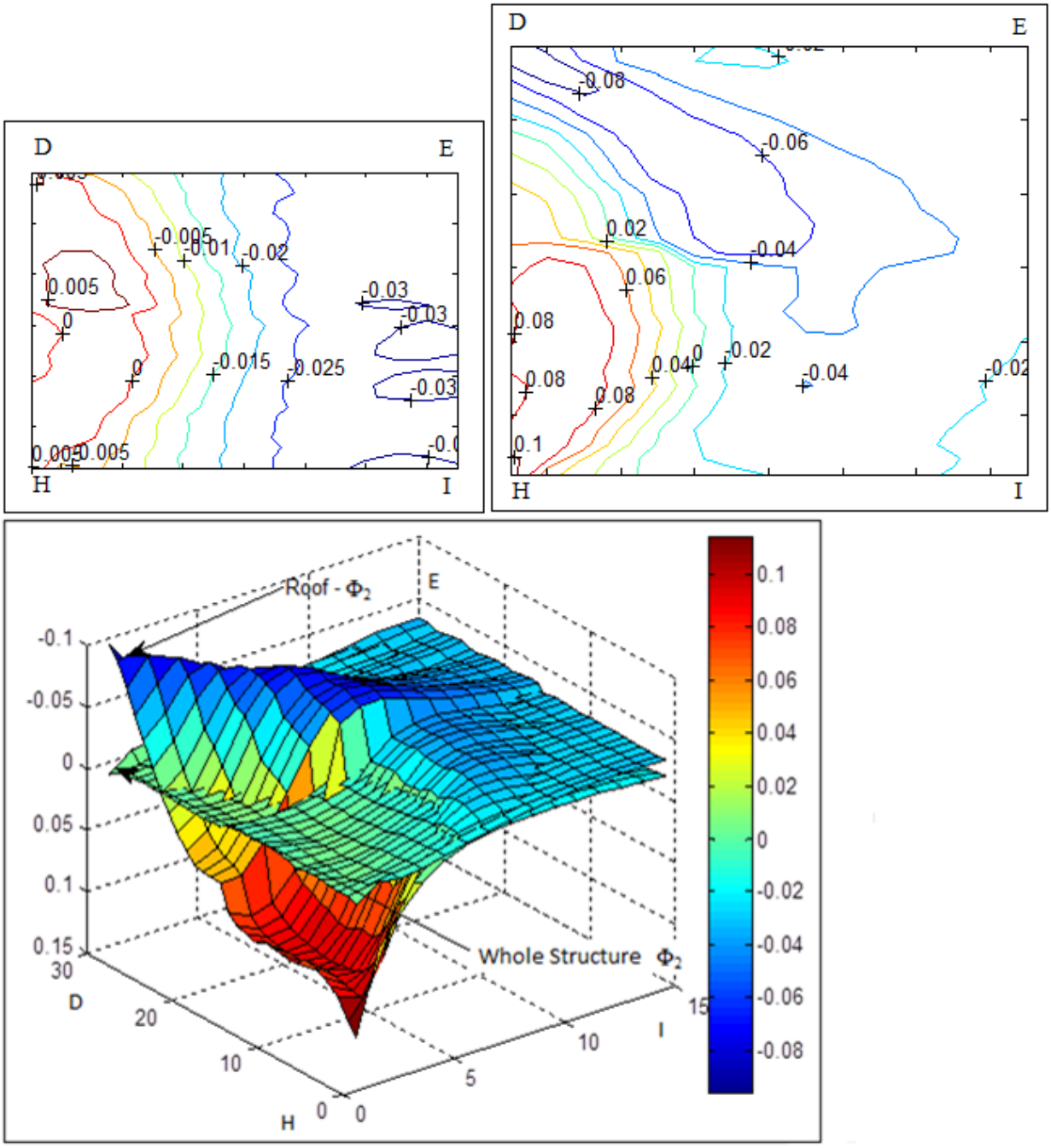

Figure 4.19 : 2nd Eigenvector calculated for roof and whole structure separately for α = 90

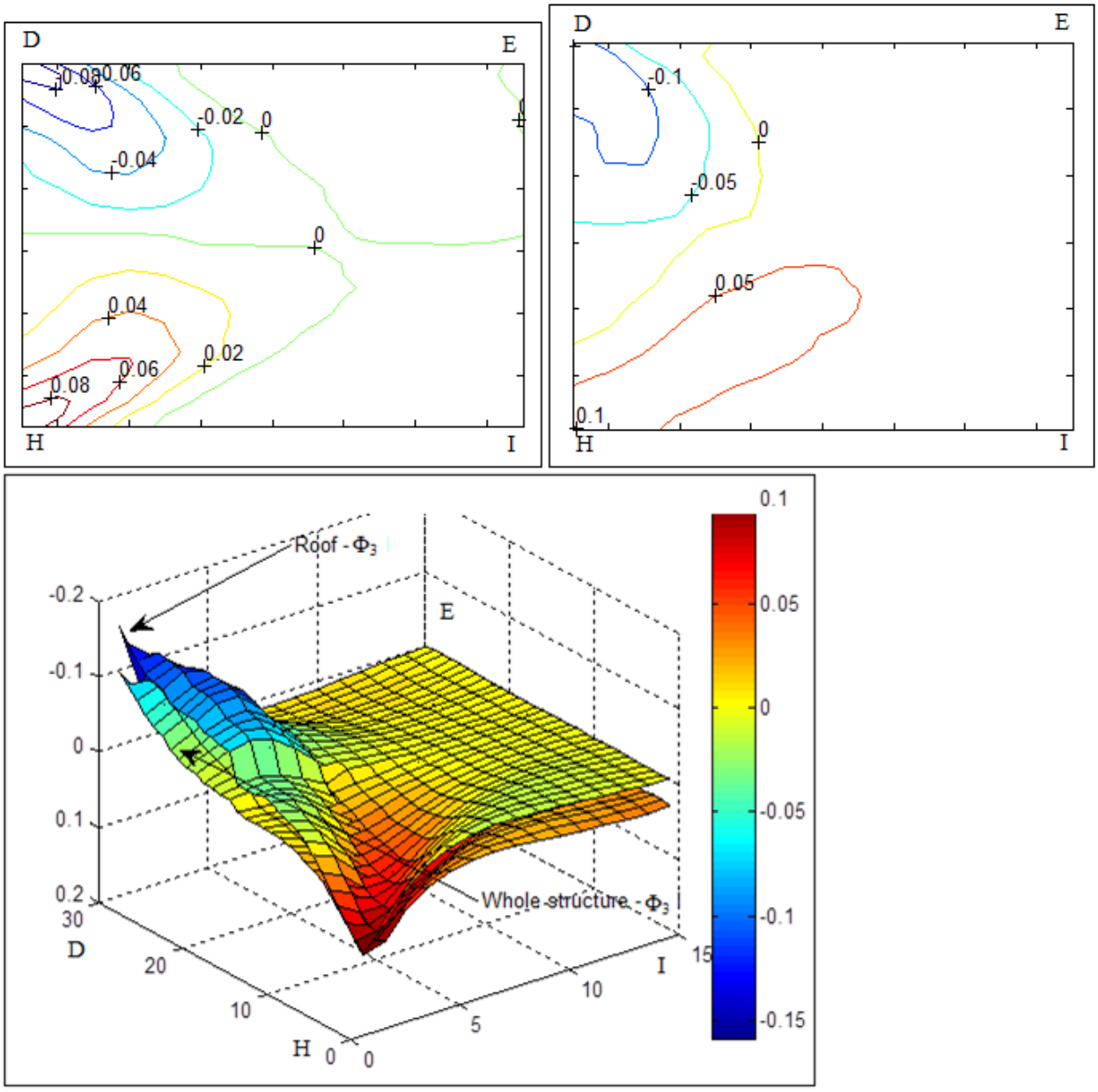

Figure 4.20 : 3rd Eigenvector calculated for roof and whole structure separately for α = 90

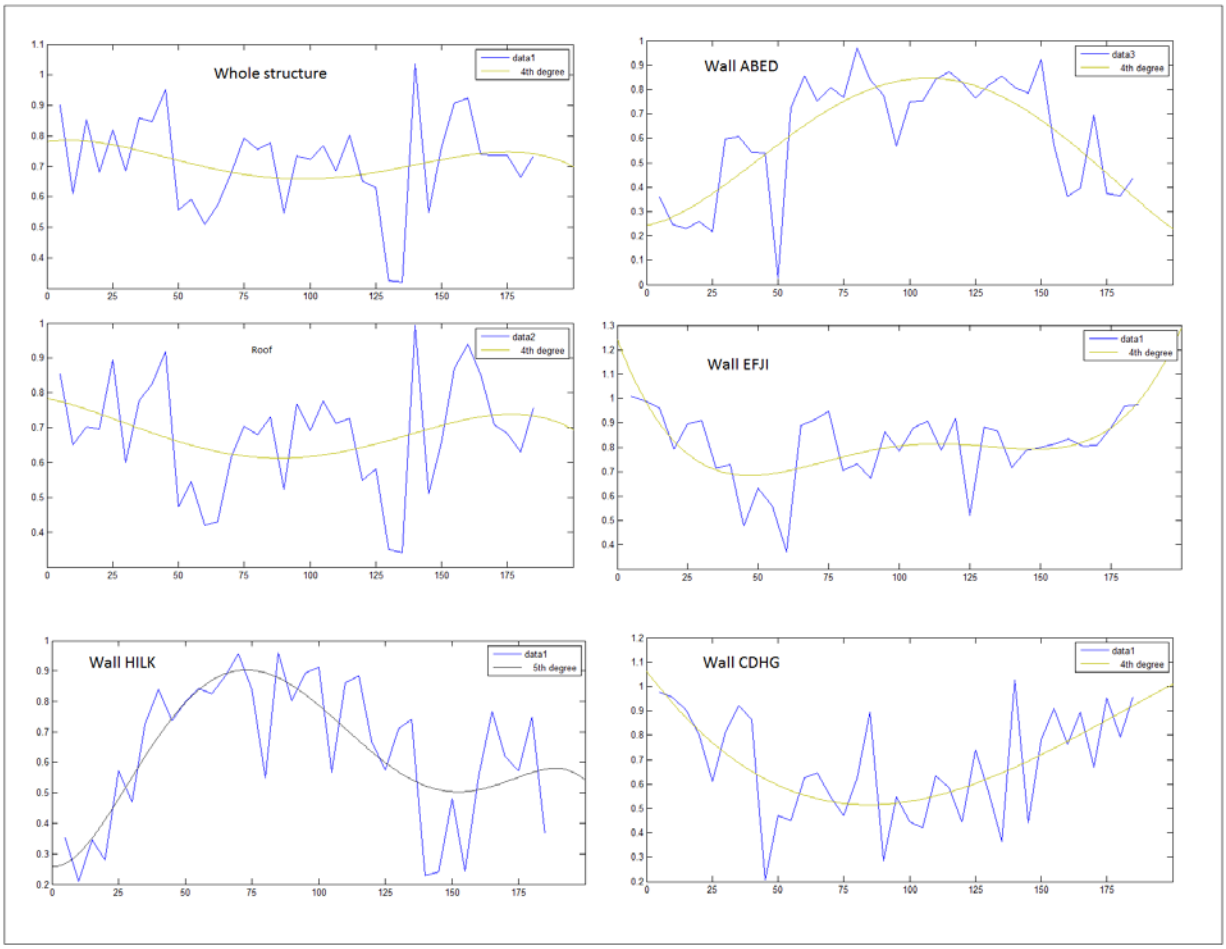

Figure 4.21: First mode contribution for different regions and different angles

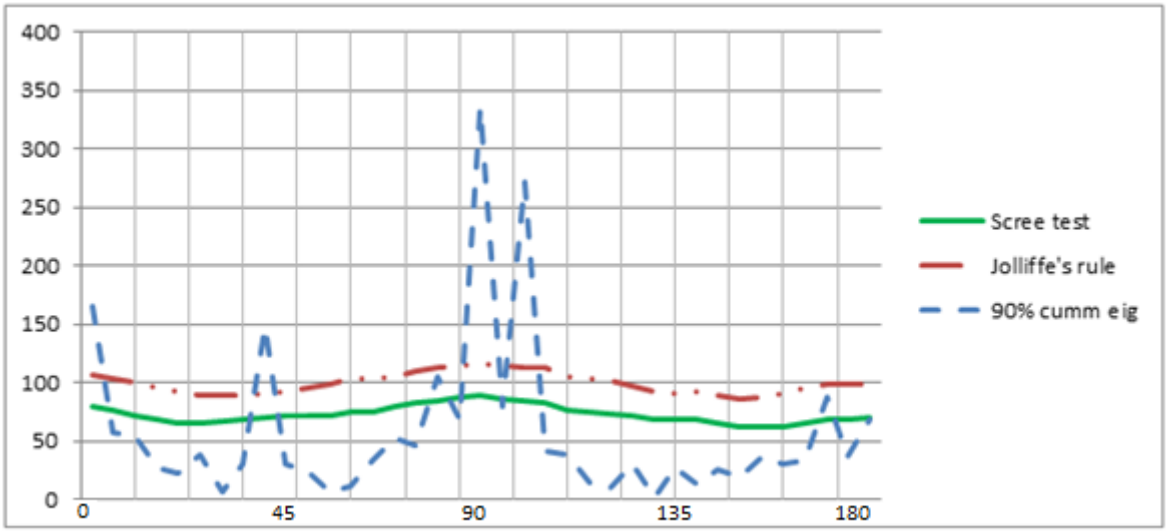

Figure 4.22 : Significant eigenvalues as given by different rules for different wind directions

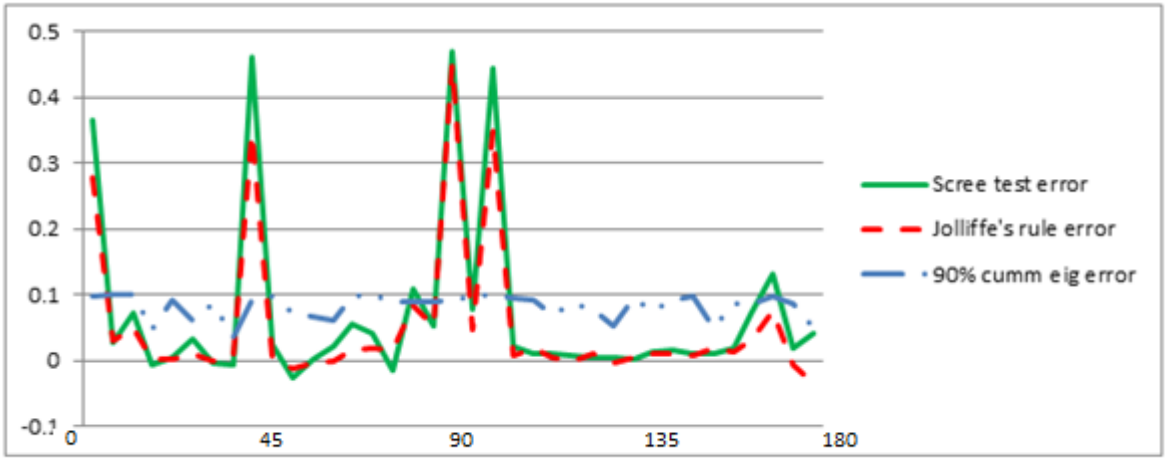

Figure 4.23 : Errors from reconstruction using the three rules for different angles

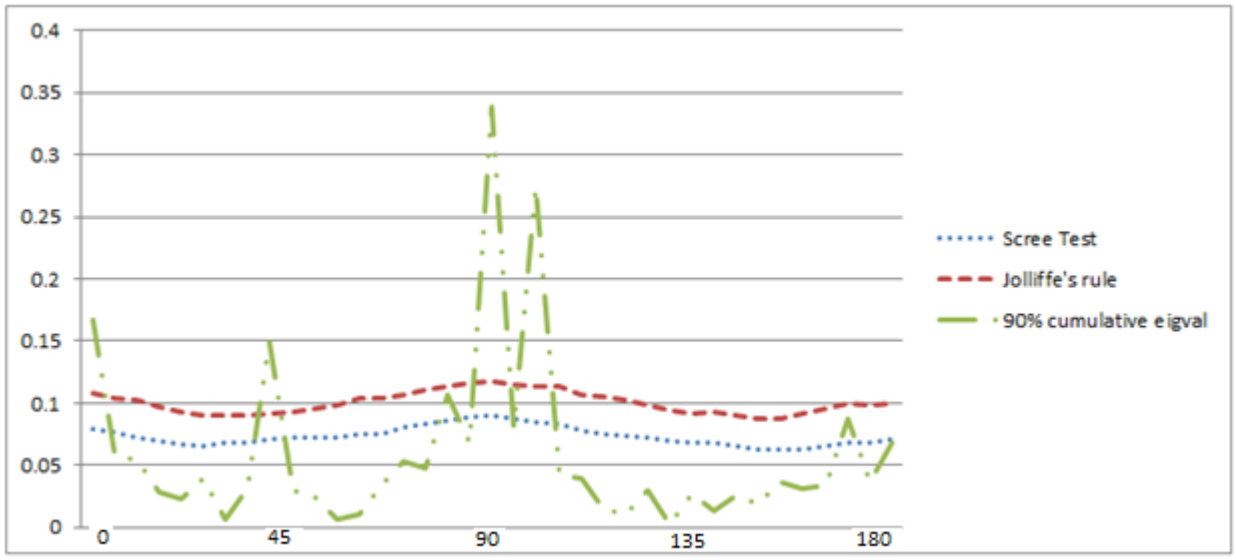

Figure 4.24 : Relative memory used

Chapter 5

Conclusions

- As expected, the largest peak pressures occurred for cornering wind directions, approximately 45 and 135 degrees.
- Wind directions at which large peak pressures occurred, required smaller number of modal contributions, to be employed in pressure reconstructions, to attain 90% of the pressure peaks.
- For walls, the above number was higher. For the windward wall it was bigger than for the leeward wall. This dependency was attributed to higher level of pressure fluctuations occurring on the windward wall.
- Among the three methods tested to determine the number of the significant modes, the 90% cumulative eigenvalue method was found to be the most effective. The Jolliffe's rule was more conservative than the scree test. All the methods showed similar effects of wind direction.
- The normalized eigenvalues obtained for the whole building were smaller than those obtained for walls and roof, analyzed separately. The shorter wall exhibited larger number of the modes required to attain 90% reconstruction of peak pressures. This dependency is expected as the energy is distributed, for the whole building, among 990 modes, while it is spread over 450, 90 and 180 modes, respectively, for the roof, and the shorter and longer walls.

- The magnitudes of the modal contributions on the roof were larger than those on the remaining surfaces of the building. This is consistent with the fact that the pressure magnitude and fluctuations on the roof are the largest.
- Overall, the obtained results were found to be consistent with findings of related POD studies reported by other researchers.
- High spatial and temporal resolutions of the wind loading data used in the present research made possible improved (than those reported by other researchers) quantification of the effects of the studied parameters and POD analyses.

References

- Bienkiewicz, B. at al (1993), “Proper Orthogonal Decomposition of Roof Pressure, Department of Civil and Environmental Engineering, Colorado State University, Colorado 80523, U.S.A”. Journal of Wind Engineering and Industrial Aerodynamics, 50 (193) 193-202.
- Cattell, R. B. (1966). “ The Scree Test For The Number Of Factors”. Multivariate Behavioral Research, 1, 245-276.
- Davenport, A. G. Chapter 2, Wind Tunnel Testing : A General Outline, (2007), The Boundary Layer Wind Tunnel Testing Laboratory, The Uni8versity of Western Ontario, Faculty of Engineering Science, London, Ontario, Canada N6A 5B9; Tel: (519) 661-3338; Fax: (519) 661-3339
- Endo, M. (2005), “ Wind tunnel modeling and analysis of wind effects on low rise buildings”’ Ph.D Dissertation, Department of Civil and Environmental Engineering, Colorado State University.
- Ham, H. J. (1998), Ph.D. Dissertation, “ Turbulence Effects On Wind-Induced Building Pressure”. Department of Civil and Environmental Engineering, Colorado State University, Colorado 80523, U.S.A.
- Jackson, D. A. (1993),”Stopping Rules In Principal Component Analysis : A Comparison Of Heuristical And Statistical Approaches”, Department of Zoology, University of Toronto, Toronto, Canada. Ecology, 74(8), 1993, pp. 204-2214

- Jolliffe, I. T., Chapter – 4 2nd Ed," Principal Component Analysis", Department of Mechanical Sciences, King's College, University of Aberdeen, Aberdeen AB24, UK. 2002, 1986- Springer Veriag, New York Inc.
- Lu, L. J. and Smith, C. R. (1991), "Velocity Profile Reconstruction Using Orthogonal Decomposition" Department of Mechanical Engineering, Lehigh University, Bethlehem, PA 18025, USA, Experiments in Fluids 11, 247-254(1991)
- Lumley, J. L. (1967) ," The Structure Of Inhomogeneous turbulent flows, Atmospheric Turbulence And Radio Wave Propagation", Yaglom, A. Y. and Tatarsky, 4th Ed, Nauka, Moscow, 1967.
- Main, J. A. and Fritz, W. P., (2006), Database Assisted Design For Wind : Concepts, Software, And Examplaes For Rigid And Flexible Buildings, National Institute Of Standards And Technology.
- Raiche, G. et al (2012), " Non-Graphical Solution For Catell's Scree Test", University of Montreal, Canada. Methodology 2013; Vol.9(1):23-29.
- Wu, C. H. (2012), Master's Thesis Dissertation, " Application Of Model Reduction Tools In Analysis Of Wind Induced Pressures On Low Rise Buildings", Department of Civil and Environmental Engineering, Colorado State University, Colorado 80523, U.S.A.